Thesis for the degree of Doctor of Philosophy

Experiments in Solenoidal Spectrometers – from Isospin Breaking to Nuclear Fission

Anna Kawęcka

Department of Physics and Astronomy
Chalmers University of Technology
Gothenburg, Sweden 2026

Experiments in Solenoidal Spectrometers – from Isospin Breaking to Nuclear Fission
Anna Kawęcka
ISBN: 978-91-8103-427-1.

Doktorsavhandlingar vid Chalmers tekniska högskola
Ny serie nr 5884
ISSN 0346-718X
https://doi.org/10.63959/chalmers.dt/5884

Department of Physics and Astronomy
Chalmers University of Technology
SE-412 96 Gothenburg
Sweden
Telephone +46 (0)31-7721000

Cover: Simulated trajectories of charged particles propagating in a uniform field created by a solenoid magnet, shown as a frontal (transverse) projection.

Chalmers Reproservice
Gothenburg, Sweden 2026

Experiments in Solenoidal Spectrometers – from Isospin Breaking to Nuclear Fission

Anna Kawęcka
Department of Physics and Astronomy
Chalmers University of Technology

Abstract

The outcome of two nuclear physics experiments extracting very different physics information is presented. They both employ (d,p) reactions in inverse kinematics, demonstrating the versatility of solenoidal spectrometers.

The first experiment at Argonne National Laboratory, using the HELIOS setup, studied breaking of the isospin symmetry in excited states of ^{18}O and ^{18}F. Relative spectroscopic factors of the populated states are compared to investigate the similarity of isobaric analogue states in the isospin multiplet $A = 18$. The results show overall good agreement between analogue states and consistency with shell-model predictions for most levels. No statistically significant evidence for enhanced isospin symmetry breaking was observed within the experimental uncertainties.

The second part of the thesis focuses on extending the ISS setup at ISOLDE, CERN, to allow studies of fission of neutron-rich isotopes. To cope with the limited intensity available at radioactive beam facilities, an efficient setup for the detection of fission fragments was designed, installed, and commissioned. The setup performed as expected and enabled a proof-of-principle measurement of the fission of ^{233}U. While the full extraction of physics observables has not yet been performed, the work demonstrates the feasibility of the method and establishes a foundation for future studies of fission in exotic nuclei.

Keywords: Nuclear Physics, Isospin, Isobaric Analogue States, Nuclear Shell Model, Nuclear Fission, r-process, ANL, HELIOS, CERN, ISOLDE, ISS

Statement of contributions

This work is the result of a collaborative effort of the Experimental Subatomic Physics Group at Chalmers and many international collaborators, which is typical in our field.

The experiment presented in Chapter 2 was performed at Argonne National Laboratory with the HELIOS setup, measuring $^{17}\mathrm{O}(\mathrm{d},\mathrm{p})^{18}\mathrm{O}$ and $^{17}\mathrm{F}(\mathrm{d},\mathrm{p})^{18}\mathrm{F}$ reactions, proposed by Jack Henderson, University of Surrey. The author worked on preparing and executing the experiment. The data analysis and DWBA calculations were performed by the author of this thesis. The calibration of the HELIOS silicon array, as well as shell model calculations were not part of this work and were provided by collaborators. The author actively participated in the subsequent interpretation of the results and discussions with the spokesperson of the project.

The decision to participate in the HELIOS experiment was motivated on the one hand by the fact that the Chalmers group lacked prior to this project experience with solenoidal spectrometers and on the other hand, that the beam time for the other part of this project, fission studies with solenoidal spectrometers, was scheduled later than planned. This opened the possibility to not only participate in the HELIOS experiment, but also to work on the data analysis resulting from it.

Fission studies with solenoidal spectrometers, originally thought to be the entire focus of this project, were performed within the IS739 experiment at ISOLDE, CERN, using the ISOLDE Solenoidal Spectrometer (ISS) with a number of new detectors developed within this project (Chapter 3). The author was one of the spokespersons of the experiment. The design of the experiment was a collaborative effort of the members of the Chalmers group. The author of this thesis was one of two PhD students working on this project. She worked on the design of the experiment from the early stages, the choice of detector types and their configuration, the preparation of analysis tools, the writing of the proposal, the mounting and testing the detectors. Moreover, the author worked on testing digital data acquisition modules and the development of the data acquisition system used in the IS739 experiment. After the experiment, the author was responsible for the calibration of the ISS silicon array and worked within the Chalmers group on extracting physics information, which is ongoing as of the writing of this text.

The author of this thesis participated in several other experiments at ISOLDE, CERN. The reason for participating in those experiments was twofold: to obtain experience with the ISS and ISOLDE and, because members of the ISS collaboration, are expected to help others with their experiment, enhancing support during IS739. In particular the author participated in the following

experiments: IS659 – β-decay of ^{9}Li and ^{8}He at IDS; IS677 – ^{11}Be(d,p)^{12}Be reaction at ISS; IS710 – ^{27}Na(d,p)^{28}Na reaction at ISS; IS686 – spectroscopy of ^{107,108,109}Sn through (d,p) transfer reactions at ISS; IS587 – ^{68}Ni(d,p)^{69}Ni at ISS; IS727 – ^{50}Ca(d,p) at ISS; IS742 – ^{132}Sn(d,p) at ISS. The author also participated in a fusion-fission experiment at INFN Legnaro studying exotic $N = 50$ nuclei via fusion-fission using the AGATA-PRISMA setup, and in an experiment at Argonne National Laboratory investigating the d(^{48}Ca, t)^{47}Ca and d(^{48}Ca, p)^{49}Ca reactions.

Acknowledgements

The nearly five years I spent working on this project were both eventful and intellectually rewarding. The work presented in this thesis would not have been possible without the support of many people.

First, I would like to express my sincere gratitude to my supervisor, Andreas Heinz, for his guidance and support throughout this process. I have learned a great deal from you, and I am truly grateful for the opportunity to work under your supervision. I am very grateful to my co-supervisor, Thomas Nilsson, for valuable suggestions and discussions. I would also like to thank my examiner, Christophe Demaziere, for his guidance and valuable suggestions. I am especially grateful to Håkan Johansson for his detailed comments on this thesis, his insights into nuclear physics experiments, and for introducing me to the world of data acquisition systems. Working with you was a great pleasure.

I would like to thank Björn Jonson for the inspiring physics discussions and for sharing his extensive experience in nuclear physics with me. Special thanks go to my former colleague Hans Törnqvist for his help with programming whenever challenges arose and for his work on the preparation and running of IS739. I am also grateful to my former colleague Matthias Holl for his support when simulation codes proved difficult. I would like to thank the postdoctoral researchers in our group, Erik Jensen and Henna Joukainen, for their help during the experiment and analysis. Many thanks to former students in the group, Alice Svärdström and Björn Johansson, for their help with the experiment preparation and data taking. I am deeply thankful to the entire group for their support and for fostering such a welcoming and collaborative environment.

I am grateful to have shared this journey with my fellow PhD student, Maria Vittoria Managlia. It was a pleasure to work alongside you and to share both the joyful and challenging moments–even those late nights in the control room. I gained not only a colleague but also a friend.

I would not have been able to complete this work without the support of Ben Kay, whose valuable insights contributed to the preparation of the IS739 experiment and who warmly welcomed me to ANL during my visits there. I owe you my sincere thanks, as your support was instrumental in making this work possible.

I am extremely grateful to have worked with Jack Henderson. Thank you for the opportunity to join your experiment and to contribute to the data analysis. I learned a great deal from you and greatly appreciate your insights, suggestions, and support throughout the process.

To both Ben Kay and Jack Henderson, I would like to thank you for the time invested in analysis meetings. Thank you, Jack, for also coming to Chalmers to work on the paper. I was very lucky to work with both of you!

During my PhD, I had the opportunity to meet many wonderful people, far too many to name individually. Special thanks to the IS739 collaboration and all the people who helped us with the experiment! I would also like to thank the entire ISS collaboration for their guidance and support, especially Liam Gaffney, Patrick MacGregor and David Sharp.

Finally, I would like to express my deepest gratitude to my husband, Wojtek. Thank you for your unwavering support and understanding throughout this journey. Having gone through this process yourself, your support meant more than I can express. I am also deeply grateful to my parents and siblings for their constant encouragement.

Contents

Chapter 1

Introduction

Atomic nuclei are extremely small—on the order of 10^{-12} to 10^{-13} cm in diameter—and can contain anywhere from a single proton to a few hundred protons and neutrons. These nucleons give rise to a mean field potential and interact primarily through the nuclear and Coulomb forces. As a result, the nucleus is a highly complex many-body system, where the interplay between nucleon-nucleon interactions and many-body dynamics gives rise to diverse behaviour (see e.g. [1–3]).

Understanding the structure of atomic nuclei is challenging. Despite more than a century of study [4], no single theoretical framework has succeeded in describing all known isotopes and their excitations across the entire nuclear chart. The complex nature of the nucleon-nucleon interaction and the collective behaviour of many interacting particles give rise to a wealth of phenomena [3], including diverse nuclear shapes and the appearance of halo structures [5].

Nuclear physics seeks to explain these emergent many-body features and to understand one of nature's most fundamental systems—the atomic nucleus. It aims to describe the underlying nuclear forces and determine how they shape the properties of nuclei from the lightest to the heaviest elements. Achieving this understanding is essential for explaining the wide range of observed nuclear phenomena and how and why the manifestations of these phenomena change from one nucleus to another. In turn, this knowledge is crucial for understanding processes in the universe, such as the creation of elements, as well as for applications, including energy production and medical utilisation [6].

To deepen our understanding of nuclei, experimental investigations are essential. They typically aim to populate specific nuclear states and probe their properties. A state can be populated using direct or compound nuclear reactions or decay processes that bring the nucleus into an excited configuration of interest. Note that this is not a complete list, e.g. electromagnetic processes such as Coulomb excitations, can serve the same purpose. Ideally, the popula-

tion is done selectively so that only the state of interest is populated and there is no interference from other states.

Once populated, the state is probed by measuring observables such as excitation energies, spins, parities, lifetimes, and transition strengths. It is important to note that only a limited number of nuclear properties can be measured directly, and most of the quantities mentioned above are inferred from transitions to and from the state. These measurements allow quantum numbers to be assigned and key properties of the populated states to be determined. This provides us with deep insights into nuclear forces and symmetries. For example, the approximate isospin symmetry [7], the evolution of shell structure [8], and pairing correlations [9] can be tested and quantified. Measurements provide essential input for theoretical models.

There are many experimental approaches to study nuclei (see for example Ref. [10] for a modern overview). These include *scattering experiments*, which probe the internal structure of nuclei by observing how projectiles are deflected; *spectroscopy studies*, which detect and characterise excited nuclear states through the particles or radiation they emit; *decay studies*, which explore how unstable nuclei transform spontaneously over time; and *nuclear reaction experiments*, in which nuclei are formed through collisions between projectile and target nuclei.

Nuclear reactions typically require sufficient kinetic energy to overcome the Coulomb repulsion arising from their positive charge, although quantum tunnelling permits some processes to occur at sub-barrier energies. Above the Coulomb barrier, a wide variety of reaction mechanisms can become accessible. Among them is an important class – *transfer reactions* [11], in which a small number of nucleons are transferred between the reactants during the interaction. Transfer reactions can be divided into two groups: *direct transfer reactions* [12] and *compound nuclear reactions*. For direct reactions, the transfer occurs in a single, relatively fast step and involves only a limited number of degrees of freedom. It is typically considered peripheral. Direct reactions differ from the compound nuclear mechanism, where the projectile and target form a highly excited intermediate system where the energy is distributed across the available internal degrees of freedom before one or several ejectiles are emitted in a process known as *fusion-evaporation*.

Direct transfer reactions allow for the study of excited states in nuclei and serve as sensitive probes of single-particle structure, pairing correlations, and shell evolution. What makes them particularly valuable is their ability to provide information on the angular momentum transferred during the reaction, which in turn helps to determine the spin and parity of the populated nuclear levels. The angular distributions of the reaction ejectiles exhibit characteristic shapes that depend on the transferred orbital angular momentum. This is illustrated in Fig. 1.1, which shows theoretical angular distributions calculated for different angular momentum transfers in a (d,p) reaction (neutron adding).

For more details, see Section 2.2.

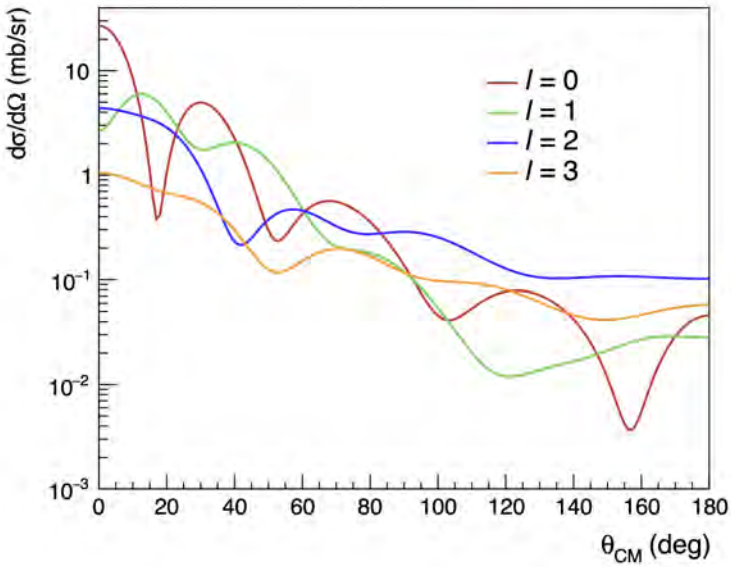

Figure 1.1: Distorted-wave Born approximation (DWBA) [11] calculations of differential cross sections for the ^{17}O(d, p)^{18}O neutron transfer reaction at a ^{17}O beam energy of 10.12 MeV/u. The angular distributions are shown as a function of the centre-of-mass angle for different orbital angular momentum transfers ℓ.

In heavier nuclei, where collective states and high level densities lead to strong configuration mixing, transfer reactions may also populate so-called *doorway states* [13]. These states serve as a gateway, allowing the redistribution of excitation energy from single-particle-like configurations into more complex compound-nucleus formation.

Traditionally, nuclear physics experiments have been performed using a light, accelerated beam (typically protons, deuterons, and helium isotopes) impinging on a stable, often heavier, targets. This method is therefore called *normal kinematics* and was a necessity, given the technical challenges associated with accelerating heavy ions in earlier periods of the field. The target material must also be a stable or at least long-lived isotope for practical, safety, and production-related reasons. However, of more than 3300 isotopes discovered to date, only about 250 are stable, which significantly restricts the range of nuclei accessible with conventional techniques. To break this limitation, experiments began to employ *inverse kinematics*, in which a heavier ion, potentially radioactive, is accelerated and directed onto a lighter target. This became possible only with

the technical developments of accelerator and beam-production technologies, which now allow the delivery of sufficiently intense and high-quality heavy-ion beams. Inverse kinematics opens up a much wider variety of beam-target combinations than normal kinematics and enables studies of unstable nuclei far from the valley of β stability [14].

1.1 Scope of the thesis

The work presented in this thesis addresses two fundamental questions in nuclear physics using a versatile experimental approach. First, a study of isospin symmetry and its breaking [15], with an investigation whether the observed symmetry breaking can be reproduced by theoretical calculations. Second, it aims to deepen our understanding of fission of neutron-rich nuclei, which plays an essential role in the formation of the heaviest elements in the universe [16–18].

Although these two topics are very different in nature, they are connected by the experimental approach—neutron addition in solenoidal spectrometers [19] in inverse kinematics—used to study them. The experimental method used is sufficiently flexible to address both problems.

The original motivation was the study of fission barriers in neutron-rich nuclei through the $(\mathrm{d}, \mathrm{p}f)$ reaction with a solenoidal spectrometer. However, experimental delays opened an opportunity to apply the same experimental approach to an investigation of isospin symmetry breaking through studies of the mirror nuclei ^{18}O and ^{18}F, formed via $^{17}\mathrm{O}(\mathrm{d}, \mathrm{p})^{18}\mathrm{O}$ and $^{17}\mathrm{F}(\mathrm{d}, \mathrm{p})^{18}\mathrm{F}$ reactions in inverse kinematics. As a result, this thesis demonstrates how a single experimental approach can address two different but fundamental problems in nuclear physics: the origin of heavy elements in the universe and the nature of isospin symmetry in atomic nuclei.

1.2 Transfer reactions in normal and inverse kinematics

Inverse kinematics enables the use of unstable ion beams for direct reaction studies and therefore provides access to nuclear structure properties far from stability. However, it also introduces kinematic effects that limit the achievable experimental energy resolution. To understand the origin of these effects, it is instructive to consider the kinematics of a transfer reaction in both inverse and normal kinematics.

A diagram of a transfer reaction in the centre-of-mass (CM) and laboratory frame is presented in Fig. 1.2. A heavy beam and a light target, with masses m_a and m_b respectively, interact to produce ejectiles of masses m_1 (the light

product) and m_2 (the heavy recoil). The velocity of particle i in the laboratory frame is denoted as $\vec{u}_i$, and its velocity in the centre-of-mass frame is denoted $\vec{v}_i$. The corresponding scattering angles are written as $\theta_{\mathrm{lab},i}$ in the laboratory frame and $\theta_{\mathrm{cm},i}$ in the centre-of-mass frame. This general description applies, for example, to neutron-adding (d, p) reactions, where m_1 is the outgoing proton and m_2 is the recoil nucleus.

In the centre-of-mass frame, transfer reactions in normal and inverse kinematics are indistinguishable. In the laboratory frame, however, the emission angle of the light ejectile changes considerably in inverse kinematics. This is illustrated in Fig. 1.3, which shows the relationship between the centre-of-mass frame velocity, $\vec{v}_{\mathrm{cm}}$, the ejectile velocity in the laboratory frame $\vec{u}_i$, the ejectile velocity in the centre-of-mass frame $\vec{v}_i$, and the corresponding scattering angles $\theta_{\mathrm{lab},i}$ and $\theta_{\mathrm{cm},i}$.

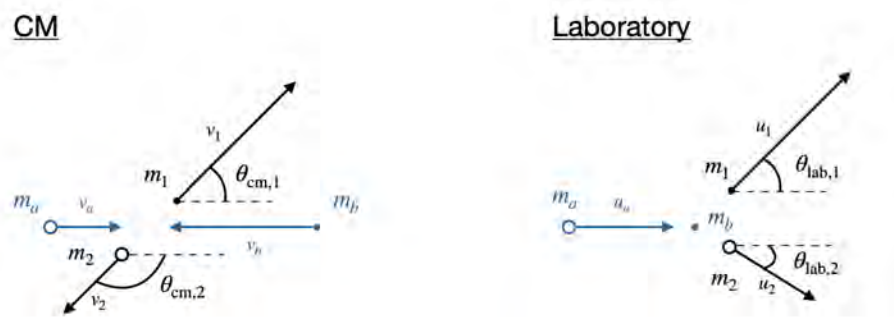

Figure 1.2: A schematic representation of a two-body reaction in the centre-of-mass and the laboratory frames in inverse kinematics. Definitions of symbols are given in the text.

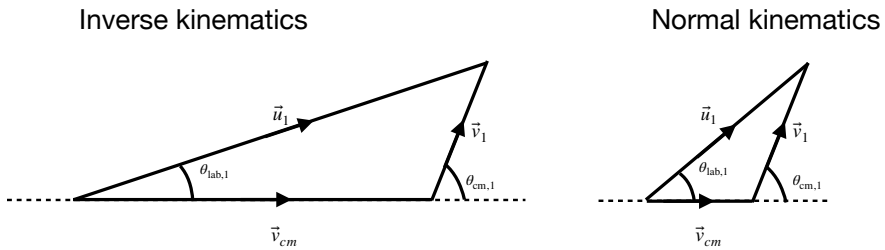

Figure 1.3: Schematic illustration of the relationship between centre-of-mass and laboratory quantities for normal and inverse kinematics.

The relationship between the velocity of a particle i in the centre-of-mass frame and its velocity in the laboratory frame is

$$\vec{v}_i = \vec{u}_i - \vec{v}_{\text{cm}}, \tag{1.1}$$

where the centre-of-mass frame velocity, $\vec{v}_{\text{cm}}$, is given by

$$\vec{v}_{\text{cm}} = \frac{m_a\vec{u}_a + m_b\vec{u}_b}{m_a + m_b}. \tag{1.2}$$

Since the target is stationary in the laboratory frame, $\vec{u}_b = 0$, $\vec{v}_{\text{cm}}$ reduces to

$$\vec{v}_{\text{cm}} = \frac{m_a\vec{u}_a}{m_a + m_b}. \tag{1.3}$$

In inverse kinematics, the projectile is the heavy nucleus, so the numerator $m_a\vec{u}_a$ in Eq. (1.3) is large, leading to a significantly larger $\vec{v}_{\text{cm}}$ than in normal kinematics, where the light particle is the moving projectile.

Using Eq. (1.1), the centre-of-mass velocities of the projectile and the target can be expressed as

$$\vec{v}_a = \frac{m_b}{m_a + m_b}\vec{u}_a, \tag{1.4}$$

$$\vec{v}_b = -\frac{m_a}{m_a + m_b}\vec{u}_a. \tag{1.5}$$

The initial kinetic energies in the centre-of-mass frame, T_i^{cm}, and in the laboratory frame, T_i^{lab}, are expressed as

$$T_i^{\text{cm}} = \frac{1}{2}m_a v_a^2 + \frac{1}{2}m_b v_b^2, \tag{1.6}$$

$$T_i^{\text{lab}} = \frac{1}{2}m_a u_a^2. \tag{1.7}$$

Using the centre-of-mass frame definition, $m_a v_a + m_b v_b = 0$, and Eq. (1.4), T_i^{cm} can be written as

$$T_i^{\mathrm{cm}} = \frac{1}{2} m_a v_a^2 \left(1 + \frac{m_a}{m_b}\right) = \frac{1}{2} m_a u_a^2 \frac{m_b}{m_a + m_b} = T_i^{\mathrm{lab}} \frac{m_b}{m_a + m_b}. \tag{1.8}$$

The final kinetic energy in the centre-of-mass frame is

$$T_f^{\mathrm{cm}} = \frac{1}{2} m_1 v_1^2 + \frac{1}{2} m_2 v_2^2 = T_i^{\mathrm{cm}} + Q - E_x, \tag{1.9}$$

where E_x is the excitation energy of the residual nucleus and Q is the ground-state Q-value[1] of the reaction given by

$$Q = \left[(m_a + m_b) - (m_1 - m_2)\right] c^2. \tag{1.10}$$

It is useful to determine the relationship between the velocity of the light ejectile (proton) in the centre-of-mass frame and the centre-of-mass frame velocity, $\vec{v}_{\mathrm{cm}}$. From the definition of the centre-of-mass frame

$$\vec{v}_2 = -\frac{m_1}{m_2} \vec{v}_1. \tag{1.11}$$

Inserting this into Eq. (1.9) gives

$$v_1 = \sqrt{\frac{2 m_2 \left(T_i^{\mathrm{cm}} + Q - E_x\right)}{m_1 \left(m_1 + m_2\right)}}. \tag{1.12}$$

Together with the centre-of-mass frame velocity that can be expressed as

$$v_{\mathrm{cm}} = \frac{m_a u_a}{m_a + m_b} = \frac{\sqrt{2 T_i^{\mathrm{lab}} m_a}}{m_a + m_b}, \tag{1.13}$$

and their combination gives

$$\frac{v_1}{v_{\mathrm{cm}}} = \sqrt{\frac{m_2 m_b}{m_1 m_a} \frac{m_a + m_b}{m_1 + m_2} \left(1 + \frac{Q - E_x}{T_i^{\mathrm{cm}}}\right)}. \tag{1.14}$$

Equation (1.14) expresses the ratio of the ejectile velocity in the centre-of-mass frame, v_1, to the centre-of-mass velocity, v_{cm}, and therefore characterises the kinematics of a two-body transfer reaction. There are three different scenarios: (1) $v_1 = v_{\mathrm{cm}}$, (2) $v_1 > v_{\mathrm{cm}}$, (3) $v_1 < v_{\mathrm{cm}}$. The first case, $v_1 = v_{\mathrm{cm}}$, corresponds to elastic scattering, where the internal structure of the interacting

[1] Q-value of a decay or reaction is the total energy released during the decay or reaction, representing the difference between the initial (parent) and final (daughter) atomic masses. Note that reactions with a negative Q-value are only allowed if energy is provided.

nuclei remains the same, and no excitations are induced, $Q = E_x = 0$. The second case, $v_1 > v_{\mathrm{cm}}$, corresponds to nucleon-adding reactions, such as (d, p), where the projectile transfers a nucleon to the target. Here, the mass factor in Eq. (1.14), $\frac{m_2 m_b}{m_1 m_a} \frac{m_a + m_b}{m_1 + m_2}$, is greater than 1 because $m_1 < m_b$ and $m_a \approx m_2$. The third case, $v_1 < v_{\mathrm{cm}}$, corresponds to nucleon-removal reactions, such as (p, d).

Expanding on the (d,p) case, the kinetic energy of the proton, T_1, can be expressed as

$$\begin{aligned} T_1 &= \frac{1}{2} m_1 \vec{u}_1 \cdot \vec{u}_1 \\ &= \frac{1}{2} m_1 \left(\vec{v}_1 + \vec{v}_{\mathrm{cm}}\right) \cdot \left(\vec{v}_1 + \vec{v}_{\mathrm{cm}}\right) \\ &= \frac{1}{2} m_1 v_1^2 + \frac{1}{2} m_1 v_{\mathrm{cm}}^2 + m_1 v_1 v_{\mathrm{cm}} \cos\theta_{\mathrm{cm},1}. \end{aligned} \tag{1.15}$$

The measured energy of the proton is dependent on its emission angle and the centre-of-mass frame velocity. In normal kinematics, v_{cm} is close to zero, and the last term of the above equation is almost negligible. This makes T_1 less sensitive to the emission angle. However, in inverse kinematics v_{cm} is significantly larger than in normal kinematics. Thus, T_1 becomes more dependent on the emission angle. This is illustrated in Fig. 1.4, which shows the variation of the measured energy of the proton with θ_{cm} for different excited states populated in the ^{229}Ac(d,p)^{230}Ac reaction at a beam energy of 8 MeV/u.

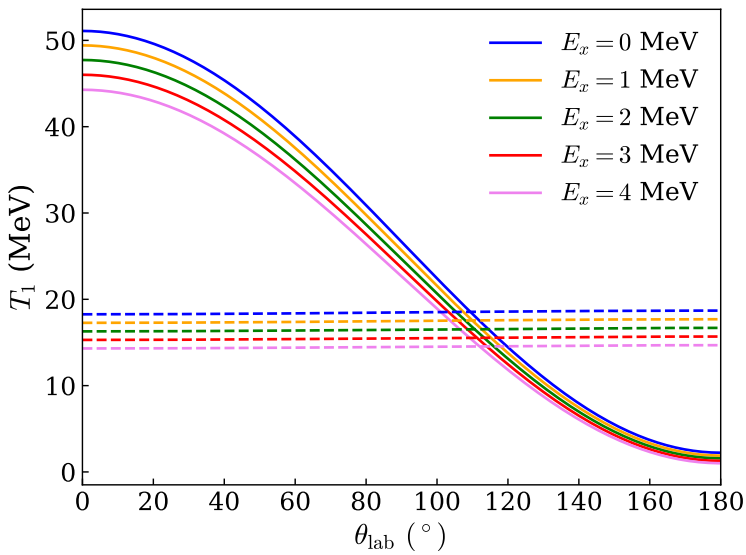

Figure 1.4: The light ejectile energy as a function of laboratory angle for different excited states populated in the ^{229}Ac(d,p)^{230}Ac reaction at a beam energy of 8 MeV/u. Solid lines show calculations performed in inverse kinematics, while dashed lines show calculations in normal kinematics.

The derivative of Eq. (1.15) with respect to $\theta_{\mathrm{lab},1}$ is

$$\frac{\mathrm{d}\,T_1}{\mathrm{d}\,\theta_{\mathrm{lab},1}} = -m_1 v_1 v_{\mathrm{cm},1} \sin\theta_{\mathrm{cm},1} \frac{\mathrm{d}\,\theta_{\mathrm{cm},1}}{\mathrm{d}\,\theta_{\mathrm{lab},1}}. \tag{1.16}$$

The derivative is dependent on $v_{\mathrm{cm},1}$ as well. Therefore, for a detector measuring the outgoing proton with an opening angle $\Delta\theta_{\mathrm{lab},1}$, the associated measured energy spread is significantly larger in inverse kinematics than in normal kinematics. This effect is known as *kinematic shift* and it affects the experimental energy resolution in inverse kinematics.

The second kinematic effect in inverse kinematics is *kinematic compression*. If we consider protons corresponding to two different excited states populated in the recoil of energy $E_{x,0}$ and $E_{x,1}$, respectively, the difference in the ejectile energy, ΔT_1, is

$$\begin{aligned}\Delta T_1 = {} & \frac{m_2}{m_1+m_2}\left(E_{x,0}-E_{x,1}\right) \\ & + 2\sqrt{\frac{m_a}{m_b}\frac{m_1 m_2\, T_i^{\mathrm{cm}}}{(m_a+m_b)(m_1+m_2)}} \\ & \times\left(\sqrt{T_i^{\mathrm{cm}}+Q-E_{x,1}} \quad -\sqrt{T_i^{\mathrm{cm}}+Q-E_{x,0}}\right)\cos\theta_{\mathrm{cm},1}.\end{aligned} \tag{1.17}$$

This can be expressed as

$$\Delta T_1 = A + B\sqrt{\frac{m_a}{m_b}}\cos\theta_{\mathrm{cm},1}. \tag{1.18}$$

The factor $\sqrt{\frac{m_a}{m_b}}$ is large in inverse kinematics and small in normal kinematics. Because of this, ΔT_1 has a stronger dependence on $\theta_{\mathrm{cm},1}$ in inverse kinematics, and the states are more compressed, especially at forward angles (small $\theta_{\mathrm{cm},1}$).

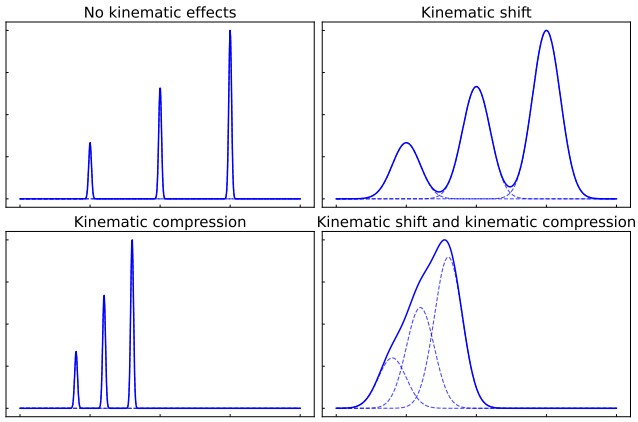

Figure 1.5: Schematic illustration of kinematic shift and kinematic compression in the excitation energy spectrum of protons calculated based on their measured kinetic energy in a (d, p) reaction in inverse kinematics.

In inverse kinematics, both kinematic shift and kinematic compression significantly limit the energy resolution of the measured ejectile, with the latter providing the dominant contribution. Figure 1.5 illustrates how these kinematic effects limit the achievable energy resolution in a (d, p) reaction in inverse kinematics. By using a *solenoidal spectrometer*, it is possible to mitigate these effects, in particular the kinematic compression.

1.3 The solenoidal spectrometer concept

In a solenoidal spectrometer [19] the reaction takes place inside a large-bore superconducting solenoid that provides a strong, uniform magnetic field along the beam axis. The beam is directed onto a thin target located in the centre of the magnet along the magnet's symmetry axis. The reaction products are then separated according to their mass-to-charge ratios, thanks to circular motion due to any transverse velocity.

Protons emitted in a (d, p) reaction thus follow helical trajectories in the magnetic field and return to the beam axis after T_{cyc} (one cyclotron period), where they are detected by an array of position-sensitive silicon detectors that is hollow to allow the beam to pass through it. A schematic layout of a solenoidal spectrometer is shown in Fig. 1.6.

For a given excitation energy of the populated recoil, the kinetic energy in the laboratory frame of the ejectile proton, T_1, depends linearly on the distance from the target, z:

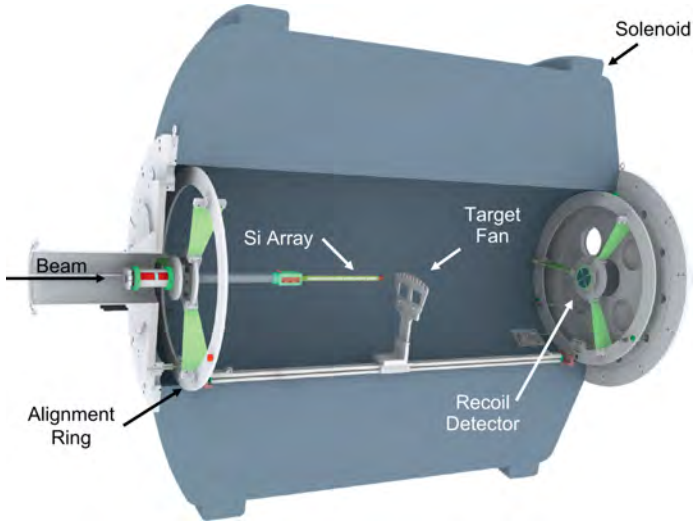

Figure 1.6: Schematic layout of a solenoidal spectrometer – HELIOS. The beam enters the superconducting large-bore solenoid magnet (92.5 cm diameter), travels through a hollow silicon array up to a target (CD_2), where the (d,p) reaction can occur. Ejectile protons emitted in the reaction are detected in the silicon array positioned upstream of the target, whereas the recoils are detected in the downstream recoil detector. Figure from Ref. [20].

$$T_1 = \frac{1}{\gamma} q - m_1 + \alpha\beta z. \tag{1.19}$$

Note that, in contrast to previous expressions derived classically, this expression is obtained from a relativistic treatment, where γ denotes the relativistic Lorentz factor.

In contrast to Eq. (1.15), where the ejectile energy depends linearly on $\cos\theta_{\mathrm{cm}}$ and, therefore, non-linearly on θ_{cm}, leading to kinematic shift and kinematic compression, the solenoidal geometry provides a linear relationship between T_1 and z for a fixed excitation energy. The use of a solenoidal spectrometer thus mitigates these kinematic distortions. A detailed derivation of the above expression and definitions of the α, β, and q symbols can be found in [21].

An illustration of this relationship is shown in Fig. 1.7, which presents calculated examples for the ^{229}Ac(d,p)^{230}Ac reaction at a beam energy of 8 MeV/u in a magnetic field of 2.5 T. The upper panel shows the relationship assuming an on-axis ejectile detector of zero radius. In reality, however, the finite radius of the hollow silicon array causes protons to be detected slightly before com-

pleting a full orbit, which leads to the characteristic low-energy end-point shape observed in the lower panel.

By measuring both the proton kinetic energy T_1 and its axial hit-position z, it is possible to reconstruct the excitation energy and the emission angle of the residual nucleus in the centre-of-mass frame using the following expressions:

$$E_x = -m_2 + \sqrt{M_c^2 + m_1^2 - 2\gamma M_c(E - \alpha\beta z)}, \text{ and} \tag{1.20}$$

$$\cos\theta_{\mathrm{cm},1} = \frac{\gamma(E\beta - \alpha z)}{\sqrt{\gamma^2(E - \alpha\beta z)^2 - m_1^2}}, \tag{1.21}$$

where $E = T_1 + m_1$ is the total energy of the detected proton.

Moreover, by measuring the cyclotron period of the particle, it is possible to identify different particle species according to their mass-to-charge $\left(\frac{m}{Z}\right)$ ratio,

$$T_{\mathrm{cyc}} = \frac{2\pi}{cB}\frac{m}{Z}, \tag{1.22}$$

where B is the magnetic field strength and c is the speed of light.

The heavy recoil nucleus, in contrast to the light ejectile, continues primarily in the forward direction and is only weakly deflected in the magnetic field due to its larger mass. Importantly, in experiments of this kind, the beam energy is nearly constant while states of different excitation energies are populated. This allows to study a whole range of excitation energies within a single measurement. A full derivation of the kinematics of the transfer reaction in the solenoidal field is provided in [21].

From the angular distributions of the emitted protons, the orbital angular momentum transferred in the reaction can be determined, as discussed in Section 2.2.

The solenoidal spectrometer method is particularly well suited for studying the (d,p) reaction by detecting protons emitted in the backward direction in the laboratory frame. Due to the reaction kinematics, with the light target essentially all other ejectiles are forward-focused [22]. By focusing on backward-emitted protons, the background from unwanted reaction channels is significantly reduced.

There are currently three solenoidal spectrometers suited for this kind of experiments: the HELIcal Orbit Spectrometer (HELIOS) at Argonne National Laboratory (ANL) [19], the SOLenoid spectrometer Apparatus for ReactIon Studies (SOLARIS) [23] at FRIB, and the ISOLDE Solenoidal Spectrometer (ISS) [24] at CERN. The designs of ISS and SOLARIS were inspired by HELIOS, shown in Fig. 1.6, and therefore share similar layouts.

Although originally designed for nuclear structure studies, the solenoidal spectrometer technique can also be applied to transfer-induced fission measurements [25]. The combination of high efficiency, good resolution, and the capa-

bility to measure multiple reaction products in coincidence makes it a powerful and versatile tool. This allows not only for spectroscopy of nuclear states but also for investigation of more complex processes like fission, where correlations between emitted particles carry important information. The ability of such a spectrometer to address both nuclear structure and transfer-induced fission studies is demonstrated in this thesis, where the same experimental approach is applied to investigate isospin symmetry (see Chapter 2) and transfer-induced fission (see Chapter 3).

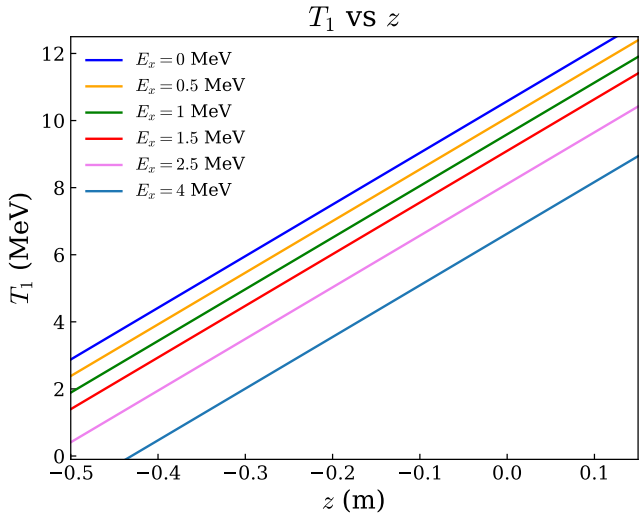

(a)

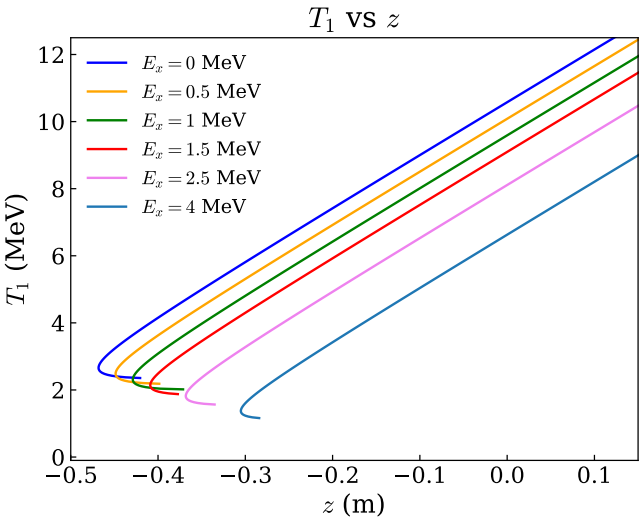

(b)

Figure 1.7: Kinetic energy T_1 of the proton as a function of the axial distance z of its detection from the target for several excitation energies in the ^{229}Ac(d,p)^{230}Ac reaction at a beam energy of 8 MeV/u and a magnetic field of 2.5 T (a) assuming an infinitely small detector, and (b) for an on-axis ejectile detector with a radius of 25 mm.

Chapter 2

Transfer across an isobaric multiplet: (d,p) on ^{17}F and ^{17}O

This chapter presents the analysis of data from an experiment studying the ^{17}F(d,p)^{18}F and ^{17}O(d,p)^{18}O reactions, performed at Argonne National Laboratory, using the HELIOS setup. The chapter begins with an introduction to the concept of isospin, isobaric multiplets, and isobaric analogue states in Section 2.1, followed by discussion of mechanisms that break the isospin symmetry. A theoretical framework is then outlined in in Section 2.2, including a simplified description of the nuclear shell model, nuclear potentials, optical model approaches, and the distorted-wave Born approximation (DWBA).

The motivation for studying ^{18}F and ^{18}O is subsequently presented in Section 2.3, highlighting their suitability for investigating isospin symmetry and its breaking, together with a summary of the known experimental properties of these nuclei. The experimental approach is described in Section 2.4, including an overview of the ATLAS accelerator, the HELIOS setup, and the detector systems used in the measurement.

The data analysis procedure is described in Section 2.5, presenting the steps taken to extract the excitation energies and the angular distributions for states populated in ^{18}F and ^{18}O via the (d,p) reactions. These angular distributions are used to extract spectroscopic factors, with the corresponding DWBA calculations presented. The chapter concludes with a discussion of the results (Section 2.6) and an outlook (Section 2.7).

2.1 Studying mirror nuclei

Isospin is an approximate symmetry that treats protons and neutrons as two states of the same particle—the nucleon. Both consist of up (u) and down (d) quarks: a proton contains two up and one down valence quarks (uud), while a neutron contains one up and two down valence quarks (udd). The up and down quarks differ slightly in mass, and exchanging one for the other (converting a proton into a neutron or vice versa) changes the nucleon's mass only marginally compared to its total mass.

However, the up and down quarks carry different electric charges—$+2/3\,e$ for the up quark and $-1/3\,e$ for the down quark—resulting in total charges of $+1\,e$ for the proton and 0 for the neutron. Consequently, although the strong nuclear interaction acts similarly on both states, their electromagnetic interactions differ because of the Coulomb force. Their weak interactions also differ, since the weak force couples differently to up and down quarks.

While the strong nuclear force dominates nucleon-nucleon interactions, it is not identical for proton-proton, neutron-neutron, and neutron-proton pairs. Small differences arise from *charge-symmetry breaking* (the fact that the proton-proton and neutron-neutron interactions are not identical) and *charge-independence breaking* (the average proton-proton and neutron-neutron interactions differ slightly from the neutron-proton interaction). Nevertheless, these differences are small compared to the overall strength of the strong nuclear force. As a result, when the Coulomb force is neglected, protons and neutrons behave similarly under the nuclear interaction and they can be treated, to a good approximation, as two isospin projections of a single particle—the nucleon.

In this framework, both the proton and the neutron share the same isospin quantum number T and are distinguished only by their isospin projection T_z, with $T_{z_p} = -\frac{1}{2}$ for the proton and $T_{z_n} = +\frac{1}{2}$ for the neutron (this convention follows that of Ref. [15] and is used throughout this text). For a system containing both protons and neutrons, the total isospin projection is given as $T_z = (N - Z)/2$, where N is the number of neutrons and Z is the number of protons.

Because the nuclear interaction is approximately charge independent, nuclei with the same mass number A but different numbers of protons and neutrons—known as *isobars*—can exhibit states characterised by the same isospin T. Such related nuclei form an *isobaric multiplet*, and states across a multiplet that share the same isospin quantum number are called *isobaric analogue states* (IAS). Although isospin is not an exact quantum number, it provides a useful framework for organising and interpreting nuclear structure and reactions. Deviations from exact isospin symmetry, arising from the Coulomb interaction and small charge-dependent components of the nuclear force, offer important information about the nature of the nuclear interactions.

The IAS have nearly identical wave functions (except for the Coulomb in-

teraction) and therefore exhibit similar excitation energies and decay properties. The study of IAS provides a powerful probe of isospin symmetry and its breaking, especially in nuclei near the $N = Z$ line. Energy differences between analogue states arise primarily from isospin non-conserving forces, such as the Coulomb interaction between protons. By examining *Coulomb energy differences* (CED) between members of an isobaric multiplet, one can study the degree of isospin breaking in nuclei.

To illustrate this, consider a neutron and a proton in a nuclear mean field. The neutron experiences only the attractive nuclear force and occupies a deeply bound potential well. The proton, however, feels both the attractive nuclear potential and the repulsive Coulomb potential from other protons in the nucleus. This Coulomb repulsion raises the energy of proton single-particle states, making them less tightly bound than the corresponding neutron states in the same orbitals. These shifts in binding energy give rise to the observed CED between states in an isobaric multiplet, which differ only by the exchange of a proton and a neutron in the same orbital.

Consequently, IAS in a pair of mirror nuclei M_1 and M_2 appear at slightly different excitation energies. The CED for a given isobaric analogue state i at excitation energy $E_{x,i}$ is defined as:

$$\mathrm{CED}_i = E_{x,i}(M_1) - E_{x,i}(M_2). \tag{2.1}$$

At the same time, the Coulomb interaction changes the total binding energy of a nucleus when a neutron is replaced by a proton. The *Coulomb displacement energy* (CDE), defined as the energy required to replace a neutron with a proton in IAS (aside from the neutron-proton mass difference), corresponds to the mass difference between the higher-Z and the lower-Z members of an analogue pair. Thus, while the CED describes the energy differences between specific analogue states within a multiplet, the CDE reflects the overall energy shift between mirror nuclei.

However, theoretical CDE calculations that include only Coulomb effects systematically underestimate the experimental values. This discrepancy is known as the *Nolen-Schiffer anomaly* [26]. It reflects additional charge-dependent components of the nuclear force, such as charge-symmetry breaking and charge-independence breaking.

Another important aspect is the investigation of the effects of weak binding. In weakly bound states (for excited states at excitation energies close to or above the neutron or proton separation energy), the observed CEDs often significantly exceed those of deeply bound states (i.e., states well below the particle separation threshold). This can be illustrated as follows. When both the proton and the neutron states are deeply bound, their wave functions are mostly confined inside the nucleus, and the Coulomb force shifts all proton levels upward relative to neutron levels. However, for weakly bound states near

the particle-emission threshold, the wave function can extend far outside the nucleus into the continuum, meaning that the nucleon spends more time outside the nuclear core. The nucleon also experiences a centrifugal barrier arising from its orbital motion:

$$V_{\text{cent}} = \frac{\hbar^2 \ell(\ell+1)}{2\mu r^2}, \tag{2.2}$$

where $\hbar$ is the reduced Planck's constant, ℓ is the orbital angular momentum quantum number, μ is the reduced mass, and r is the distance from the centre of the nucleus. For s-wave states ($\ell = 0$), the centrifugal barrier vanishes, allowing the particle to "leak out" more easily. Consequently, the average Coulomb repulsion experienced by a weakly bound proton is actually smaller than expected, as it spends less time in the region with high-charge density of the nucleus. This lowers its energy relative to what would be predicted by a simple Coulomb shift. This effect is known as the *Thomas-Ehrman shift* [27, 28] and leads to enhanced energy shifts between analogue states involving weakly bound or unbound single-particle configurations.

IAS and mirror nuclei also play an important role in nuclear astrophysics. Thanks to the symmetry in their structure, one can infer the single-particle properties of an unbound state in a neutron-deficient nucleus from those of a bound state in its isobaric mirror. These more stable isobaric mirrors are often experimentally more easily accessible and can therefore be used to accurately determine the strengths of resonances [29]. Reactions involving such mirror states are key to understanding nucleosynthesis processes, such as the rapid proton-capture (rp) process in explosive stellar environments [30].

2.2 Single-particle structure of atomic nuclei

Describing atomic nuclei from first principles is extremely difficult. To address this challenge, the *shell model* was introduced. It aims to reproduce the wide range of phenomena observed experimentally across the nuclear chart while relying on relatively simple assumptions. In particular, the shell model successfully explains the existence of the magic numbers[1].

Within the shell model framework, nucleons move independently in a common mean-field potential, which effectively replaces the individual two-body interactions between nucleons. The nuclear potential describing this motion reflects the attractive nature of the strong nuclear force. Simple approximations of this potential include the square well and the harmonic oscillator potentials. While these models are easy to use, they fail to reproduce the observed magic numbers. In contrast, the Woods-Saxon potential with an additional spin-orbit

[1]Magic numbers (2, 8, 20, 28, 50, 82, 126) are specific numbers of protons or neutrons in nuclei that lead to exceptionally stable configurations.

coupling term successfully accounts for them. The spin-orbit coupling term arises from the coupling of the orbital angular momentum, $\vec{\ell}$, and the spin of the nucleus, $\vec{s}$. Examples of mean-field potentials are shown in Fig. 2.1.

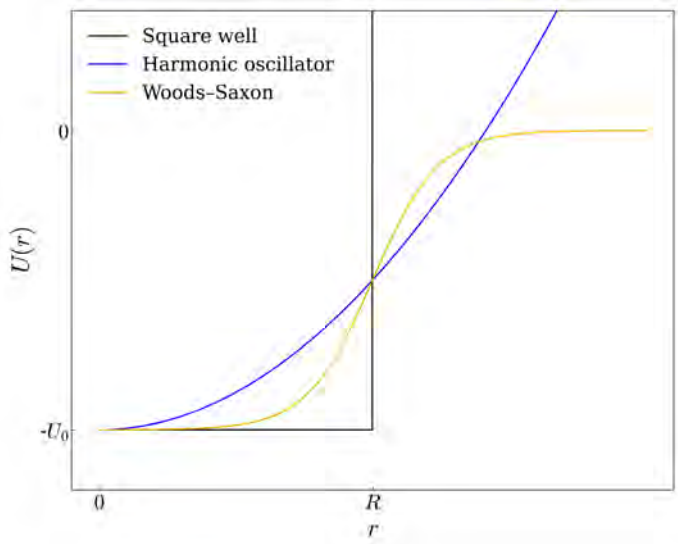

Figure 2.1: Square well, harmonic oscillator, and Woods-Saxon potentials plotted as a function of distance to the centre of the nucleus (r). R and U_0 represent the nuclear radius and the potential well depth, respectively.

Nucleons moving in this mean-field potential occupy discrete *single-particle states*, commonly referred to as *orbitals*. Each orbital is characterised by a specific set of quantum numbers that arise from solving the Schrödinger equation in the chosen potential. Due to the Pauli exclusion principle, each orbital can be occupied by only a limited number of nucleons.

A *shell* consists of a group of orbitals that are close in energy and separated from other such groups by large energy gaps. As nucleons fill successive orbitals, large energy gaps appear after certain numbers of nucleons that have been accommodated. These numbers correspond to the magic numbers. When all orbitals in a shell are completely filled, the shell is said to be *closed*, and the resulting nucleus exhibits enhanced stability compared to nuclei with shells that are only partially filled. This description, the so-called independent particle model (IPM), is necessarily simplified and does not account for effects such as residual nucleon-nucleon interactions, pairing correlations, and configuration mixing. A more detailed discussion of the nuclear shell model can be found, for example, in Ref. [1].

A schematic representation of the single-particle energy levels and the result-

ing shell structure predicted with a harmonic oscillator potential, Woods-Saxon potential, and Woods-Saxon including spin-orbit coupling is shown in Fig. 2.2.

The shell model provides a framework for a basic understanding the arrangement of nucleons in orbitals. However, it is a simplified model, and experimental data are needed to refine its predictions. To probe the structure of nuclei experimentally, direct reactions are particularly powerful. In these reactions, the projectile interacts with the target nucleus in a single-step, allowing for the selective study of specific nuclear degrees of freedom. Single nucleon transfer reactions, such as the neutron adding (d, p) reaction, are especially valuable. In this reaction, a neutron is transferred from the deuteron to the target nucleus. The final state can be described as the original core plus one neutron. Because only a single nucleon is added, the final state is relatively simple to describe theoretically, and the measured cross section is directly related to the degree of overlap between the initial and final nuclear states.

The transferred neutron can occupy different single-particle orbitals in the residual nucleus. The orbital angular momentum ℓ of the transferred neutron determines which orbital is populated. Conservation of angular momentum links the angular momentum of the emitted proton to the orbital angular momentum of the transferred neutron. By measuring the angular distribution of protons in the (d, p) reaction, it is possible to determine the angular momentum transfer ℓ in the reaction and identify which orbital has been populated in the residual nucleus. Each ℓ-transfer produces a characteristic angular distribution, reflecting the spatial structure of the corresponding neutron wave function, which can be used to assign the quantum numbers of the populated single-particle state. An example of calculated angular distributions for different angular momentum transfers is shown in Fig. 2.3.

Interpretation of the measured angular distributions in (d, p) reactions requires a theoretical framework to account for the interaction between the incoming deuteron, the target nucleus, and the outgoing proton. This description is provided by *optical model potentials*, which represent an effective interaction between the projectile and the target in the the incoming channel, and between the ejectile and the recoiling nucleus in the outgoing channel. Optical potentials typically use simple, parametrised forms such as the Woods-Saxon potential and its derivatives, often including a spin-orbit term and a Coulomb potential for charged particles. The parameters of these potentials are fitted to experimental scattering data and reflect the average interaction of the projectile with all nucleons in the target.

Optical models and DWBA

Optical potentials usually include a real part, which describes elastic scattering, and an imaginary part, which accounts for absorption into non-elastic channels. Elastic scattering can be treated as the leading order contribution in the plane-

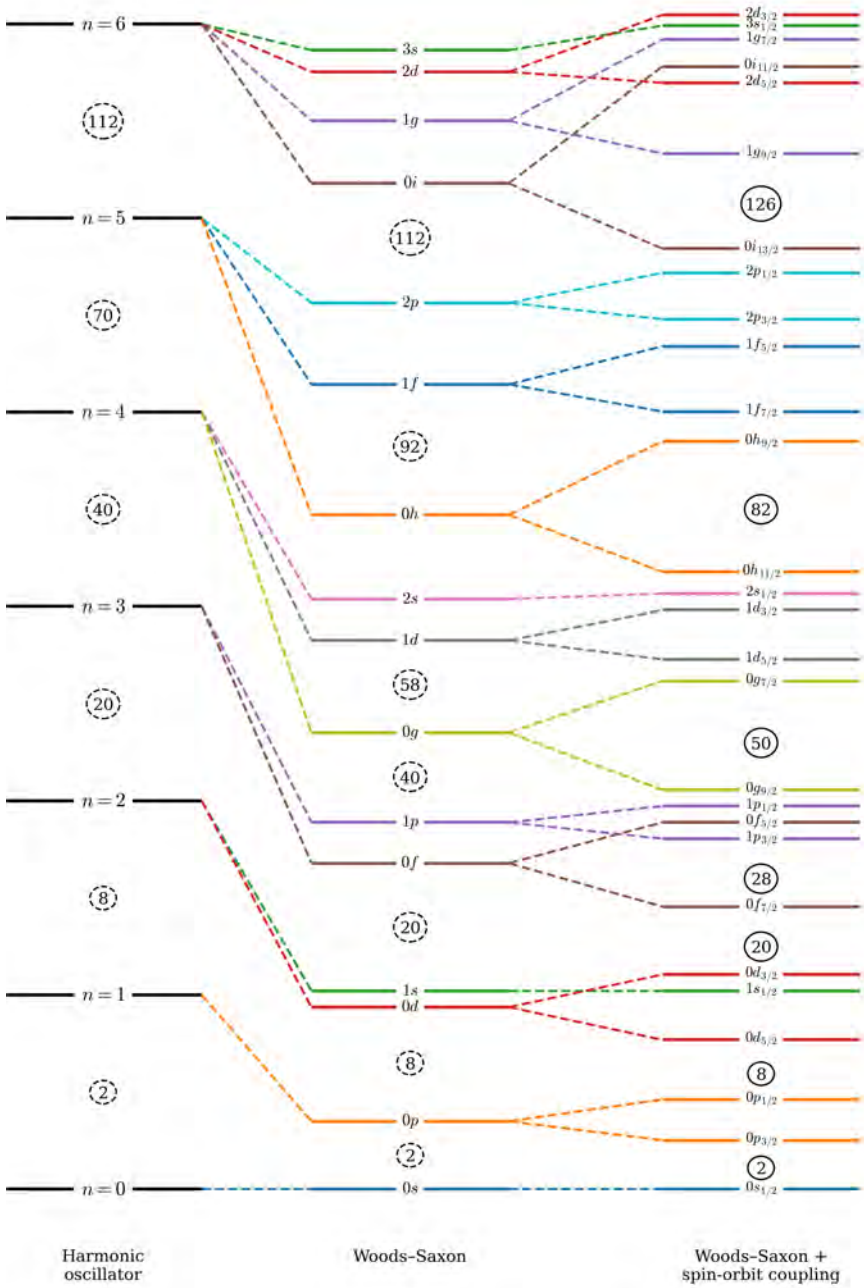

Figure 2.2: Diagram of the orbitals in the shell model predicted with the harmonic oscillator potential, Woods-Saxon potential, and Woods-Saxon potential including the spin-orbit coupling. Magic numbers are shown in the circles.

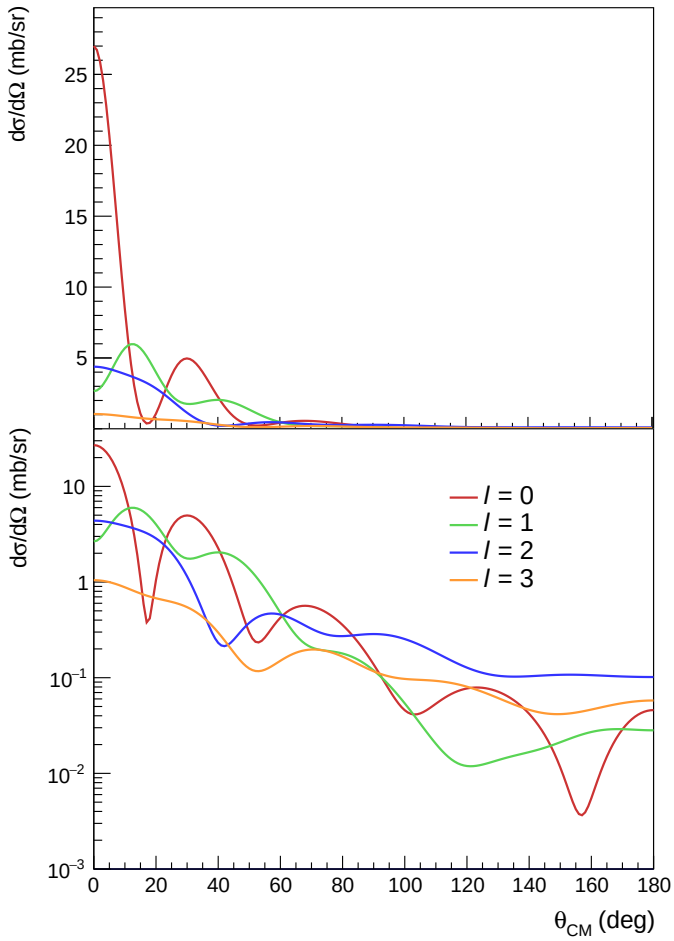

Figure 2.3: Distorted-wave Born approximation (DWBA) calculations of differential cross sections for the $^{17}\mathrm{O}(\mathrm{d},\mathrm{p})^{18}\mathrm{O}$ neutron transfer reaction at a $^{17}\mathrm{O}$ beam energy of 10.12 MeV/u. The angular distributions are shown as a function of the centre-of-mass angle for different orbital angular momentum transfers ℓ. The upper panel presents the results on a linear scale, while the lower panel uses a logarithmic scale on the y-axis.

wave Born approximation (PWBA), in which the projectile and ejectile are described by plane waves. However, this approximation neglects the distortions of the wave functions caused by the interaction with the target and recoil nucleus. These distortions are included by replacing plane waves with distorted waves, giving rise to the distorted-wave Born approximation (DWBA).

DWBA provides a practical and widely used method for calculating the probability amplitude of single-neutron transfer reactions, such as (d, p). In this approach, the incoming deuteron and outgoing proton are represented as distorted waves generated from the optical potentials, while the transferred neutron is treated as a perturbation. The resulting transition amplitudes depend explicitly on the quantum numbers of the orbitals involved, particularly the orbital angular momentum ℓ, linking measured angular distributions to the single-particle structure of the residual nucleus. Many DWBA codes exist, including the PTOLEMY reaction code [31] used in the present work.

Spectroscopic factors

Spectroscopic factors quantify the single-particle character of nuclear states populated in nucleon transfer reactions. In a transfer reaction, a nucleon is added or removed from the target nucleus, leading to the formation of final states in the residual nucleus. Final states that can be well described as a simple configuration of the target nucleus with a single nucleus added or removed from that core in the independent-particle model (IPM) are expected to be strongly populated. Other states, which do not have a single-particle structure, such as collective excitations or configurations involving strong correlations among several nucleons, are generally populated with lower probability in transfer reactions.

The spectroscopic factor is defined as a ratio between the experimental cross section of the populated final state and the theoretical cross section expected for a pure single-particle configuration. In practical terms, the theoretical differential cross sections are calculated within the DWBA approximation, which assumes that the transferred nucleon occupies a well-defined orbital in the IPM and that there are no correlations between nucleons in the nucleus. DWBA calculations provide reference cross sections corresponding to a fully occupied single-particle state.

In real nuclei, residual interactions between nucleons lead to configuration mixing and correlations that produce more complex wave functions. As a result, the single-particle strength associated with a given orbital is fragmented over several nuclear states. Consequently, spectroscopic factors extracted from experimental data are generally less than one.

2.3 Single-neutron transfer in the $A = 18$ isobaric multiplet

Motivated by the considerations listed in the previous sections, an experiment was performed to investigate the single-particle structure within the $A = 18$ isobaric triplet using neutron transfer reactions. States in ^{18}F and ^{18}O were populated through the ^{17}F(d,p)^{18}F and ^{17}O(d,p)^{18}O reactions, respectively, both carried out in inverse kinematics. The nuclei ^{18}F and ^{18}O have the same mass number ($A = 18$) and, under exact isospin symmetry, their $T = 1$ configurations would be identical. Figure 2.4 shows a portion of the nuclear chart around the ^{18}F and ^{18}O region.

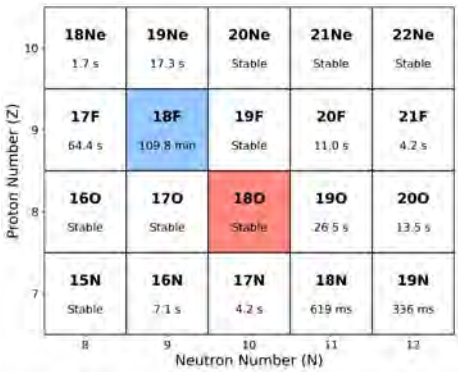

Figure 2.4: Portion of the nuclear chart around the ^{18}F and ^{18}O region. Half-lives are indicated for each isotope. Data from [32].

To probe this structure, the (d, p) reaction was chosen. In this reaction, performed in inverse kinematics, a neutron is transferred from the deuteron target to the projectile nucleus, forming a residual nucleus with one additional nucleon. The proton is ejected from the deuteron, and by measuring its energy and position, as described in Section 1.3, information can be obtained about the single-particle states populated in the reaction. The proton energies provide information on the excitation energies of the populated states, while their angular distributions allow for the extraction of the transferred angular momentum. From this, spectroscopic factors can be derived, which quantify the single-particle structure of the populated states.

Alternative approaches to studying IAS include charge-exchange reactions, such as (p, n) or (^{3}He, t), and β-decay measurements. However, these methods are generally less selective for individual single-particle states or, as in the case of β-decay, are constrained by selection rules and limited by decay Q-values, which restrict access to many states of interest.

The (d, p) reaction, by contrast, offers a direct and sensitive probe of single-particle configurations through neutron transfer. It enables the population of specific nuclear states, allows for extraction of spectroscopic factors, and can be applied in inverse kinematics to short-lived radioactive beams such as ^{17}F.

Some basic information about the studied final nuclei is summarised in Table 2.1. In ^{18}O, only $T = 1$ states are populated, while in ^{18}F, population of both $T = 0$ and $T = 1$ is possible. The $T = 1$ states in these two nuclei are isobaric analogue states and, assuming perfect isospin symmetry, should be identical. Studying both systems under the same experimental conditions enables a direct comparison of analogue states in ^{18}O and ^{18}F.

Figure 2.5 shows low-lying positive-parity states in ^{18}F and ^{18}O. IAS with $T = 1$ are connected by a dashed line. The CED for states above 5 MeV in ^{18}O and their IAS in ^{18}F are significantly larger than that for the states below 5 MeV.

Nucleus	Z	N	$T_z = (N - Z)/2$	Populated states	S_p
^{18}F	9	9	0	$T = 0, 1$	5.6 MeV
^{18}O	8	10	+1	$T = 1$	15.9 MeV

Table 2.1: Basic properties of the final nuclei studied in the (d, p) transfer reactions. S_p denotes the proton separation energy. Data taken from [32].

As shown in the table, exchanging a proton for a neutron results in a significant change in the proton separation energy, from $S_p = 5.6$ MeV in ^{18}F to $S_p = 15.9$ MeV in ^{18}O. The chosen beam energies (see Section 2.4.2 for more details) were selected to populate states up to excitation energies approaching and beyond the proton separation threshold S_p in ^{18}F, while the corresponding analogue states in ^{18}O remain deeply bound.

This approach allows for the investigation of weak-binding effects on the single-particle structure of isobaric analogue states. These effects are probed through the analysis of spectroscopic factors extracted for states in both ^{18}F and ^{18}O. As discussed earlier, weak binding near or above the particle-emission threshold can significantly modify the low-ℓ (especially s-wave, $\ell = 0$) orbitals. Because the s-wave experiences no centrifugal barrier, its wavefunction extends further outside the nucleus when weakly bound. This extension reduces the overlap between the single-particle wave function and the core wave function, leading to a smaller spectroscopic factor.

Comparing spectroscopic factors for analogue states in ^{18}F and ^{18}O allows to investigate whether weak binding modifies the single-particle character of IAS, particularly for s-wave or states with a s-wave component.

The final nuclei, ^{18}F and ^{18}O, can be viewed as systems consisting of a pair of nucleons outside of the doubly-magic ^{16}O core. This simple structure makes them suitable candidates for comparison with shell-model calculations, allowing

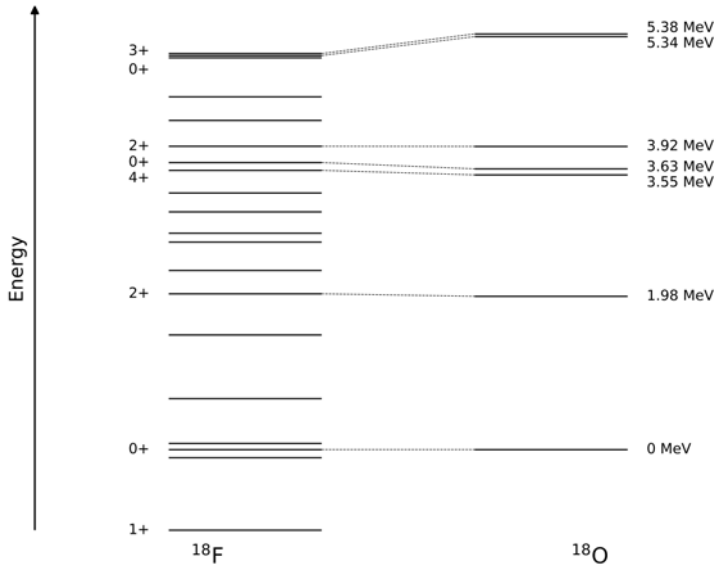

Figure 2.5: Positive-parity states in ^{18}F and ^{18}O. IAS with $T = 1$ are connected by a dashed line. Data taken from [32].

for detailed tests of nuclear structure models.

2.3.1 What do we know about ^{18}O and ^{18}F?

The ^{17}O(d, p)^{18}O has previously been studied in normal kinematics in the 1960s [33–36]. This is because ^{17}O is a stable isotope, making it possible to fabricate a target[2], and the final nucleus ^{18}O, which lies only two nucleons beyond the doubly-magic ^{16}O core, is of particular theoretical interest for nuclear structure studies. Table 2.2 summarises the known levels in ^{18}O populated via the ^{17}O(d, p)^{18}O reaction. The spin and parity (J^π), angular momentum transferred in the reaction (ℓ), and spectroscopic factors (SF) are indicated for each state where available.

[2]The referenced experiments used nickel oxide targets [34] and tungsten oxide targets [33, 35] enriched in oxygen.

E (level) (MeV)	J^π	ℓ	SF
0.000	0^+	2	1.22
1.982	2^+	$0 + 2$	$0.21 + 0.83$
3.552	4^+	2	1.57
3.630	0^+	2	0.28
3.920	2^+	$0 + 2$	$0.35 + 0.66$
4.460	1^-	1	0.03
5.100	3^-	3	0.03
5.255	2^+	0	0.35
5.340	0^+	2	0.16
5.375	3^+	0	1.01
6.200	1^-	1	0.03
6.350	(2^-)	1	$0.03 - 0.04$
7.100	4^+	2	
7.855			
7.962			
9.000	4^+		

Table 2.2: Energy levels in ^{18}O populated via the ^{17}O(d, p)^{18}O reaction. Spin and parity (J^π), transferred angular momentum ℓ, and spectroscopic factors (SF) are indicated where available. Data from [37, 38].

On the other hand, the energy levels in ^{18}F are generally known, but not through the ^{17}F(d, p)^{18}F reaction. Since ^{17}F is an unstable isotope, this reaction could not be studied in normal kinematics. The work presented in this thesis investigates this reaction for the first time.

Earlier studies have examined the ^{17}O(^{3}He, d)^{18}F reaction in normal kinematics, in which a proton from the ^{3}He beam is transferred to ^{17}O [39, 40]. In this reaction, only the states listed in Table 2.3 for which the transferred angular momentum and spectroscopic factors are indicated were observed. The other states, known from different reactions, were not populated in this reaction. For the observed states, the angular momentum transfer corresponds to the single-particle orbital of the added proton, which is effectively the same as in the ^{17}F(d, p)^{18}F reaction. This makes the spin-parity assignments and spectroscopic information directly comparable for these states.

E (level) (MeV)	J^π	ℓ	SF	E (level) (MeV)	J^π	ℓ	SF
0.000	1^+			4.963	2^+	0 + 2	0.17 + 0.51
0.937	3^+	0 + 2	0.102 + 0.306	5.298	4^+	2	0.02
1.042	0^+	2	0.96	5.502	$3^{(-)}$		
1.081	0^-			5.603	1^+	2	0.12
1.121	5^+	2	0.89	5.605	1^-		
1.701	1^+	2	0.035	5.673	1^-	1 + 3	0.006 + 0.014
2.101	2^-	1 + 3	0.01 + 0.04	5.786	2^-	1 + 3	†
2.523	2^+	0 + 2	0.014 + 0.011	6.096	4^-		
3.062	2^+	0 + 2	0.21 + 0.62	6.108	(1^+)		
3.134	1^-	1 + 3	0.007 + 0.039	6.136	0^+		
3.358	3^+	0	0.014	6.163	3^+		
3.724	1^+			6.240	3^-		
3.791	3^-			6.242	3^-		
3.839	2^+			6.262	1^+		
4.116	3^+	0 + 2	0.17 + 0.68	6.283	2^+		
4.226	2^-	1 + 3	0.012 + 0.018	6.310	3^+		
4.360	1^+	2	0.074	6.385	2^+		
4.398	4^-	1 + 3	0.022 + 0.015	6.485	3^+		
4.652	4^+	2	1.04	6.567	5^+		
4.753	0^+	2	0.18	6.633	1		
4.848	5^-			6.644	2^-		
4.860	1^-	3	0.078	6.647	1^-		

† Upper limit of spectroscopic factor: $< 0.002 + < 0.004$.

Table 2.3: Energy levels in ^{18}F. Only states for which transferred angular momentum ℓ and spectroscopic factors (SF) were populated in the ^{17}O(^{3}He, d)^{18}F reaction. Spin and parity (J^π), transferred angular momentum ℓ, and spectroscopic factors (SF) are indicated where available. Data from [32, 40].

2.3.2 Shell-model calculations

The extracted spectroscopic factors are compared with those predicted using shell-model calculations. Shell model calculations were obtained from Ref. [41]. These calculations were performed using the NuShellX@MSU code [42], a widely used shell-model framework for describing nuclear structure within a restricted valence space. In these calculations, the nucleus is treated as a ^{16}O core with valence nucleons occupying the 0 $d_{5/2}$,1 $s_{1/2}$, and 0 $d_{3/2}$ single-particle orbitals.

The calculations were carried out in the full *sd*-shell space using the USDI interaction, which includes isospin-breaking terms derived from *ab initio* theory [43]. Shell-model spectroscopic factors were computed as overlaps between the

initial and final shell-model wave functions corresponding to one-nucleon transfer, providing a theoretical estimate of the likelihood of populating specific final states in transfer reactions.

For comparison, the FSU interaction was also employed. This interaction allows for 1p–1h cross-shell excitations and includes configurations spanning the *s*-*p*-*sd*-*fp* shells, thereby accounting for intruder configurations beyond the conventional *sd*-shell. Further details on the FSU interaction can be found in Refs. [44, 45].

2.4 Experiment

This section presents the experimental approach employed to investigate the single-particle structure within the $A = 18$ isobaric triplet using the $^{17}\mathrm{F}(\mathrm{d},\mathrm{p})^{18}\mathrm{F}$ and $^{17}\mathrm{O}(\mathrm{d},\mathrm{p})^{18}\mathrm{O}$ reactions. The reactions were studied in inverse kinematics, meaning that a heavy beam was used in combination with a light target, contrary to the conventional approach. This choice is motivated by the fact that ^{17}F is a radioactive isotope with a 64.4 s half-life, and it is not possible to create a target lasting for the duration of the experiment out of it.

The measurement was carried out at the Argonne Tandem Linac Accelerator System (ATLAS) at Argonne National Laboratory. In this section, an overview of the ATLAS facility and beam production is first presented, followed by a description of the experimental setup and procedures.

2.4.1 ATLAS

ATLAS is a superconducting linear accelerator for heavy ions that provides beams with energies of up to approximately 18 MeV/u. A schematic layout of the facility is shown in Fig. 2.6. ATLAS delivers both stable and radioactive ion beams.

The stable ion beams originate in Electron Cyclotron Resonance (ECR) ion sources [46]. First, neutral atoms of the material from which the beam is to be produced are fed into the source. A plasma is formed from a gas (or from a material that has been volatilised into a gas or vapour) that fills the plasma chamber. The plasma is confined by a combination of axial solenoidal coils and a radial hexapole magnet, which together generate a magnetic field configuration that traps charged particles. The magnetic field is weakest at the centre of the chamber and strongest near the walls. The high magnetic fields surrounding the volume of the plasma prevent the escape of both electrons and ions.

Microwaves are injected into the chamber at a frequency that matches the electron cyclotron frequency in the magnetic field, allowing electrons to absorb the microwave energy resonantly. The heated electrons ionise the gas through collisions with atoms, stripping them of their electrons. The ECR plasma traps the ions long enough (several milliseconds) for multiple collisions with the energetic electrons to occur, which, in turn, leads to the production of ions with high charge states (i.e. with several electrons removed).

Currently, there are two ECR ion sources at ATLAS – ECR2 and ECR3 [47, 48]. In this experiment, the ECR3 source was used.

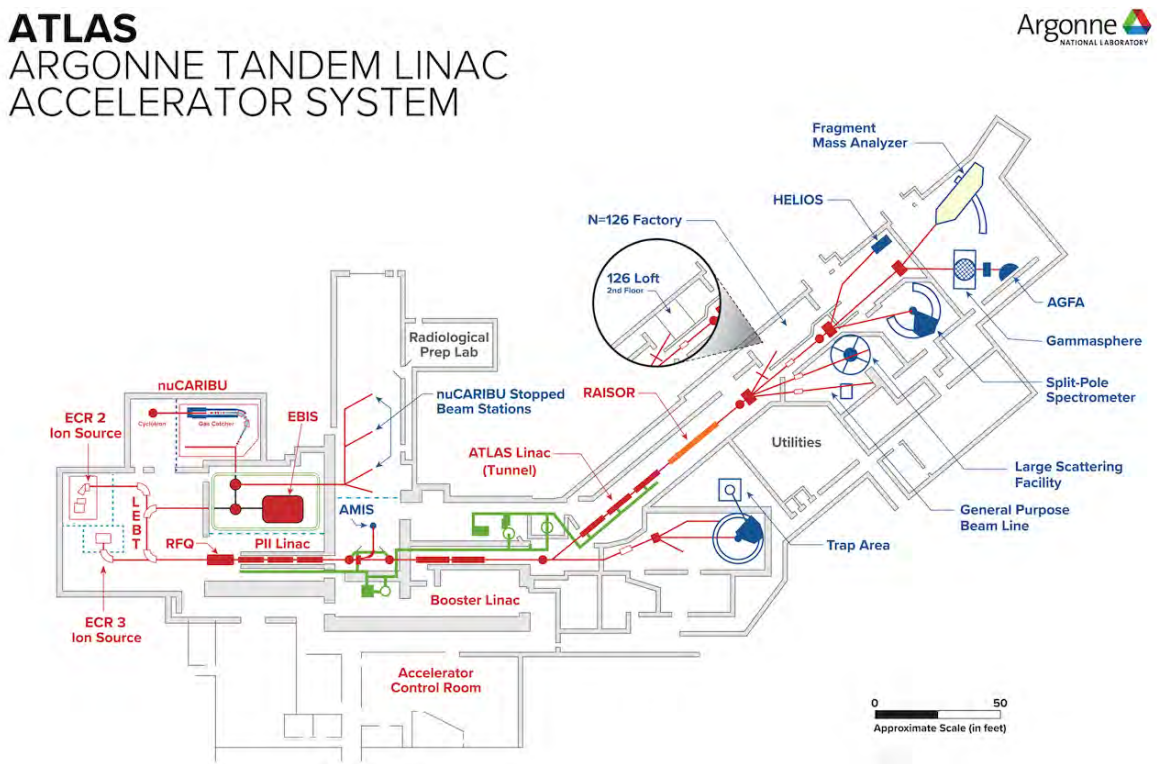

Figure 2.6: A schematic layout of the ATLAS facility with beam locations. A stable $^{17}O^{6+}$ primary beam from the ECR3 ion source was accelerated through the PII and the Booster linacs and delivered directly to the HELIOS experimental area. For radioactive beam operation, the same primary beam was delivered to RAISOR, where the in-flight produced $^{17}F^{9+}$ secondary beam was selected and transported to HELIOS. Figure adapted from [49].

Once the desired charge state population is reached, the ions are extracted from the ECR through an aperture at the end of the source and injected into the subsequent acceleration stages. For the experiment presented in this thesis, a ^{17}O primary beam at charge state 6+ was used. The extracted beam is first magnetically analysed and then bunched. It is subsequently passed through a higher-resolution magnetic analyser. A beam chopper then removes unbunched ions, and a second buncher rebunches the beam to maintain high beam quality [50]. The primary beam has a fixed time structure of one pulse every ∼82.47 ns, corresponding to a frequency of 12.125 MHz. These pulses are typically less than 1 ns in width (on the order of a few hundred picoseconds). The beam is then injected into the linear accelerator system, which consists of several main sections: the Positive Ion Injector (PII) linear accelerator (linac), the Booster linac, and the ATLAS linac.

The PII begins with a normal-conducting radio-frequency quadrupole (RFQ) that bunches and accelerates the continuous beam from the ECR source. Downstream from the RFQ, the superconducting PII linac further accelerates the ions and injects them into the superconducting Booster and ATLAS linac sections. Together, these linacs form a single accelerating structure that has been expanded over time. The linacs comprise arrays of radio-frequency (RF) accelerating resonators alternating with focusing solenoids, which together increase the beam energy and maintain beam focus.

There are two techniques for producing radioactive beams at ATLAS: the in-flight method, used in the presented work, and the nuCARIBU approach.

The nuCARIBU facility [51] is an upgrade of the Californium Rare Isotope Breeder Upgrade (CARIBU). Its goal is to provide beams of neutron-rich isotopes far from stability. nuCARIBU uses neutron-induced fission on an actinide foil via a neutron generator. In this setup, neutrons are produced by a 6 MeV proton beam from a compact cyclotron that accelerates H^- ions and strips them to protons using carbon foils. These protons strike a ^{7}Li target to produce neutrons, which are moderated to thermal energies and directed onto an actinide foil, such as ^{235}U, to induce fission.

The fission fragments are slowed down by passing through ultra-high purity helium gas inside a gas-catcher. They are then extracted into the beam line and mass-separated to select the desired components. If the beam is to be further accelerated, its charge state is increased using an Electron Beam Ion Source (EBIS) [52] coupled to nuCARIBU.

In the EBIS, ions of relatively low charge state are injected into a trap containing a high-current, focused electron beam confined by strong magnetic and electrostatic fields. The electrons collide with the trapped ions and strip additional electrons from the ions, increasing their charge state. After a time corresponding to maximise the probability of reaching the desired charge state, the ions are extracted and injected into the linac, where they are accelerated using the same structures described previously for the ECR-based beams.

The in-flight technique, which is relevant to the present work, uses the Argonne In-Flight Radioactive Ion Separator (RAISOR) system [53]. In this approach, a stable beam from the ECR source is accelerated through the linac and then directed onto a production target located immediately upstream of RAISOR. A 6 T superconducting solenoid placed upstream of the target focuses the primary beam. The production target can be either a self-supported solid foil or a cryogenically-cooled gas cell [54]. In the experiment described in this thesis, a hydrogen gas cell was used as the production target.

RAISOR is a magnetic separation and purification system designed to select the desired reaction products produced in the target [53]. It consists of a sequence of quadrupole and dipole magnets for selecting and focusing of the secondary beam, along with adjustable midplane slits that act as a primary beam dump, as shown in Fig. 2.7. The system also includes a superconducting RF cavity for beam rebunching and an RF sweeper for further purification of the separated beam. The RF sweeper is located about 21 m downstream of the production target while the RF resonator is located approximately 23 m downstream of the target.

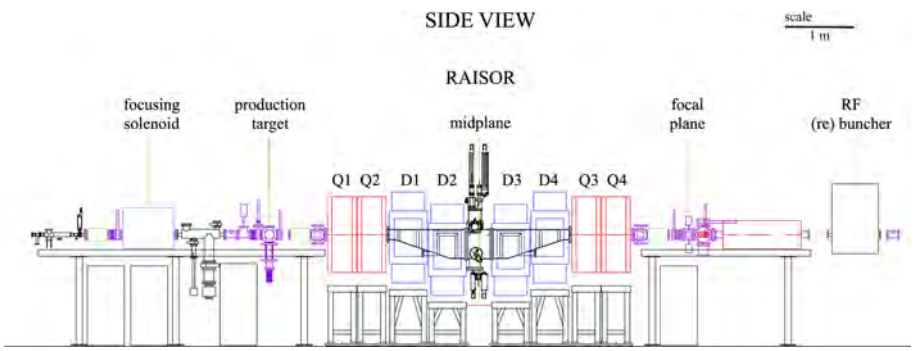

Figure 2.7: A partial side view of the layout of RAISOR. Quadrupoles (Q) and dipoles (D), have been labelled. The RF Sweeper and second RF (re)bunching cavity are not shown as they are 21 m and 23 m downstream of the production target, respectively. Figure from [53].

The purpose of the sweeper is to remove the remaining unreacted primary beam and other unwanted species that survive the slit separation after magnetic selection when they have the same magnetic rigidity as the radioactive beam of interest. Although such contaminants can have the same magnetic rigidity, their velocities will differ from the desired reaction products. The RF sweeper exploits that time/velocity difference. By applying a time-dependent transverse magnetic field synchronised to the bunch structure, the sweeper deflects contaminant particles out of the beam. This technique significantly improves

secondary-beam purity and reduce background [55].

In the present experiment, the sweeper was set to transmit a $^{17}F^{6+}$ secondary beam. The purified secondary beam from RAISOR is then delivered to downstream experimental areas – such as the HELIOS spectrometer.

2.4.2 Beams used in the experiment

The $^{17}F^{6+}$ beam, with an energy of 9.95 MeV/A and a typical intensity of $\sim 3 \times 10^5$ particles per second (pps), was produced in flight from the stable $^{17}O^{6+}$ primary beam via the ^{17}O(p,n)^{17}F reaction. The main contaminant in the ^{17}F beam was ^{17}O. A stable ^{17}O beam was delivered directly from the ion source at an energy of 10.12 MeV/u. Before the experimental setup, a beam attenuator was inserted to limit the ^{17}O beam intensity to $\sim 10^6$ pps.

The ^{17}F beam was used at the experiment for two and a half days, and the stable ^{17}O was used for one day.

2.4.3 Experimental setup

The experimental setup was located inside the HELIOS spectrometer. HELIOS is the first solenoidal spectrometer to have been built, and it was commissioned in 2010 [20]. The device consists of a large-bore superconducting solenoid (repurposed MRI magnet) with an inner diameter of 0.92 m and a length of 2.35 m, operated at a magnetic field strength of 2.85 T for this experiment.

The experimental setup consisted of an on-axis silicon array for detecting the protons, and a silicon telescope in a $\Delta E - E$ configuration, mounted downstream from the target, for detecting the recoils. The secondary beam passed through the hollow array of twenty-four position-sensitive silicon detectors (PSDs) arranged around the magnetic field axis, with six detectors mounted along each of the four sides of the array. The array was positioned within the uniform magnetic field region and covered distances between 220 and 570 mm upstream of the target, where the beam impinged on a solid deuterated polyethylene (CD_2) foil target. In the experiment, targets of 231 μg/cm^2 and 132 μg/cm^2 were used for the ^{17}F and ^{17}O beams, respectively. The use of CD_2 targets is motivated by the fact that it is not possible to manufacture a solid pure deuteron target. The recoil detector was placed 100 cm downstream the target.

In the following sections, a detailed description of the detectors used in the experiment will be provided.

2.4.4 Silicon array

To detect ejectile protons, the HELIOS silicon-detector array was used. The array consists of 24 position-sensitive silicon detectors (PSDs) mounted on a four-sided aluminium support rod, with six detectors on each face (see Fig. 2.8). Each PSD has a size of 12 mm $\times$ 56 mm and a thickness of 700 ± 15 μm. The active area is 9 mm $\times$ 50.5 mm. This is due to the fact that the detectors are bonded at the edges, which reduces the active area. The aluminium rod has an outer diameter of 20.3 mm and an inner diameter of 10 mm, allowing the beam to pass through its centre. The total length of the rod is 710 mm long [56].

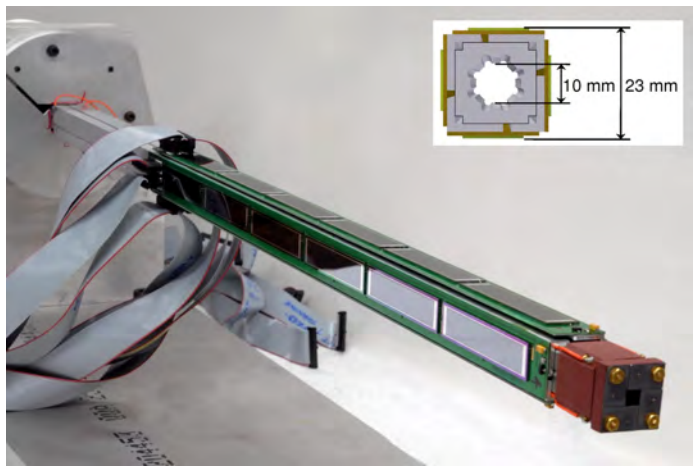

Figure 2.8: The HELIOS silicon-detector array. Six detectors are mounted on each of the four sides. The target would be in the lower-right corner of the picture. The red piece in front shields the array from low energy protons which would complete multiple turns in the magnetic field before hitting the array (multi-turn protons). The insert gives the dimensions of the front plate of the array. Figure from Ref. [20].

A photograph of one of the PSDs from the Si array is shown in Fig. 2.9. Each silicon wafer is mounted on a printed circuit board. Each PSD has three readout channels: a total energy output c_{t}, collected from the back face, and two energy readouts at both edges of the front face of the detector, c_{n} and c_{f}.

Figure 2.9: One Si PSD from the HELIOS Si array. There are electrical contacts at both short edges of the front face of each PSD (the lighter-colour part of a PSD) as well as one full-area contact at the back face. Figure from Ref. [20].

The resistance between the front edges of a detector is approximately 17 kΩ, and using resistive division of the signals between c_n and c_f, the position of the hit along the z-axis can be extracted with a resolution of approximately 1 mm [56].

The relative position along a PSD can be represented as x, $x \in (-1, 1)$: $x = \frac{c'_\mathrm{f} - c'_\mathrm{n}}{c_\mathrm{t}}$, where c'_f and c'_n are gain-matched to the energy signal c_t.

The c_f and c_n signals arise from resistive division of the charge deposited in the PSD by a particle. When a particle hits the centre of a PSD, amplitudes of both signals c_f and c_n are equal. It could however be that a particle hits very close to one side of the detector, for example the f edge, and produces a high-amplitude c_f signal. At the same time, the corresponding c_n would be small and depending on the electronics settings, it could be below the detection threshold. In principle, three situations are possible:

1. both c_f and c_n are available, as well as c_t,
2. only c_n is available together with c_t and c_f is missing,
3. only c_f is available together with c_t and c_n is missing.

Thus x can be calculated in three ways:

1. $$x = \frac{c'_\mathrm{f} - c'_\mathrm{n}}{c_\mathrm{t}}, \tag{2.3}$$
2. $$x = 1 - \frac{2c'_\mathrm{n}}{c_\mathrm{t}}, \tag{2.4}$$
3. $$x = \frac{2c'_\mathrm{f}}{c_\mathrm{t}} - 1. \tag{2.5}$$

The absolute hit position along the z-axis can be calculated as

$$z = (x - 1)\frac{l}{2} - d_{\text{target}} - d_{\text{i}}, \tag{2.6}$$

where l is the length of one PSD, d_{target} is the distance between the upstream edge of the active area of the Si array and the target (220 mm for the present experiment), and d_{i} is the distance from the end of the Si array to the centre of detector i.

Each PSD also provides flight times of the impinging particles relative to the recoil detectors, with a time resolution of ∼10 ns full width at half maximum (FWHM). This allows for a clear identification of single-orbit protons returning to the axis and thus a significant reduction of the background from multi-turn trajectories and other particles, which will have a different cyclotron period in the solenoid.

Because the silicon detectors do not cover the entire aluminium rod, a single PSD has an azimuthal angle ϕ angular coverage of approximately 42.7°, leading to a total geometrical efficiency in ϕ of about 47%.

Depending on their position along the axis of the solenoid, different PSDs have a different laboratory polar angle θ_{lab} coverage. In HELIOS, θ_{lab} of the proton is mapped onto the z position along the axis of the magnet at which the particle returns to the axis. Therefore, different PSDs have a different polar angle coverage, which also depends on the excitation energy of the populated state.

The PSDs have intrinsic energy resolutions between 27 and 53 keV FWHM, depending on the detector, decreasing with lower energy. These values have been determined by measuring a proton beam at varying energies between 2.0 and 5.0 MeV elastically scattered on a carbon target [56].

The silicon array can be calibrated with an alpha source (detailed description provided, for example, in [21]) or using known states of the studied isotope. In the presented experiment, the silicon-detector array was energy-calibrated using well known states in ^{18}O which was not a part of the present work.

In the present experiment, two out of the 24 PSDs in total were not functional.

2.4.5 Recoil detectors

For the detection of recoils, two layers of annular single-sided silicon detectors were used in a $\Delta E - E$ configuration. Each layer consisted of four segments (quadrants). The first layer measured the energy loss (ΔE) in a 80 μm thick Si layer. The second layer measured the residual energy (E) and was 1000 μm thick, sufficient to stop the recoils. Both layers consisted of Micron Semiconductor QQQ1 detectors [57]. The detector is shown in Fig. 2.10 and the dimensions of each quadrant are detailed in Table 2.4. The detector was placed 100 cm downstream the target.

The purpose of the recoil detector is to measure and identify recoils from the reactions of interest. The beams delivered onto the secondary target contained some impurities, while only the ^{17}F(d,p)^{18}F and ^{17}O(d,p)^{18}O reactions were relevant for this study. By gating on events that populate only ^{18}F (for the ^{17}F beam) and ^{18}O (for the ^{17}O beam), background from contaminant reactions and other unwanted channels (specifically fusion-evaporation) could be significantly reduced.

The recoils are identified in $\Delta E - E$ detectors based on the unique energy-loss patterns that ions exhibit in the two layers. For the same initial energy, ions of different charge deposit different amounts of energy in the ΔE and E layers, allowing them to be distinguished from one another.

Radii (mm)		Thickness and angular coverage	
Si chip inner	11.50	Azimuthal angular coverage (°)	82
Si chip outer	103.00	ΔE thickness (μm)	80
Si inner	18.00	E thickness (μm)	1000
Si outer	100.00		

Table 2.4: Dimensions of the individual QQQ1 detectors [57].

The recoils and the protons emitted in the reactions are geometrically correlated through two-body kinematics. As already mentioned in Section 2.4.4, the Si array does not cover the full azimuthal angle ϕ and only a limited range of proton trajectories are detected. Therefore, the recoil detector was rotated so that its active area covered the trajectories of the recoils associated with the protons detected in the silicon array.

The recoil detector was not calibrated in absolute energy units in the present experiment. The relative differences between individual recoils in a ΔE-E plot are sufficient for the analysis.

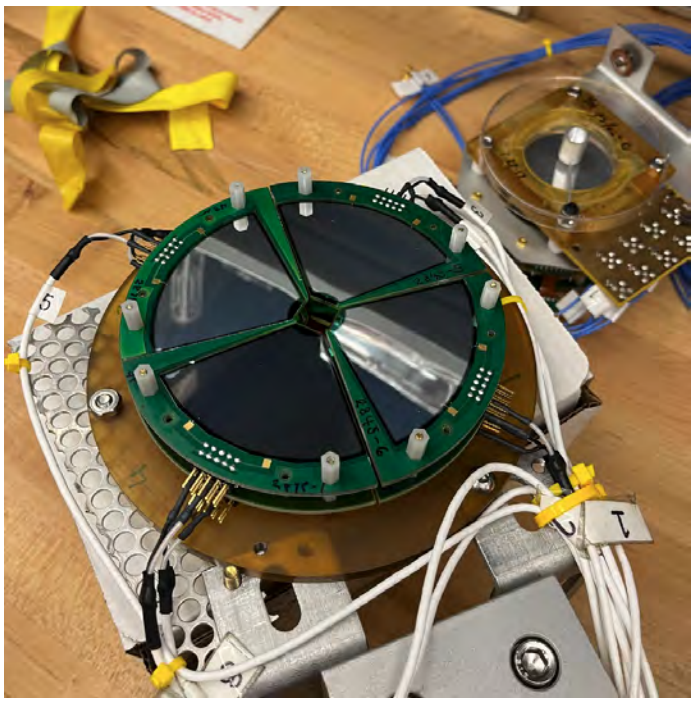

Figure 2.10: A photograph of the recoil detector used in the experiment. It consists of two layers of four quadrants each. In total eight signals are read from the detector. It was placed 100 cm downstream the target.

2.5 Data analysis

Figure 2.11 shows the energy of the detected ejectiles plotted against their distance of return to the solenoid axis relative to the target (the E versus z plot). The plot includes all data taken with the ^{17}O beam, without software cuts applied. Diagonal structures are visible on top of an otherwise approximately uniform background. These diagonal bands correspond to different excited states populated in the recoil nucleus. The wavy pattern at the bottom is caused by the higher threshold for detection with all three signals (c_{t}, c_{f}, c_{n}) above the threshold in the middle of each Si strip detector. Based on the detected energy of the ejectile and its hit position, the excitation energy of the recoil can be reconstructed. The resulting excitation energy spectrum is shown in Fig. 2.12. The diagonal structures in Fig. 2.11 map onto peaks in the excitation energy spectrum. However, the spectrum in Fig. 2.12 is dominated by background. The first step in reducing this background is to require a recoil detected in coincidence with each proton in the Si array.

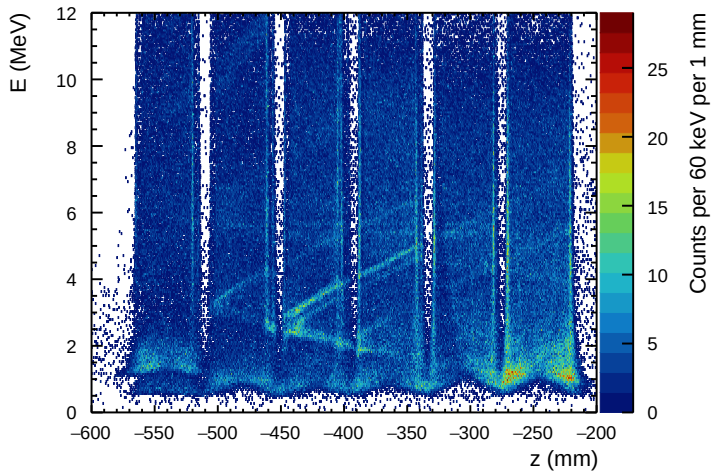

Figure 2.11: Energy of the ejectiles detected in the Si array versus their hit positions relative to the target for the ^{17}O beam. No software gates are applied. Clear "upwards-slante" lines correspond to various excited states in ^{18}O. The uppermost line corresponds to the ground state of ^{18}O. The wavy pattern at the bottom shows the higher threshold for detection with all three signals above the threshold in the middle of each Si strip detector.

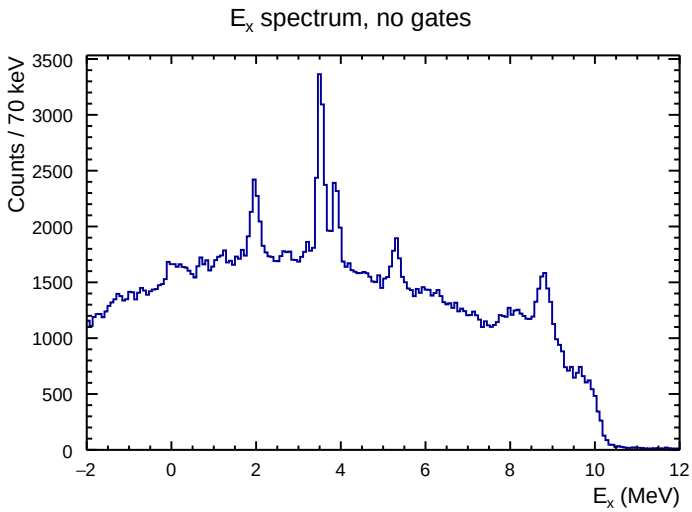

Figure 2.12: Excitation energy spectrum for the ^{17}O beam with no software gates applied. This spectrum corresponds to a one-dimensional projection of the diagonal structures in Fig. 2.11. Peaks are clearly visible, although the spectrum is dominated by background.

2.5.1 Recoil selection

Figure 2.13 shows the $\Delta E - E$ spectra for the four QQQ1 quadrants obtained with the ^{17}O beam. Recoils of the same mass form distinct groups and can be readily identified. These groups corresponding to ^{18}O recoils are indicated by black lines. An analogous set of spectra obtained with the ^{17}F beam, highlighting the ^{18}F recoils, is presented in Fig. 2.14.

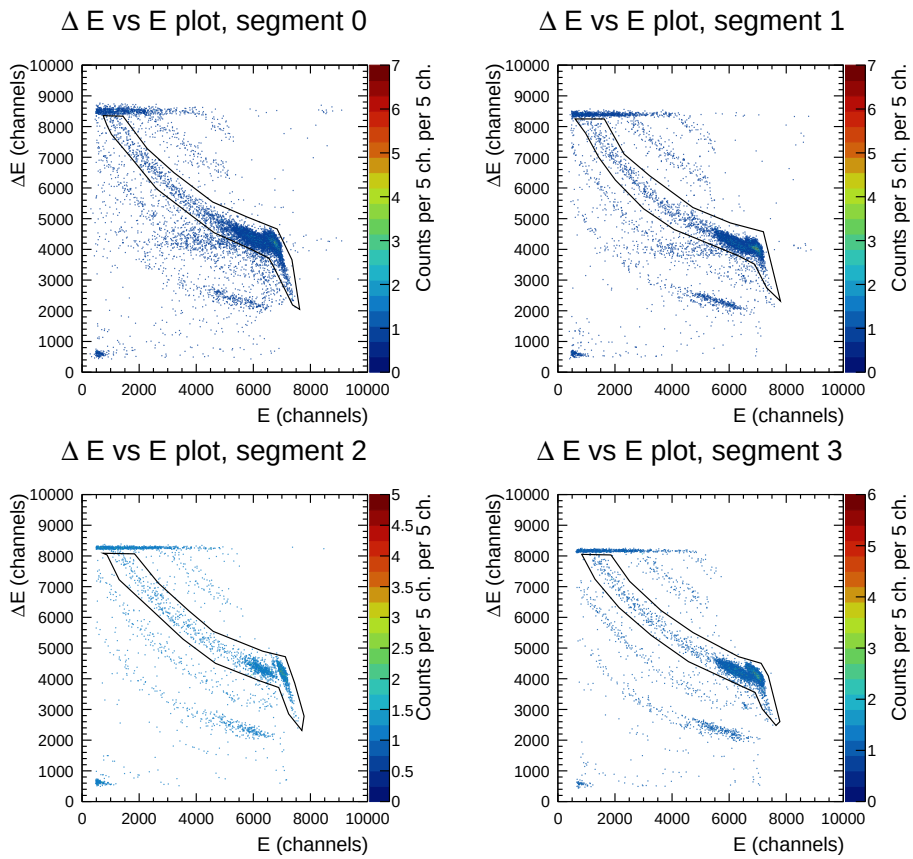

Figure 2.13: $\Delta E - E$ spectra for the four QQQ1 quadrants obtained with the ^{17}O beam. The bands corresponding to ^{18}O recoils are indicated with black lines.

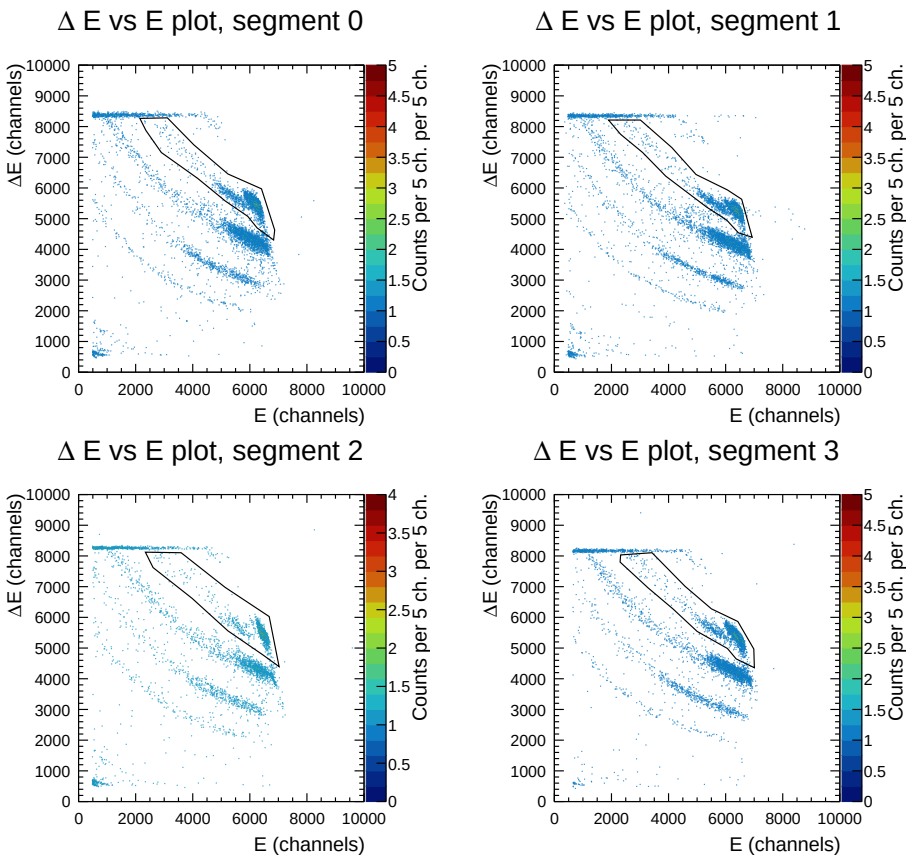

Figure 2.14: $\Delta E - E$ spectra for the four QQQ1 quadrants obtained with the ^{17}F beam. The bands corresponding to ^{18}F recoils are indicated with black lines.

By requiring the ejectile in the Si array to have a corresponding recoil in the Recoil Detector Telescope (RDT), and further requiring that the recoil lies within the ^{18}O detection region, the background is significantly reduced, and the excitation energy spectrum shown in Fig. 2.15 is obtained. Note how few counts are lost in the peaks between Fig. 2.12 and Fig. 2.15.

A corresponding spectrum plotted separately for each Si sensor is shown in Fig. 2.16. In this figure, each row represents sensors located on the same side of the array. The leftmost column corresponds to sensors placed furthest from the target, while the rightmost column corresponds to sensors closest to the target. As shown, sensors positioned at different distances from the target cover different excitation energy ranges.

Figure 2.17 shows the same spectra, but gated on recoils detected in recoil detector segment 3. It is evident that protons detected on a given side of the Si array have corresponding recoils detected in one of the four recoil detector segments.

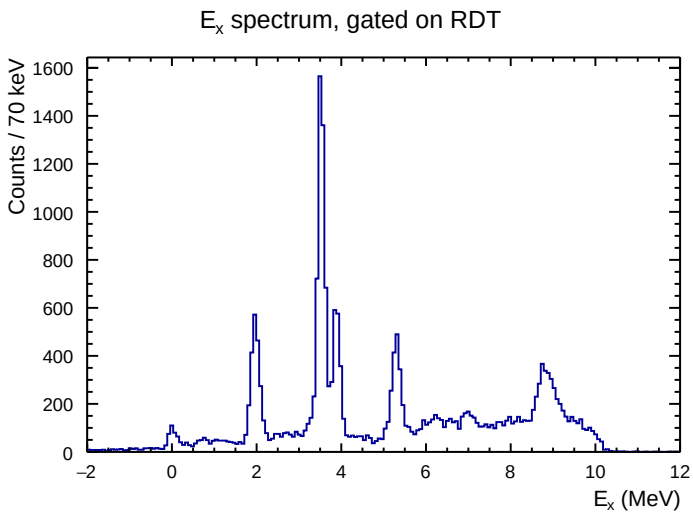

Figure 2.15: Excitation energy spectrum for the ^{17}O beam with software gates applied to the recoils.

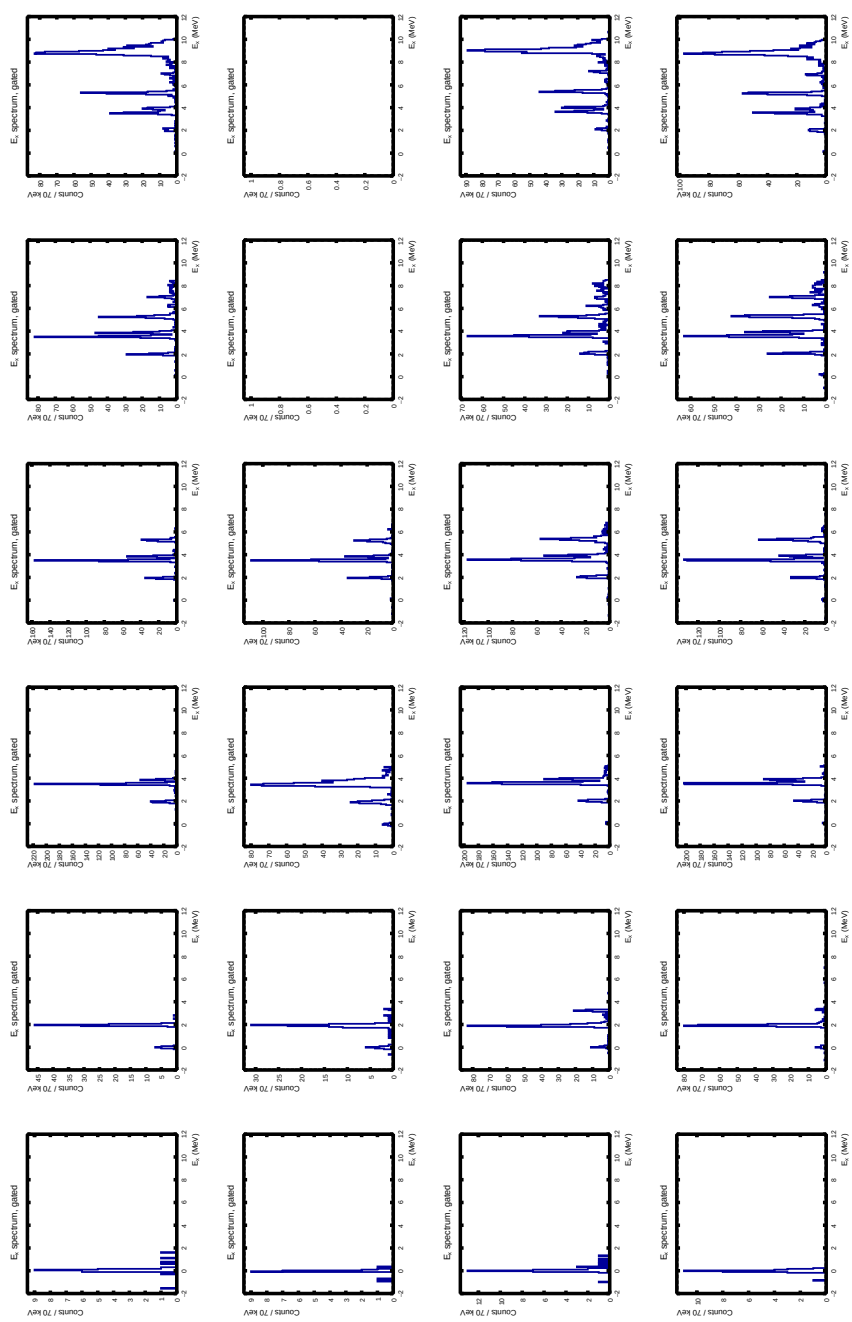

Figure 2.16: Excitation energy spectrum for the ^{17}O beam with software gates applied to the recoils for each sensor. Sensors 10 and 11 were not functional during the experiment.

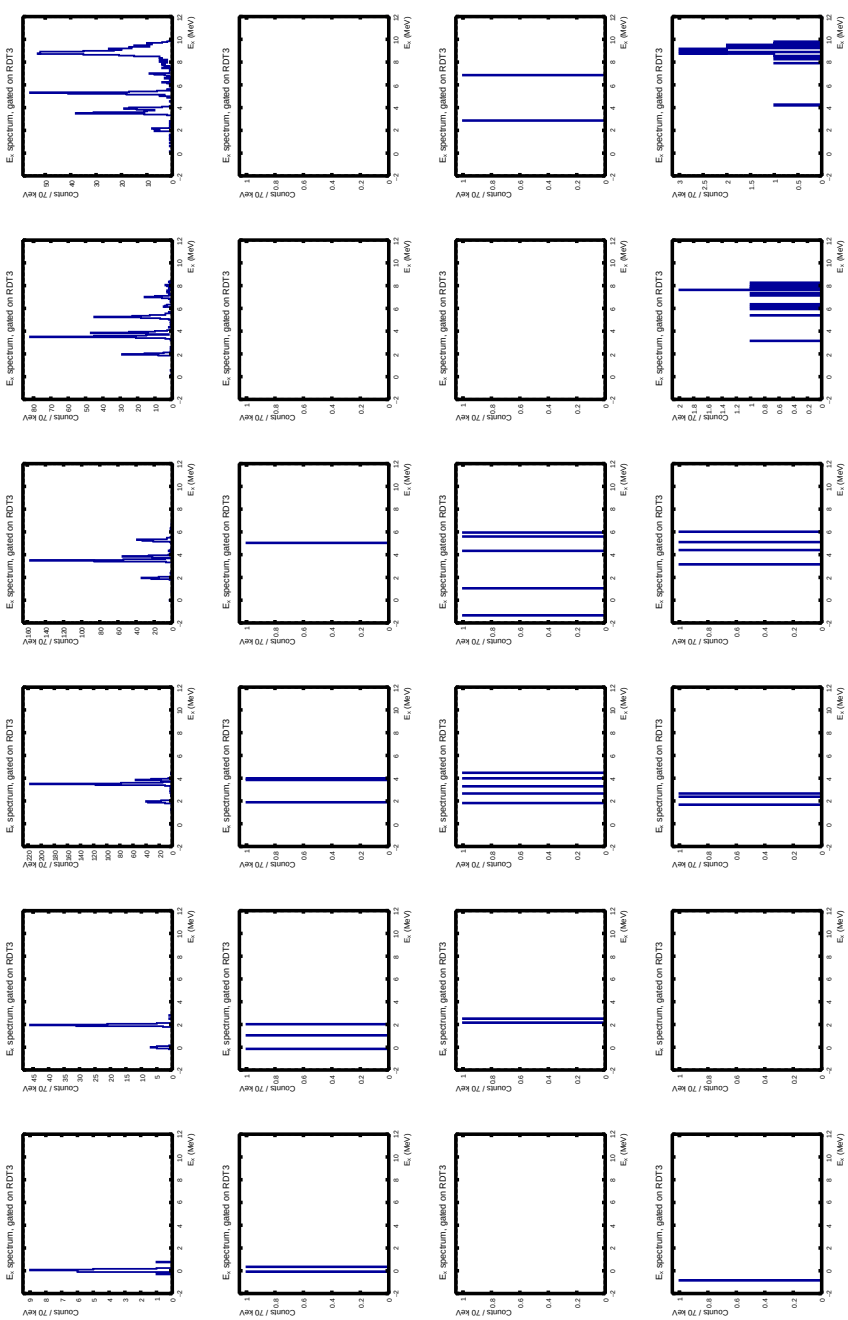

Figure 2.17: Excitation energy spectrum for the ^{17}O beam gated on events in which a recoil was detected in recoil detector segment 3. Sensors 10 and 11 were not functional during the experiment.

2.5.2 Coincidence time

Additional background reduction can be achieved by applying a gate on the coincidence time between the Si array and the recoil detectors. This allows to select only ejectiles corresponding to single-turn protons in the solenoidal magnetic field.

Figure 2.21 shows the coincidence time between the Si array and the recoil detectors plotted as a function of the x position along each sensor. Sensors 10 and 11 were not operational during the experiment. As shown in the figure, the coincidence time exhibits a clear dependence on the distance from the centre of the sensor, introducing nonlinearities that vary from detector to detector.

Multiple bands are visible for each detector. These bands correspond to particles with different times of return to the solenoid axis, such as particles with different mass-to-charge ratios or particles completing multiple turns before reaching the detector.

The position dependence of the coincidence time can be described by a polynomial function, with the polynomial degree varying from sensor to sensor. This is likely a walk effect due to the amplitude of the signal changing when the position changes. As an example, a comparison between sensors 8 and 22 is shown in Fig. 2.18. For sensor 8, the dependence can be described as a second-order polynomial, while for sensor 22 a fourth-order polynomial is required. By gating on the band corresponding to single-turn protons and fitting each sensor with a polynomial of the appropriate degree, the correlation can be linearised.

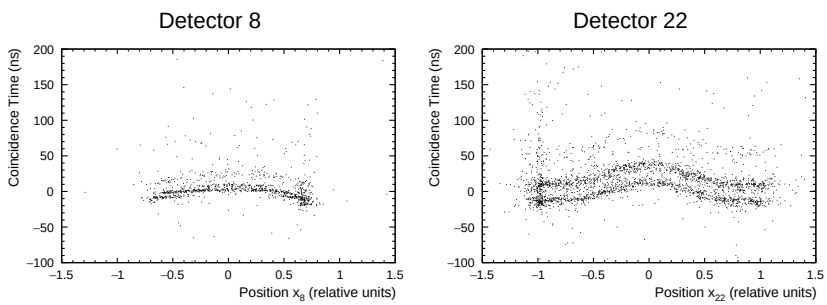

Figure 2.18: Coincidence time between Si array and recoil detector as a function of the x position along the Si array segment for sensor 8 (left) and 22 (right), before applying any correction, for the ^{17}O beam.

Figure 2.19 shows the same distributions for sensors 8 and 22, gated on the single-turn proton band and fitted with polynomial functions of degree 2 and 4, respectively. The corresponding rescaled spectra are shown in Fig. 2.20. The degrees of the polynomial functions used for each detector are summarised in Table 2.5.

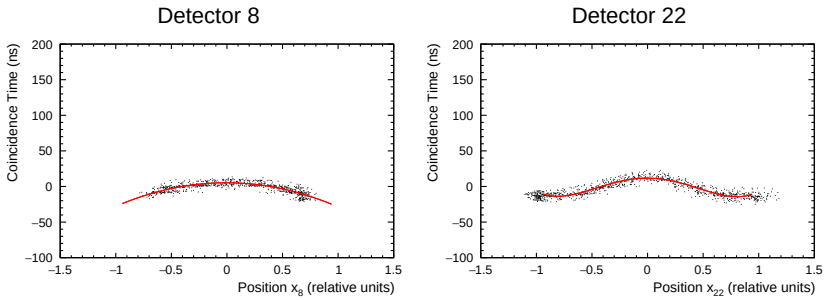

Figure 2.19: Coincidence time as a function of the x-position along the sensor plotted for sensors 8 (left) and 22 (right) gated on a band corresponding to single-turn protons and fitted with a polynomial of degree 2 (for detector 8) and degree 4 (for detector 22) for the ^{17}O beam.

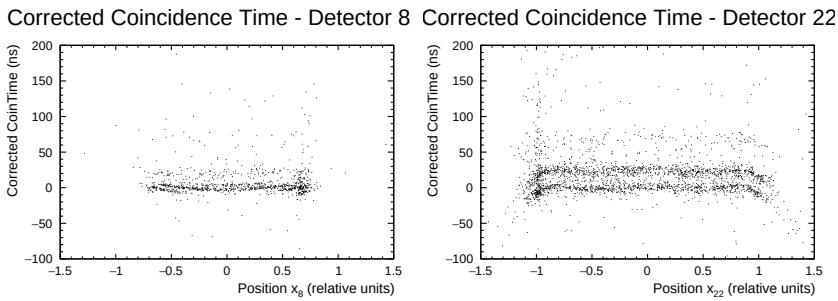

Figure 2.20: Corrected coincidence time as a function of the x-position along the sensors plotted for detectors 8 (left) and 22 (right) for the ^{17}O beam.

Detector 0	4
Detector 1	4
Detector 2	4
Detector 3	4
Detector 4	4
Detector 5	4
Detector 6	2
Detector 7	2
Detector 8	2
Detector 9	4
Detector 10	–
Detector 11	–

Detector 12	2
Detector 13	2
Detector 14	2
Detector 15	2
Detector 16	4
Detector 17	4
Detector 18	4
Detector 19	4
Detector 20	4
Detector 21	4
Detector 22	4
Detector 23	4

Table 2.5: Degrees of polynomials for Detectors 0 — 23

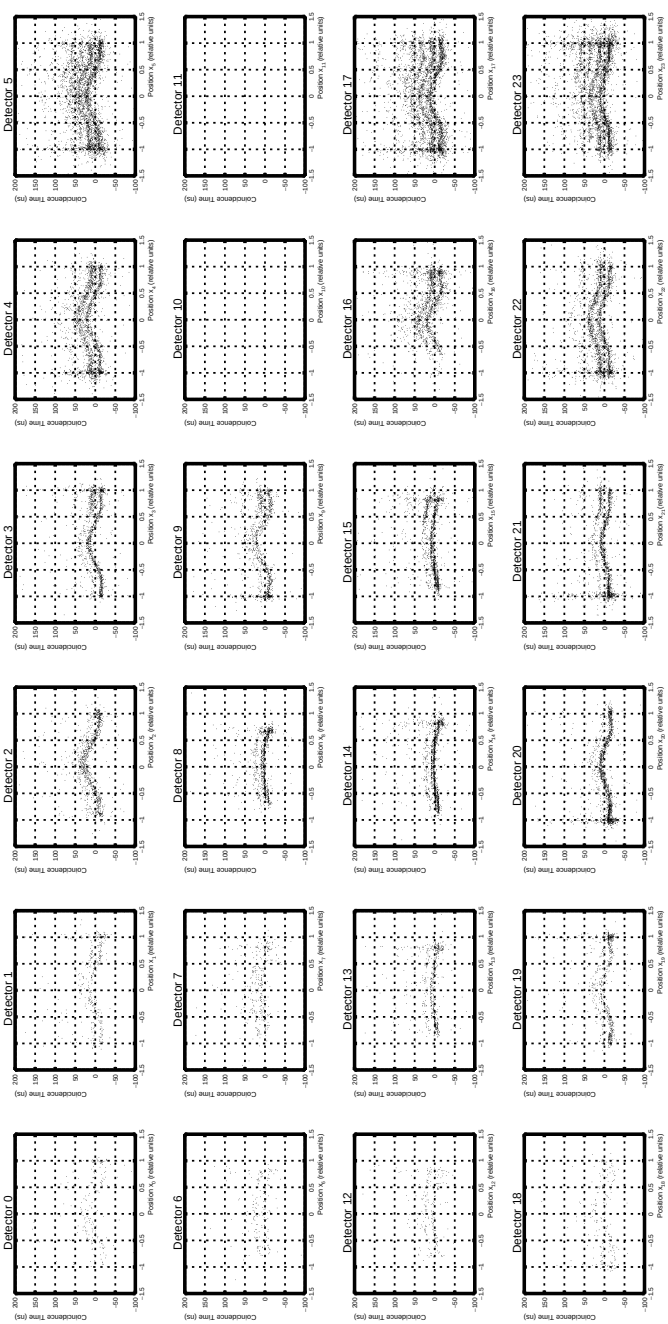

Figure 2.21: Coincidence time as a function of the x-position along the sensor for each PSD for the ^{17}O beam. Sensors 10 and 11 were not functional during the experiment.

As can be seen in Fig. 2.20, the relationship between the coincidence time and the position x remains nonlinear near to the edges of the sensors even after correction. This behaviour originates from the bonding regions at the edges of each PSD, where the particle positions cannot be reconstructed reliably. Consequently, only events with hit positions in the range $x \in (-0.95, 0.95)$ are considered in the further analysis.

Figure 2.22 shows the combined, corrected coincidence time spectrum for all detectors for the ^{17}O beam, gated on events with ^{18}O recoils. Peaks corresponding to particles with different mass-to-charge ratios or particles completing multiple turns before reaching the detector can be clearly distinguished. The highest peak corresponds to single-turn protons, for which the time resolution is estimated to be approximately 10 ns FWHM.

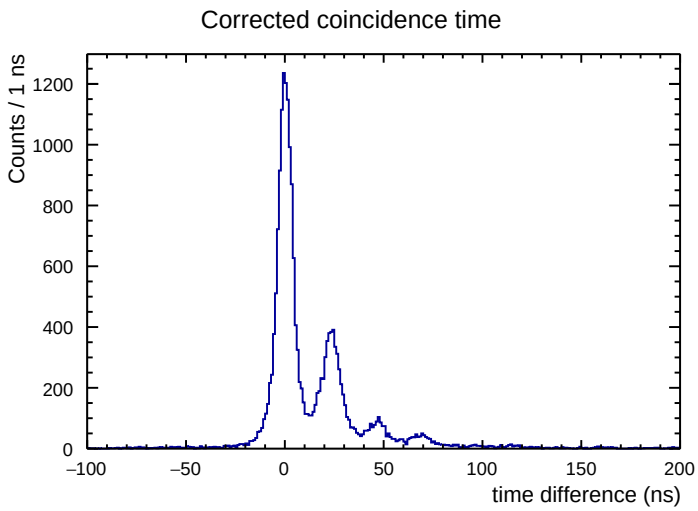

Figure 2.22: Combined, corrected coincidence time between ejectile proton and recoil spectrum for all Si array sensors for the ^{17}O beam, gated on events with ^{18}O recoils.

Figure 2.23 shows the energy of the detected ejectile plotted against its distance of return to the solenoidal axis relative to the target, with gates applied on ^{18}O recoils, the x position along the PSD $x \in (-0.95, 0.95)$, and the single-turn proton band in the coincidence time spectrum (time window from -20 ns to 15 ns). Compared to Fig. 2.12, the background is strongly reduced, and the remaining structures correspond to excited states populated in ^{18}O.

Figure 2.24 shows the resulting excitation energy spectrum. Peaks associated with individual excited states in ^{18}O are clearly visible, with the peak at 0.0 MeV corresponding to the ground state.

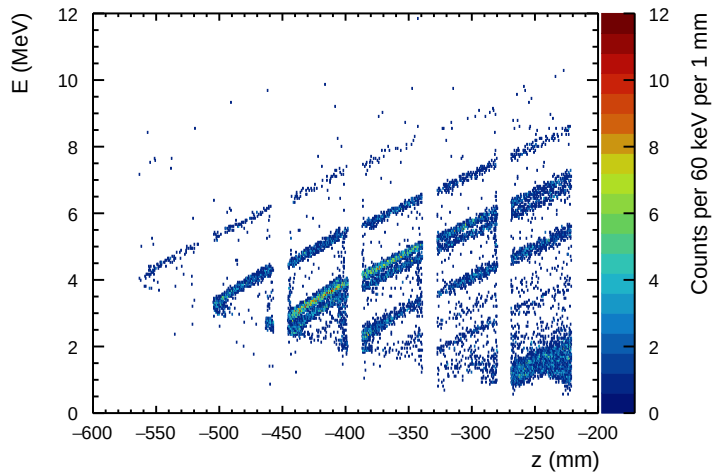

Figure 2.23: Energy of the ejectile detected in the Si array versus its hit position relative to the target for the ^{17}O beam with software gates applied to the recoils, the x position along the PSD, and the single-turn proton band in the coincidence time spectrum.

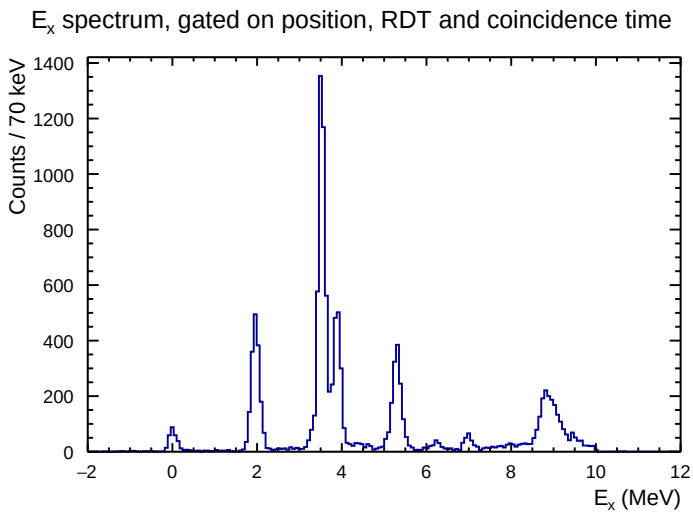

Figure 2.24: Excitation energy spectrum for the ^{17}O beam with software gates applied to the recoils, the position x along the PSD, and the single-turn proton band in the coincidence time spectrum.

It is also instructive to consider protons completing two or three turns before reaching the Si array. The upper panel in Fig. 2.25 shows the E vs z distribution gated on the double-turn proton band, while lower panel shows the corresponding distribution gated on the triple-turn proton band. The slopes of the diagonal structures corresponding to different excited states populated in ^{18}O change for double- and triple-turn protons. However, due to limited statistics, events corresponding to double- and triple-turn protons were not analysed further. In addition, the two-turn flight time for protons coincides with the single-turn flight time for alpha particles, leading to an unavoidable ambiguity.

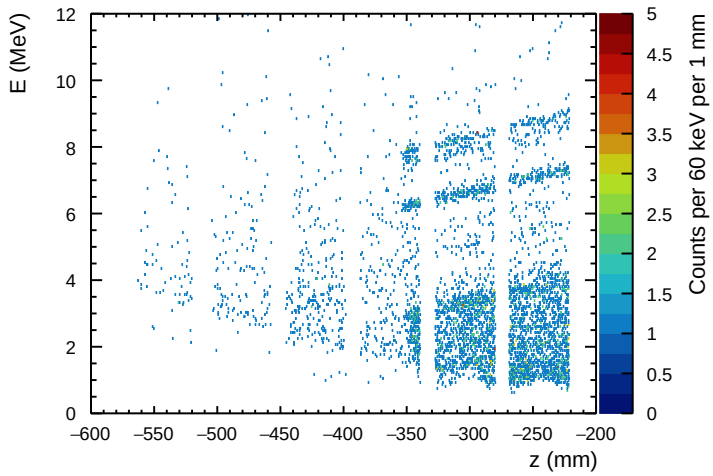

(a) Gated on the double-turn proton band.

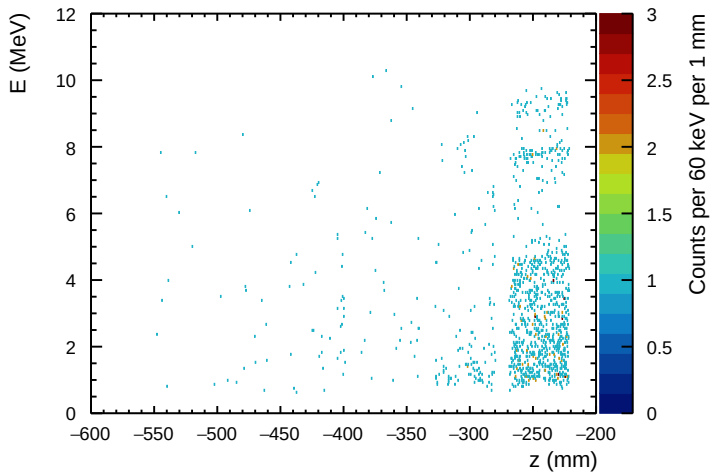

(b) Gated on the triple-turn proton band.

Figure 2.25: Energy of the ejectile detected in the Si array versus its hit position relative to the target for the ^{17}O beam with software gates applied to the recoils and the x position along the PSD. (a) Double-turn protons. (b) Triple-turn protons.

Figures 2.26, 2.27, 2.28, 2.29 and 2.30 repeat the analysis for the ^{17}F beam data. Figures 2.26 and 2.27 show the ungated E vs z plot and the corresponding excitation energy spectrum obtained with the ^{17}F beam. After applying gates on the ^{18}F recoils (Fig. 2.28) and subsequently applying additional gates on the x position along the PSD ($x \in (-0.95, 0.95)$) and the single-turn proton band in the coincidence time spectrum (Figs. 2.29 and 2.30), a clean excitation energy spectrum is obtained in Fig. 2.30. Distinct peaks are observed up to an excitation energy of approximately 5.5 MeV. This upper limit corresponds to the proton separation energy of ^{18}F, $S_p = 5.6$ MeV (see Table 2.1). States populated above this energy are proton unbound and decay before reaching the recoil detector.

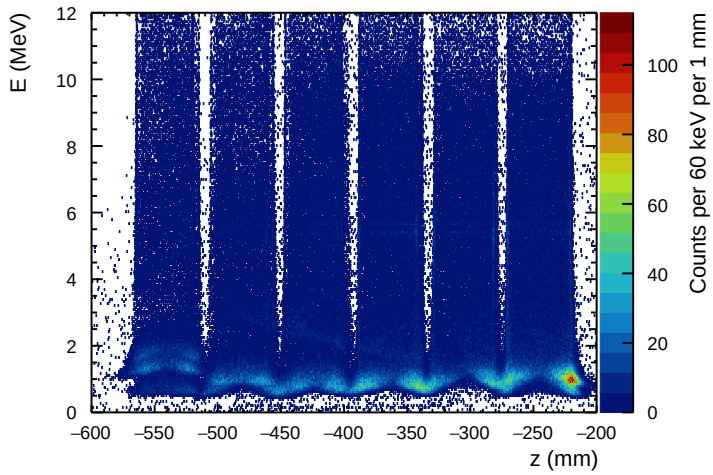

Figure 2.26: Energy of the ejectile detected in the Si array versus its hit position relative to the target for the ^{17}F beam. No software gates are applied.

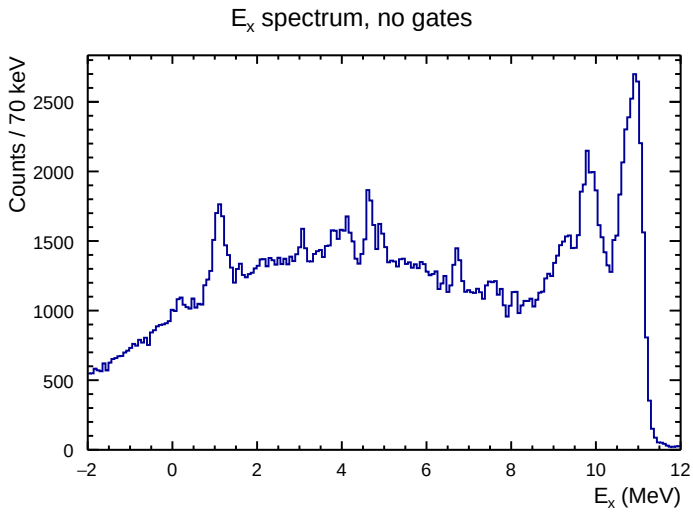

Figure 2.27: Excitation energy spectrum for the ^{17}F beam with no software gates applied.

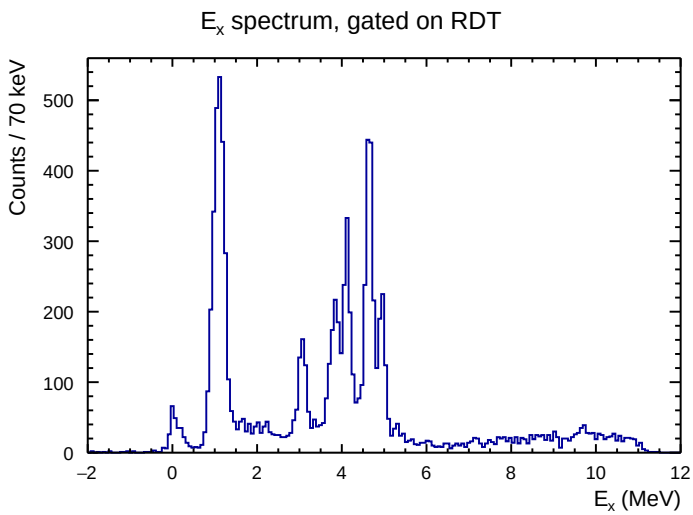

Figure 2.28: Excitation energy spectrum for the ^{17}F beam with software gates applied to the recoils.

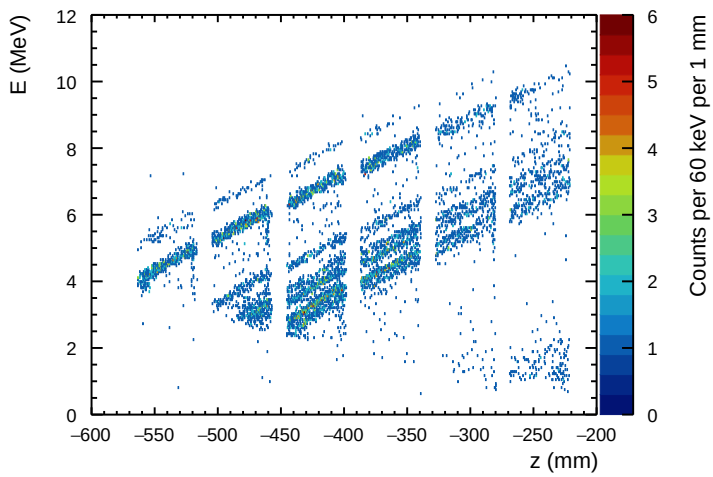

Figure 2.29: Energy of the ejectile detected in the Si array versus its hit position relative to the target for the ^{17}F beam with software gates applied to the recoils, the position x along the PSD, and the single-turn proton band in the coincidence time spectrum.

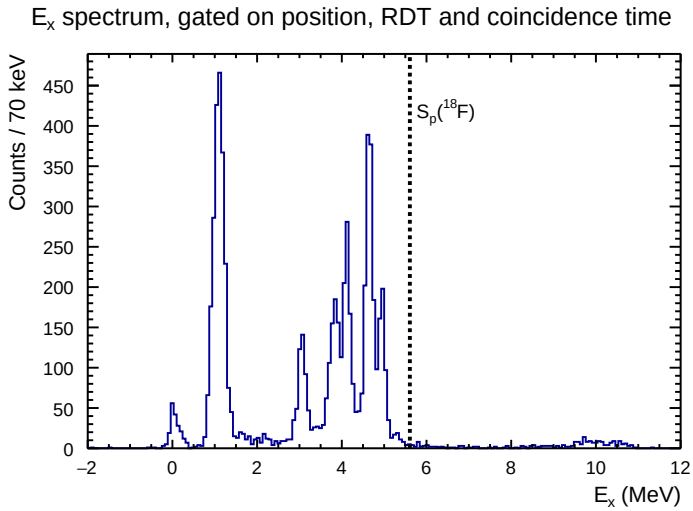

Figure 2.30: Excitation energy spectrum for the $^{17}\mathrm{F}(\mathrm{d},\mathrm{p})$ reactions with software gates applied to the recoils, the position x along the PSD, and the single-turn proton band in the coincidence time spectrum. No states are observed above the ^{18}F proton separation energy $S_p(^{18}\mathrm{F}) = 5.61$ MeV [32].

Inspection of Fig. 2.14 shows that reactions with the ^{17}F beam also populate ^{17}O recoils, visible as a band below the ^{18}F recoils. In addition, a band corresponding to ^{14}N recoils is visible below the ^{17}O recoils. By gating on events with ^{17}O recoils, it is possible to study proton-unbound states populated in the $^{17}\mathrm{F(d,p)}^{18}\mathrm{F}$ reaction that decay via proton emission to ^{17}O, and by gating on events with ^{14}N recoils—unbound states populated in the $^{17}\mathrm{F(d,p)}^{18}\mathrm{F}$ reaction that decay via α emission to ^{14}N.

The difference in efficiency for the detection of ^{18}F recoils, compared to the efficiency of detecting recoils after proton emission (^{17}O recoils), was calculated using the excitation energy spectrum for the ^{17}F beam with no software gates applied (Fig. 2.27). In this spectrum, peaks around 1.2 MeV and 6.8 MeV are visible above the background. The lower-energy peak, below the proton separation energy in ^{18}F, $S_p(^{18}\mathrm{F}) = 5.61$ MeV, corresponds to a deeply bound state. In contrast, the state around 6.8 MeV lies above the proton separation energy and is therefore unbound, decaying via proton emission to ^{17}O.

By calculating the integrals of the states in the excitation energy spectrum with no software gates applied and comparing them to the integrals obtained from the excitation energy spectra gated on the corresponding recoils, the position x along the PSD, and the single-turn proton band in the coincidence time spectrum (Fig. 2.30 for the ^{18}F recoils and Fig. 2.31 for the ^{17}O recoils), it is possible to determine the difference in detection efficiency between ^{18}F recoils and ^{17}O recoils. The calculated scaling factor between the ^{17}O and the ^{18}F recoils, ϵ, equals

$$\epsilon = 1.4(2).$$

The same scaling factor is assumed for detecting the ^{14}N recoils.

Figure 2.31 shows the excitation energy spectrum obtained with the ^{17}F beam after applying software gates on the x position along the PSD, the single-turn proton band in the coincidence time spectrum, and the ^{17}O recoils. The observed peaks correspond to the proton-unbound states in ^{18}F.

2.5.3 Statistics

The gated excitation energy spectra contain different numbers of events for the various beam and recoil combinations. A summary is provided in Table 2.6.

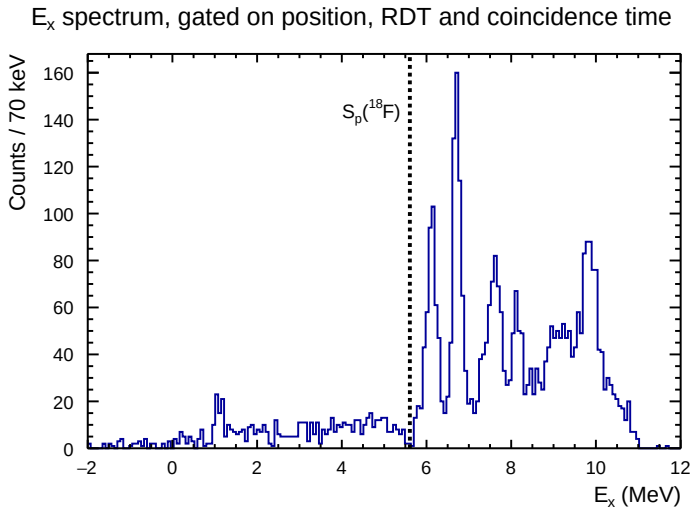

Figure 2.31: Excitation energy spectrum for the ^{17}F beam with software gates applied to the x position along the PSD, the single-turn proton band in the coincidence time spectrum, gated on ^{17}O recoils. The states correspond to proton-unbound states in ^{18}F, i.e. above $S_p(^{18}\mathrm{F}) = 5.61$ MeV [32].

Beam	Recoil	# of events
^{17}O	^{18}O	12 723
^{17}F	^{18}F	6 997
^{17}F	^{17}O	8 534

Table 2.6: Number of events remaining after all analysis gates for the different beam and recoil combinations.

2.5.4 States observed in the experiment

The schematic level scheme in Fig. 2.32 lists the states observed in the experiment for ^{18}O and ^{18}F. As can be seen, not all states listed in Tables 2.2 and 2.3 were observed. Isobaric analogue states between ^{18}O and ^{18}F are connected by arrows, with their corresponding spin and parity J^π indicated. While the states were identified in the present experiment, the excitation energy values as well as J^π listed are generally taken from the NNDC database [32]. Due to the limited excitation energy resolution of the Si array, states that are close in energy cannot be resolved individually. Such states are therefore grouped together and indicated using braces.

2.5.5 Excitation energy resolution

By inspecting well-isolated peaks in the excitation energy spectra, the excitation energy resolution of the silicon detector array can be determined. The resolution was extracted by fitting a Gaussian function to the selected peaks. Using the 1.982 MeV state in the ^{18}O spectrum and the 3.062 MeV state in the ^{18}F spectrum, the excitation energy resolution was found to be approximately 230 keV FWHM for ^{18}O and 290 keV FWHM for ^{18}F. The poorer resolution observed in ^{18}F can be attributed to the worse quality of a radioactive beam, which displays a larger energy and emittance spread compared to the stable ^{18}O beam.

2.5.6 Calculating differential cross sections

The differential cross section can be expressed as

$$\frac{\mathrm{d}\sigma}{\mathrm{d}\Omega} = \frac{Y}{\Delta\Omega\, s}, \tag{2.7}$$

where Y is the yield of a given excited state, $\Delta\Omega$ is the solid angle acceptance, and s is a scaling factor. The scaling factor s takes into account the product of the detector efficiency and the total number of beam particles and target particles per unit area (luminosity).

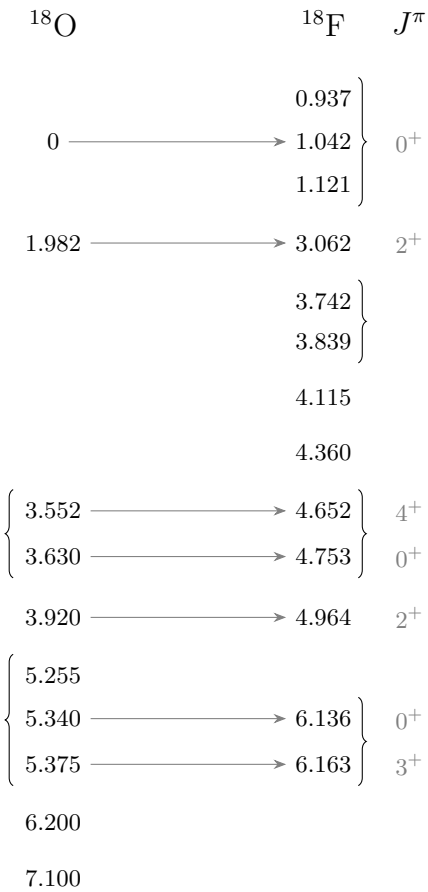

Figure 2.32: Energies (MeV) of the experimentally observed states in ^{18}O and ^{18}F. Isobaric analogue states are connected with arrows. Excitation energies and J^π are taken from NNDC [32]; unresolved nearby states are grouped with braces.

The standard normalisation procedure employed by HELIOS involves measuring deuterons elastically scattered from the target within a defined angular range and comparing the measured yields with theoretical calculations, for example, using the code PTOLEMY [31]. This allows to determine the total number of incident beam ions times target particles per unit area. Since the necessary hardware was not available in the present experiment, absolute differential cross sections and absolute spectroscopic factors cannot be extracted. Consequently, the differential cross sections presented in the following sections are given in arbitrary units and are calculated without applying the scaling factor s.

As described in Section 2.4.4, the silicon detector array consists of four sides, each equipped with six PSDs. This configuration naturally provides six distinct angular ranges for the extraction of differential cross sections. For states populated with sufficient statistics, each PSD can be further subdivided into two halves, effectively yielding twelve angular ranges.

The angular ranges covered by each detector (or detector half) and their corresponding solid angle acceptances were calculated using the `digios` code [58], an analysis package developed for HELIOS experiments. In general, the centre-of-mass emission angles covered by each detector (or detector half) depend on the excitation energy of the populated state, as seen in Fig. 2.23.

2.5.7 Angular distributions for ^{18}O

Figure 2.33 shows the excitation energy spectra obtained with the ^{17}O beam for six different z ranges (six "rings"). The angular coverage and corresponding peak intensities vary between these intervals. Each spectrum was fitted with a sum of Gaussian functions using the MINUIT package within the ROOT framework [59]. The peak energies were constrained relative to the ground state, allowing the spectrum an overall shift to account for calibration variations. A common Gaussian width was used for all peaks, with σ allowed to vary linearly with excitation energy E_x. The resulting fits provide the yields for each excited state within a given angular range, with the uncertainties taken from the fit parameters. For the most intense states, each z range was further subdivided, resulting in 12 effective z ranges.

As mentioned above, two of the 24 PSDs were not functional during the experiment. The peak yields in the corresponding angular ranges were therefore scaled by a factor of 4/3 to account for the missing detectors.

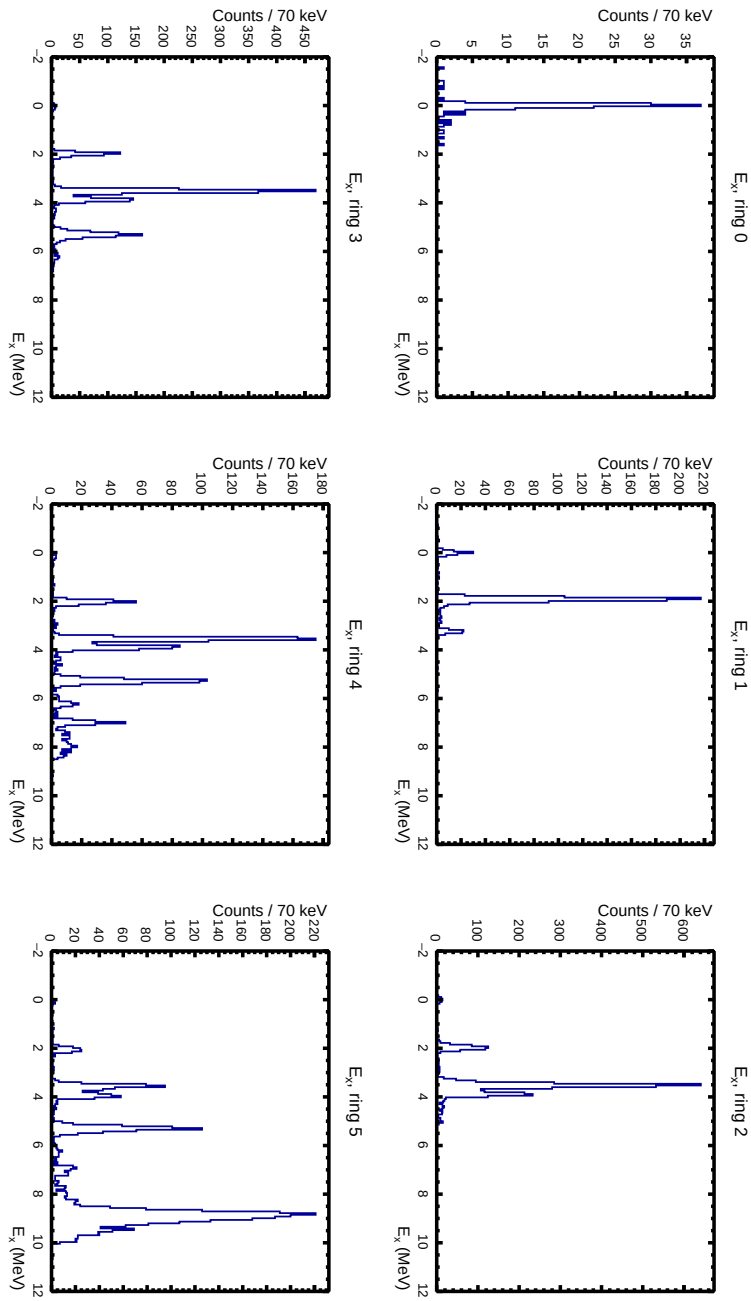

Figure 2.33: Excitation energy spectra obtained with the ^{17}O beam for six different z ranges (rings) of the silicon detector array. The angular dependence of the counts in the peaks are seen in Figs. 2.36 and 2.37.

The obtained differential cross sections for states populated in ^{18}O can be compared with angular distributions calculated using the DWBA code PTOLEMY.

Choice of optical potentials

The DWBA code PTOLEMY requires a number of input parameters to calculate the differential cross section for the population of a given state:

- the spin of the initial (ground) state,
- the populated single-particle orbital, characterised by the transferred angular momentum ℓ and the total angular momentum j of the transferred nucleon,
- the excitation energy of the populated state,
- the spin and parity J^π of the populated state,
- the beam energy in the laboratory frame,
- the optical model potentials for the incoming and outgoing channels.

It is important to note that DWBA calculations are more sensitive to variations in the transferred angular momentum ℓ than to variations in the spin and parity J^π. For a given excitation energy E_x, calculating differential cross sections for two states with the same J^π but different ℓ values results in significantly different angular-distribution shapes. In contrast, when the same ℓ value is assumed and only the J^π values vary, the calculated angular distributions are very similar in shape, differing mainly in their absolute magnitude.

This means that while ℓ can often be assigned by comparing measured differential cross sections with DWBA calculations, determination of J^π is, in most cases, not straightforward. This behaviour is illustrated in Fig. 2.34, which shows DWBA-calculated differential cross sections for a state populated in the $^{17}\mathrm{O}(\mathrm{d},\mathrm{p})^{18}\mathrm{O}$ reaction at a beam energy of 10.12 MeV/u and an excitation energy of 5.315 MeV. Calculations corresponding to different ℓ transfers and different J^π assignments are shown. As can be seen, states with different ℓ values lead to angular distributions that are significantly different in shape, whereas states with the same ℓ and different J^π produce nearly identical distributions, with only small differences in amplitude.

A number of different optical model parameters were used to model the $^{18}\mathrm{O}(\mathrm{d},\mathrm{p})^{18}\mathrm{O}$ and $^{18}\mathrm{F}(\mathrm{d},\mathrm{p})^{18}\mathrm{F}$ reactions. The possible choices include the global parameters listed in Table 2.7.

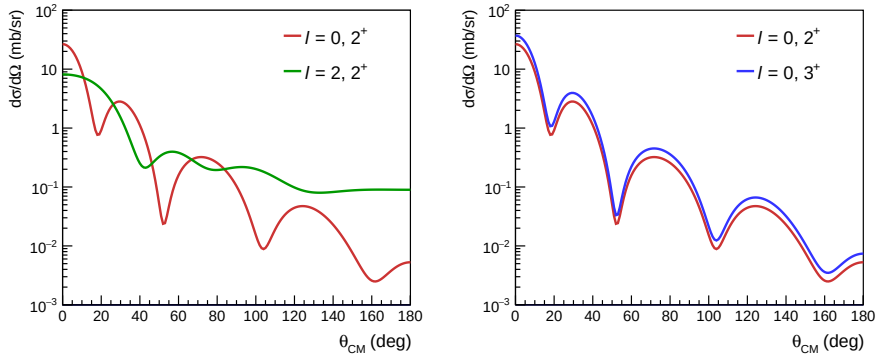

Figure 2.34: DWBA-calculated differential cross sections for a state populated in the ^{17}O(d, p)^{18}O reaction at beam energy 10.12 MeV/u and an excitation energy of 5.315 MeV. Calculations corresponding to different ℓ transfers (left panel) and different J^π assignments (right panel) are shown. Transfers with different ℓ values lead to angular distributions that are significantly different in shape, whereas transfers with the same ℓ but different final J^π produce nearly identical distributions, with only small differences in amplitude.

Deuteron models (incoming channel)		
A	An, Cai, 2006	[60]
H	Han, Shi, Shen, 2006	[61]
B	Bojowald et al., 1988	[62]
D	Daehnick, Childs, Vrcelj, 1980	[63]
L	Lohr and Haeberli, 1974	[64]
Q	Perey and Perey, 1963	[65]
Z	Zhang, Pang, Lou, 2016	[66]
Proton models (outgoing channel)		
K	Koning and Delaroche, 2003	[67]
V	Varner et al., 1991	[68]
M	Menet et al., 1971	[69]
G	Becchetti and Greenlees, 1969	[70]
P	Perey, 1963	[71]

Table 2.7: Optical model potentials tested to describe the incoming channel (deuteron models) and the outgoing channel (proton models).

To determine which potentials should be used, well-known excited states in ^{18}O were used. By fitting the experimentally obtained differential cross sections with corresponding DWBA calculations using different potential combinations,

	Real volume			Imaginary volume			Imaginary surface			Real spin orbit			Imaginary spin orbit			Coulomb
	V_v	$r_{0,v}$	a_v	W_v	$r_{0,v}$	a_v	W_D	r_D	a_D	V_{so}	$r_{0,so}$	a_{so}	W_{so}	$r_{0,so}$	a_{so}	R_c
A [60]	88.855	1.149	0.751	2.363	1.344	0.598	10.211	1.393	0.690	3.557	0.972	1.011	0	0	0	1.303
H [61]	80.066	1.174	0.809	0	0	0	16.808	1.328	0.581	3.703	1.234	0.813	-0.206	1.234	0.81	1.698
B [62]	80.922	1.180	0.726	0	1.270	0.822	10.474	1.270	0.822	6.000	0.878	0.878	0	0	0	1.300
D [63]	85.01	1.170	0.741	0.507	1.331	0.669	12.121	1.331	0.669	6.552	1.070	0.66	0	0	0	1.300
L [64]	97.975	1.050	0.860	0	0	0	32.973	1.430	0.586	7.000	0.750	0.500	0	0	0	1.300
Q [65]	82.770	1.150	0.810	0	0	0	19.258	1.340	0.680	0	0	0	0	0	0	1.150
Z [66]	94.407	1.052	0.776	4.798	1.727	0.744	3.040	1.727	0.744	0	0	0	0	0	0.59	1.300
K [67]	48.852	1.149	0.675	2.558	1.149	0.675	7.575	1.301	0.528	5.212	0.939	0.59	-0.136	0.939	0.59	1.405
V [68]	47.791	1.164	0.690	2.393	1.170	0.690	7.125	1.170	0.690	5.900	0.882	0.63	0	0	0	1.286
M [69]	48.321	1.160	0.750	3.545	1.370	0.643	4.619	1.370	0.643	6.040	1.064	0.78	0	0	0	1.250
G [70]	49.548	1.170	0.750	3.033	1.320	0.588	6.410	1.320	0.588	6.200	1.100	0.75	0	0	0	1.300
P [71]	43.188	1.250	0.650	0	0	0	13.500	1.250	0.470	7.500	1.250	0.470	0	0	0	1.250

Table 2.8: Input parameters used for the PTOLEMY calculations for the ground state 0^+ in ^{18}O. The leftmost column corresponds to the potential symbol specified in Table 2.7.

it is possible to determine which potentials describe the data best. For this, three states in ^{18}O were selected, located at 0.000 MeV (the ground state), 1.982 MeV, and 3.920 MeV. These states are well separated in energy from neighbouring states and can be resolved experimentally without ambiguities. It is important to note that the absolute magnitudes of the DWBA calculations cannot be compared directly to the experimental data as the data was not normalised to be in an appropriate unit (mb/sr). Input parameters used for the PTOLEMY calculations for the ground state 0^+ in ^{18}O are shown in Table 2.8. Figure 2.35 shows the obtained spectra. From a visual inspection of the DWBA calculations obtained with PTOLEMY and fitted to the experimental data, it is not clear which potential describes the data best.

Table 2.9 presents χ^2 values extracted from fitting DWBA calculations to experimental data for each excited state shown in Fig. 2.35. The obtained values are rather consistent, independently of which potential combination is used. It is important to note that it was not possible to calculate the $\ell = 0$ component in the excited state in ^{18}O at the excitation energy 1.982 MeV with the "L" potential as it diverged. The last column in the table presents summed χ^2/ndf (number of degrees of freedom) for all three states considered. Even though some values are smaller than others, choosing potential combinations based solely on this number is not optimal. For example, by looking at Fig. 2.35, one can see that the experimental data points exhibit noticeable scatter and the uncertainty does not always account for that adequately. For this reason, the "AK" potential combination was chosen as it is used often in the literature, for example in a study across a large range of nuclei in Ref. [72].

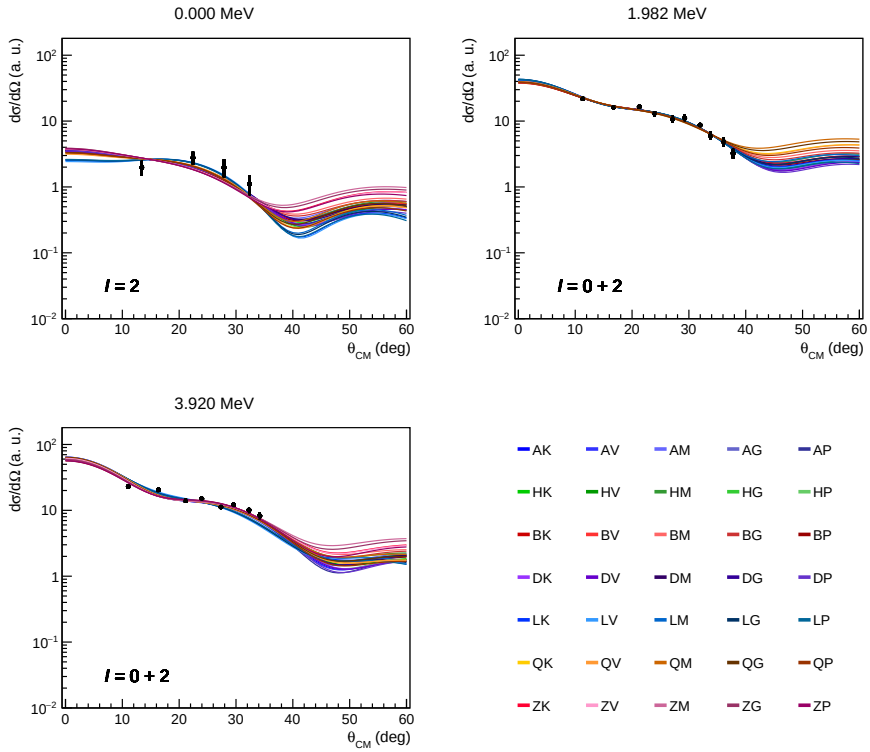

Figure 2.35: DWBA calculations (lines) with PTOLEMY using different optical potential parameter combinations for the incoming and outgoing channels for states in ^{18}O. The first letter in potential combinations corresponds to potential parameters used for the incoming channel (deuteron potential) and the second letter corresponds to potential parameters for the outgoing channel (proton potential). Values of the parameters are listed in Table 2.7. The data points correspond to experimental data.

potentials	χ^2			χ^2_{tot}	$\frac{\chi^2_{\mathrm{tot}}}{\mathrm{ndf}_{\mathrm{tot}}}$
	0.000 MeV	1.982 MeV	3.920 MeV		
AK	8.269	10.883	48.357	67.509	16.877
AV	7.712	11.084	56.651	75.447	18.862
AM	8.339	11.549	49.712	69.600	17.400
AG	8.336	11.062	48.267	67.664	16.916
AP	8.739	9.764	43.341	61.843	15.461
HK	7.885	10.105	33.303	51.293	12.823
HV	7.287	10.000	38.421	55.708	13.927
HM	7.928	11.062	34.236	53.226	13.306
HG	8.122	10.462	33.623	52.207	13.052
HP	8.493	9.209	30.934	48.637	12.159
BK	8.579	11.054	29.836	49.469	12.367
BV	8.005	10.777	34.718	53.500	13.375
BM	8.577	12.581	30.974	52.132	13.033
BG	8.730	11.730	30.379	50.840	12.710
BP	9.129	9.978	28.319	47.426	11.856
DK	7.671	10.163	40.254	58.088	14.522
DV	7.118	10.076	46.718	63.912	15.978
DM	7.780	10.882	41.817	60.479	15.120
DG	7.766	10.467	40.544	58.777	14.694
DP	8.191	9.269	37.251	54.712	13.678
LK	4.847		66.872	71.718	17.930
LV	4.295		71.673	75.968	18.992
LM	4.718		66.220	70.938	17.734
LG	4.950		67.911	72.861	18.215
LP	5.353		62.539	67.892	16.973
QK	7.587	10.189	42.765	60.542	15.135
QV	6.927	10.338	49.642	66.906	16.727
QM	7.516	10.572	43.255	61.344	15.336
QG	7.855	10.252	43.308	61.415	15.354
QP	8.207	9.399	38.672	56.278	14.070
ZK	10.337	16.013	30.418	56.768	14.192
ZV	9.829	15.615	36.481	61.924	15.481
ZM	10.032	20.437	31.780	62.249	15.562
ZG	10.395	17.808	30.681	58.884	14.721
ZP	10.748	13.518	28.136	52.402	13.101

Table 2.9: χ^2/ndf values obtained from DWBA fits using different combinations of optical model potentials for the three selected states in ^{18}O.

Fitting and extracting spectroscopic factors

The ^{17}O(d, p)^{18}O reaction has already been studied, and the spins and parities of the excited states, J^π, as well as the transferred angular momenta ℓ, are generally known (see Section 2.3.1 and Table 2.2). For isolated states in ^{18}O (0.0 MeV, 1.982 MeV, 3.920 MeV, 6.200 MeV, 7.100 MeV), the experimentally obtained differential cross sections were fitted with DWBA calculations assuming the ℓ and J^π values listed in Table 2.2.

For both ^{18}O and ^{18}F, the only significantly populated orbital with $\ell = 0$ transfer is the $2s_{1/2}$ orbital. For $\ell = 2$, two orbitals are possible: $1d_{3/2}$ or $1d_{5/2}$. For consistency, all $\ell = 2$ states were fitted assuming population of the $1d_{5/2}$ orbital.

When a state contains contributions from different ℓ values, as for example in the case of the 1.982 MeV state in ^{18}O, which has $J^\pi = 2^+$ with both $\ell = 0$ and $\ell = 2$ components, the differential cross section was fitted using a combination of two DWBA calculations, one for each ℓ. The relative contributions of the individual DWBA curves were treated as free parameters and determined by the fitting routine. This procedure is referred to as the **free fit** method and was applied to all states that are experimentally resolved in both the ^{18}O and ^{18}F final nuclei. The thus observed scaling of each DWBA calculation is the spectroscopic factor.

As discussed in Section 2.5.4, several states in ^{18}O and ^{18}F could not be resolved experimentally due to the limited excitation energy resolution of the experimental setup. Such unresolved states are grouped in braces in Fig. 2.32. In the present work, two methods of fitting the DWBA calculations to such unresolved states were used. They are referred to as **Option 1** and **Option 2**:

Option 1 Unresolved states are treated as a single effective state and fitted using a simple combination of DWBA calculations corresponding to the relevant ℓ transfers present in the multiplet. The relative strength of each ℓ contribution is not constrained and is determined freely by the fitting routine, analogously to the free fit method used for isolated mixed-ℓ states. The DWBA differential cross section was calculated at the mean energy of the states in the multiplet.

As an example, for the doublet at excitation energies 3.552 – 3.630 MeV in ^{18}O, an excitation energy of 3.591 MeV was used as input to PTOLEMY. Both states correspond to $\ell = 2$ transfer. However, the lower has $J^\pi = 4^+$, while higher has $J^\pi = 0^+$. Since DWBA calculations for the same ℓ and different J^π differ mainly in magnitude and not in shape, it is not possible within this approach to extract information on the relative strength of these two contributions in the multiplet. Consequently, a single J^π is chosen for the effective state, and the fit is performed accordingly.

Option 2 In this approach, unresolved multiplets are fitted using relative spec-

troscopic strengths taken from literature. For each state in the multiplet, the relative contribution of each ℓ transfer is fixed according to the corresponding literature spectroscopic strengths. The individual DWBA contributions are then summed with these relative weights, and the combined distribution is scaled to the experimental data using a single free normalisation parameter. Spectroscopic factors are obtained by multiplying the extracted normalisation factor with the relative ℓ components for each state in literature.

The obtained differential cross sections for states populated in ^{18}O are presented in Figs. 2.36 and 2.37 as a function of the centre-of-mass angle. The black points are experimental data, and the lines correspond to angular distributions calculated using PTOLEMY fitted to the experimental data with Option 1. The experimental data uncertainty on the y-axis corresponds to the uncertainty of the Gaussian fit to the peak. From these fits, raw spectroscopic factors were extracted.

Overall, the measured angular distributions are reasonably well reproduced by DWBA calculations for all observed states. However, some of the states, in particular the states at 0.0 MeV, 6.200 MeV, and 7.100 MeV, suffer from limited statistics, which results in larger error bars. Consequently, the agreement between the experimental data and the calculated angular distributions for these states is less convincing than for the more strongly populated states.

The first data point for the doublet of states at 3.552 and 3.630 MeV, corresponding to $\theta_{\mathrm{CM}} \approx 13^{\circ}$, exhibits a significantly larger spread and lies noticeably further from the DWBA curve than the other data points. The impact of this point on the extracted spectroscopic factor was investigated by performing fits both including and excluding it. The resulting spectroscopic factors were found to be consistent within the uncertainties, regardless of whether this data point was included in the fit.

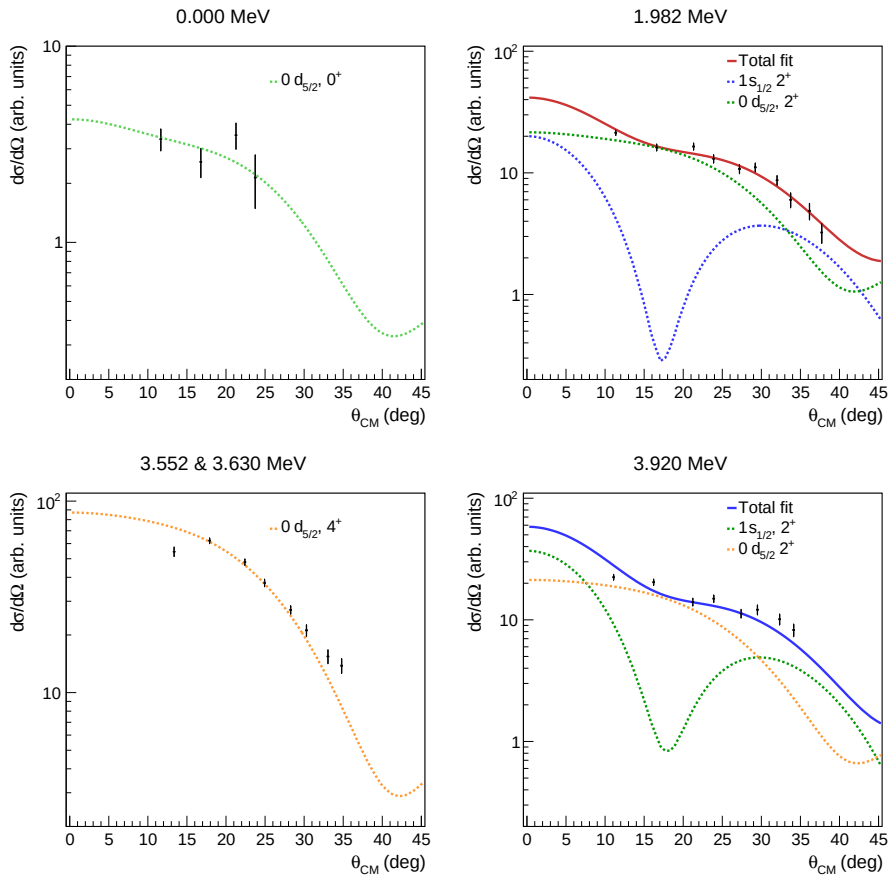

Figure 2.36: Angular distributions for several states in ^{18}O (excitation energy of each state is given in the title of each graph). Black points are experimental data; lines are DWBA fits using a free fit with adjustable amplitudes of all relevant angular momentum (ℓ) transfers (Option 1, see text for a more detailed description) with PTOLEMY.

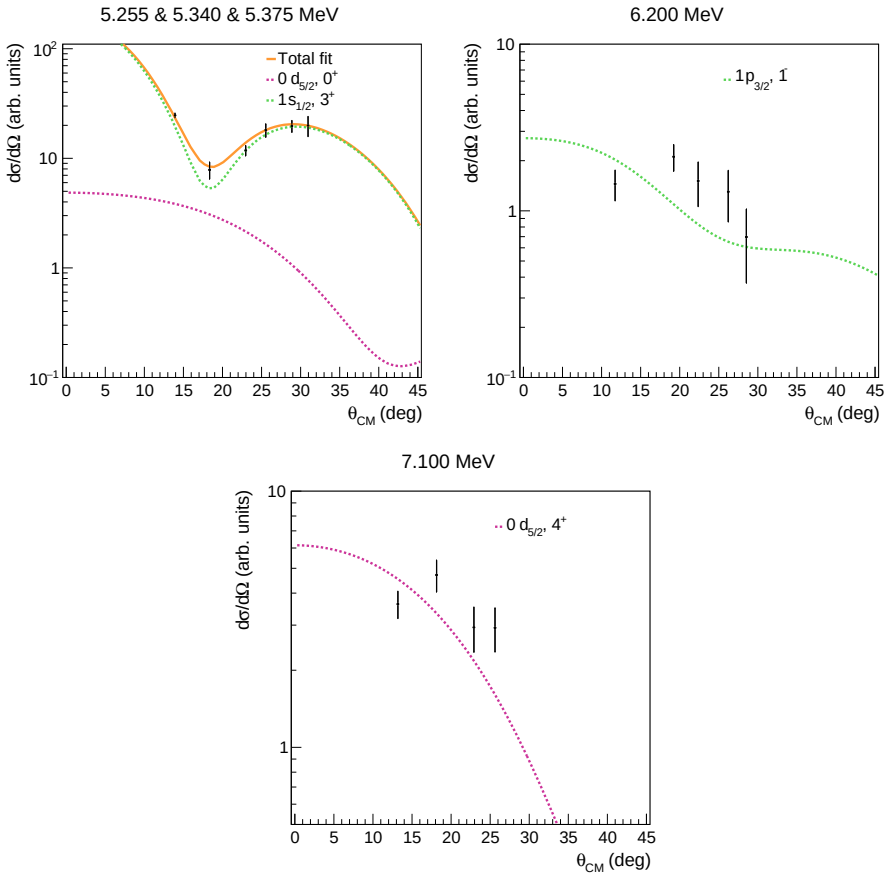

Figure 2.37: Angular distributions for several states in ^{18}O (excitation energy of each state is given in the title of each graph). Black points are experimental data; lines are DWBA fits using a free fit with adjustable amplitudes of all relevant angular momentum (ℓ) transfers (Option 1, see text for a more detailed description) with PTOLEMY.

2.5.8 Angular distributions for ^{18}F

Figures 2.38 and 2.39 present the differential cross sections for states populated in ^{18}F with fitted DWBA calculations. As for the ^{18}O, the differential cross sections fitted with Option 1 are shown.

Similarly as for states populated in ^{18}O, the the measured angular distributions are reasonably well reproduced by DWBA calculations for all observed states. However, due to less statistics for the ^{17}F beam, the data points exhibit larger uncertainties and a generally larger spread.

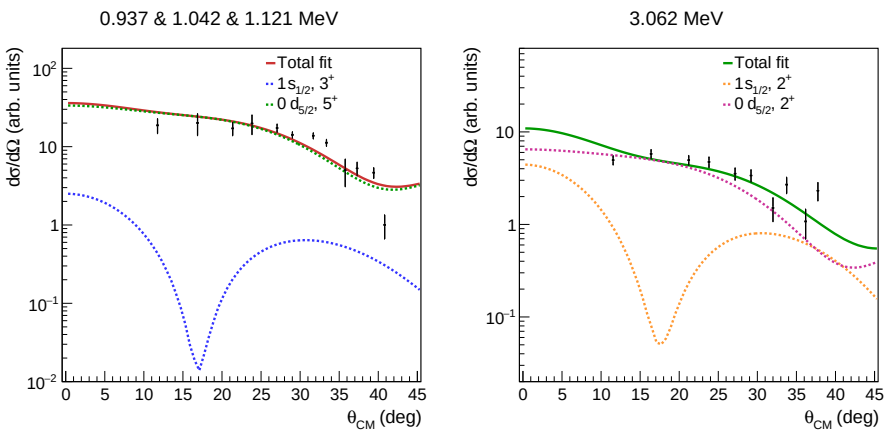

Figure 2.38: Angular distributions for several states in ^{18}F (excitation energy of each state is given in the title of each graph). Black points are experimental data; lines are DWBA fits using a free fit with adjustable amplitudes of all relevant angular momentum (ℓ) transfers (Option 1, see text for a more detailed description) with PTOLEMY.

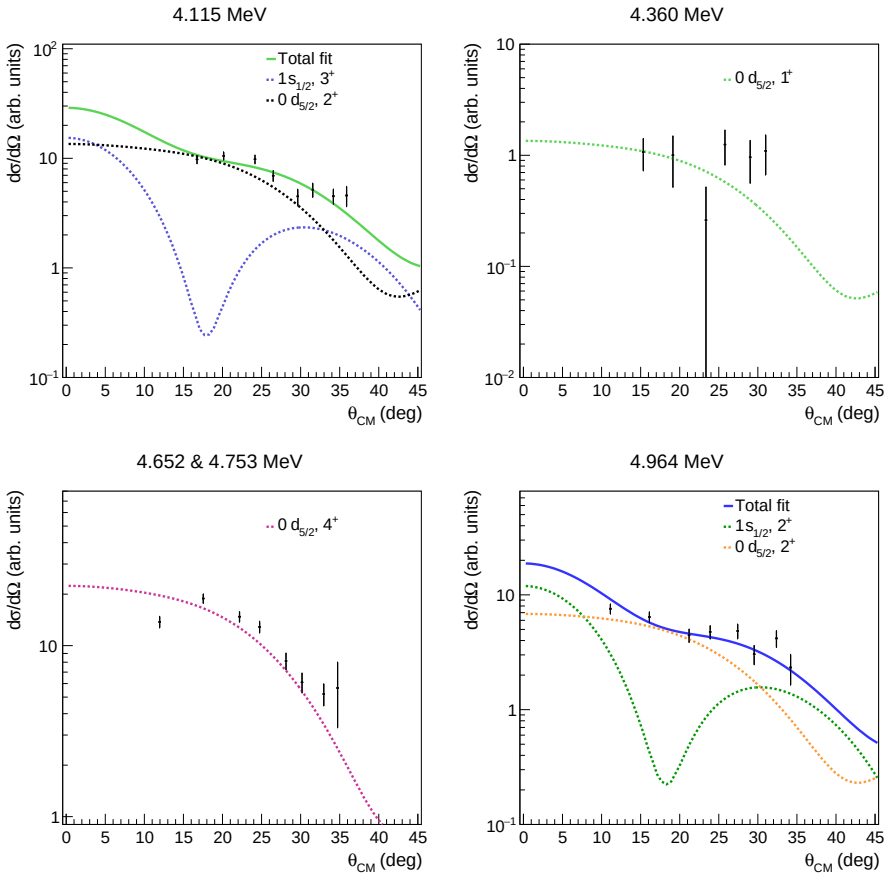

Figure 2.39: Angular distribution for several states in ^{18}F. Black points are experimental data; lines are DWBA fits using a free fit with adjustable amplitudes of all relevant angular momentum (ℓ) transfers (Option 1, see text for a more detailed description) with PTOLEMY.

2.5.9 Angular distributions for proton-unbound states in ^{18}F

DWBA calculations performed with PTOLEMY for unbound states use the weak-binding approximation, in which the unbound single-particle state is artificially treated as a very weakly bound state. Figure 2.40 shows DWBA calculations carried out with PTOLEMY for $\ell = 0$ transfer (s-wave) for states at several excitation energies in ^{18}F, including a proton-unbound state at $E_x = 6.136$ MeV.

For the bound states, a systematic trend is observed: as the excitation energy of the state increases (corresponding to decreasing binding energy), the first minimum in the differential cross section shifts toward larger centre-of-mass angles. In contrast, the calculation for the proton-unbound state exhibits a different trend, with the minimum of the differential cross section shifting toward smaller angles. This behaviour highlights a limitation of the weak-binding approximation when applied to proton-unbound states. This discrepancy suggests that a different treatment of unbound states is needed for a reliable extraction of spectroscopic factors.

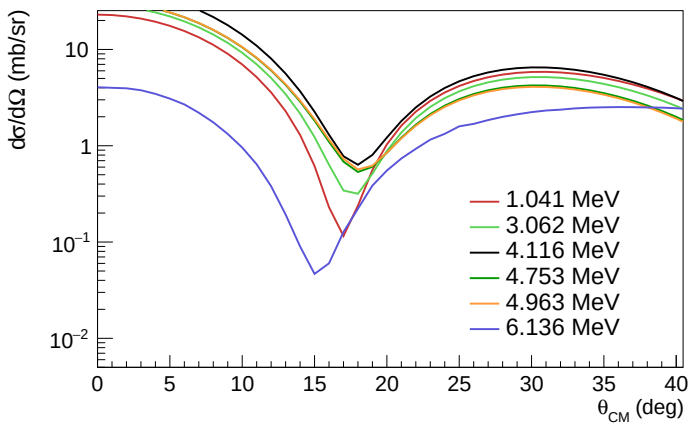

Figure 2.40: Angular distributions from DWBA calculations with PTOLEMY for $\ell = 0$ transfer states in ^{18}F at different excitation energies, illustrating the contrasting behaviour between bound and unbound states.

One possible approach is to study the systematic behaviour of DWBA calculations for bound states with energies ranging from near zero up to the separation energy, and to fit the experimentally obtained angular distributions using

calculations below the threshold. The spectroscopic factor for the unbound state can be then inferred by extrapolating this trend to the appropriate excitation energy [73].

The states in the doublet at 6.136 MeV (0^+) and 6.163 MeV (3^+) are isobaric analogue states of the 5.340 MeV (0^+) and 5.375 MeV (3^+) states in ^{18}O, which correspond to $\ell = 2$ and $\ell = 0$ transfer, respectively. The doublet in ^{18}F is therefore also expected to have predominantly $\ell = 2$ and $\ell = 0$ character. However, due to finite experimental energy resolution, the doublet may include contributions from nearby states.

To account for this possibility, the experimentally obtained differential cross sections were fitted with DWBA using two assumptions:

- $\ell = 0$ and $\ell = 2$ transfer,
- $\ell = 0$ and $\ell = 1$ transfer.

The extracted spectroscopic factors as a function of excitation energy, together with the corresponding fitted curves, are shown in Fig. 2.41. Up to an excitation energy of approximately 5.5 MeV, the data points exhibit a smooth and consistent trend. The three highest-energy data points (above 5.5 MeV) were excluded from the fit due to their significantly different behaviour.

The *s*-wave behaviour is found to be robust. Independent of the fitting assumptions, the *s*-wave spectroscopic strength follows the same energy dependence, and the extrapolated spectroscopic factor for $\ell = 0$ transfer is consistent between the different methods within uncertainties. The extracted value is 1.47(16).

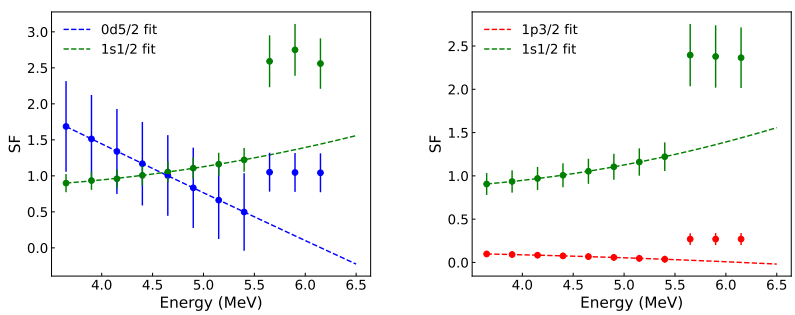

Figure 2.41: Extracted spectroscopic factors as a function of excitation energy, together with fitted trends used for extrapolation to the unbound region.

The *d*-wave contribution in that doublet, however, cannot be reliably determined. As shown in Fig. 2.41, the extracted spectroscopic factor for the

$\ell = 2$ transfer at the energy of 6.136 MeV is consistent with zero, with an uncertainty of 0.6. Consequently, only an upper limit can be placed on the $\ell = 2$ spectroscopic factor, which is estimated to be 0.6.

2.5.10 Normalisation

Due to the significantly lower intensity of the radioactive ^{17}F beam compared to the stable ^{17}O beam, as well as the different data-taking periods for the two measurements, a direct comparison of absolute yields between the two datasets is not straightforward. Instead, the normalisation was performed using the *d*-wave component of the first 2^+ states, corresponding to the 1.982 MeV state in ^{18}O and the 3.062 MeV state in ^{18}F. These states are well isolated, strongly populated, and have well-established spectroscopic properties, making them suitable reference points for the normalisation.

The strength of the *d*-wave component of the first 2^+ states was determined by fitting the 1.982 MeV state in ^{18}O and the 3.062 MeV state in ^{18}F with DWBA calculations assuming mixed $\ell = 0$ and $\ell = 2$ transfer, using the free fit method. The obtained *d*-wave component for ^{18}O, $N_{^{18}\mathrm{O}}$, was then divided by the corresponding *d*-wave component for ^{18}F, $N_{^{18}\mathrm{F}}$, to obtain the normalisation factor N:

$$N = \frac{N_{^{18}\mathrm{O}}}{N_{^{18}\mathrm{F}}} = 3.2(5). \tag{2.8}$$

The calculation is performed using the spectroscopic strengths listed in Section 2.5.12. Figure 2.42 shows the excitation energy spectra for the $^{17}\mathrm{F}(\mathrm{d},\mathrm{p})$ reaction with ^{18}F recoils, the $^{17}\mathrm{O}(\mathrm{d},\mathrm{p})$ reaction with ^{18}O recoils, the $^{17}\mathrm{F}(\mathrm{d},\mathrm{p})$ reaction with ^{17}O recoils, and the $^{17}\mathrm{F}(\mathrm{d},\mathrm{p})$ reaction with ^{14}N recoils, scaled by a factor of 7. The ^{17}F beam data is scaled by the normalisation factor N to match the oxygen data. Events from the $^{17}\mathrm{F}(\mathrm{d},\mathrm{p})$ reaction leading to ^{17}O recoils appear at excitation energies above the proton separation energy of ^{18}F, $S_p = 5.61$ MeV, and events from the $^{17}\mathrm{F}(\mathrm{d},\mathrm{p})$ reaction leading to ^{14}N recoils appear at excitation energies above the negative Q-value of α separation of ^{18}F, $-Q_\alpha = 4.415$ MeV.

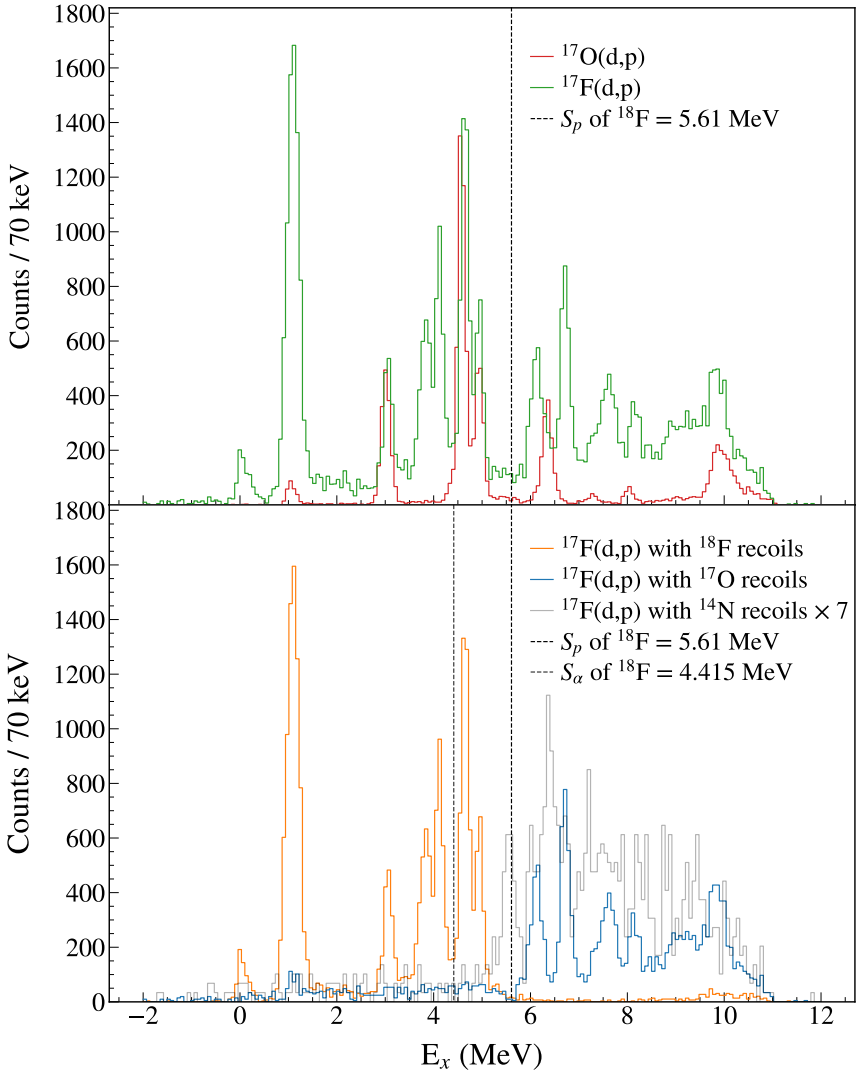

Figure 2.42: Upper panel: excitation energy spectra for the ^{17}F(d, p) reaction (green line) and the ^{17}O(d, p) reaction (red line). Lower panel: excitation energy spectra for the ^{17}F(d, p) with ^{18}F recoils (orange line), with ^{17}O recoils (blue line), and with ^{14}N recoils scaled by factor 7 (gray line). The proton separation energy of ^{18}F, $S_p = 5.61$ MeV, is indicated by the black dashed line, and the α separation energy of ^{18}F, $S_\alpha = 4.415$ MeV, is indicated by gray dashed line. The ^{17}F beam data are scaled such that the d-wave component strength of the first 2^+ state at 3.062 MeV matches the corresponding d-wave component strength of the first 2^+ state in ^{18}O at 1.982 MeV.

2.5.11 Alternative reaction codes

In addition to PTOLEMY, several other reaction codes are available for modelling direct reactions. One such code is TWOFNR [74], a program for calculating one-step transfer reactions using either the DWBA or the Johnson–Soper/Johnson–Tandy adiabatic approximation (ADWA) to account for deuteron breakup effects. Finite range effects can be treated using either the zero-range approximation or the local energy approximation (LEA) [75, 76]. In contrast to DWBA, which treats the deuteron using an effective deuteron–target interaction and neglects the breakup effects, ADWA is based on a three-body description of the reaction, in which the deuteron is treated explicitly as a system consisting of a proton and a neutron. In this approach, nucleon–target optical model potentials are used to construct an effective adiabatic deuteron potential. A front-end interface, FRONT, is available for TWOFNR. An example input file for the FRONT interface, including the optical model potential parameters used in the calculation of the 1.982 MeV state in ^{18}O, is provided in Appendix A.

To estimate the systematic uncertainty associated with the choice of reaction model and code, differential cross sections calculated using PTOLEMY and TWOFNR were compared for different transferred angular momenta ℓ and for several excited states in ^{18}O. Figures 2.43 and 2.44 show such comparisons for the states at excitation energies of 1.982 MeV and 3.920 MeV, respectively.

The overall shapes and angular distribution trends of the differential cross sections calculated with PTOLEMY and TWOFNR are in agreement. However, there are noticeable differences in the absolute magnitudes of the calculated cross sections. It is important to note that the angular ranges θ_{CM} measured in the experiment are between 10° and 40°.

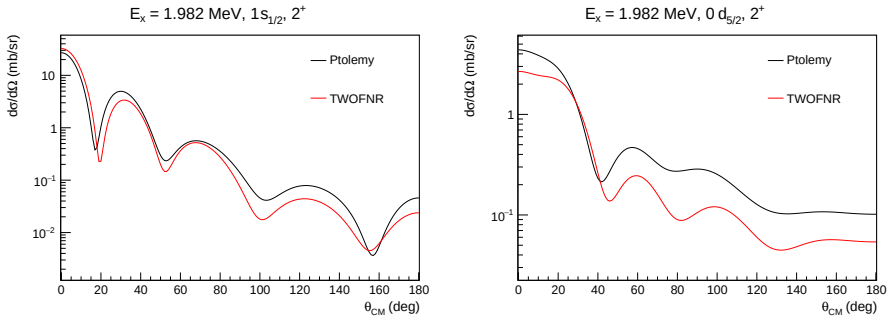

Figure 2.43: Comparison of DWBA-calculated differential cross sections for the 1.982 MeV state in ^{18}O obtained using PTOLEMY and TWOFNR. The PTOLEMY calculation uses the An–Cai potential [60] for the incoming channel and the Koning–Delaroche potential [67] for the outgoing channel. The TWOFNR calculations employ the zero-range Johnson–Soper [75] adiabatic potential for the deuteron entrance channel, constructed using Koning–Delaroche (KD02) nucleon optical potentials, and the Koning–Delaroche potential for the outgoing proton channel. The left panel shows the $\ell = 0$ ($1s_{1/2}$) component, and the right panel shows the $\ell = 2$ ($0d_{5/2}$) component.

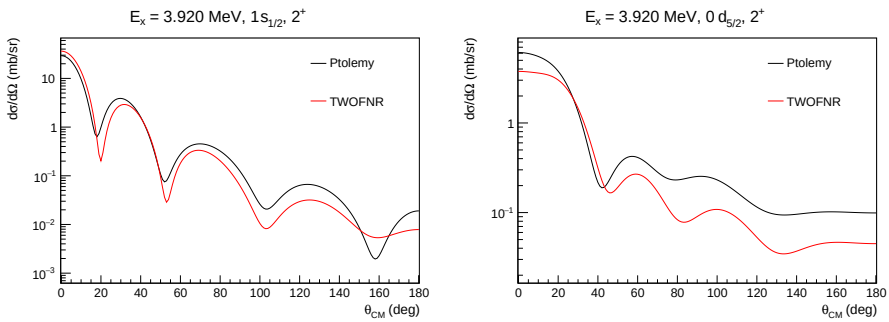

Figure 2.44: Comparison of DWBA-calculated differential cross sections for the 3.920 MeV state in ^{18}O obtained using PTOLEMY and TWOFNR. The PTOLEMY calculation uses the An–Cai potential [60] for the incoming channel and the Koning–Delaroche potential [67] for the outgoing channel. The TWOFNR calculations employ the zero-range Johnson–Soper [75] adiabatic potential for the deuteron entrance channel, constructed using Koning–Delaroche (KD02) nucleon optical potentials, and the Koning–Delaroche potential for the outgoing proton channel. The left panel shows the $\ell = 0$ ($1s_{1/2}$) component, and the right panel shows the $\ell = 2$ ($0d_{5/2}$) component.

2.5.12 Spectroscopic factors for ^{18}O

Table 2.10 presents spectroscopic factors obtained for the states populated in ^{18}O. Experimentally resolved states are fitted using the free fit method. For unresolved states, the fitting method used is specified in the leftmost column. The table lists the excitation energies of the fitted states in MeV, their spin and parity (J^π), the populated orbital used in the calculations, the extracted spectroscopic factor (SF), and the corresponding χ^2/ndf values. For states fitted with Option 2, the relative strengths of the states populated in the multiplet are given in the column labelled "Lit. ratio", together with the scaling factor S obtained from the fit.

The quoted uncertainties of the spectroscopic factors include several contributions. First, the statistical uncertainty obtained from the fit is propagated to the spectroscopic factor. When $\chi^2/\mathrm{ndf} > 1$, the fit uncertainty is scaled by a factor $\sqrt{\chi^2/\mathrm{ndf}}$ to account for possible underestimation of the experimental uncertainties, following the recommendation of Ref. [77].

For states fitted with a single component (free-fit method or Option 1), the spectroscopic factor is obtained directly from the fitted normalization parameter A,

$$\mathrm{SF} = A.$$

The corresponding uncertainty is therefore given by

$$\sigma_{\mathrm{SF}} = \sigma'_A,$$

where σ'_A denotes the normalisation uncertainty after the $\sqrt{\chi^2/\mathrm{ndf}}$ scaling.

For unresolved multiplets fitted with Option 2, the fit returns a common scaling factor S describing the overall strength of the multiplet. The spectroscopic factors for individual states are obtained by multiplying this scaling factor by the literature ratios R_i that describe the relative population strengths of the states in the multiplet,

$$\mathrm{SF_i} = S\,R_i.$$

In this case, the uncertainty of the literature ratios, quoted as 15 % [36], is propagated to the final spectroscopic factor, assuming independent uncertainties,

$$\sigma_{\mathrm{SF_i}} = \mathrm{SF_i}\sqrt{\left(\frac{\sigma_S}{S}\right)^2 + \left(\frac{\sigma_{R_i}}{R_i}\right)^2},$$

where σ_S denotes the normalization uncertainty after the χ^2/ndf scaling, R_i is the literature ratio, and σ_{R_i} is the uncertainty of the literature ratio.

Method	State(s) (MeV, J^π)	Orbital, J^π	SF	χ^2/ndf	Lit. ratio	S
Free fit	0.000 (0^+)	$0\,d_{5/2}$, 0^+	6.2(9)	2.75		
Free fit	1.982 (2^+)	$1\,s_{1/2}$, 2^+ $0\,d_{5/2}$, 2^+	0.74(11) 4.92(24)	1.27		
Option 1	3.552 (4^+) 3.620 (0^+)	$0\,d_{5/2}$, 4^+	8.4(5)	9.97		
Option 2	3.552 (4^+) 3.620 (0^+)	$0\,d_{5/2}$, 4^+ $0\,d_{5/2}$, 0^+	8.3(13) 1.47(24)	9.97	1.57(24) 0.28(4)	5.27(29)
Free fit	3.920 (2^+)	$1\,s_{1/2}$, 2^+ $0\,d_{5/2}$, 2^+	1.3(4) 3.5(6)	7.38		
Option 1	5.255 (2^+) 5.340 (0^+) 5.375 (3^+)	$0\,d_{5/2}$, 0^+ $1\,s_{1/2}$, 3^+	2.9(15) 4.9(5)	1.08		
Option 2	5.255 (2^+) 5.340 (0^+) 5.375 (3^+)	$1\,s_{1/2}$, 2^+ $0\,d_{5/2}$, 0^+ $1\,s_{1/2}$, 3^+	1.55(24) 0.71(11) 4.5(7)	1.33	0.35(5) 0.16(2) 1.01(15)	4.44(19)
Free fit	6.200 (1^-)	$1\,p_{3/2}$, 1^-	0.29(7)	3.79		
Free fit	7.100 (4^+)	$0\,d_{5/2}$, 4^+	0.28(5)	5.19		

Table 2.10: Spectroscopic factors (SF), uncertainties, χ^2/ndf values, literature (Lit.) ratios [37, 38], and scaling factors for selected states in ^{18}O. For unresolved multiplets, orbital contributions are shared among all states in the multiplet.

2.5.13 Spectroscopic factors for ^{18}F

Table 2.11 presents spectroscopic factors obtained for the states populated in ^{18}F. The spectroscopic factors and their uncertainties were calculated analogously to those of the states populated in ^{18}O. However, due to the normalisation of the fluorine data to match the oxygen data, as described in Section 2.5.10, the spectroscopic factors obtained from the fit are additionally scaled by the factor $N = 3.2(5)$. The uncertainty of this scaling factor is propagated to the final spectroscopic factors.

For states fitted with free fit method or Option 1, the final spectroscopic factor is therefore given by

$$\mathrm{SF} = N\,\mathrm{SF}^{(\mathrm{fit})},$$

where $\mathrm{SF}^{(\mathrm{fit})}$ is the spectroscopic factor obtained from the fit.

Assuming independent uncertainties, the corresponding uncertainty is calculated as

$$\sigma_{\mathrm{SF}} = \mathrm{SF}\sqrt{\left(\frac{\sigma_{\mathrm{fit}}}{\mathrm{SF}^{(\mathrm{fit})}}\right)^2 + \left(\frac{\sigma_N}{N}\right)^2},$$

where σ_{fit} denotes the uncertainty obtained from the fit (after the χ^2/ndf scaling) and σ_N is the uncertainty of the normalisation factor.

For multiplets fitted with Option 2, the spectroscopic factors are calculated as

$$\mathrm{SF_i} = N\,S\,R_i,$$

where S is the fitted scaling factor and R_i is the literature ratio describing the relative population of the states within the multiplet. The uncertainty is then obtained by propagating all independent contributions,

$$\sigma_{\mathrm{SF_i}} = \mathrm{SF_i}\sqrt{\left(\frac{\sigma_N}{N}\right)^2 + \left(\frac{\sigma_S}{S}\right)^2 + \left(\frac{\sigma_{R_i}}{R_i}\right)^2},$$

where the uncertainty of the literature ratios is quoted as 20 % [40].

The spectroscopic factors for the proton unbound states are calculated by extrapolation (described in Section 2.5.9). Aside from normalisation to the oxygen data, they need to be additionally scaled to account for the lower detection efficiency of recoils after proton emission, $\epsilon = 1.4(2)$. Thus, the uncertainty from that factor also needs to be propagated to the final formula:

$$\sigma_{\mathrm{SF}} = \mathrm{SF}\sqrt{\left(\frac{\sigma_{\mathrm{SF}^{(\mathrm{extr})}}}{\mathrm{SF}^{(\mathrm{extr})}}\right)^2 + \left(\frac{\sigma_N}{N}\right)^2 + \left(\frac{\sigma_\epsilon}{\epsilon}\right)^2},$$

where $SF^{(extr)}$ is spectroscopic factor obtained with the extrapolation method and $\sigma_{SF^{(extr)}}$ is the associated uncertainty.

The spectroscopic factor for the $\ell = 2$ transfer for the proton unbound states is given as the upper bound rather than a value, as explained in Section 2.5.9. Thus, no uncertainty is provided.

Method	State(s) (MeV, J^π)	Orbital	SF norm.	χ^2/ndf	Lit. ratio	S
Free fit	0.000 (1^+)	$0\,d_{3/2}$, 1^+	7.4(13)	0.79		
Option 1	0.937 (3^+)					
	1.042 (0^+)	$1\,s_{1/2}$, 3^+	0.3(9)	8.07		
	1.121 (5^+)	$0\,d_{5/2}$, 5^+	15(4)			
Option 2		$1\,s_{1/2}$, 3^+	1.02(29)		0.102(20)	
	0.937 (3^+)	$0\,d_{5/2}$, 3^+	3.1(9)	7.85	0.31(6)	3.1(4)
	1.042 (0^+)	$0\,d_{5/2}$, 0^+	9.6(27)		0.96(19)	
	1.121 (5^+)	$0\,d_{5/2}$, 5^+	8.9(25)		0.89(18)	
Free fit	3.062 (2^+)	$1\,s_{1/2}$, 2^+	0.5(3)	3.05		
		$0\,d_{5/2}$, 2^+	4.9(10)			
Option 1	3.727 (1^+)	$1\,s_{1/2}$, 2^+	2.3(5)	0.45		
	3.839 (2^+)	$0\,d_{5/2}$, 2^+	4.5(10)			
Free fit	4.115 (3^+)	$1\,s_{1/2}$, 3^+	1.2(4)	2.41		
		$0\,d_{5/2}$, 3^+	6.2(11)			
Free fit	4.360 (1^+)	$0\,d_{5/2}$, 1^+	1.4(5)	2.21		
Option 1	4.652 (4^+)					
	4.753 (0^+)	$0\,d_{5/2}$, 4^+	7.2(13)	7.95		
Free fit	4.964 (2^+)	$1\,s_{1/2}$, 2^+	1.2(5)	2.30		
		$0\,d_{5/2}$, 2^+	3.7(8)			
Extrapolation	6.136 (0^+)	$0\,d_{3/2}$, 0^+	≤ 1.9			
	6.163 (3^+)	$1\,s_{1/2}$, 3^+	6.7(16)			

Table 2.11: Spectroscopic factors (SF), uncertainties, χ^2, literature (Lit.) ratios [40], and normalisation factors for states in ^{18}F. For unresolved multiplets, orbital contributions are shared among all states in the multiplet.

2.5.14 Additional uncertainties in spectroscopic factors

It is important to distinguish between uncertainties affecting the absolute scale of spectroscopic factors and those affecting their relative values between different states. Many of the systematic effects discussed below predominantly affect an overall scaling of the calculated cross sections and therefore mainly impact the absolute normalisation of the extracted spectroscopic factors.

Since spectroscopic factors are extracted by comparing experimentally measured cross sections with theoretical model calculations, their uncertainties have two primary sources: the experimental cross sections and the theoretical models.

As mentioned earlier, different theoretical approaches, such as the DWBA and the adiabatic approximation (ADWA), can be used to calculate theoretical scattering cross sections. The dependence of the extracted spectroscopic factors on the chosen reaction model can be evaluated by comparing values obtained using DWBA and ADWA.

In addition, the theoretically calculated cross sections depend on the optical model parameters employed. As discussed in Section 2.5.7, different sets of optical model parameters can be used, each leading to slightly different results.

To quantify the uncertainty associated with the choice of optical model potentials, spectroscopic factors for the 1.982 MeV state in ^{18}O were extracted using various optical model parameter sets with the fitting Option 1 described in Section 2.5.7. The average deviation from the reference potential combination AK was approximately 14 % , while a maximum deviation of about 30 % was observed for the QP potentials.

To study the dependence of the reaction model (DWBA vs ADWA), spectroscopic factors for the 1.982 MeV state in ^{18}O were extracted using the TWOFNR code and the potentials described in Section 2.5.11 using the fitting Option 1. The variation between spectroscopic factors obtained with PTOLEMY and TWOFNR is approximately 40 %.

On the experimental side, the largest source of uncertainty arises from the extraction of the peak yields by fitting the experimental spectra with Gaussian functions. Depending on the state and the specific projection, the uncertainties associated with the fitted yields are typically around 10 %, with a maximum uncertainty of about 18 %.

Finally, there is an additional uncertainty associated with the position resolution of the detector array, which is approximately 1 mm and contributes to the uncertainty in the solid angle coverage. However, given the significantly larger uncertainties associated with the optical model choice, reaction model, and peak yield extraction, this contribution is neglected in the present analysis.

The uncertainties quoted in Sections 2.5.12 and 2.5.13 include only the uncertainties associated with the fitted yields. Additional systematic uncertainties arising from the choice of reaction model and optical model parameters are not included and predominantly affect the absolute normalisation of the spectro-

scopic factors. Based on the model dependence discussed above, an additional systematic uncertainty of approximately 50 % should be therefore associated with the absolute scale of the extracted spectroscopic factors. However, since the spectroscopic factors in the present work are renormalised to literature values, the impact of these systematic effects on the relative spectroscopic factors between states is expected to be significantly reduced.

2.6 Discussion

Figure 2.45 shows angular distributions for several isobaric analogue states in ^{18}O (left column) and ^{18}F (right column). Even from a visual inspection, it is evident that these states exhibit similar characteristics and can be described by a mixture of $\ell = 0$ and $\ell = 2$ transfer components in both nuclei, with comparable relative contributions.

Table 2.12 presents spectroscopic factors for the $\ell = 0$ and $\ell = 2$ components of states in ^{18}O and ^{18}F observed in the experiment, together with their energy (E), spin and parity (J^π), and isospin (T). Isobaric analogue states are listed in the same rows.

The spectroscopic factors for both ^{18}O and ^{18}F are normalised to the literature values of the $\ell = 2$ component of the first 2^+ state in each nucleus. Literature values are also included for comparison (column "Lit. (^{3}He, d)" for ^{18}F and column "Lit. ^{17}O(d,p)" for ^{18}O). In addition, spectroscopic factors obtained from shell-model calculations using the USDi interaction are presented. An analogous table for the FSU shell-model interaction is given in Table 2.13.

The method used to extract the spectroscopic factors is indicated by superscripts. Values marked with ^{a} were obtained using Option 1, in which unresolved multiplets are treated as a single effective state and fitted with a free combination of DWBA coefficients (see Section 2.5.7 for more details). Values marked with ^{b} were obtained using Option 2, where relative spectroscopic strengths from the literature are used to constrain the contributions of individual states within a multiplet. Values marked with ^{e} correspond to states analysed using the extrapolation method described in Section 2.5.9. When no superscript is given, the spectroscopic factors were extracted using the free fit method, applied to isolated or experimentally resolved states, in which the relative ℓ contributions were treated as independent fit parameters.

It is important to note that states in ^{18}F at 0.0, 3.727, and 3.839 MeV, as well as the proton-unbound states at 6.136 and 6.163 MeV, were not reported in Ref. [40]. The 3.839 MeV state was reported in Ref.[39]. However, only constraints on the spectroscopic factors were presented there, which are not included in the tables. The spectroscopic factors obtained for states in ^{18}F are generally consistent, within uncertainties, with the values reported in the literature, with the exception of the $\ell = 0$ component of the 3.062 MeV state, where the extracted value is lower than that reported in the literature, and the 4.360 MeV state, where the spectroscopic factor for the $\ell = 2$ transfer is higher than the literature value.

In the case of states in ^{18}O, the extracted spectroscopic factors are also in overall agreement with the literature values. However, the extracted $\ell = 0$ transfer component for the 2^+ state at 1.982 MeV (the isobaric analogue state of the 3.062 MeV state in ^{18}F) is significantly lower than the literature value, consistent with the discrepancy observed for the corresponding state in ^{18}F. In

addition, the extracted spectroscopic factor for the multiplet of states at 3.552 and 3.632 MeV is lower than the reported literature value.

			^{18}F Exp		Lit. (^{3}He, d) [40]		SM USDi ^{17}F(d, p)		^{18}O Exp			Lit. ^{17}O(d,p) [37, 38]		SM USDi ^{17}O(d, p)	
E (MeV)	J^π	T	$\ell = 0$	$\ell = 2$	$\ell = 0$	$\ell = 2$	$\ell = 0$	$\ell = 2$	E (MeV)	$\ell = 0$	$\ell = 2$	$\ell = 0$	$\ell = 2$	$\ell = 0$	$\ell = 2$
0.000	1^+	0		0.94(16)				0.50							
0.937	3^+	0	0.13(4)^b	0.38(11)^b	0.102(20)	0.31(6)	0.32	0.29							
1.042	0^+	1		1.2(3)^b		0.96(19)		0.75	0		1.05(14)		1.22(18)		1.54
1.121	5^+	0		1.1(3)^b		0.89(18)		1.00							
3.062	2^+	1	0.06(4)	0.62(13)	0.21(4)	0.62(12)	0.15	0.57	1.982	0.130(18)	0.83(4)	0.21(3)	0.83(12)	0.33	1.23
3.727	1^+	0	0.28(6)^a	0.57(12)^a				0.39							
3.839	2^+	0					0.34	0.08							
4.116	3^+	0	0.15(5)	0.78(14)	0.17(3)	0.68(14)	0.14	0.66							
4.360	1^+	0		0.17(6)		0.074(15)									
4.652	4^+	1		0.90(16)^a		1.04(21)		0.96	3.552		1.42(8)^a		1.57(24)		1.93
4.753	0^+	1				0.18(4)			3.630				0.28(4)		
4.964	2^+	1	0.16(6)	0.47(10)	0.17(3)	0.51(10)			3.920	0.21(7)	0.59(9)	0.35(5)	0.66(10)	0.62	0.73
	2^+	1							5.255	0.26(4)^b		0.35(5)			
6.136	0^+	1	0.84(20)^e	$\leq 0.25^e$				0.18	5.340		0.120(19)^b		0.16(2)		
6.163	3^+	1					0.53	0.0	5.375	0.76(12)^b		1.01(15)		0.99	

Table 2.12: Spectroscopic factors for $\ell = 0$ and $\ell = 2$ transfer to states in ^{18}F and ^{18}O. Experimental values are compared with literature data from (^{3}He, d) reactions for ^{18}F and ^{17}O(d,p) reactions for ^{18}O, as well as with shell-model calculations using the USDi interaction. All experimental spectroscopic factors are normalised to the $\ell = 2$ component of the first 2^+ state in each nucleus. Isobaric analogue states are listed in the same rows. Superscripts indicate the fitting procedure: ^{a} denotes Option 1 (unresolved multiplets fitted as a single effective state), ^{b} denotes Option 2 (fits constrained by literature relative strengths), and ^{e} denotes the extrapolation method described in Section 2.5.9. Values without superscripts were obtained using the free fit method for isolated or resolved states. Uncertainties are given in parentheses.

			^{18}F Exp		Lit. (^{3}He, d) [40]		SM USDi ^{17}F(d, p)		^{18}O Exp			Lit. ^{17}O(d,p) [37, 38]		SM USDi ^{17}O(d, p)	
E (MeV)	J^π	T	$\ell = 0$	$\ell = 2$	$\ell = 0$	$\ell = 2$	$\ell = 0$	$\ell = 2$	E (MeV)	$\ell = 0$	$\ell = 2$	$\ell = 0$	$\ell = 2$	$\ell = 0$	$\ell = 2$
0.000	1^+	0		0.94(16)				0.52							
0.937	3^+	0	0.13(4)^b	0.38(11)^b	0.102(20)	0.31(6)	0.33	0.31							
1.042	0^+	1		1.2(3)^b		0.96(19)		0.78	0		1.05(14)		1.22(18)		1.55
1.121	5^+	0		1.1(3)^b		0.89(18)		1.00							
3.062	2^+	1	0.06(4)	0.62(13)	0.21(4)	0.62(12)	0.17	0.61	1.982	0.130(18)	0.83(4)	0.21(3)	0.83(12)	0.34	1.21
3.727	1^+	0	0.28(6)^a	0.57(12)^a				0.35							
3.839	2^+	0													
4.116	3^+	0	0.15(5)	0.78(14)	0.17(3)	0.68(14)									
4.360	1^+	0		0.17(6)		0.074(15)									
4.652	4^+	1		0.90(16)^a		1.04(21)		0.97	3.552		1.42(8)^a		1.57(24)		1.93
4.753	0^+	1				0.18(4)			3.630				0.28(4)		
4.964	2^+	1	0.16(6)	0.47(10)	0.17(3)	0.51(10)	0.30	0.38	3.920	0.21(7)	0.59(9)	0.35(5)	0.66(10)	0.61	0.75
	2^+	1							5.255	0.26(4)^b		0.35(5)			
6.136	0^+	1	0.84(20)^e	$\leq 0.25^e$				0.18	5.340		0.120(19)^b		0.16(2)		
6.163	3^+	1					0.49	0.0	5.375	0.76(12)^b		1.01(15)		0.99	

Table 2.13: Spectroscopic factors for $\ell = 0$ and $\ell = 2$ transfer to states in ^{18}F and ^{18}O. Experimental values are compared with literature data from (^{3}He, d) reactions for ^{18}F and ^{17}O(d,p) reactions for ^{18}O, as well as with shell-model calculations using the FSU interaction. All experimental spectroscopic factors are normalised to the $\ell = 2$ component of the first 2^+ state in each nucleus. Isobaric analogue states are listed in the same rows. Superscripts indicate the fitting procedure: ^{a} denotes Option 1 (unresolved multiplets fitted as a single effective state), ^{b} denotes Option 2 (fits constrained by literature relative strengths), and ^{e} denotes the extrapolation method described in Section 2.5.9. Values without superscripts were obtained using the free fit method for isolated or resolved states. Uncertainties are given in parentheses.

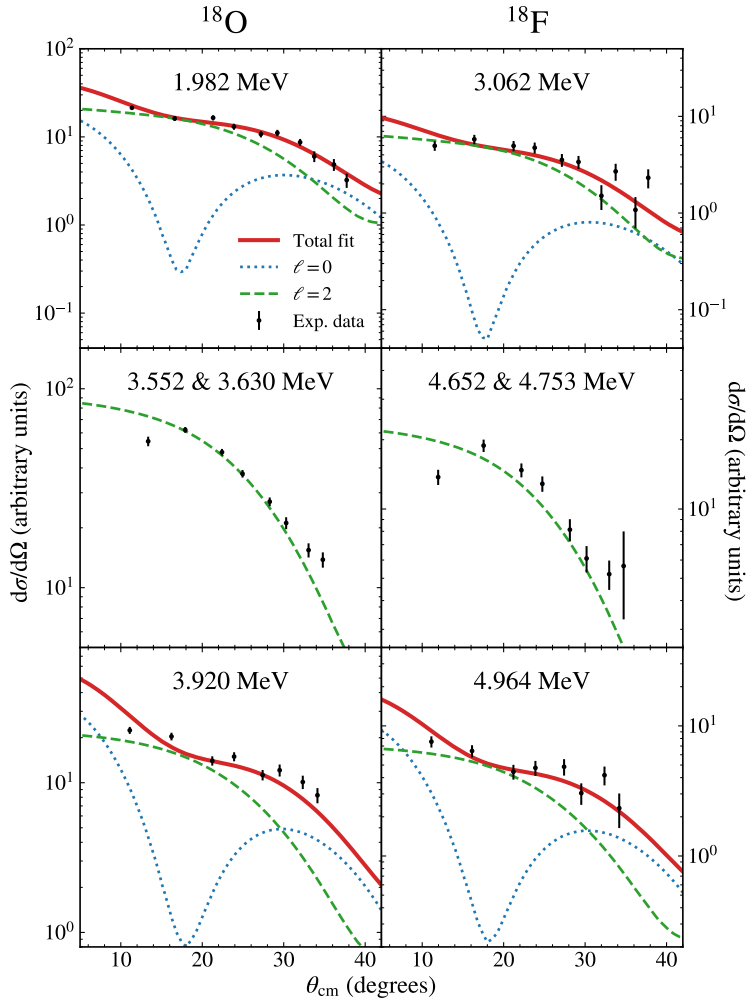

Figure 2.45: Angular distributions for selected IAS in ^{18}O (left column) and ^{18}F (right column). The experimental data (points) are fitted with DWBA calculations for $\ell = 0$ and $\ell = 2$ transfer, shown as separate components, as well as their combined fit. The similarity in both the shapes of the angular distributions and the relative contributions of the $\ell = 0$ and $\ell = 2$ components demonstrates the analogous structure of these states in these two nuclei.

Figures 2.46 and 2.47 present a graphical comparison of the experimentally extracted spectroscopic factors with those calculated using the shell-model employing the USDi and FSU interactions, respectively. In the figures, blue bars indicate the $\ell = 0$ transfer component, while the orange bars represents the $\ell = 2$ transfer component. The left panel corresponds to ^{18}O, and the right panel to ^{18}F.

For states observed experimentally, the spin and parity of the state is annotated near the horizontal bar, which represents the corresponding spectroscopic factor. For multiplets of states that are not resolved experimentally, spins and parities of all states constituting the multiplet are given. Dashed lines connect experimentally observed states to the corresponding shell-model calculations (note that the energies of the calculated states may differ from the experimental values), while dotted lines connect experimentally unresolved multiplets of states to their shell-model counterparts. For multiplets unresolved experimentally, the shell-model strengths are indicated as wide, semi-transparent bars that show the summed contributions of the $\ell = 0$ and $\ell = 2$ transfer components in addition to the individual states.

Not all experimentally observed states are reproduced by the shell-model calculations. In particular, the excited 0^+ states in ^{18}O (beyond the ground state) as well as the third 2^+ state, are not described by either the USDi or FSU interactions. This discrepancy has been reported previously [34, 78], and is generally attributed to the presence of cross-shell excitations involving the ^{16}O core, which lie outside the standard *sd*-shell model space.

These states are understood to have significant contributions from multi-particle-multi-hole configurations across the *psd*-shells, corresponding to excitations of nucleons from the *p*-shell core into the *sd*-shell (see Fig. 2.2). Such configurations are associated with enhanced collectivity and can be interpreted as core-excited states, analogous to the deformed excited states in ^{16}O, which can be described as an analogue of the ^{20}Ne ground rotational band [78].

While these states can be reproduced by theoretical calculations that implicitly include shell model excitations spanning the *psd*-shells [36, 79], they are not captured within the *sd*-shell model space of the USDi interaction. Although the FSU interaction extends the model space to include 1p-1h excitations, this level of configuration mixing appears insufficient to reproduce these states.

When considering the shell-model description of states in ^{18}F, several experimental levels are not reproduced by either the USDi or FSU interactions. In particular, the 1^+ state at 4.360 MeV is not reproduced by either interaction. Similarly, the second 0^+ state at 4.753 MeV shell model calculations are not reproduced within these shell-model calculations.

This is not unexpected, since these states are IAS of the 0^+ state at 3.630 MeV and the 2^+ state at 3.920 MeV in ^{18}O, which, as discussed above, are also not reproduced by shell-model calculations. Their absence in the calculations therefore reflects the same underlying limitation, namely the lack of sufficient

cross-shell excitations in the model space.

The FSU interaction reproduces the 2^+ state at 4.964 MeV, which is IAS of the 2^+ state at 3.920 MeV in ^{18}O. However, the calculated energy of this state (5.842 MeV) is significantly shifted compared to the experimental value, indicating that, although the configuration is partially captured, its energy is not correctly described.

In addition, the FSU interaction fails to reproduce the 2^+ state at 3.839 MeV and the 3^+ state at 4.115 MeV. This suggests that while the inclusion of hole excitation improves description of some states, important correlations still remain missing.

The states in ^{18}O and ^{18}F that are reproduced by the shell-model calculations show overall good agreement with the experimental cross sections. In particular, the general trends are reasonably well reproduced. This indicates that, despite the limitations discussed above, the shell-model provides an effective description of states in the vicinity of closed-shell nuclei such as ^{18}O and ^{18}F. Consequently, the calculated spectroscopic factors are, in most cases, consistent with the experimental data.

To determine whether unbound states in ^{18}F exhibit any change in the strength of their $\ell = 0$ component relative to bound states, the ratio of the $\ell = 0$ and $\ell = 2$ transfer components between states populated in ^{18}F and in ^{18}O was calculated for their IAS at several excitation energies and shown in Fig. 2.48. The $\ell = 0$ ratios are shown in blue with their associated uncertainties, while the $\ell = 2$ ratios are shown in orange. The black horizontal line represents the average ratio for $\ell = 0$ across the states, and the grey band indicates the 1σ spread around this average. To assess whether the ratio corresponding to the proton-unbound state is consistent with the overall trend, a p-value of $p = 0.24$ was calculated, as indicated in the figure. This corresponds to a deviation between 1σ to 2σ from the mean. Therefore, the ratio for the unbound state is consistent with the average value, and no statistically significant variation in the $\ell = 0$ strength can be identified. Thus, within the experimental uncertainties, no indication of isospin symmetry breaking is observed. However, it is important to note that the experimental uncertainties are rather large, and to draw conclusions on the isospin symmetry breaking, higher statistics data would be required.

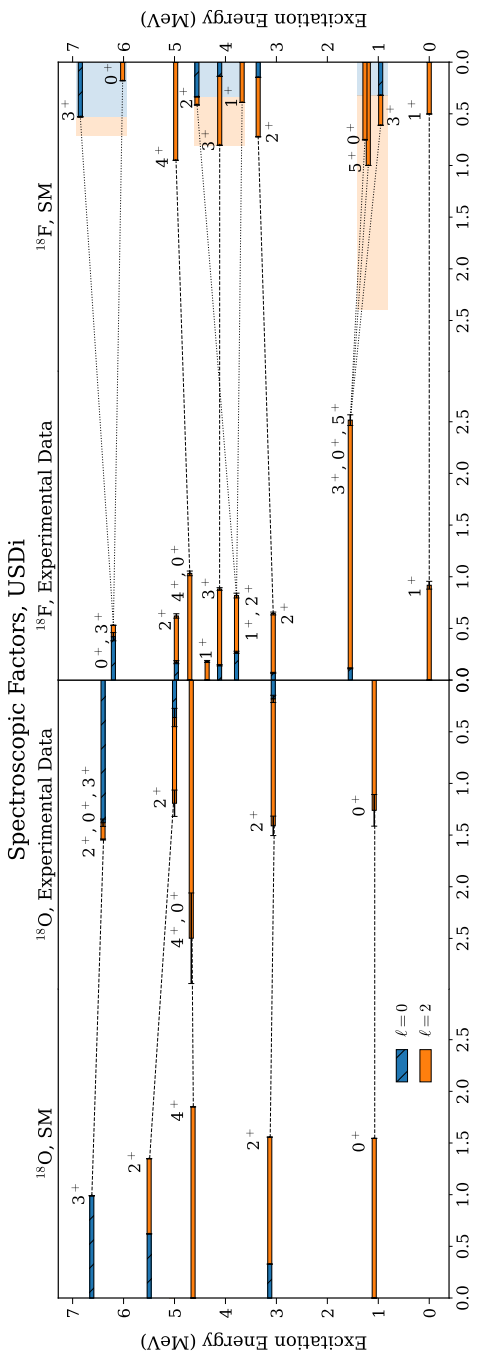

Figure 2.46: Comparison of spectroscopic factors for ^{18}O (left panel) and ^{18}F (right panel) obtained experimentally using Option 2a with shell-model calculations using the USDi interaction.

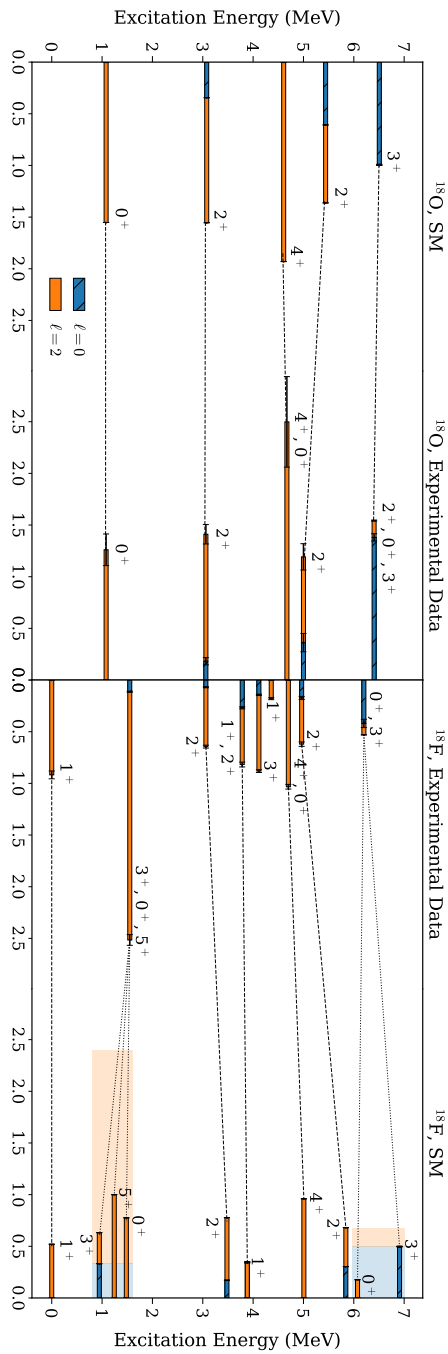

Figure 2.47: Comparison of spectroscopic factors for ^{18}O (left panel) and ^{18}F (right panel) obtained experimentally using Option 2a with shell-model calculations using the FSU interaction.

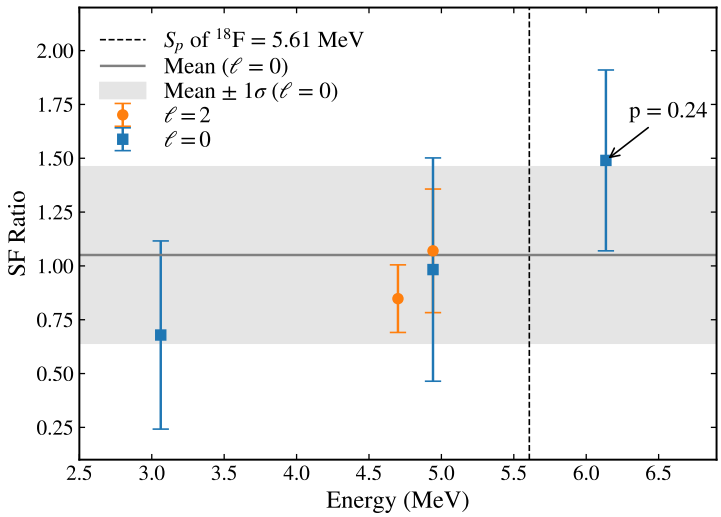

Figure 2.48: Ratio of $\ell = 0$ (blue) and $\ell = 2$ (orange) transfer components for states populated in ^{18}F relative to ^{18}O at selected excitation energies. Error bars represent experimental uncertainties. The black horizontal line represents the average ratio for $\ell = 0$ across the states, while the grey band shows the corresponding 1σ spread. The p-value quantifies the consistency of the proton-unbound state with the overall trend, indicating no significant deviation from the average.

2.7 Outlook

In the present study, multiple excited states in ^{18}F and ^{18}O were populated via the neutron adding (d,p) reaction. The experimental approach—neutron transfer measured in a solenoidal spectrometer—proved effective for populating and identifying states in both nuclei. In addition, also proton- and α-decay channels in ^{18}F were observed by selecting specific signatures in the recoil detectors.

A natural extension of this work would be to repeat the measurement with coincident γ-ray detection. This would significantly improve the energy resolution and enable disentangling of closely spaced states, which is challenging when relying on charged-particle detection due to its limited resolution. The addition of γ-ray spectroscopy would therefore allow for a more precise identification of individual nuclear levels. However, so far only $CeBr_3$ γ detectors were used inside a solenoidal spectrometer, which have a limited energy resolution [80], and thus may not allow for a straightforward identification of individual states. It is important to note that this approach would not provide additional

information for the states that decay by proton emission.

Another important direction for future studies is the population of higher-lying states, in particular proton-unbound states in ^{18}F at increased excitation energies, as well as higher excited states in ^{18}O. This would enable a more systematic study of weak-binding effects across a broader range of states. In the present work, only a single multiplet of states with isobaric analogue states above the proton separation energy in ^{18}F was populated. Increasing the beam energy, or optimising the experimental setup for the detection of higher excitation energies, would provide access to a larger set of proton-unbound states. A systematic comparison of these states with their analogues in ^{18}O would offer a deeper insight into the structure and behaviour of unbound nuclear systems.

Additionally, it would be interesting to see if the 6.136 MeV state in ^{18}F could be populated in the ^{17}O(^{3}He, d)^{18}F reaction. Although this state was not reported in Refs. [39, 40], repeating the measurement with better statistics could help clarify its population mechanism. A comparison of the extracted spectroscopic factors between the (^{3}He,d) and (d,p) reactions would provide additional insights into the single-particle structure of this state and the reaction selectivity. In (d,p) reactions, the transferred neutron is probed, whereas the proton is the weakly bound particle. As a result, sensitivity to the weak-binding of the proton arises only indirectly, through its pairing with the neutron. In contrast, the (^{3}He,d) reaction offers a more direct route to probe this. Such a measurement would likely require the use of a gas target in inverse kinematics.

As shown in Fig. 2.49, several proton- and α-unbound states were populated in the present work. However, the available statistics were not sufficient for a detailed analysis of their angular distributions. Of particular interest is the 1^- α-unbound state in ^{18}F at 5.604 MeV, which may have relevance for nuclear astrophysics. This state can contribute to the inverse of the ^{14}Ne$(\alpha, \gamma)^{18}$F reaction, which plays a role in energy generation in stars following hydrogen burning via the CNO cycle [81]. However, a nearby 1^+ state at 5.603 MeV can possibly interfere with the 1^- state. Disentangling these contributions requires higher statistics in order to separate the even- and odd-ℓ transfer components and reliably determine the properties of the 1^- state.

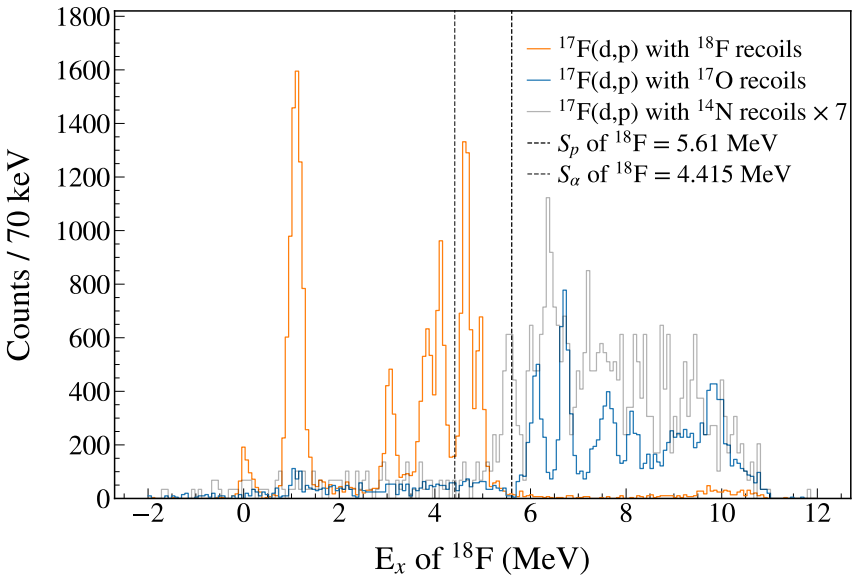

Figure 2.49: Excitation energy spectra for the ^{17}F(d, p) with ^{18}F recoils (orange line), with ^{17}O recoils (blue line), and with ^{14}N recoils scaled by factor 7 (gray line). The proton separation energy of ^{18}F, S_p = 5.61 MeV, is indicated by the black dashed line, and the α separation energy of ^{18}F, S_α = 4.415 MeV, is indicated by gray dashed line. The ^{17}F beam data are scaled such that the d-wave component strength of the first 2^+ state at 3.062 MeV matches the corresponding d-wave component strength of the first 2^+ state in ^{18}O at 1.982 MeV.

Chapter 3

Fission at ISS

This chapter presents an experiment studying the fission of ^{233}U in the ^{232}U(d, pf) reaction performed at ISOLDE, CERN, using the ISOLDE Solenoidal Spectrometer (ISS). The chapter begins with a discussion of the astrophysical origin of elements in the Universe (Section 3.1), highlighting the role of the r-process in the formation of elements heavier than iron. Section 3.2 then explores how experimental nuclear physics can contribute to a better understanding of the astrophysical r-process, emphasising the importance of fission properties of neutron-rich nuclei for modelling the r-process path and improving theoretical predictions. The role of fission in the r-process motivates this work.

A general overview of the production of radioactive ion beams at ISOLDE is then presented in Section 3.3, together with a description of the HIE-ISOLDE and the ISS setup. This is followed by a detailed account of the preparation of an experiment designed to study fission induced in (d, p) reactions in inverse kinematics using a solenoidal spectrometer and a radioactive ion beam presented in Section 3.7. The development of a dedicated detection setup, optimised for efficient detection of various reaction products, is described, along with supporting simulation results.

The commissioning of the experimental setup with a stable beam is presented in Section 3.8, followed by a description of the IS739 experiment Section 3.9, carried out at ISS in July 2025. The chapter concludes with an overview of the data analysis performed for this experiment.

3.1 Origin of heavy elements and the r-process

There are 118 known elements, 94 of which occur naturally on Earth.

The most mass-abundant element in the universe is hydrogen, making up around three-quarters of all matter. The remaining 25% is primarily composed

of helium. The third-most abundant element is oxygen[1]. All other elements are generally uncommon.

Concerning the composition of the Earth, the situation is quite different. Elements making up the most mass of the Earth's crust include oxygen (about 47%), silicon (28%), aluminium (8%), iron (5%), calcium (4%), sodium (3%), magnesium (2%), and potassium (2.5%). Additionally, heavier elements can be found on Earth, such as platinum, gold, lead, thorium and uranium. A question arises — how were these elements formed?

The lightest elements—hydrogen, helium, and trace amounts of lithium—were formed during the first minutes after the Big Bang through nuclear reactions in a process known as Big Bang Nucleosynthesis (BBN)[2]. Elements heavier than hydrogen—including helium—are created inside the cores of stars by fusion reactions. When light elements fuse, energy is released because the binding energy per nucleon of the resulting nuclei is higher than that of the initial nuclei. Energy released by this process keeps the star from collapsing. The formed elements can be released into the surrounding galaxy by explosive stellar scenarios. However, elements heavier than iron and nickel cannot be formed in fusion reactions. They are the most tightly bound nuclei, and fusion of such elements no longer releases energy. Some light elements—lithium, beryllium, and boron—are thought to be formed in cosmic ray spallation, where they are remnants from collisions of heavier elements with high-energy cosmic rays[3] [82].

Elements occurring naturally in the Solar System, along with their astrophysical origin, are presented in Fig. 3.1.

[1]Stars burn hydrogen as their primary fuel source. Later in the lifetime of a star, after it has stopped burning hydrogen to helium, it transitions to burning helium to produce heavier elements. Massive stars undergo catalytic cycles involving carbon, nitrogen, and oxygen, known as the CNO cycles. Lighter elements – lithium, beryllium, and boron – are not produced in stellar nucleosynthesis. However, in the later stages of the life of a star, helium burning leads to the formation of carbon, and the fusion of helium and carbon results in the production of oxygen. This causes oxygen to become the third most abundant element in the Universe.

[2]In the BBN, only very few elements heavier than helium were produced because of a bottleneck: the absence of any stable nuclei with either 5 or 8 nucleons. Consequently, the production of heavier nuclei, including lithium-7, during this early cosmic phase was constrained. In stars, the bottleneck is overcome through triple-collisions of helium-4 nuclei, leading to the formation of carbon (the triple-alpha process). However, this process is slow and requires high densities, taking tens of thousands of years to convert a substantial amount of helium into carbon within stars. As a result, its contribution in the immediate minutes following the Big Bang was minimal.

[3]Cosmic rays mainly consist of protons and atomic nuclei (most of which are alpha particles).

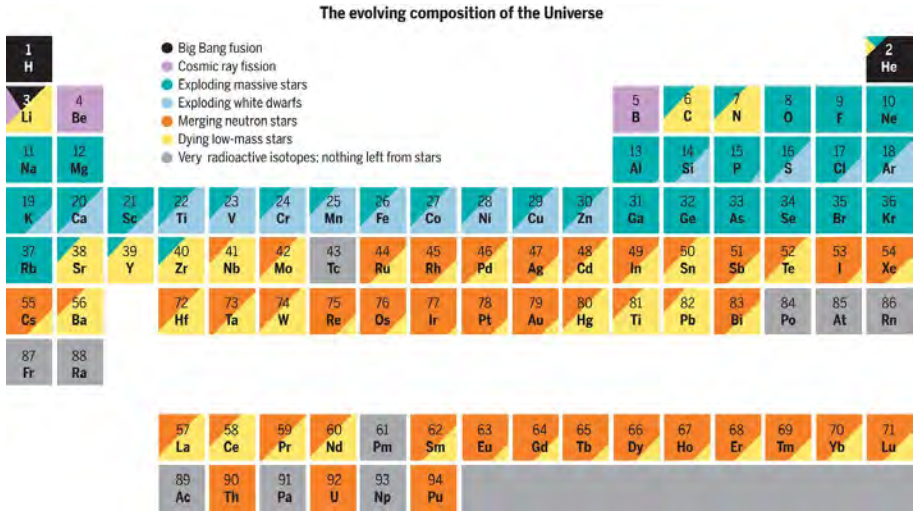

Figure 3.1: Elements occurring naturally in the Solar System and the astrophysical sources that are responsible for their creation. Figure from [83].

How elements heavier than iron are formed has been a mystery for many decades. In 1957, it was proposed that they are mainly synthesised by neutron-capture reactions [84, 85]. However, the mean life of free neutrons is 878.4 seconds [86]. This means that nearly all neutrons produced in the Big Bang have already decayed before neutron capture reactions could even take place. Thus, neutron capture processes need to take place in specific astrophysical sites where sufficient fluxes of neutrons are available.

Neutron capture reaction networks can be distinguished based on the neutron flux, and important for this thesis are the slow neutron capture (s) and rapid neutron-capture (r) processes. The s-process only requires a low flux of neutrons. It is believed to occur mostly in the outer layers of Asymptotic Giant Branch[4] (AGB) stars. Neutrons for the s-process are supplied mainly by the $^{13}\mathrm{C}(\alpha,n)^{16}\mathrm{O}$ and $^{22}\mathrm{Ne}(\alpha,n)^{25}\mathrm{Mg}$ reactions, depending on the mass of the star[5] [87–89]. The s-process is a relatively slow process in which neutrons are caught one at a time, followed by β^--decay, forming isotopes close to the line of β stability. The timescale of the s-process is between thousands to millions

[4]An AGB star, short for Asymptotic Giant Branch star, is a type of evolved star that is in a late stage of stellar evolution. These stars, usually ranging from low to intermediate mass (approximately 0.6 to 10 times that of the Sun), have exhausted the hydrogen in their cores and have entered the late phases of their lives.

[5]The $^{13}\mathrm{C}(\alpha,n)^{16}\mathrm{O}$ reaction takes place at temperatures around 100 MK, while the $^{22}\mathrm{Ne}(\alpha,n)^{25}\mathrm{Mg}$ reaction happens only if the temperature reaches above $\simeq$ 300 MK. In AGB stars with masses less than 4–5 Solar masses the temperature hardly reaches 300 MK so only the first reaction can take place [87].

of years, typically with decades elapsing between successive neutron captures. The s-process can synthesise elements up to bismuth and it is believed that it has created around half of the elements heavier than iron in the universe. More information on the s-process can be found in Ref. [90].

Unlike the s-process, the r-process requires a high flux of free neutrons. The astrophysical site has been an open question for decades. Possible candidates proposed were neutron-star mergers and certain types of core-collapse supernovae. The first strong observational evidence that a neutron star merger produces a neutron flux sufficient for the r-process was provided in 2017 through a multi-messenger observation of such a merger [91]. First, the gravitational-wave detectors LIGO and VIRGO observed a neutron star merger, GW170817 [92], which was followed by a kilonova[6] observation, AT2017gfo, in the electromagnetic spectrum ranging from radio- up to γ-frequency radiation. A neutron-capture element, strontium, was identified in the measured spectra. Strontium is one of the elements that can be produced through multiple neutron captures, and its isotopic composition and abundance patterns indicate that a neutron star merger can supply a neutron flux sufficient for the r-process [91].

During the r-process, several neutrons are captured sequentially through (n,γ) reactions, resulting in the formation of very neutron-rich isotopes. Eventually, the formed isotopes are sufficiently far from the line of β stability that β^- decay starts to compete with the capture of another neutron. After β^- decay, neutron capture is often again the next step. Neutron capture and β^- decay may also compete with photodissociation, i.e. (γ,n) reactions. The entire process is a complex reaction network extending across hundreds of neutron-rich isotopes far off the line of β stability. As the masses of the formed isotopes increase, at some point they become so heavy that nuclear fission becomes a possible decay channel. Thus, fission plays a crucial role insofar as it limits the mass of isotopes formed in the r-process.

Understanding the contribution of the r-process to the Solar System abundances is challenging because most of the isotopes involved in this process are very neutron-rich, thus far away from the β stability line. It is, in most cases, presently not possible to produce and study such isotopes in the laboratory. There is much more information available on the isotopes participating in the s-process[7], and traditionally the r-process abundances have been inferred by first fitting the calculated s-process abundance distributions to the total isotopic abundances measured in meteorites and attributing the remaining portion to the r-process [93]. The isotopic abundances in the solar system, separated into

[6] A kilonova is a transient astronomical event that occurs when two objects in a binary system, such as two neutron stars or a neutron star and a black hole, merge, resulting in a strong release of electromagnetic radiation. The term *kilonova* characterizes the peak brightness that reaches about 1000 times (*kilo*) that of a classical nova.

[7] Isotopes involved in the s-process are more stable, making them easier to produce and study.

components from the r-process and s-process, are presented in Fig. 3.2. Elements primarily formed by the r-process include gold, platinum, and some rare-earth elements (like europium and gadolinium), as well as long-lived thorium and uranium isotopes (not shown in the figure).

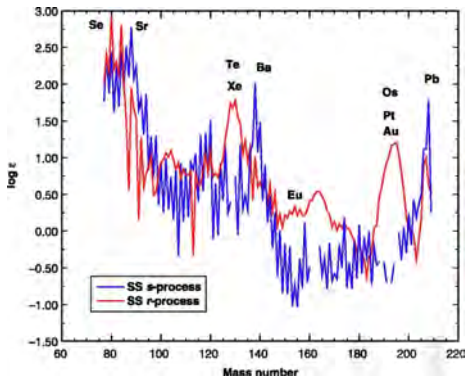

Figure 3.2: The solar system (SS) isotopic abundances, separated into components from the r-process and s-process. The s-process abundances are determined from the composition of solar meteorites. The observed abundances of elements in the mass region of gold and platinum, rare-earth elements, and tellurium and xenon cannot be explained without invoking the r-process. Figure from Ref. [93].

As mentioned earlier, the r-process involves a complex network of reactions and decays of hundreds of isotopes. Some nuclear properties of isotopes involved significantly influence the entire process of creating heavy elements in the universe, such as β-decay rates and nuclear masses of the participating isotopes. However, the r-process is ultimately limited once fission becomes possible. Then, a nucleus splits into two smaller fragments.

This makes fission, which effectively constrains the mass of isotopes formed by the r-process, to be of particular importance to understand this process. Moreover, the two fission fragments can subsequently capture additional neutrons, broadening the range of nuclei involved in the r-process. Thus, more information on fission of isotopes along the path of the r-process is essential for a deeper understanding of the formation of heavy elements.

3.2 Fission of neutron-rich nuclei

One of the key ingredients for r-process model calculations are the fission barriers and fission probabilities of the heavy r-process isotopes. The fission barrier refers to the energy barrier that prevents a nucleus from splitting into two fission

fragments. However, as mentioned before, neutron-rich nuclei are very challenging to produce and study in the laboratory, which is the reason why the fission barriers of such isotopes are not known.

There are two ways for fission to happen: spontaneous fission (SF), and compound nucleus fission, neglecting pre-equilibrium fission processes here. SF plays a role for nuclei heavier than the nuclei which are the focus of this work. Here, we rather focus on the second alternative—the formation of a compound nucleus. One possibility to populate such a state is neutron-induced fission, where a target made of stable nuclei is bombarded with neutrons. Another option is fission induced by Light Charged Particles (LCPs), where light particles like protons or alpha particles impinge on a target. Fission can also be induced by bombarding a target with high-energy photons (real or virtual). Heavy-ion-induced fission, using multi-nucleon transfer reactions or fusion-fission reactions, allows for reaching elements further away from the β stability line than otherwise accessible. Exploring beta-delayed fission enables the study of unstable nuclei, when β-decay leads to the population of excited states in the daughter nucleus that are situated at excitation energies above the fission barrier. However, to study unstable nuclei, these methods are often not applicable due to the lack of appropriate target and beam combinations given by the overall shape of the β-stability line.

To get as close as possible to the r-process in the laboratory, one would need to use a target made of an element that is already quite rich in neutrons, bombard it with neutrons, and observe at which neutron energy fission becomes possible. Unfortunately, there are no stable targets that allow us to study isotopes directly interesting in terms of the r-process, and the available neutron fluxes are not high enough.

This problem can be circumvented by using inverse kinematics. In inverse kinematics, a target made of a light, stable element is bombarded with a heavy beam, which can be unstable. As it is currently not possible to produce a target made of neutrons, a different approach is required. One such approach involves the use of surrogate reactions, for example a (d,p) reaction. In this reaction, a heavy ion beam impinges on a CD_2 target, where the deuteron in the target is transferred to the beam ion. Because of high state density in the beam nucleus and configuration mixing, the transferred neutron does not populate single particle states, as it was discussed in the case of the $^{17}\mathrm{F}(\mathrm{d},\mathrm{p})^{18}\mathrm{F}$ and $^{17}\mathrm{O}(\mathrm{d},\mathrm{p})^{18}\mathrm{O}$ reactions in Chapter 2. Instead, the transfer reaction leads to the population of doorway states, which redistribute excitation energy from single-particle-like configurations to collective excitations, or, more generally, to all open degrees of freedom, forming a compound-nucleus formation.

As shown in Section 1.3, the excitation energy of the formed nucleus can be extracted using the measured energy of the ejectile (proton in case of the (d,p) reaction). This allows to study neutron-rich nuclei and their fission barrier.

3.3 Experiments with radioactive beams at ISOLDE, CERN

To study exotic and short-lived isotopes, we have to use radioactive beams. This section will cover the production of radioactive elements at the ISOLDE facility at CERN. Following that, an experiment which aimed at the investigation of fission of ^{230}Ac (IS739) will be discussed.

3.4 The ISOLDE Facility at CERN

The ISOLDE Facility is a nuclear physics laboratory at CERN in Geneva, Switzerland. The main focus of ISOLDE is the production of radioactive nuclei with the on-line isotope mass separation technique and experiments with those.

At ISOLDE, more than 1000 isotopes of 74 elements can be produced. As the number of available beams increases, it becomes possible to explore areas of the nuclear chart that have never been studied before, including neutron-rich actinides (see Ref. [14]).

3.4.1 Beam production

Radioactive isotope production at ISOLDE is executed as follows. First, negative hydrogen ions H^- are accelerated in the CERN Linear accelerator 4 (LINAC4) to an energy of 160 MeV. After that, the ions are transferred to the Proton Synchrotron Booster (PSB). During injection into the PSB, two electrons are removed from each H^- ion using a stripping foil, leaving only a proton [94]. In the PSB, the protons are accelerated to an energy of 1.4 GeV. After the acceleration, the now pulsed proton beam with an average current up to 2.0 μA is transferred and impacts directly onto an around 20 cm thick ISOLDE target positioned in a tubular tantalum target container. The path H^- ions and protons take to reach the destination can be seen in Fig. 3.3, which shows the CERN accelerator complex.

As the proton beam impacts the ISOLDE target, fission, spallation, and fragmentation reactions can take place, creating a plethora of different isotopes. Reaction products, trapped in the thick target, can be released by heating the target container (up to 2000°C). The target material needs to be carefully chosen to fit the experimental needs.

The next step is ionization of the extracted isotopes to a 1^+ state. There are three different ion sources that can be used: surface ion sources, plasma ion sources, and laser ion sources. In surface ion sources, ions can be ionized by passing them through a metal tube (such as tantalum or tungsten) that captures electrons from them. Plasma ion sources operate by ionizing a gas mixture (typically Ar and Xe) through electrons accelerated between the transfer line

and the extraction electrode with a voltage of about 130 V, all within a magnetic field. Laser ion sources utilize multi-step photo-ionization.

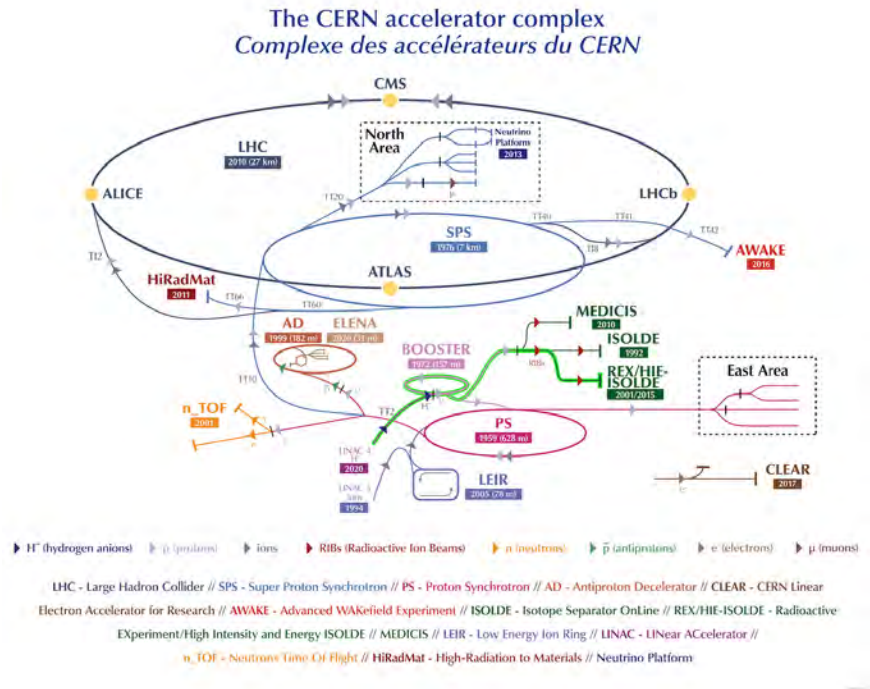

Figure 3.3: The CERN accelerator complex. Negatively-charged hydrogen ions, delivered from LINAC4, are injected into the PSB. During the injection, two electrons are removed from each ion. Then protons are accelerated to an energy of 1.4 GeV. The pulsed proton beam is extracted from the PSB into an ISOLDE target, from where radioactive beams are further distributed to experimental stations. The path H^- ions and protons take to reach ISOLDE is marked in green. Figure adapted from Ref. [95].

To then select the isotope of interest, the ionised beam is sent through a mass separator. At ISOLDE, one of two on-line mass separators can be used – the General Purpose Separator (GPS) and the High Resolution Separator (HRS). The GPS's mass resolution $m/\Delta m$ is approximately 800 and allows for simultaneous extraction of two more beams in addition to the central beam. The HRS's mass resolution has been measured to be approximately 6000 [96].

3.4.2 Post-acceleration

Isobars are selected using electric dipole magnets and this mass separated beam is then sent either to the low-energy beam lines or, after charge breeding, to the superconducting post accelerator and the HIE-ISOLDE experiments.

The mass-separated beam with energies up to 60 keV can be directed into low-energy beam lines. However, in certain fields of research involving radioactive nuclei, the use of beams with energies in the order of MeV/u is crucial to allow for nuclear reactions. To meet this need, REX- and HIE-ISOLDE post-acceleration installations have been developed. REX-ISOLDE is capable of post-accelerating nuclei to energies of up to 3 MeV/u, while HIE-ISOLDE is anticipated to reach eventually energies as high as 10 MeV/u. This subsection focuses on the design and performance of REX-ISOLDE.

After the ions are mass-separated, the continuous beam (with varying intensity) from a mass separator needs to be cooled, bunched, and charge-bred in order to post-accelerate it.

First, the beam is injected into REXTRAP—a large, gas-filled Penning trap surrounded by a superconducting solenoid. It accumulates the beam, which is first slowed down by the potential of the trap at the entrance to energies of the order of eV. The beam enters a high magnetic field of 3 T and is then further cooled down by collisions with the atoms of a buffer gas. After accumulation, the beam is extracted in bunches from the REXTRAP by an electric potential that is reverse to the one at the entrance; thus, the ions retain the original energy they had when they entered. For the process to be effective, the cooling time inside the trap needs to be at least 10 ms [97]. REXTRAP has about 50–60 % combined transmission efficiency for the injection, cooling, and extraction processes.

Subsequent to leaving REXTRAP, the beam is directed into EBIS, an Electron Beam Ion Source where 1^+ ions are bred to a higher charge state to make further acceleration more efficient. To be able to trap the 30–60 keV ions coming from REXTRAP, the EBIS is situated on a high-voltage platform. The ions are trapped inside the EBIS by an electrostatic barrier. Low-charged ions, when trapped, undergo a step-wise ionization through collisions with a dense electron beam from an electron gun. This continues until the ions are eventually extracted. The entire process leads to the distribution of charge states in the outgoing ions. The chosen breeding time depends on the required charge state and may range from milliseconds for light ions up to hundreds of milliseconds for heavy nuclei. The EBIS efficiency varies between a few percent and forty percent, depending on the beam. More technical details about the EBIS can be found in Ref. [98].

Following their extraction from the EBIS, the ions are directed into a mass-separator to choose a specific charge state and suppress the residual gas. The mass-separator system consists of an electrostatic 90° cylinder deflector and

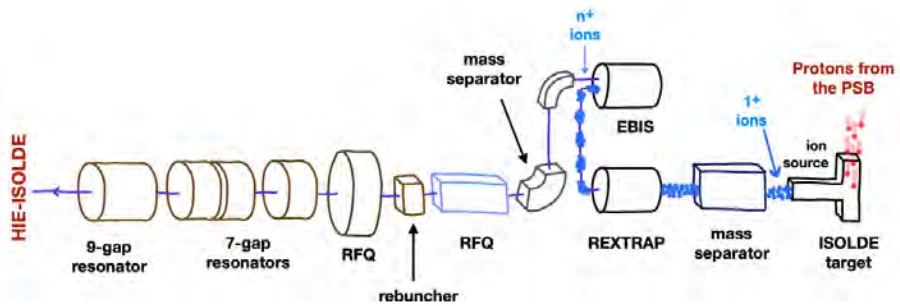

Figure 3.4: Schematic diagram of the ISOLDE–REX-ISOLDE–HIE-ISOLDE layout. Protons from the PSB impinge onto a thick ISOLDE target. Reaction products are released by heating the target and are then ionised to an 1^+ state. The ionised beam is sent trough a mass separator to select the isotope of interest. After being mass-separated, the low-energy beam is post-accelerated with REX-ISOLDE. First, the beam is bunched with REXTRAP. Then it is charge-bred using EBIS which allows to subsequently accelerate it efficiently with a sequence of RFQs and resonators. Figure adapted from Ref. [99].

a 90° magnetic bender. Then the ions are injected into the linear accelerator of REX-ISOLDE. The first element of the REX-ISOLDE LINAC is the Radio-Frequency Quadrupole (RFQ), which accelerates ions from 5 keV/u to 300 keV/u. The beam is rebunched in order to fit into the following Interdigital-H-type (IH) structure. The IH structure is a drift-tube which further accelerates the beam to an energy of 1.2 MeV/u. Following this, the beam is directed to three 7-gap spiral resonators and a 9-gap resonator. The final energy of the beam may reach maximum 3 MeV/u for beams of $A/q \leq 4.5$. The LINAC achieves a transmission of approximately 90 %.

A schematic diagram of the ISOLDE layout with post-acceleration is shown in Fig. 3.4.

3.4.3 HIE-ISOLDE

HIE-ISOLDE is an energy upgrade of ISOLDE which allows to increase the energy of the radioactive ion beams (RIBs) from 3 MeV/u up to 10 MeV/u [100]. It consists mainly of superconducting cryomodules. The energy upgrade installation is structured into three separate phases. During the initial phase, two cryomodules were added to the existing REX-ISOLDE LINAC. That allowed to increase of the energy up to 5.5 MeV/u. In the second phase, an additional pair of cryomodules was included in order to reach an expected beam energy of

10 MeV/u for $A/q = 4$. In the last phase, the 7-gap resonator and 9-gap structure of REX-ISOLDE are planned to be substituted with two cryomodules, enabling an energy range from 0.45 to 10 MeV/u.

3.5 The ISOLDE Solenoidal Spectrometer

The ISOLDE Solenoidal Spectrometer (ISS) is an experimental setup at HIE-ISOLDE. The design of the ISS draws its inspiration from HELIOS at ANL [19]. It consists of a former-MRI magnet operating at a maximum of 2.5 T (the maximum field of the magnet magnet—4 T—cannot be used due to safety restrictions in the ISOLDE hall). Its total diameter and length are 2396 and 2732 mm, respectively. The ISS was developed for inelastic scattering and transfer reactions studies mainly using (d, p) reactions, where the detection of the proton allows for good energy resolution, as described in Section 1.3. Reactions take place inside the solenoidal field, and reaction products deposit their energy in detectors placed inside the magnet on a dedicated platform. The position of ISS inside the ISOLDE facility is indicated in Fig. 3.5.

More details about the detectors used in the IS739 experiment are provided in the following sections.

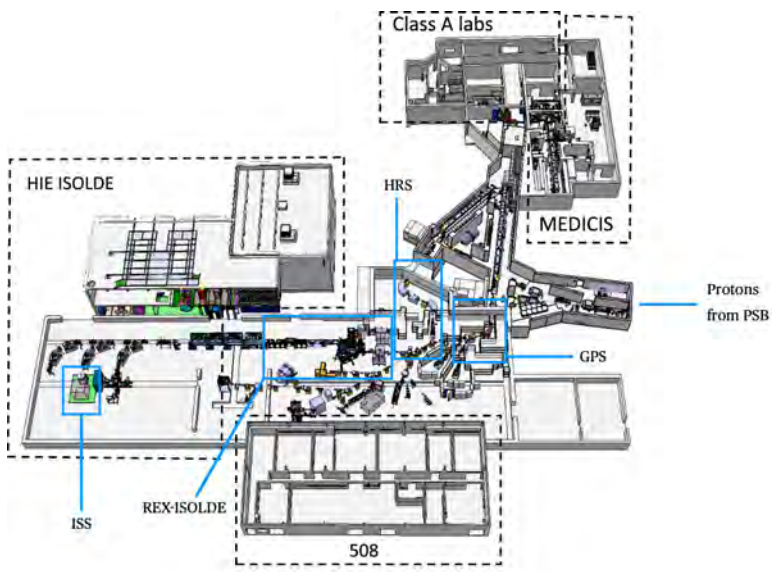

Figure 3.5: A schematic layout of the ISOLDE facility. The relevant sections of the beam line are highlighted. Figure adapted from Ref. [96].

3.6 Fission of ^{230}Ac

The path of the r-process lies far away from the $\beta-$stability line and includes highly neutron-rich nuclei. Our interest lies in exploring fission of these isotopes. Given their low stability and the technical challenges in their production, beams of such isotopes are presently unavailable. Our approach involves examining the fission of alternative less-exotic neutron-rich isotopes (which lie closer to the $\beta-$stability line) to establish a measurement method. This methodology aims to be transferable to other, even more neutron-rich nuclei. Furthermore, model predictions for nuclei within our experimental reach can be tested, thereby increasing their predictive power for isotopes we cannot reach, i.e. those relevant for the r-process.

As the initial physics case for an experiment of this kind, the fission of ^{230}Ac was proposed to study. This choice was motivated by several factors: available beam intensities, anticipated fission probabilities, and the absence of definitive fission data at low excitation energies for this particular isotope. However, as discussed in Section 3.9, it was ultimately not possible to use the ^{229}Ac beam, and the experiment was instead performed using a ^{232}U beam.

At the time of writing of the proposal to the INTC (the advisory committee which approves experiments at ISOLDE), it was predicted that ISOLDE is capable of delivering an 8 MeV/u ^{229}Ac beam with an intensity of 1.3×10^7 pps, which was expected to provide sufficient statistics to successfully run the experiment. In order to achieve such beam rates, ^{229}Ac needs to be extracted in a molecular form as ^{229}AcFF$^+$ from a ThC_x (thorium carbide) or UC_x (uranium carbide) target with a plasma ion source. Yields above 10^7 μC^{-1} ^{229}AcFF$^+$ have been measured for a UC_x target and a plasma ion source combination at target temperatures above 2000°C. Predictions from FLUKA simulations [101] indicate even higher production rates for ThC_x within the target (1.8×10^{10} μC^{-1} vs. 3.3×10^8 μC^{-1} for UC_x). It was expected that the produced beam will not contain significant contaminants, as proven in the ISOLTRAP MR-ToF MS [102] study of the beam composition of ^{229}AcFF$^+$ [103].

There are no conclusive data on fission of ^{230}Ac at low excitation energies. It is important to highlight that data exists from three experiments involving ^{230}Ac. The first experiment recorded two inconclusive $\beta-$delayed fission events in mica photo-emulsion foils[8] [104], while the second experiment concentrated on heavy-ion-induced fission at high excitation energies [105], focusing on the extraction of fission transient times (the time fission takes). A recent study of ^{230}Ac gives only a lower limit on the beta-delayed fission probability [106].

There are predictions of the ^{230}Ac fission barrier height. A fission barrier of 5.37 MeV [107] is extracted in a study conducted by Eckert et al. in 1990 [108],

[8]Mica is a material that belongs to a group of silicate materials. It has excellent thermal and electrical insulating properties.

which investigated the fission of highly excited target residue nuclei resulting from collisions between ^{40}Ar and ^{232}Th. A prediction of a 7.01 MeV fission barrier is available from the General Description of Fission Observables (GEF) model [109]. Another estimation places the fission barrier between 5.7 and 6.8 MeV [110], derived from the analysis of the aforementioned two $\beta-$delayed fission candidate events [104]. For experiment planning, the more challenging value of 7.01 MeV was assumed.

3.7 Experimental setup

In order to successfully measure the fission barrier height and the fission cross section of a fissioning nucleus in a (d,pf) reaction, several observables need to be determined. First, the detection of back-scattered protons in coincidence with fission fragments is crucial to establish whether a (d,pf) reaction has occurred. By measuring the energy and hit position of the protons, the excitation energy E_x of the fissioning system can be calculated, identical to the procedure used for the HELIOS setup (see Section 1.3 and Eq. (1.20) therein). Subsequently, the fission barrier height can be determined as a function of excitation energy. To obtain the fission cross section, it is essential to calculate the product of the beam intensity and the number of target particles per unit area, which can be determined by measuring elastically scattered deuterons within a specified angular range. Lastly, the measurement of γ rays emitted from fission fragments enables the extraction of their total energy and multiplicity.

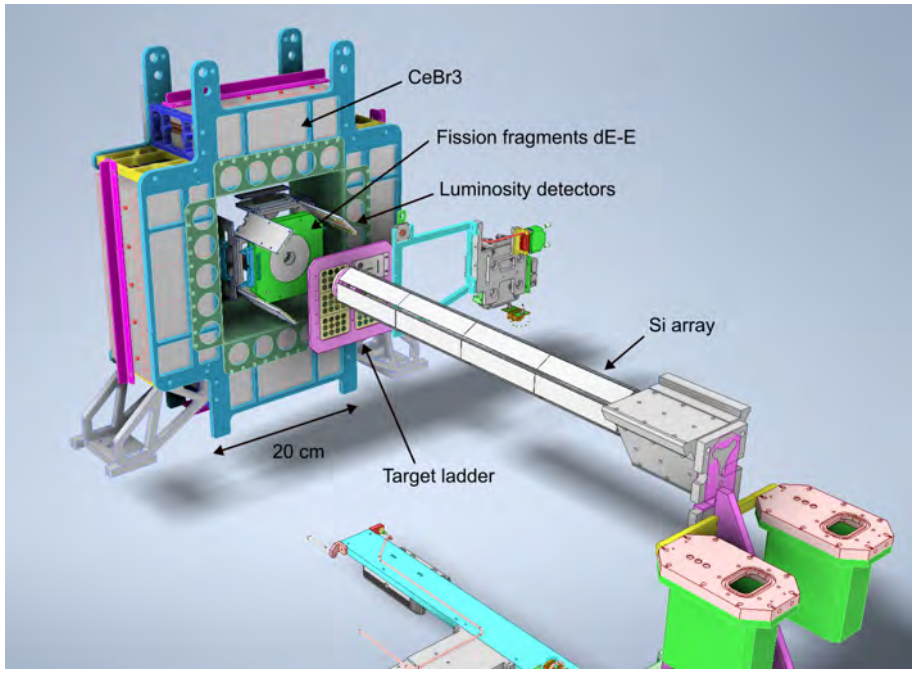

Figure 3.6: Schematic illustration of the detectors inside the vacuum chamber of the ISS magnet. Beam enters from the lower right through the hollow upstream silicon array and impinges on the target mounted in the target ladder. Deuterons elastically scattered from the target are detected by the four luminosity detectors. Fission fragments move in the forward direction and are detected by the ΔE-E CD-shaped Si detector. Gamma-rays emitted from the fission fragments are detected by a $CeBr_3$ detector array. Detectors used for beam tuning are not shown. All dimensions and positions are to scale with placements optimized by simulations. Figure from Ref. [111].

A schematic figure of the experimental setup is shown in Fig. 3.6. The chosen setup has been designed to optimise detection efficiency. Further details regarding the detectors and their configuration will be provided below.

3.7.1 Detection of protons

For proton detection, a hexagonal array of double-sided silicon strip detectors (DSSSDs), shown in Fig. 3.7, is used, which is a standard part of the ISS setup. Similarly to the HELIOS Si array, it is placed on-axis with the beam and magnetic field. The array is hollow, cooled with alcohol to about $-20°$ C and allows the beam to pass through its centre. It consists of three modules,

each covering two sides of the hexagonal array. Each module comprises eight DSSSDs, each 125 mm long and 25 mm wide. The detectors have 128 strips with a pitch of 0.95 mm on the front (p-side) and 11 strips with a pitch of 2 mm on the back (n-side). The total length of the active Si region, including 0.5 mm gaps between detectors, is 501.5 mm. The total solid-angle coverage of the Si array is 94 % in the direction parallel to the beam axis and 70 % in the azimuthal direction. The radius of the array, measured from the beam axis to the middle n-side strip on a Si wafer, is 27 mm. Each DSSSD is $\sim$1000 μm thick[9].

The p-side strips are electrically bonded across adjacent Si wafers within a given module and read out as a single signal channel, providing the z-position of the interaction. The azimuthal position is determined from the 11 n-side strips.

The detector readout is based on application-specific integrated circuits (ASICs). Each module is equipped with six ASICs: four are used for the p-side channels and two for the n-side channels. The mapping of detector channels to the ASICs is shown in Fig. 3.8.

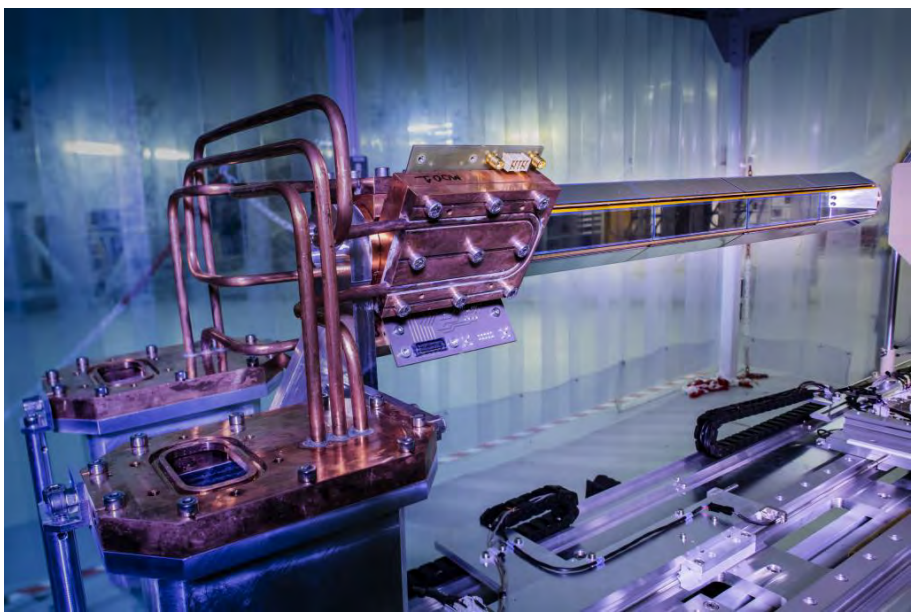

Figure 3.7: A photograph of the ISS Si array on the support structure. On the left side cooling lines are visible. Figure from Ref. [112].

[9]Detector thickness varies within 5 % for each detector.

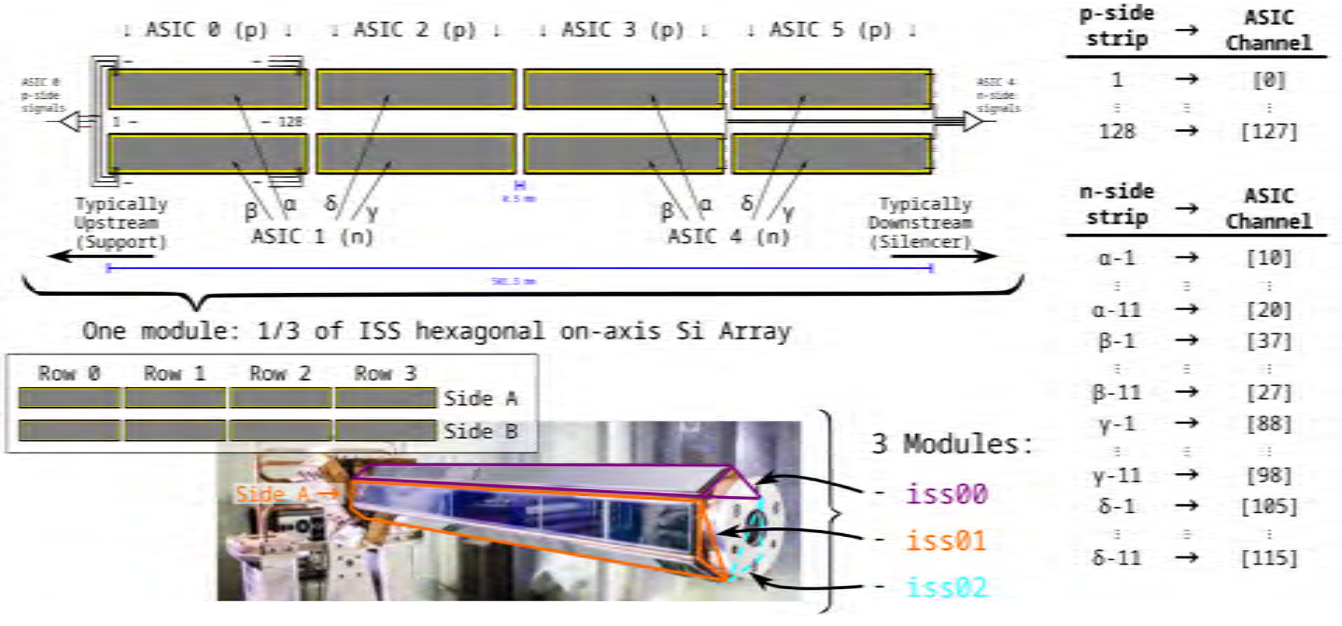

Figure 3.8: Diagram showing the mapping of the p-side and n-side channels to the ASICs and division of the Si array into modules. Figure from [113].

Fig. 3.9 shows the kinetic energy of a proton (T_{proton}) as a function of its hit position along the z-axis (z) for excitation energies of the fissioning nucleus ranging from 6 MeV to 10 MeV. The simulated beam energy is 8 MeV/u. It can be seen that different ranges of excitation energy can be covered by changing the placement of the Si array.

In order to determine the fission barrier (assuming that the prediction is sufficiently close to reality) of a given isotope unambiguously, it is necessary to register excitation energies at least 2 MeV above and below the predicted barrier. In case of ^{230}Ac, the GEF model predicts a fission barrier of 7.01 MeV. This means that coverage of excitation energies in the range of approximately 5 MeV and 9 MeV is desired.

When a compound nucleus with high excitation energy is formed, the kinetic energy of the emitted proton is low. Consequently, the proton has a smaller momentum, including in the direction opposite to the beam. As a result, it travels a shorter distance along the z-axis before completing an orbit in the magnetic field. As shown in Fig. 3.9, to detect protons ejected in reactions forming nuclei with high excitation energies, the silicon array should be positioned as close to the target as possible. At the same time, placing the array too close to the target interferes with the trajectories of the protons emitted from the target. A compromise distance of 1.85 mm between the Si array and the target was therefore chosen. This corresponds to a distance of 3.7 mm between the target and the edge of the first silicon, since the sensors are mounted on an aluminium support structure.

Each channel of the Si array is typically calibrated using an α source containing four different isotopes: ^{148}Gd, ^{239}Pu, ^{241}Am, and ^{244}Cm, with the energies of the emitted α-particles listed in Table 3.4.

In the magnetic field, particles with different mass-to-charge ratio, $\frac{m}{Z}$, have different cyclotron period. Referring to Eq. (1.22),

$$T_{\text{cyc}} = \frac{2\pi}{B}\frac{m}{Z},$$

we observe that for a proton (with a mass-to-charge ratio $A/Z = 1$) in the magnetic field of strength $B = 2$ T, the cyclotron period is $T_{\text{cyc}} = 32.8$ ns. This magnetic field strength of 2 T was chosen to maximise the proton detection efficiency. For a particle with a $A/Z = 2$, such as a deuteron or an alpha particle, the cyclotron period will be twice as long: $T_{\text{cyc}} = 65.6$ ns. The same applies to protons making two turns. Therefore, having a time resolution that enables the distinction between these cases helps to suppress background. However, time resolution of the ISS Si array is of the order of μs [114], which does not allow for distinguishing particles based on their cyclotron period.

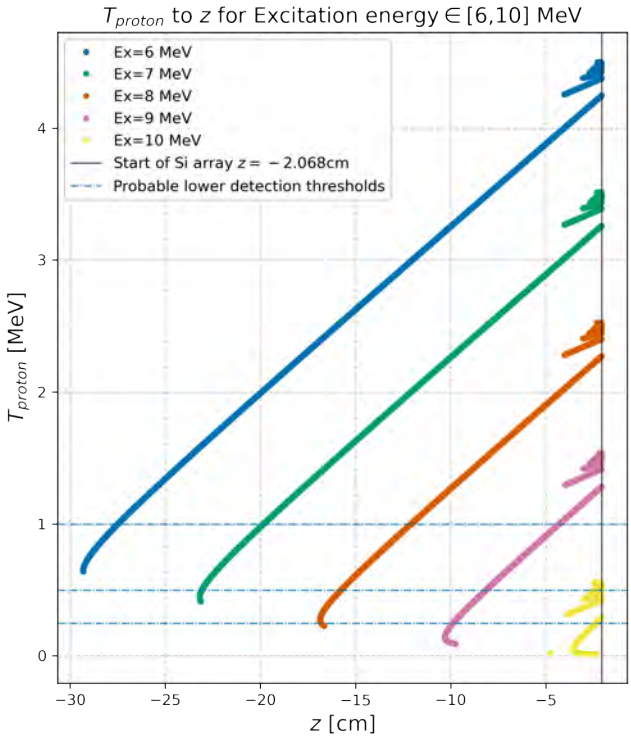

Figure 3.9: Kinetic energy of a proton (T_{proton}) versus its hit position along the z-axis (z) for excitation energies of the fissioning nucleus ranging from 6 MeV to 10 MeV (the simulated beam energy is 8 MeV/u). For each excitation energy, the long line corresponds to protons completing a single turn before hitting the detector, while the shorter lines to the right correspond to multi-turn events. Figure from Ref. [115].

3.7.2 Detection of fission fragments

Fig. 3.10 shows the nuclear charge distribution (upper panel) and the pre-neutron emission mass distribution (lower panel) of fission fragments for 10^5 events simulated by GEF [109] for fission of ^{230}Ac at an excitation energy $E^* = 7$ MeV above the ground state. The two fission fragments are expected to have charges within the range of $30 \leq Z \leq 60$ and masses spanning $80 \leq A \leq 150$.

The setup was intended and optimised for studying fission of ^{230}Ac, using a ^{229}Ac beam. Beam with an energy of 8 MeV/u impinging on a CD_2 (deuterated plastic) target. There, a (d,p) reaction may occur. The resulting compound nucleus ^{230}Ac* moves forward with an energy roughly similar to that of the

beam. Then, if fission occurs, the fission fragments move forward within a cone with an opening angle depending on the beam energy and the transverse momentum of the specific fission fragment.

Fig. 3.11 depicts the azimuthal angle distributions of fission fragments simulated by GEF and boosted into the beam frame for the simulated experiment.

Due to the kinematics of the emitted fission fragments, the most efficient method for their detection is to employ a CD-shaped[10] detector centred at the beam axis. A central hole in such a detector allows the unreacted beam to pass through. By adjusting its distance from the target, the solid angle coverage can be optimised to maximise the detection efficiency for fission fragments without obstructing trajectories of deuterons (more details on the detection of deuterons which are scattered from the target and used for normalisation are provided in Section 3.7.3).

Among the commercially available options, the S3 detector model from Micron Semiconductor Ltd [116] was selected for use as the fission fragment detector. It is a double-sided silicon strip detector with a central opening, segmented into 24 concentric rings on the junction side and 32 azimuthal sectors on the ohmic side. The fission fragment detector is configured as a silicon telescope in a ΔE-E arrangement, consisting of a ΔE layer with a thickness of 65 μm and an E layer with a thickness of 1000 μm. The dimensions of the fission fragment detector are listed in Table 3.1, and a photograph of the detector is presented in Fig. 3.12.

[10] *CD* stands for compact disc, a commercial format previously popular for music distribution, developed by Philips and Sony in 1982.

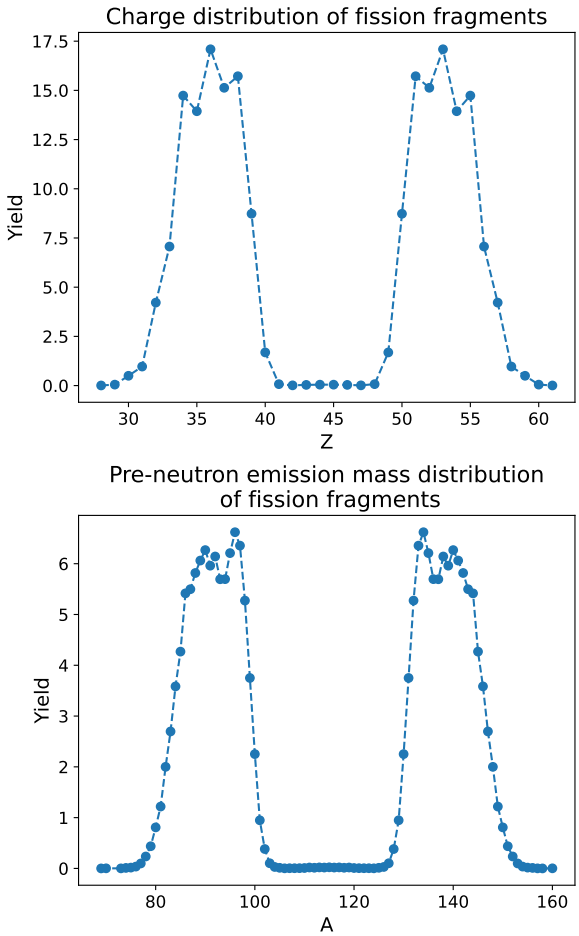

Figure 3.10: Charge distribution (upper panel) and pre-neutron emission mass distribution (lower panel) of fission fragments for 10^5 events simulated by GEF for ^{230}Ac at an excitation energy of $E^* = 7$ MeV above the ground state.

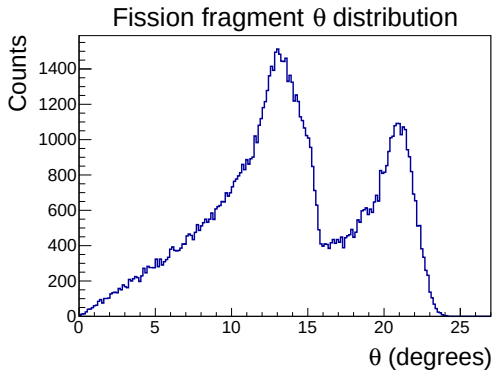

Figure 3.11: Angular distributions of ^{230}Ac fission fragments simulated by GEF and boosted to the beam frame (θ is the azimuthal angle). For the simulated ^{229}Ac beam energy of 8 MeV/u, two peaks around 13° and 21° can be distinguished, corresponding to heavy and light fission fragments, respectively.

Radii (mm)		Thickness and coverage	
Si chip inner	20.00	Junction number of elements	24 rings
Si chip outer	76.00	Junction pitch	886 μm
Si inner	22.00	Ohmic number of elements	32 sectors
Si outer	70.00	Ohmic pitch	11.25°
		ΔE thickness (μm)	65
		E thickness (μm)	1000

Table 3.1: Dimensions of the S3 detectors [116].

Fig. 3.13 shows the geometric efficiency of the simulated S3 fission fragment detector, used with a beam energy of 8 MeV/u, as a function of its distance from the target. At a distance of 8 cm downstream of the target, the efficiency is 87 % for detecting a single fission fragment and 82 % for detecting both fission fragments in coincidence. This distance was therefore chosen as the optimal detector position. The simulation considers only fission fragments detected in the ΔE layer. On average, approximately 39 % of all fragments that reach the ΔE layer pass through it and are subsequently detected in the E layer[11].

This experimental setup was not intended to identify the charge and/or mass of the fission fragments based on their energy-loss patterns in the ΔE and E layers. However, lighter nuclei, such as carbon or deuterium nuclei scattered from the target, can be distinguished if they reach the detector. Nevertheless,

[11] Especially the heavy fission fragments are not expected to punch through the ΔE detector.

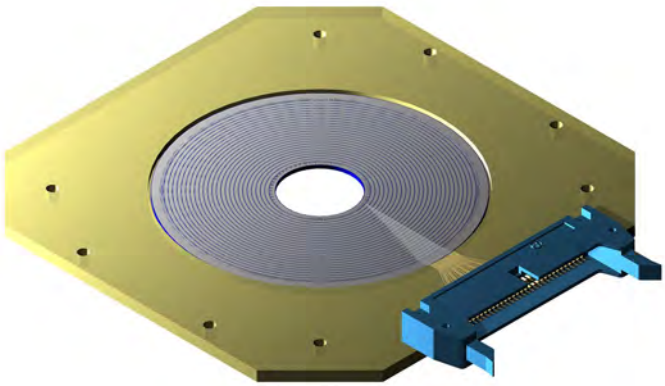

Figure 3.12: A schematic figure of the S3 detector employed for fission studies at ISS. Figure from [116].

attempts to extract the charge resolution also for fission fragments, were performed, see Section 3.9.4. Currently work on exploiting information from stored signal traces of these detectors during IS739 is ongoing as part of a Bachelor thesis project.

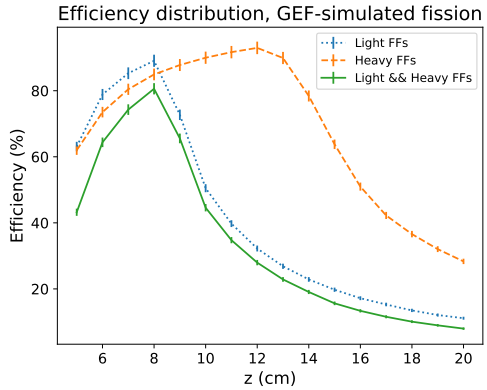

Figure 3.13: Geometric efficiency of the CD-shaped fission fragment detector at a beam energy of 8 MeV/u as a function of its distance from the target. The detector has inner and outer radii of 11 mm and 35 mm, respectively. The dotted blue line represents the efficiency of detecting only the light fission fragment, the dashed orange line corresponds to the efficiency of detecting only the heavy fragment, and the solid green line illustrates the efficiency for detecting both fission fragments in coincidence. Figure from Ref. [117].

By using a detector segmented into rings and sectors, it is possible to determine the difference in azimuthal angle between particles depositing energy in the detector on an event-by-event basis. For fission events, this difference should be 180°, since the fragments are emitted back-to-back in the compound nucleus frame, resulting in opposite transverse momenta.

The distance between the ΔE and E layers was set to 13.2 mm. In principle, a smaller separation would be preferable. However, due to mechanical constraints associated with mounting the detectors on the detector support structure, reducing this distance further would significantly complicate the mounting.

The S3 detectors exhibit significantly different dead-layer thicknesses on their front (junction) and back (ohmic) sides. The junction side, which is segmented into 24 rings, has a total dead-layer thickness of approximately 4.6 μm over most of the detector surface. In contrast, the ohmic side, which is segmented into 32 sectors, has a total dead layer thickness of approximately 0.7 μm. For this reason, it is preferable for the ohmic side of the S3 detectors to face the incoming particles, i.e. upstream. Thus, both layers were mounted in that configuration.

3.7.3 Detection of deuterons elastically scattered from the target

To extract the fission cross section as a function of excitation energy, it is necessary to determine the product of the beam intensity and the number of target particles per unit area. This quantity can be obtained using elastic scattering reaction of deuterons. By counting elastically scattered deuterons within a given angular range, the total fission yield can be normalised and the corresponding cross section extracted. To relate the number of detected deuterons to the product of beam intensity and target thickness, the elastic scattering differential cross-section as a function of scattering angle with respect to the beam axis, as well as the energy of the scattered deuterons in the ^{229}Ac + d reaction, were calculated using the LISE++ program [118]. The results are shown in Fig. 3.14.

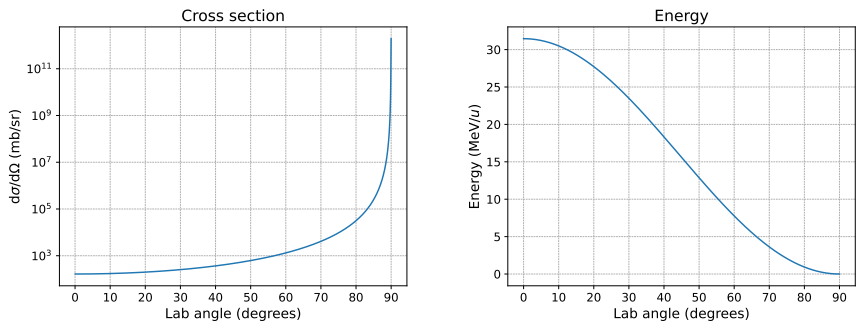

(a) (b)

Figure 3.14: (a) Calculated cross section of deuterons ejected from the target when ^{229}Ac of 8 MeV/u impinges as a function of the laboratory angle with respect to the beam axis. (b) Calculated energy of the scattered deuterons as a function of the laboratory angle with respect to the beam axis.

The elastic scattering cross-section noticeably increases for larger angles and diverges at 90°. At the same time, the kinetic energy of the scattered deuterons decreases with angle, approaching 0 MeV for angles close to 90°. In contrast, the energy reaches its maximum value of approximately 31 MeV at small forward angles near 0°. Deuterons emitted at angles very close to 90° have insufficient energy to escape the target material and therefore cannot be detected. On the other hand, deuterons emitted at very small angles, although highly energetic, cannot be detected because the unreacted beam propagates along the solenoid axis and overlaps with their trajectories. Additionally, the elastic scattering yield at very small angles is small. Therefore, a compromise configuration is

required that provides a sufficiently large scattering cross section while ensuring that the scattered deuterons have enough energy to be detected.

The standard configuration used at ISS to detect elastically scattered deuterons consists of an on-axis, CD-shaped silicon detector. The detector is shielded by an aluminium annulus and a tube passing through the centre of the annulus, as shown in Fig. 3.15. Consequently, particles can only reach the detector by passing around the outside of the shield, restricting detection to a narrow range of scattering angles. By changing the distance between the detector and the target, different angular ranges can be selected.

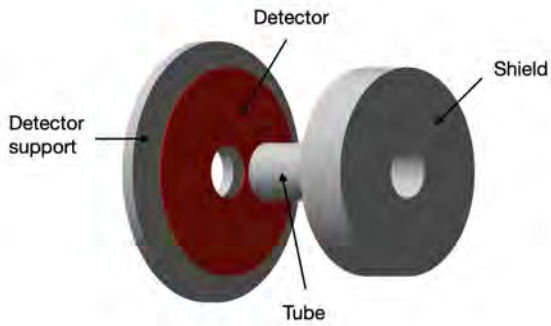

Figure 3.15: Schematic illustration of the standard luminosity detection setup for elastically scattered deuterons used at ISS (not to scale). The tube is during operation inside the detector, leaving no gap. The inner and outer radii of the detector are 24 mm and 48 mm, respectively.

Fig. 3.16 shows a configuration in which the luminosity detector is placed 12.5 cm downstream from the target, while the fission fragment detector is located 18 cm from the target. Example trajectories of detected deuterons are indicated, together with representative trajectories of light and heavy fission fragments. As illustrated in Fig. 3.16, placing the standard luminosity detector in front of the fission fragment detector is not feasible, as the fission fragments would collide with the luminosity detector. If the luminosity detector is instead placed downstream of the fission fragment detector, deuterons can be detected without disturbing the fission fragment trajectories, as demonstrated in Fig. 3.17. However, in such a configuration, only deuterons emitted at relatively small laboratory scattering angles can be detected, where the elastic scattering cross section is lower. A maximum efficiency of 0.36 % for all emit-

ted deuterons for this setup can be obtained when optimising the position of the luminosity detector. With the expected beam intensity, this would likely result in insufficient statistics.

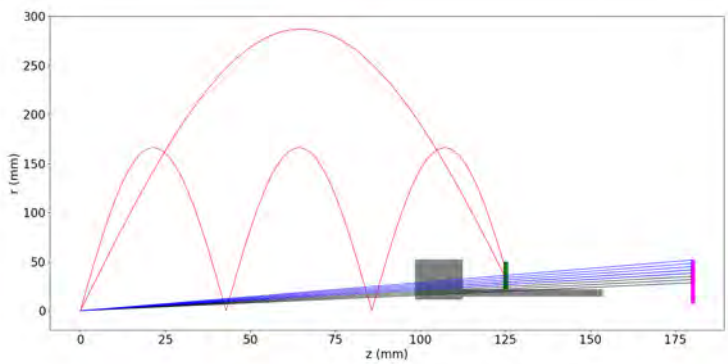

Figure 3.16: Schematic illustration of particle trajectories in the luminosity detection setup. The luminosity detector is shown in green, the shield and tube in gray, and the fission fragment detector (just one is depicted) in magenta. Example trajectories of detected deuterons are represented as red lines, while a few example trajectories of the light and heavy fission fragments are shown as blue and black lines, respectively. In this configuration, the fission fragments cannot reach the fission detector. The ordinate represents the transverse distance from the beam axis, r, while the abscissa is the distance along the beam axis, z.

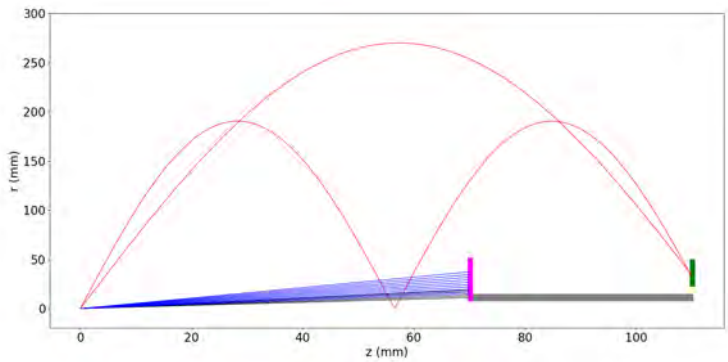

Figure 3.17: Similar to Fig. 3.16, but with the fission fragment detector (just one is depicted) placed in-between the luminosity detector and the target. Note: helical trajectories circulating around (x, y) passing through $(x, y) = (0, 0)$ and progressing in the z direction look like they are reflected when projected onto an r-z-plane.

To address this limitation, an alternative off-axis configuration has been proposed, using four position-sensitive[12] silicon detectors, as illustrated in Fig. 3.6. In this setup, the detectors are mounted parallel to the beam line, with an active area of 5 cm^2 oriented to face the beam axis. When positioned 2 cm downstream from the target and 3 cm off the beam axis, the efficiency for detecting elastically scattered deuterons reaches approximately 0.8 %. The efficiency map for this configuration, as a function of the off-axis distance and target distance from the target along the beam axis, is shown in Fig. 3.18. The efficiency is highest when the detectors are placed close to the target. However, positioning them too close is not feasible due to the presence of other detectors, the risk of blocking other reaction products, and possible transverse movements of the target holding structure itself.

As luminosity detectors, four resistive Si wafers were used. Each detector has dimensions of 10 mm $\times$50 mm, corresponding to the total active area of 5 cm^2. The thickness of each detector is 800 μm. The resistive Si detectors have the same design as the silicon sensors used in the HELIOS Si array. Each sensor is equipped three readout channels, which allow to reconstruct both the energy and hit position of the particle (see Section 2.4.4 for a detailed description), and is electrically bonded to a printed circuit board (PCB). The luminosity detectors are mounted on the same mechanical support structure as the fission fragment detectors to ensure good mechanical stability. The luminosity

[12] By using position sensitive detectors, it is possible to differentiate different particle species, as will be shown in Section 3.8.4.

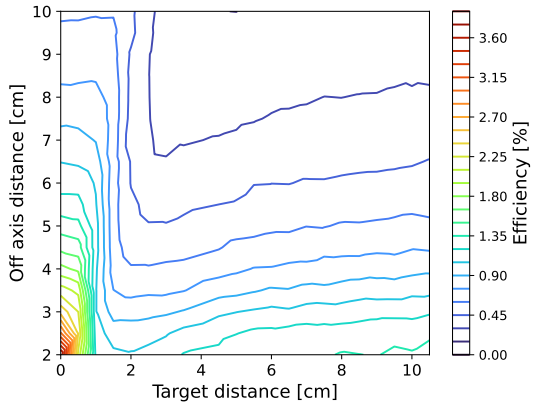

Figure 3.18: Efficiency map for a luminosity detector consisting of four position-sensitive silicon detectors mounted parallel to the beam-line, with the active surface oriented such that they face the beam axis, as a function of the off-axis distance and distance to the target plane. Figure from Ref. [117].

detectors mounted together with the fission fragment detectors are shown in Fig. 3.19. The distance between the edges of the luminosity detectors closest to the target and the target itself is 30 mm.

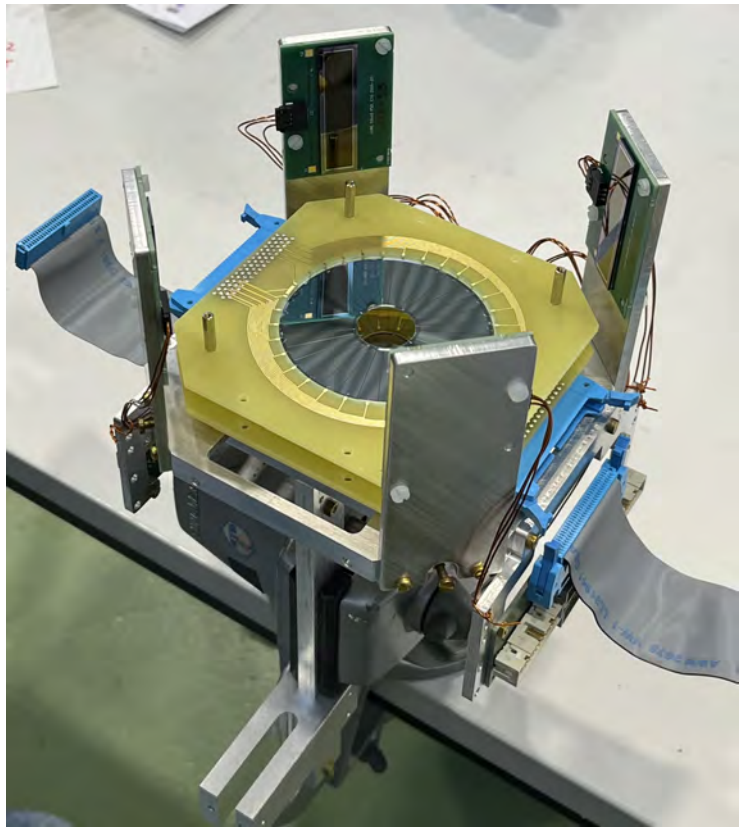

Figure 3.19: Photograph of the S3 and luminosity detectors mounted on the support structure.

3.7.4 Detection of γ rays

Due to the limited intrinsic energy resolution of the $CeBr_3$ crystals, combined with the high level density in the populated nuclei, it is not feasible to resolve and identify individual γ-ray transitions. Instead, a measurement of γ-rays is planned to acquire information on the total emitted γ-ray energy and multiplicity during fission. Such data are valuable for r-process simulations and may contribute to a better understanding of angular momentum generation in fission [119].

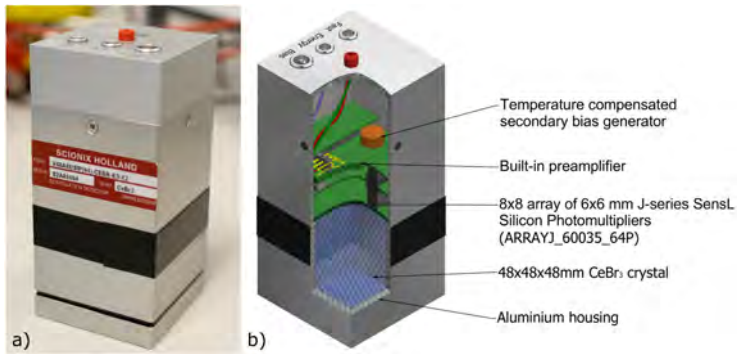

Figure 3.20: a) A single SpecMAT scintillation detector. b) The inner structure of the detector (CAD drawing). Figure from Ref. [80].

Detecting γ-rays in coincidence with (d,pf) reactions requires the use of γ-ray detectors capable of operating inside the vacuum vessel and within a strong magnetic field. The measurement was performed using $CeBr_3$ scintillation crystals from the SpecMAT detector [80], developed by the KU Leuven group. SpecMAT was designed as an active target, with $CeBr_3$ detectors placed in a cylindrical configuration around the active target.

Each detector unit consists of a $48 \times 48 \times 48$ mm^3 $CeBr_3$ crystal placed inside an aluminium housing. The aluminium housing has a thickness of 1 mm on the side facing the γ-ray window and 3 mm on the side walls. Each detector is equipped with a silicon photomultiplier, which allows using it in a strong magnetic field. A single detector and its inner structure are shown in Fig. 3.20.

However, the $CeBr_3$ detectors can also be used separately, and for this purpose, a dedicated mechanical support was constructed in which the crystals are arranged in 11 spokes, each containing three crystals, as shown in Fig. 3.21. The centre of the detector array is positioned 150 mm downstream of the target. In the following, this arrangement is referred to as the *original SpecMAT configuration*.

The SpecMAT scintillation array achieves a γ detection efficiency of approximately 2.5 % at an energy of 1 MeV [120] in the original SpecMAT configuration.

Since the primary interest of this measurement is the total γ-ray energy emitted by the fission fragments rather than the detection of individual γ lines, the main requirement is to maximise the solid angle coverage by the detector system.

Three detector geometries were considered:

- a box geometry with three rings (12 crystals per ring, 36 crystals total),
- a box geometry with two rings (16 crystals per ring, 32 crystals total),

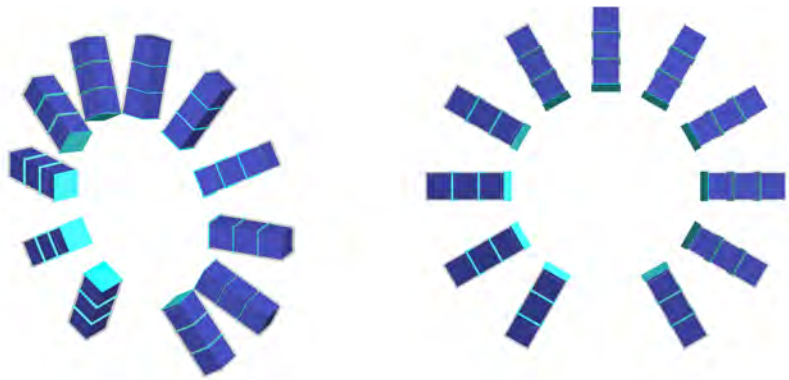

(a) (b)

Figure 3.21: The original SpecMAT configuration (11 spokes of 3 crystals). (a) Side view. (b) Face view.

- the original SpecMAT configuration (11 spokes of three crystals, 33 crystals total).

For the box geometries, two variants were studied: with and without overlap. The box with overlap aims to avoid γ rays escaping in the detector corners. In all cases, the box-shaped γ array is placed downstream of the target. Visualisations of the considered geometries are shown in Figs. 3.21 to 3.23.

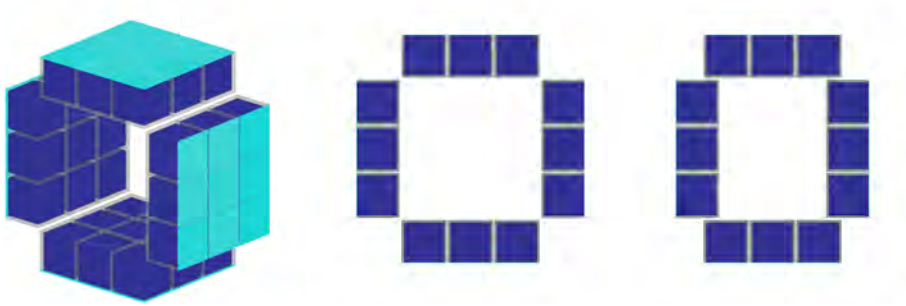

(a) (b) (c)

Figure 3.22: Box with 3 rings (12 crystals in each ring, for a total of 36). (a) Without overlap, side view. (b) Without overlap, face view. (c) With overlap, face view.

When a γ-photon interacts with matter, it may deposit energy in more than

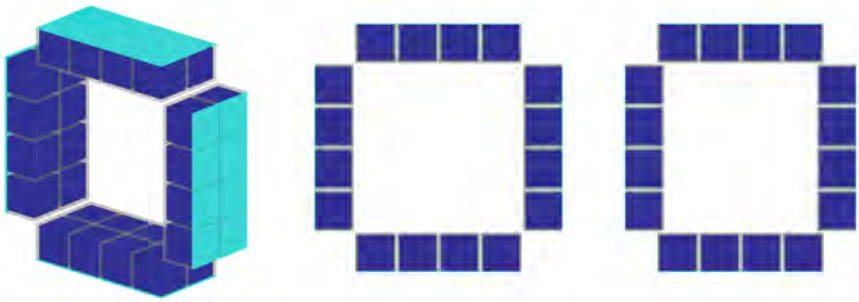

(a) (b) (c)

Figure 3.23: Box with 2 rings (16 crystals in each ring, for a total of 32). (a) Without overlap, side view. (b) Without overlap, face view. (c) With overlap, face view.

one detector crystal via Compton scattering. In such cases, the total energy of the original γ is the sum of the energies deposited in all involved crystals. The addback technique reconstructs this energy by summing coincident energy deposits. However, addback may also incorrectly combine signals originating from different γ rays.

As a first approximation, a simplified simulation was performed using `ggland` [121], a simulation wrapper for Geant4 [122], in which two fission fragments move downstream from the target and one of them emits a single γ with an energy between 0 and 10 MeV. The simplest possible addback scheme was applied by summing the energies deposited in all crystals.

Table 3.2 summarises, for each geometry, the fraction of detected events, the fraction of fully registered events (registered energy above 99 % of the original energy), the fraction of incompletely registered events (registered energy between 1 % and 99 % of the original energy), and the ratio of incomplete to fully registered events. All values are relative to the number of emitted γ rays and therefore represent primarily geometric efficiencies. Doppler effects are neglected in this comparison.

Geometry	Fraction of detected events	Fraction of fully registered events (> 99 %)	Fraction of incompletely registered events (1 % $- 99$ %)	Ratio of incomplete to complete events
orig. SpecMAT	0.045	0.0095	0.035	3.61
Box (3 rings, no overlap)	0.23	0.05	0.18	3.43
Box (3 rings, overlap)	0.24	0.06	0.18	3.28
Box (2 rings, no overlap)	0.145	0.032	0.113	3.50
Box (2 rings, overlap)	0.15	0.03	0.12	3.38

Table 3.2: Detection efficiency for different detector configurations assuming a single γ ray emitted by one fission fragment. All fractions are relative to the number of original γ rays. Due to geometric constraints, the two-ring box configuration with a photopeak efficiency of 3 % was selected.

As expected, the three-ring box configuration provides the highest detection efficiency. However, additional geometrical constraints must be considered. Each crystal has dimensions of 48 mm $\times$ 48 mm $\times$48 mm. In the three-ring configuration, the γ array would extend up to approximately 15 cm from the target along the beam axis, while the inner dimension of the array would be about 15 cm (or approximately 14 cm for the overlapping variant). In the present setup, two CD-shaped segmented silicon detectors with a diameter of about 14 cm (including active area and PCB support) are used for fission fragment detection and must be positioned approximately 8 cm from the target, thus inside the γ array. Considering that, the three-ring geometry does not provide sufficient clearance and is therefore not feasible.

In contrast, the two-ring configuration provides sufficient inner space to accommodate the fission fragment detectors as well as the off-axis luminosity detectors near the target.

The fraction of the reconstructed γ ray energy for the original SpecMAT configuration and the two-ring configuration is shown in Fig. 3.24. Events are sorted according to their reconstruction efficiency.

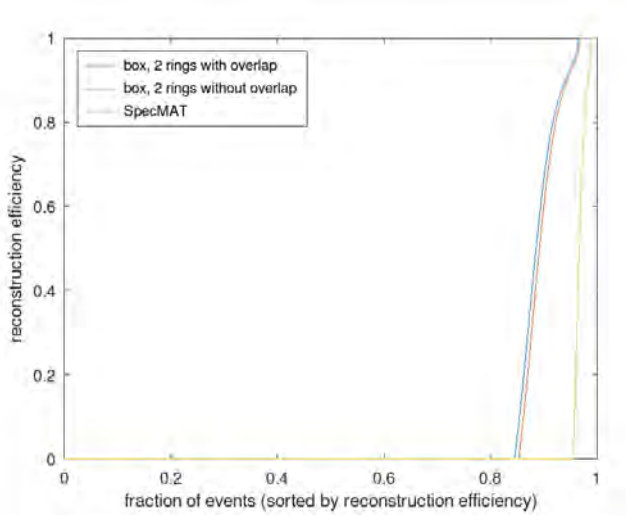

(a)

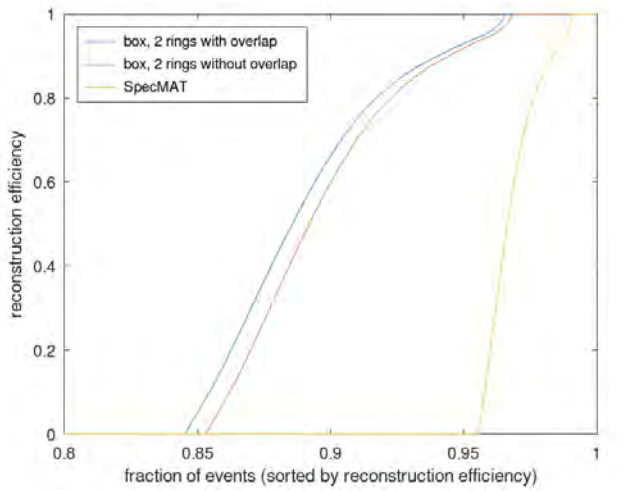

(b)

Figure 3.24: Detection efficiency for different configurations. The efficiency is calculated for each event as the registered energy divided by the originally emitted γ energy. The events are then sorted by efficiency. The top plot shows all events. On the bottom plot, the region with non-zero energy deposits is shown.

Ideally, a detector geometry would exhibit a long plateau near unity efficiency, corresponding to a large fraction of fully reconstructed γ rays.

The detector configurations were further compared using Doppler-corrected spectra, shown in Fig. 3.25. The following assumptions were used:

1. only crystals within the distance of at most two neighbouring crystals are included in a cluster, i.e., contributing to the addback,
2. the reconstructed γ-ray direction is obtained as an energy-weighted average of the included crystal positions,
3. Doppler correction is performed using the beam velocity and nominal beam direction, as the emitting fission fragment cannot be identified.

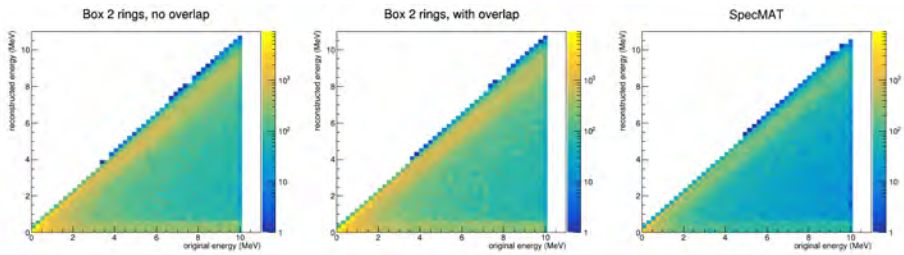

Figure 3.25: Doppler-corrected vs simulated γ energy for a box with 2 rings without and with overlap, and SpecMAT. Except for the total efficiency differences between the configurations, the Doppler-corrected energies are very similar.

Due to mechanical constraints, during the support of the $CeBr_3$ design, the selected two-ring design was modified to an overlapping geometry with four crystals above and below the beam axis and five crystals on each side in each ring. This modification enables a compact arrangement with identical inner dimensions in the vertical and horizontal directions.

Mounting the $CeBr_3$ detectors in the mechanical holder and subsequently installing it in the magnet proved to be challenging. The $CeBr_3$ holder consists of multiple aluminium components that must be assembled together. Brass screws were required, as the setup is intended to operate in a magnetic field up to 2.5 T. In addition, the ISS magnet must be sealed and pumped to provide a high-vacuum environment, which prohibits the use of plastic or other materials incompatible with vacuum conditions inside the magnet bore. Here brass was a cost-effective compromise, rather than the ideal material.

The lowest edge of the magnet bore is located approximately 120 cm above the floor, and the fully assembled $CeBr_3$ array, containing all 36 crystals, has a

total mass of about 30 kg. As a result, mounting and assembling all 36 crystals in the magnet was extremely challenging. The entire mechanical structure had to be inserted on rails inside the magnet and supported on a crescent-shaped supports, as the assembly was too heavy to be placed directly into the magnet without risking damage. Note that MRI magnets are not designed to carry weight. Patients are supported by mechanical structures outside of the magnet. This was not an option for experiments at ISS, where the ends of the magnet are covered by large flanges to achieve the needed vacuum.

For these reasons, the bottom row of detectors was not installed. This significantly reduced the total weight of the assembly and made the mounting procedure safer and more manageable. The $CeBr_3$ detector holder mounted inside the ISS magnet is shown in Fig. 3.26.

3.7.5 Beam monitors

As a beam monitor, a Faraday cup was used. It was placed downstream of the target, behind the $CeBr_3$ detector holder. The hollow centre of the fission fragment detector allowed the beam to pass through the entire setup and be collected in the Faraday cup. It was used to monitor the condition of the CD_2 targets and to check for possible beam-induced damage over time.

However, it was later realised in a subsequent experiment at ISS that the Faraday cup likely introduced additional background due to scattered beam particles. These scattered particles could reach detectors and contribute to structures observed in some of the spectra.

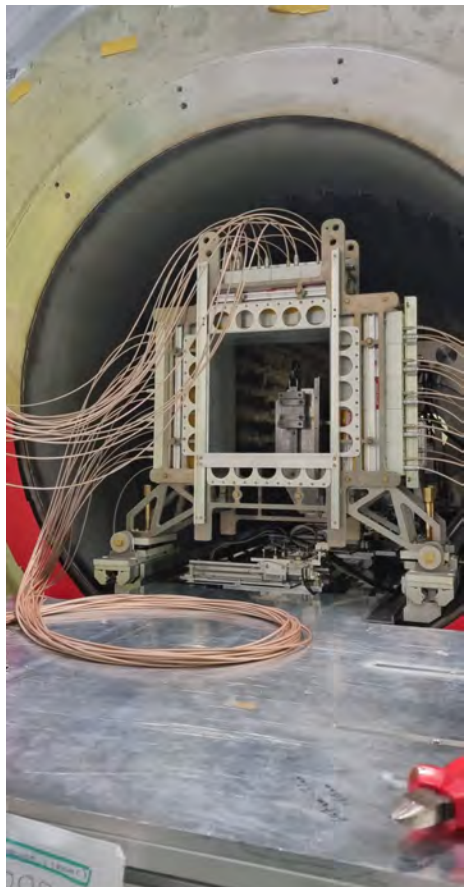

Figure 3.26: Photograph of $CeBr_3$ detector holder with detectors mounted inside the ISS magnet. A table used for mounting the support structure is visible in front of the magnet.

3.8 Stable beam commissioning

To verify the performance of the newly installed experimental setup, commissioning measurements were carried out using a stable beam in June 2025. This commissioning run served primarily to validate detector operation and resolution, data acquisition, and basic event reconstruction under realistic experimental conditions, rather than to perform a complete physics analysis.

Stable beam commissioning at ISOLDE is performed without the use of protons from the PS Booster. Instead, ions already present as buffer gas in the EBIS, or gases intentionally injected into the EBIS trap, are extracted and accelerated. This strongly constrains the choice of available isotopes and limits the mass range to relatively light nuclei. Consequently, the range of reactions accessible during commissioning is restricted.

For this commissioning, a ^{22}Ne beam with a charge state of 7^+ and at an energy of 6 MeV/u was used. The beam impinged on a secondary CD_2 target located inside ISS, with a thickness of 549 μg/cm^2. The extracted beam also contained contaminants with the same mass-to-charge ratio (A/q) originating from the EBIS buffer gas.

A critical operational constraint of ISS is the requirement to maintain a high vacuum inside the spectrometer. In order to protect the HIE-ISOLDE accelerating cavities, the beam line can only be opened to the experimental setup if the pressure inside the ISS is below 8×10^{-7} mbar. Achieving such a high vacuum in a chamber the size of the ISS (a decommissioned MRI magnet) requires a long pumping period. Reaching the required vacuum takes on the order of two weeks for an ISS experiment with a similar large number of components as in this work. Pumping starts with a mechanical roughing pump, followed by pumping phases with a turbo-molecular pump and a cryogenic pump. The alternating use of turbo and cryogenic pumps is necessary to remove different types of contaminants, as the turbo pump effectively removes residual atmospheric gases such as nitrogen and oxygen, while the cryogenic pump is particularly effective at trapping water vapour. For IS739 a key challenge was the outgassing from the $CeBr_3$ detectors, including their electronic components.

Because opening the magnet, modifying the setup, and re-establishing high vacuum is extremely time consuming, the stable beam commissioning was carried out with the experimental configuration already installed and positioned exactly as planned for the subsequent IS739 experiment. Provided that the detectors operated as expected, this strategy avoided the need to open the magnet after commissioning and repeat the pumping procedure. As a consequence, once the commissioning began, no mechanical changes to the setup were possible.

The stable beam commissioning took place in early June 2025, approximately one month before the scheduled IS739 experiment. Due to this tight timeline and the operational constraints described above, the analysis presented is limited in scope. Only a small number of representative spectra and correla-

tions are shown to demonstrate the basic functionality and performance of the detectors and data acquisition chain. A comprehensive physics analysis has not been pursued at this stage.

The recoils from the ^{22}Ne(d, p)^{23}Ne reaction have very small laboratory opening angles. As a result, the ^{23}Ne recoils pass through the central opening of the fission $\Delta E - E$ telescope. This behaviour is illustrated in Fig. 3.27, which shows the reaction kinematics inside the 2 T magnetic field of ISS. Even if a different stable beam had been available, coincidences between the recoils detected in the fission telescope and the protons detected in the Si array would remain difficult to achieve for (d, p) reactions due to inherently small recoil angles and the fixed distance between the fission detector and the target.

Nevertheless, other reaction channels remain open during commissioning. Particles from these channels are expected to be detected in the fission detectors, while deuterons elastically scattered from the target are observed in the luminosity detectors. In addition, γ rays emitted following nuclear reactions can be detected with the $CeBr_3$ array.

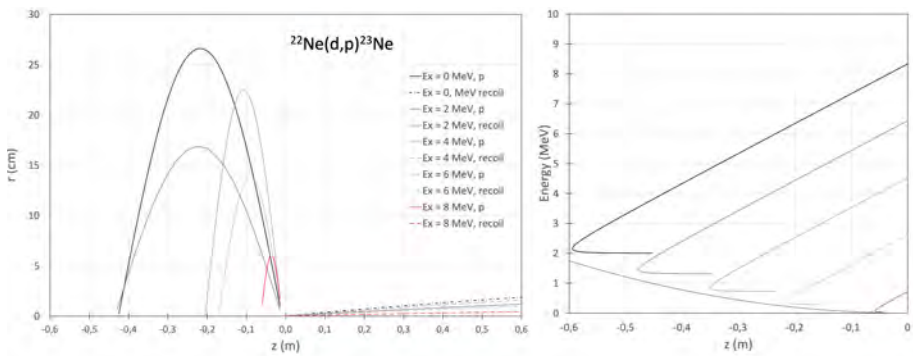

Figure 3.27: Kinematics of the ^{22}Ne(d, p)^{23}Ne reaction in a 2 T magnetic field inside ISS. The left panel shows the trajectories of recoiling ^{23}Ne nuclei (dashed lines) and ejected protons (solid lines) for different excitation energies. Due to the small opening angle of the recoils they pass through the central opening of the detector rather than intersecting the active area. The right panel shows the proton kinetic energy E versus the hit position z for protons emitted for different excitation energies of the formed ^{23}Ne recoils.

Experimental data were sorted using ISSSort [123], a data-sorting framework for ISS that converts raw detector signals into ROOT format for further analysis. The plots shown in the following sections were produced using this software.

3.8.1 The Si array

Figure 3.50 shows the detected energy of the ejectiles plotted against their distance of return to the solenoid axis relative to the target (E vs z plot). Reactions with carbon nuclei in the CD_2 target were not subtracted in this plot. The plot includes data from a single run of approximately three hours, with no software cuts applied. Several diagonal structures are visible. The uppermost band corresponds to the population of the ground state in ^{23}Ne, while the lower loci correspond to the population of excited states.

In addition, a faint structure is visible that bends in the opposite direction to the loci associated with excited states in ^{23}Ne. Although the origin of this structure is not fully understood, it is believed to originate from beam particles scattered from the Faraday cup located downstream of the target, behind the fission detectors and the $CeBr_3$ array. The Faraday cup was needed during the experiment to monitor the target integrity, i.e. that the target had not been degraded due to beam-induced damage.

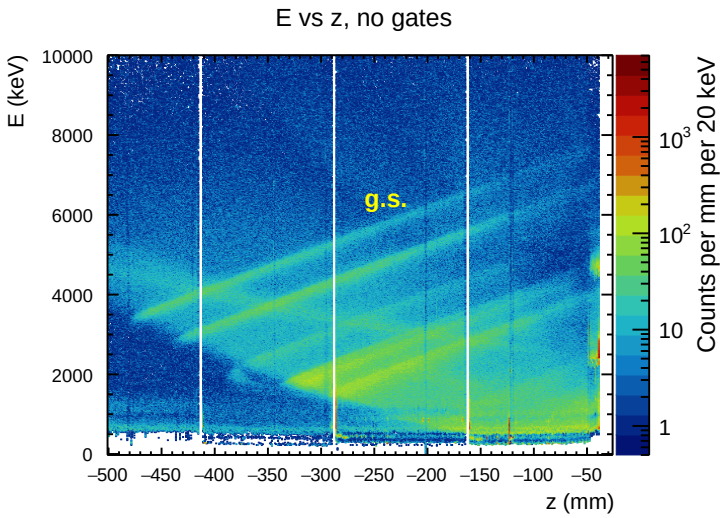

Figure 3.28: Energy of the ejectiles detected in the Si array versus their hit positions relative to the target for the stable ^{22}Ne beam. No C subtraction was performed in this spectrum. No software gates have been applied. The uppermost locus, marked as "g.s." in the figure, corresponds to population of the ground state of ^{23}Ne.

The corresponding excitation energy spectrum is shown in Fig. 3.51. Even without any software cuts, clear structures are visible in the spectrum, corresponding to excited states in ^{23}Ne, listed in Table 3.3. It should be noted that the energy calibration of the Si array was performed using calibration coefficients obtained during a previous experimental campaign. As a result, calibration of the extracted excitation energy is not perfect. New calibration data were collected after the IS739 experiment was completed and used for the analysis of data based on reactions of unstable beam ions.

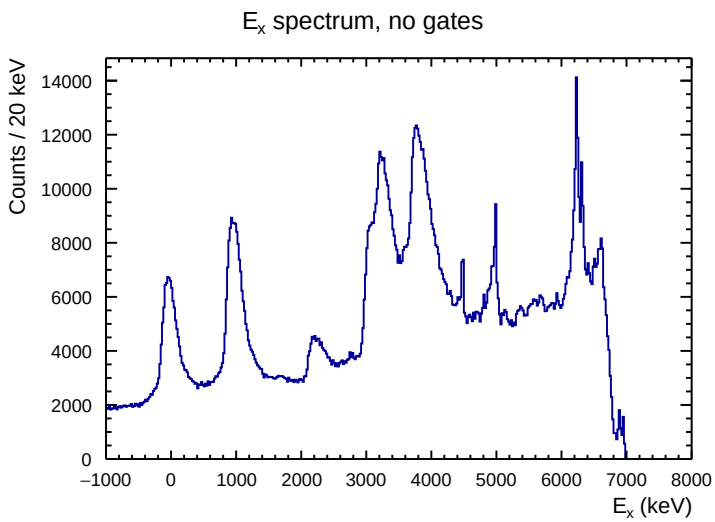

Figure 3.29: Excitation energy spectrum obtained with the ^{22}Ne beam with no software gates applied. No C subtraction was performed in this spectrum. Several peaks are clearly visible, although a significant amount of background is present. The first two prominent excited states are believed to correspond to excitation energies of 1.018 MeV and 2.314 MeV.

E (level) (MeV)	J^π	ℓ	SF
0.000		2	0.23
1.018	$1/2^+$	0	0.39
1.703			
1.826		2	0.023
2.314	$5/2^+$	2	0.07
2.520			
3.218	$3/2^-$	1	0.73
3.433	$3/2^+$	2	0.38
3.836	$1/2^-$	1	0.14
3.988	$(3/2)^+$	2	0.32
4.270			
4.431			
4.764			
4.867			
4.940			
4.995			

Table 3.3: Energy levels in ^{23}Ne populated via the ^{22}Ne(d, p)^{23}Ne reaction up to 5.0 MeV. Spin and parity (J^π), transferred angular momentum (ℓ), and spectroscopic factors (SF) are indicated where available. Data from [124].

3.8.2 Performance of the fission fragment detectors

Figure 3.52 shows the energy loss in the ΔE detector plotted versus the residual energy deposited in the E layer (the $\Delta E - E$ spectrum). Distinct loci corresponding to different particle species can be identified, reflecting their characteristic energy-loss behaviour in the silicon telescope. Different elements have been identified using the energy needed for penetration of the ΔE detector from SRIM [125] and are labelled in the plot.

The energies are plotted using the energy information from the sectors of the DSSSDs. The fission fragment detectors were calibrated using four α-emitting radionuclides: ^{148}Gd, ^{239}Pu, ^{241}Am, and ^{244}Cm. The corresponding α-particle energies are listed in Table 3.4.

Radionuclide	α-particle energy (keV)
^{148}Gd	3182.69 ± 0.02
^{239}Pu	5148.31 ± 0.34
^{241}Am	5478.62 ± 0.14
^{244}Cm	5795.04 ± 0.05

Table 3.4: Table of α-particle energies used for calibration. Data from Ref. [32].

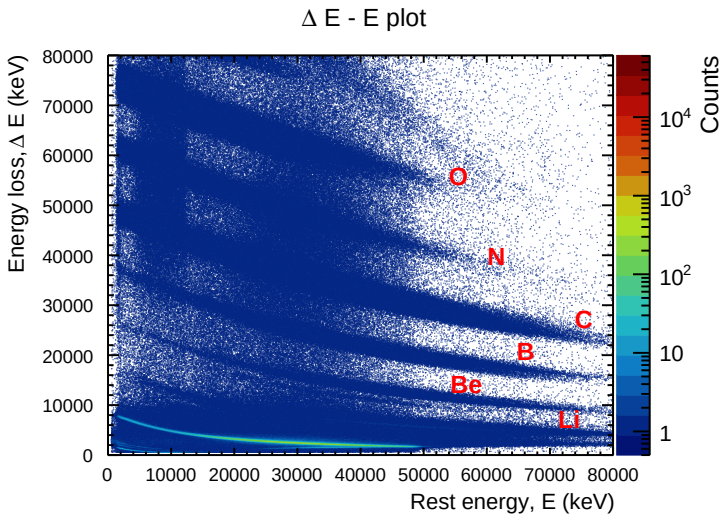

Figure 3.30: $\Delta E - E$ spectrum measured with the fission fragment telescope during the stable-beam commissioning. The energy loss in the ΔE layer is plotted as a function of the residual energy deposited in the E layer. Distinct bands corresponding to different particle species are visible.

Figure 3.31 shows the same spectrum, zoomed in on the lower-energy region. The most intense locus exhibits a characteristic 'punch-through' behaviour: particles with sufficient energy traverse the ΔE detector, depositing only a limited amount of energy in it, while the remaining energy is deposited in the E detector. Eventually, they punch through the E layer as well, and the signal in the E detector decreases as it is no longer stopping the particle. This produces the characteristic "hook" shape in the $\Delta E - E$ spectrum, with the tip of the hook corresponding to the maximum energy that can be deposited in the ΔE layer before punch-through occurs.

Given the thickness of the ΔE detector, the punch-through energy observed in this locus is consistent with α particles, allowing this band to be identified as α radiation emitted from the reactions of the beam and the target. The lower-lying loci, which are also clearly visible above the background, correspond to lighter charged particles such as protons, deuterons, and tritons, ordered from bottom to top according to increasing mass and charge.

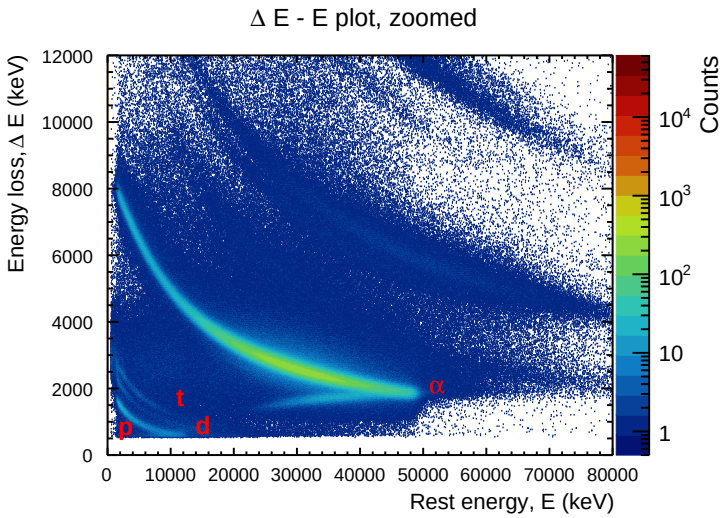

Figure 3.31: Zoomed-in view of the $\Delta E - E$ spectrum shown in Fig. 3.52. The prominent hook-shaped locus corresponds to α particles undergoing punch-through in the ΔE detector. Lower loci correspond to protons, deuterons, and tritons.

The hit pattern (hit map) of the ΔE detector is shown in Figure 3.32. This distribution reflects the angular acceptance of the ΔE detector: most particles are detected close to the inner radius of the detector, corresponding to small polar angles with respect to the beam axis. This observation is consistent with the strong forward focusing of reaction products at the beam energy used during the commissioning run.

The energy deposited in each azimuthal sector and radial ring is shown in Figs. 3.33 and 3.34 for the ΔE detector, and in Figs. 3.35 and 3.36 for the E detector. These distributions provide a consistency check of the detector response and segmentation, and illustrate the variation of the detected energy as a function of the scattering angle.

For the ΔE detector, the energy distribution across azimuthal sectors (Fig. 3.33) is approximately uniform. This is expected from the reaction kinematics, as no preferred azimuthal angle is expected. In contrast, the energy distribution as a function of radial ring number (Fig. 3.34) shows that rings with lower numbers (i.e. rings closer to the central opening of the detector) register more events and higher deposited energies. This behaviour is consistent with forward focused reaction products, which are emitted at small laboratory angles and therefore deposit more energy in the inner rings.

The response of the E detector differs significantly. As shown in Figure 3.35,

approximately 20 azimuthal sectors register energies that are significantly higher than the rest of the detector, with a pronounced accumulation of events around 120 MeV. Although the origin of this structure has not been conclusively identified, it is believed to arise from beam particles back-scattered from the Faraday cup. The Faraday cup is located downstream of the target, behind the fission fragment detectors and the $CeBr_3$ array, and scattered beam particles can therefore reach the E layer of the telescope. Such particles are not registered in the ΔE detector because they are stopped in the E layer.

The energy distribution as a function of radial ring number in the E detector (Fig. 3.36) is relatively uniform, with the exception of the innermost ring (ring number 0). This ring registers a significantly higher number of events and higher deposited energies. This behaviour is attributed to the fact that the innermost ring is not fully shielded by the ΔE detector, unlike the other rings. As a result, strongly forward focused reaction products can bypass the ΔE layer and are detected only in the E layer.

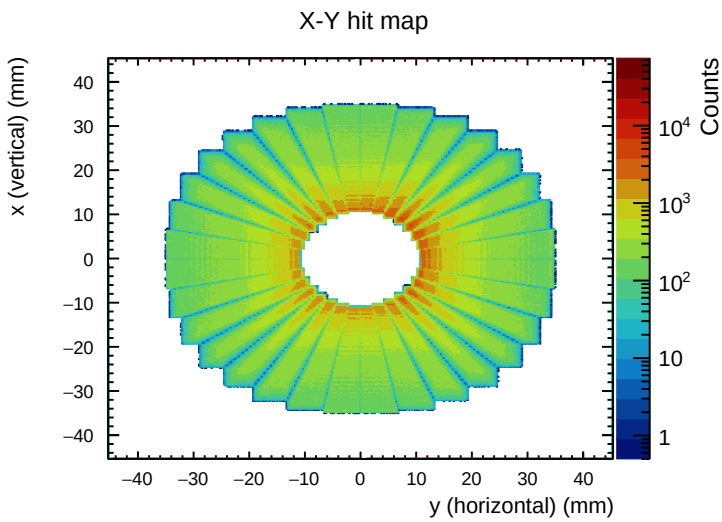

Figure 3.32: Hit map of the ΔE detector during the stable-beam commissioning run. The colour scale represents the number of detected events. The concentration of hits near the inner radius reflects the forward-focused emission of reaction products.

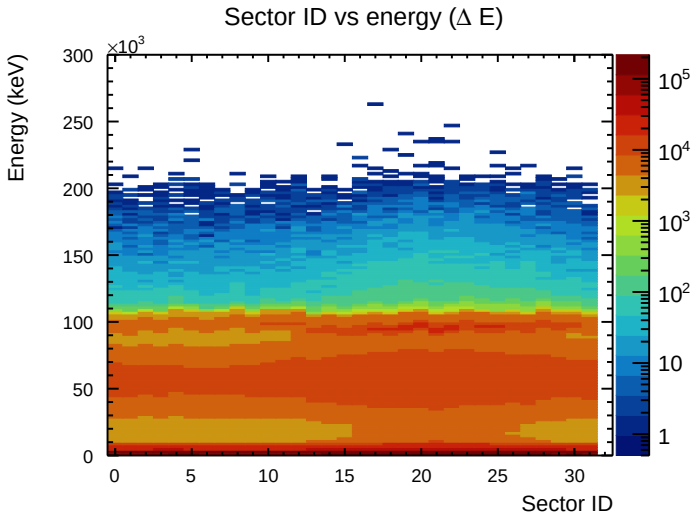

Figure 3.33: Energy deposited in the ΔE detector as a function of azimuthal sector number. Due to the symmetry of the detector, the energy deposition is expected to be similar for all sectors.

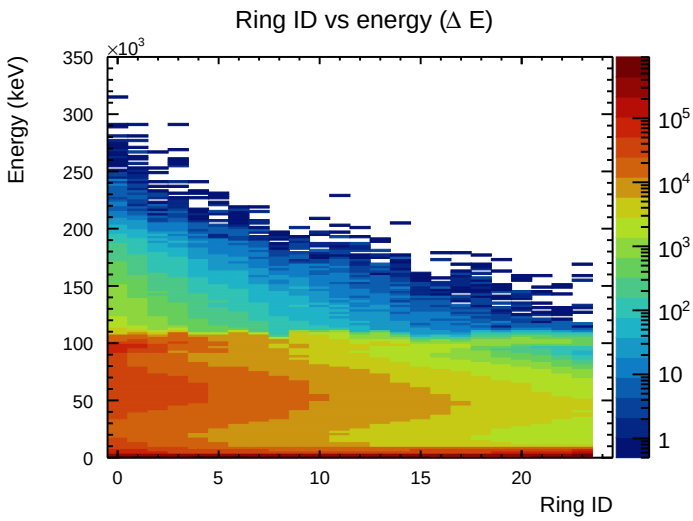

Figure 3.34: Energy deposited in the ΔE detector as a function of radial ring number. The variation reflects the angular dependence of the particle energies.

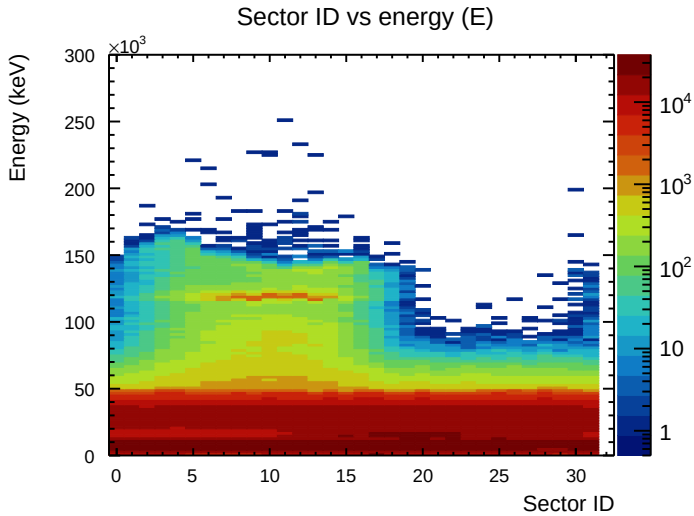

Figure 3.35: Energy deposited in the E detector as a function of the azimuthal sector number.

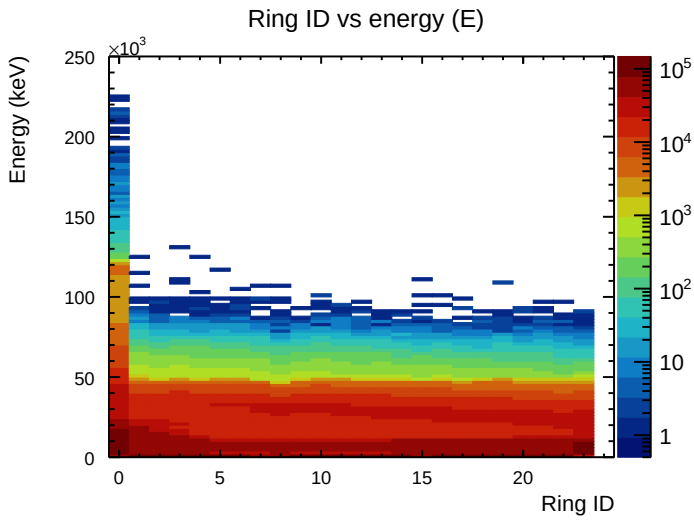

Figure 3.36: Energy deposited in the E detector as a function of the radial ring number.

3.8.3 The $CeBr_3$ detector array

Figure 3.37 presents the γ-ray energy spectrum measured with the $CeBr_3$ detector array, gated on any event in the Si array. Several peak-like structures are visible.

The $CeBr_3$ array was calibrated using a ^{60}Co γ-ray source, which emits two well-defined γ-ray lines at 1173.2 keV and 1332.5 keV.

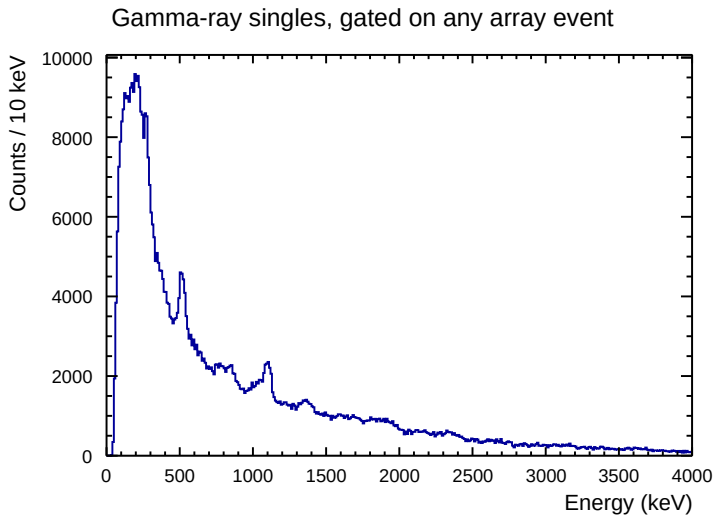

Figure 3.37: Measured γ-ray spectrum with the $CeBr_3$ detector array in coincidence with any event in the Si array.

For the present analysis, three states in ^{23}Ne were considered: the ground state and two excited states at 1.018 MeV and 2.314 MeV. By applying graphical cuts on these states in the Si-array E vs z spectrum and requiring a coincidence with a $CeBr_3$ event, the corresponding γ-rays depopulating these states could be isolated. The applied cuts are shown in Fig. 3.38.

The resulting γ-ray spectra gated on the ground state (cut 0), the 1.018 MeV state (cut 1), and the 2.314 MeV state (cut 2) are shown in Fig. 3.39, from top to bottom. In the spectrum corresponding to cut 1, a peak is observed at an energy of approximately 1.1 MeV.

This is consistent with the de-excitation of the first excited state at 1.018 MeV, taking into account Doppler-shift effects due to the velocity of the emitting recoil. A simple estimate of the Doppler shift can be obtained as follows. The recoil velocity of ^{23}Ne from the $^{22}\mathrm{Ne(d,p)}^{23}$Ne reaction can be approximated from its kinetic energy:

$$\frac{1}{2}mv^2 \approx E_{\text{kin}},$$

where m is the mass of ^{23}Ne and E_{kin} its kinetic energy. Assuming the proton takes a negligible fraction of the kinetic energy, we have $E_{\text{kin}} \approx 6\ \text{MeV}/u \cdot 23\ u$, giving

$$v \approx \sqrt{\frac{2\ E_{\text{kin}}}{m}}c \approx 0.11c, \quad \beta = v/c \approx 0.11.$$

The non-relativistic Doppler-shifted γ energy is then

$$E_\gamma \approx E_\gamma^0(1 + \beta\cos\theta),$$

where θ is the angle between the recoil velocity and the detector. Assuming the γ is detected near the centre of the $CeBr_3$ detector array, with a distance of 12 cm from the target, a detector radius of 10 cm, and $\cos\theta = 0.83$, results in

$$E_\gamma \approx 1.110\ \text{MeV},$$

in agreement with the observed peak.

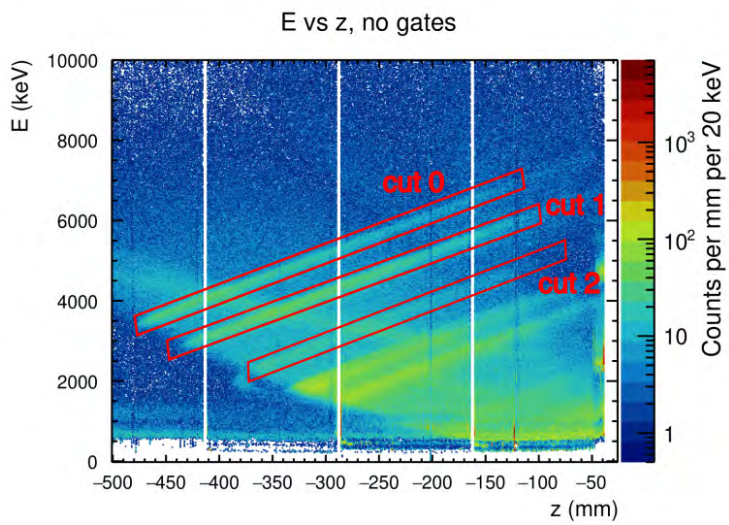

Figure 3.38: The E vs z plot for the Si array with marked graphical cuts on the ground state ("cut 0"), the 1.018 MeV state ("cut 1"), and the 2.314 MeV state ("cut 2").

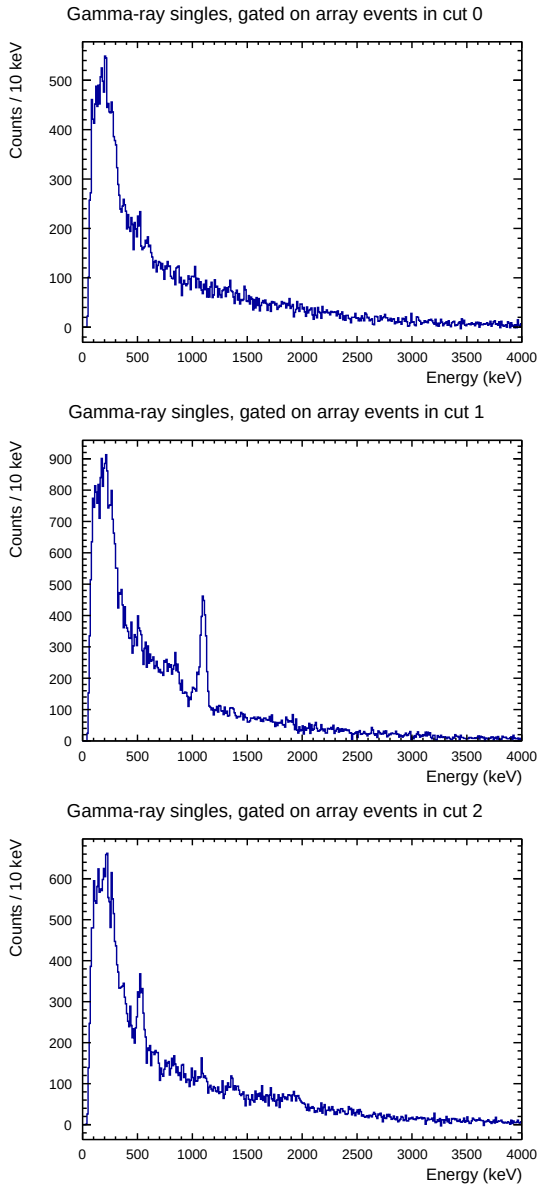

Figure 3.39: γ-ray energy spectra measured with the $CeBr_3$ detector array in coincidence with Si-array events gated on the ground state (top), the 1.018 MeV state (middle), and the 2.314 MeV state (bottom) in ^{23}Ne.

3.8.4 Luminosity detectors

Fig. 3.40 shows simulations of the response of the luminosity detectors (LUMEs) performed using `ggland` [121], a simulation wrapper for Geant4 [122]. The simulations include deuterons elastically scattered from the target (d), inelastically scattered deuterons (d'), and protons (p). When the deposited energy is plotted as a function of the hit position in relative units, where values close to -1 or $+1$ correspond to the longitudinal edges of the detector, these different particle species form distinct loci and can be clearly separated.

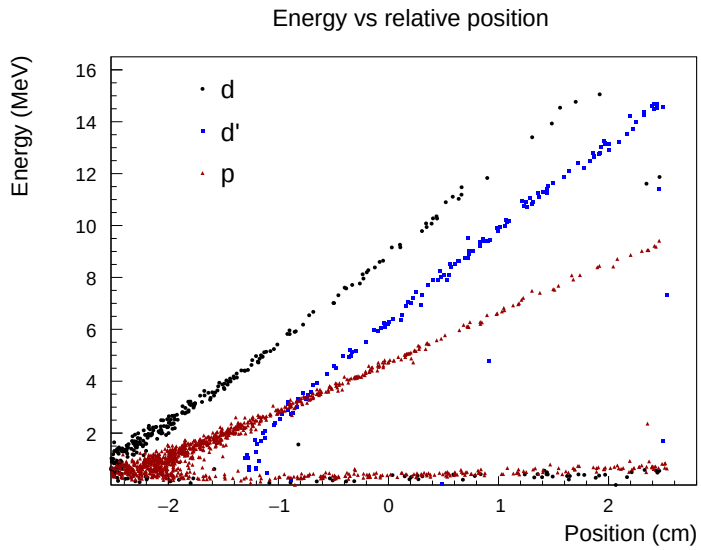

Figure 3.40: Simulated energy versus position along the detector spectra for the interaction of a ^{22}Ne beam with a CD_2 target at a beam energy of 6 MeV/u. The different structures correspond to elastically scattered (d), inelastically scattered deuterons (d'), and protons (p). Simulations are taken from Ref.[117].

Energy spectra recorded by the LUME detectors during the stable beam commissioning are shown in Fig. 3.41. The energy is not calibrated, and values on the energy axis correspond to digitiser channels. The corresponding energy versus position spectra are shown in Fig. 3.42. The position is given in relative units, where values close to -1 or $+1$ indicate hits near the longitudinal edges of the detector.

During the stable-beam commissioning, only three out of the four luminosity detectors were operational for the entire time, as one of the detectors malfunctioned during the last night of the commissioning and could not be used.

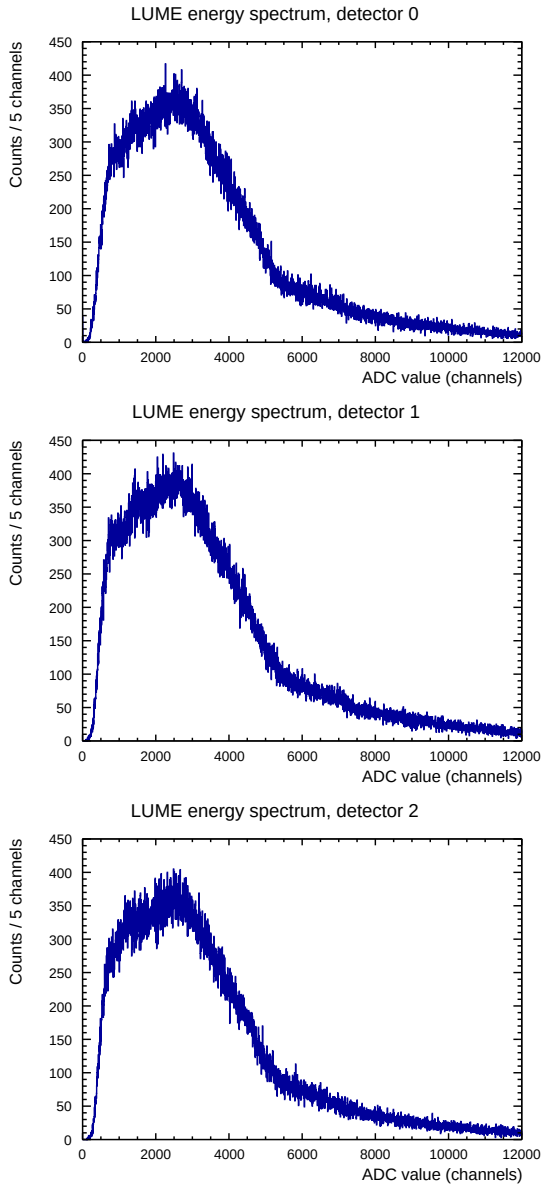

Figure 3.41: Uncalibrated energy spectra measured with the three operational LUME detectors during the stable-beam commissioning. The horizontal axis is given in units of digitiser channels.

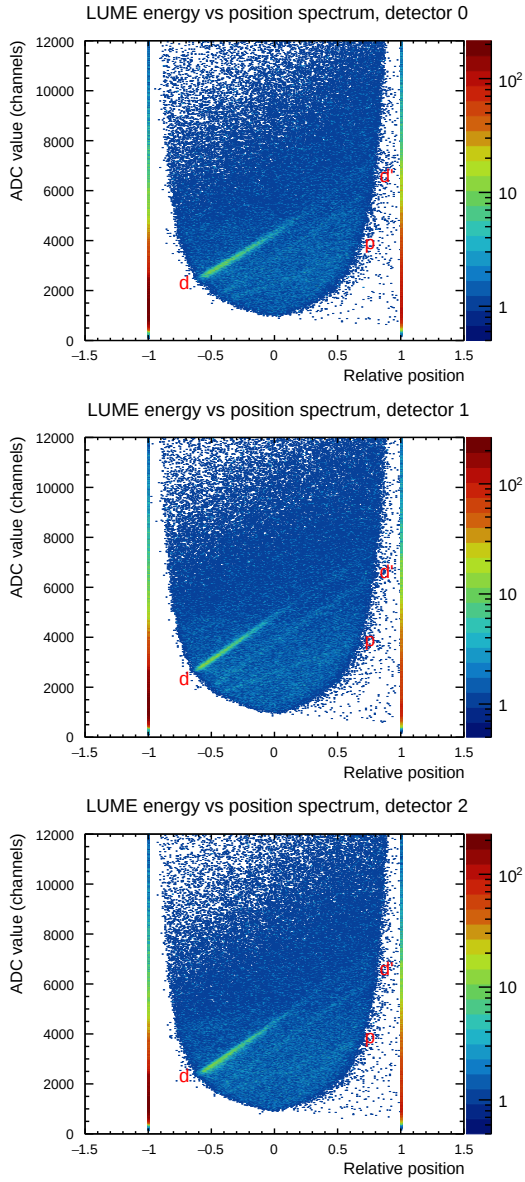

Figure 3.42: Uncalibrated energy versus relative position along the detector for LUMEs. Distinct bands correspond to elastically scattered deuterons (d), inelastically scattered deuterons (d'), and protons (p) (see Fig. 3.40).

3.8.5 Stable beam commissioning summary

With the exception of one LUME detector, all detectors operated as expected and exhibited satisfactory energy resolution. The commissioning demonstrated that the setup was fully operational and ready for the IS739 experiment.

3.9 The IS739 Experiment

With the experimental setup successfully commissioned using a stable ^{22}Ne beam one month before, the IS739 experiment was conducted in July 2025. During the beam time, several technical challenges were encountered.

The first issue was the very low intensity of the radioactive ^{229}Ac beam. The beam in difluoride form, $^{229}AcF_2$, originally planned for the experiment, was found to saturate the HIE–ISOLDE trap, likely due to contaminants in the beam. Switching to the monofluoride form reduced this problem but resulted in production yields that were too low for meaningful measurements. For this reason, the ISOLDE target group recommended and we decided to replace the thorium carbide (ThC_x) primary target, produced specifically for IS739, with a previously used uranium carbide (UC_x) target in the hope of achieving higher ^{229}Ac yields.

After switching to the UC_x target, the ^{229}Ac yield remained insufficient, making it impossible to study the fission of ^{230}Ac as originally planned. To make use of the allocated beam time, an alternative beam was selected, and ^{232}U was chosen to continue the experiment.

3.9.1 Switching from ^{229}Ac to ^{232}U beam

The selection of a ^{232}U beam was motivated by several considerations. First, it has a high production yield with the UC_x primary target. Moreover, with a half-life of 68.9 years, previously produced ^{232}U can be extracted from the target without the use of protons from the PS Booster, although with a reduced yield compared to proton irradiation.

The neutron separation energy of ^{233}U, populated via the $^{232}U(d,p)^{233}U$ reaction, is $S_n = 5.76$ MeV [32], which exceeds its predicted fission barrier, $B_f = 4.34$ MeV [109]. Consequently, the compound nucleus is energetically able to preferentially undergo fission before the neutron evaporation channel opens. In addition, the first-chance fission probability of ^{233}U, $P_f \approx 90$ %, is significantly higher than that of ^{230}Ac, which is predicted to be only about 3 % [109].

Historically, ^{233}U was discovered in 1947 [126], with its first fission cross-section estimates reported in 1953 [127]. While several datasets exist on ^{233}U fission at lower excitation energies, including [128–130], none have investigated the $^{232}U(d,pf)$ reaction. Therefore, the IS739 represents the first measurement of fission following the (d, p) reaction on ^{232}U.

It is important to note that during stable beam commissioning, no direct coincidences between the fission fragments detectors and the Si array were observed due to the small laboratory opening angle of the recoiling ^{23}Ne nucleus. In the IS739 experiment, however, measuring these coincidences is essential for the extraction of the fission barrier.

During the experiment, all detectors operated as expected, with the exception of two LUME detectors. In addition to the one detector that failed during the commissioning experiment, one more failed prior to IS739. Those two detectors remained unbiased throughout IS739.

The analysis of the IS739 experiment is ongoing at the time of writing this thesis. Therefore, no conclusive physics results are presented in this part of the thesis.

3.9.2 Energy calibration of the ISS Si array

Similarly to the fission detector, the ISS Si array was energy calibrated using the same source containing four α-emitting radionuclides: ^{148}Gd, ^{239}Pu, ^{241}Am, and ^{244}Cm. The corresponding α-particle energies are listed in Table 3.4.

The calibration was performed using the autocalibration routine implemented in ISSSort. In this procedure, four prominent peaks are first identified in the raw ADC spectrum among possible peaks and associated with the known α-particle energies. Based on the centroid positions of these peaks in ADC units, a linear calibration function (gain and offset) is determined. Each p-side and n-side strip of the array is calibrated individually to account for channel-to-channel variations in response.

The workflow of the autocalibration procedure is illustrated in Figs. 3.43, 3.44, 3.45 and 3.46, where, as an example, module 0, ASIC 0, channel 45 is shown (for details on the electronic mapping, see Fig. 3.8).

Figure 3.43 shows the initial identification of candidate peaks in the uncalibrated energy spectrum. Figure 3.44 presents the four selected peaks corresponding to the known α-particle energies. The selection is performed based on the amplitudes of the peaks. Figure 3.45 displays the fitted energy spectrum, where each peak is described by a Gaussian function; the extracted fit parameters are shown in the panel on the left. Finally, Fig. 3.46 shows the resulting linear calibration curve together with the residuals, which provide a measure of the quality of the calibration fit.

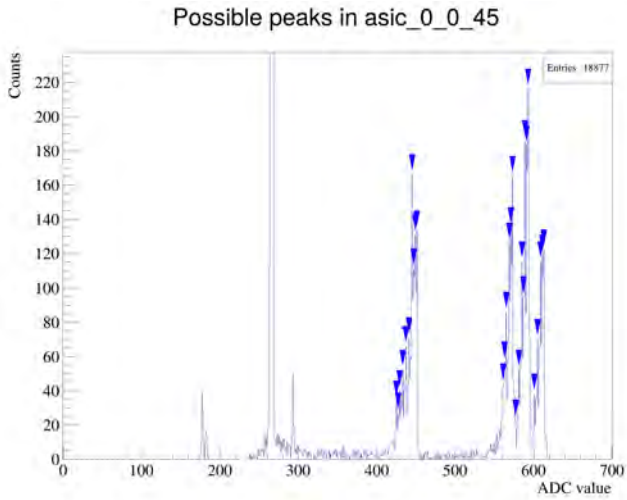

Figure 3.43: Initial peak search in the uncalibrated ADC spectrum for module 0, ASIC 0, channel 45. Multiple candidate peaks are identified before associating them with known α-particle energies.

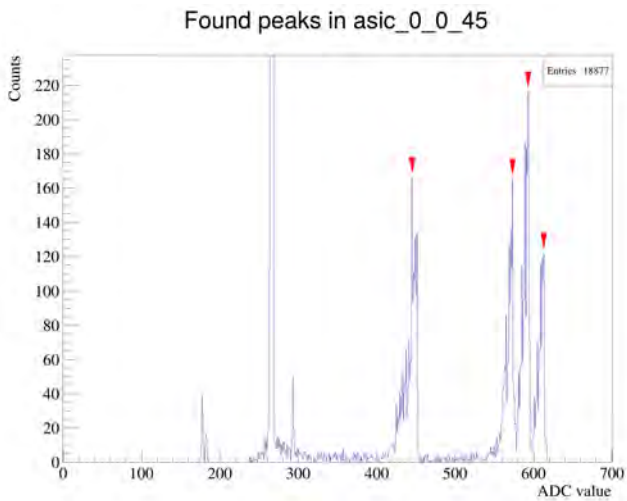

Figure 3.44: Final selection of the four peaks corresponding to the α-particle energies from ^{148}Gd, ^{239}Pu, ^{241}Am, and ^{244}Cm used for calibration of the selected channel.

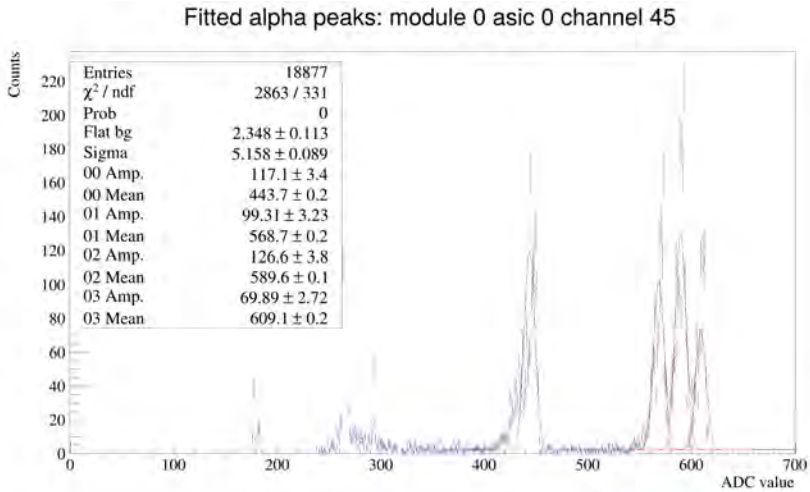

Figure 3.45: ADC spectrum for module 0, ASIC 0, channel 45 with Gaussian fits applied to the four calibration peaks. The fitted centroids are used to determine the linear energy calibration parameters.

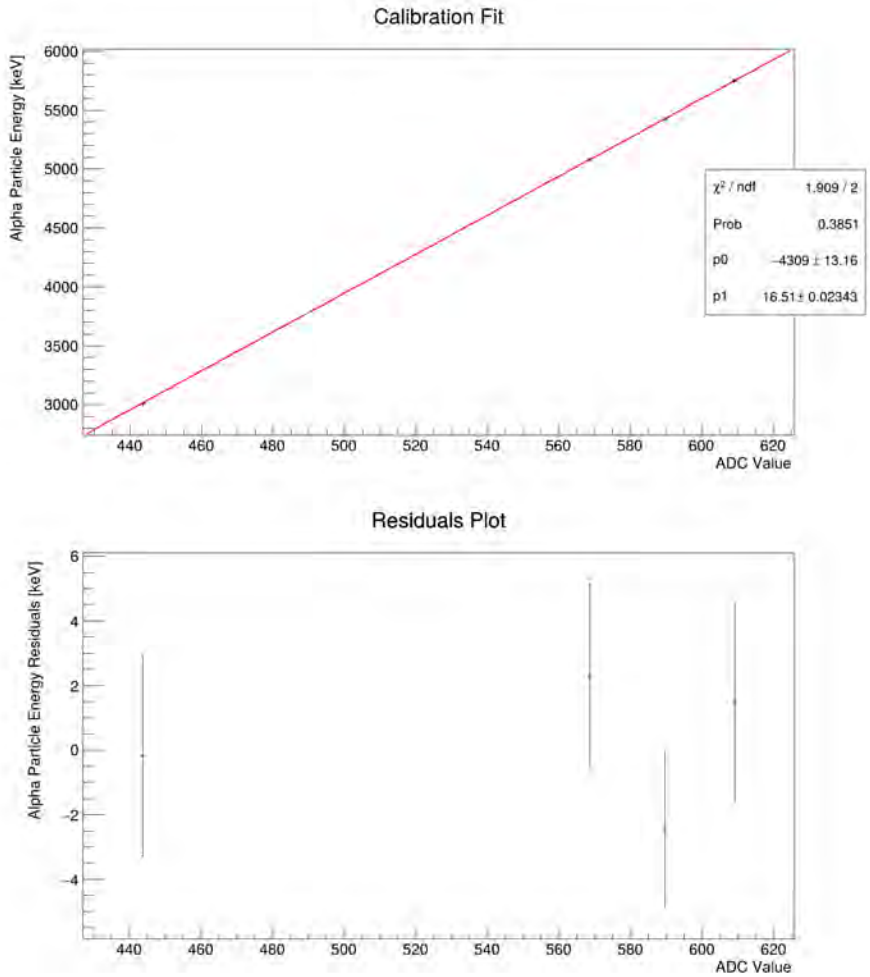

Figure 3.46: Linear energy calibration for module 0, ASIC 0, channel 45. The upper panel shows the calibration curve (energy versus ADC value), while the lower panel presents the residuals, demonstrating the quality of the linear peak.

The energy resolution of the Si array can be determined from the width of the fitted Gaussians. The resolution was quantified by extracting the full width at half maximum (FWHM) in keV for every module (during the fitting procedure, the width of the fitted peaks is set to the same value), ASIC, and channel in the array.

The resulting FWHM values are summarised in Figs. 3.47, 3.48 and 3.49,

which show energy resolution distributions for all ASICs in the three modules. These plots enable a channel-by-channel assessment of the detector performance and facilitate the identification of channels with degraded energy resolution.

It is evident that the ASICs corresponding to the n-side of the array (1 and 4) exhibit significantly worse energy resolution compared to the p-side (0, 2, 3, 5). For this reason, in the subsequent analysis, the event energy is reconstructed using only the p-side energy readout. The p-side ASICs typically exhibit an energy resolution of approximately 100 keV (FWHM), with ASIC 0 in all three modules showing noticeably worse performance, with typical FWHM values of the order of 200 keV. It is important to note that ASIC 0 is located farthest from the source. Consequently, the α particles impinging on sensors connected to ASIC 0 are detected at a smaller angle between their trajectory and the detector surface. As a result, they lose more energy in the dead layer of the Si detector and experience the largest energy straggling in this region, leading to a further degradation of the energy resolution.

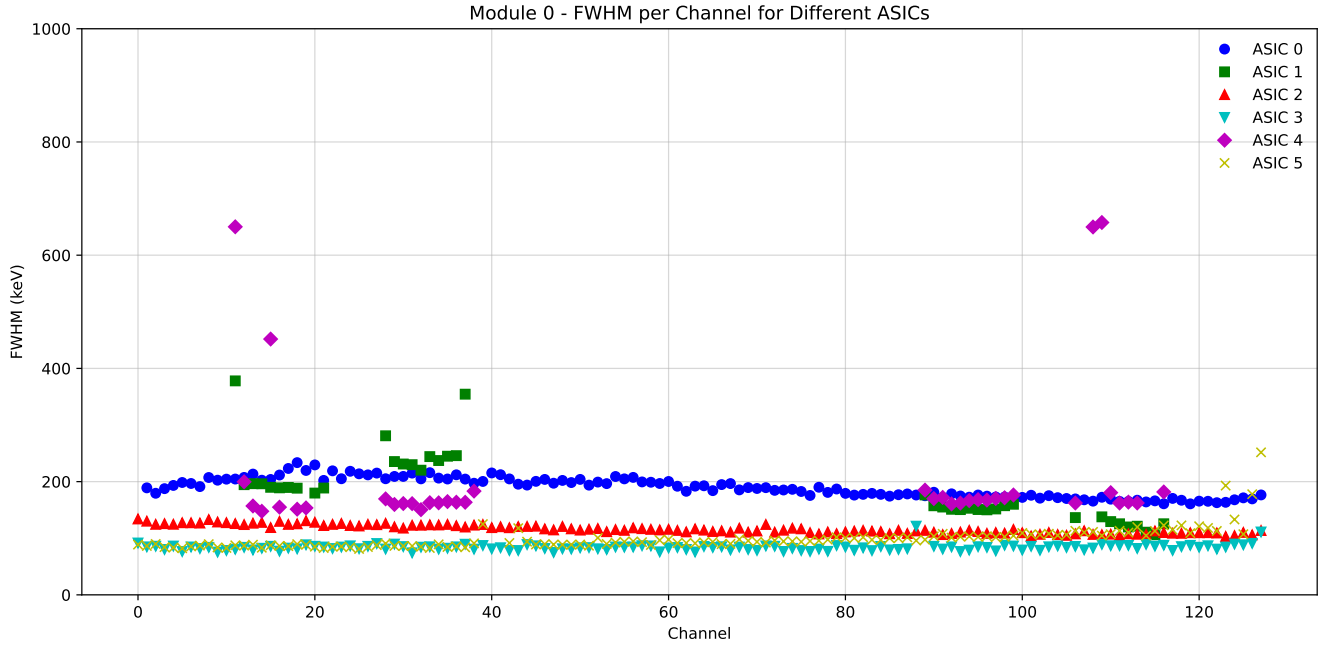

Figure 3.47: Energy resolution (FWHM in keV) for all calibrated channels connected to module 0. Each data point corresponds to an individual strip channel after linear energy calibration. ASICS 1 and 4 are connected to n-side strips. They each have 4×11 channels connected.

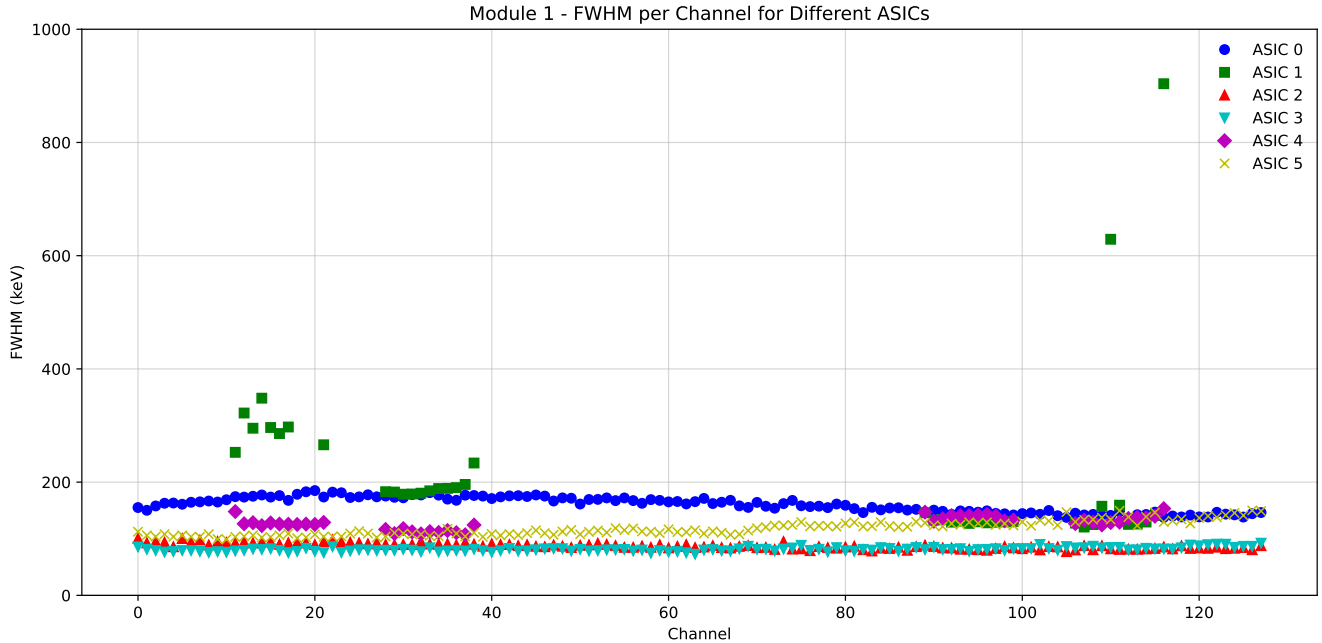

Figure 3.48: Energy resolution (FWHM in keV) for all calibrated channels connected to module 1. Each data point corresponds to an individual strip channel after linear energy calibration. ASICS 1 and 4 are connected to n-side strips. They each have 4×11 channels connected.

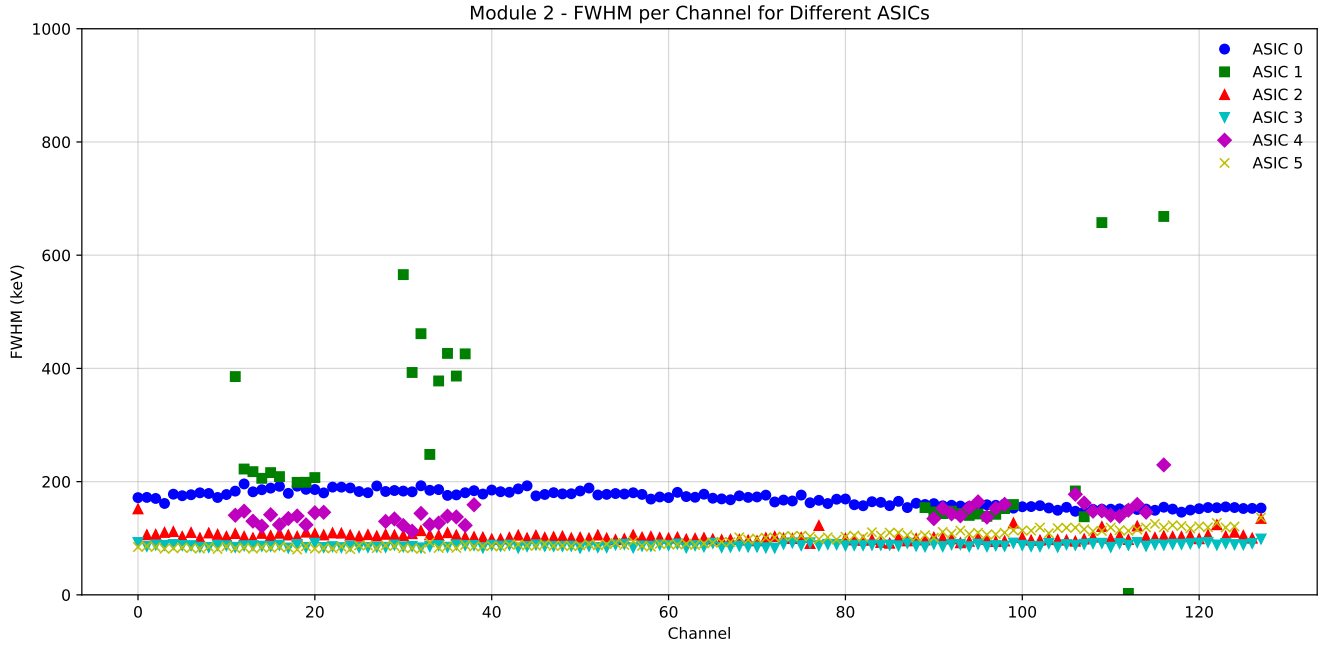

Figure 3.49: Energy resolution (FWHM in keV) for all calibrated channels connected to module 2. Each data point corresponds to an individual strip channel after linear energy calibration. ASICS 1 and 4 are connected to n-side strips. They each have 4×11 channels connected.

3.9.3 Overview of data from the ISS Si array

In this section, experimental results will be discussed, as opposed to the calibration discussed in the previous section.

Figure 3.50 shows the energies of the particles detected in the ISS Si array as a function of their detected positions relative to the target. The left panel shows data taken with the CD_2 target, while the right panel shows data taken with the C target. No software gates are applied. In the CD_2 target data, clear lines are visible in the spectrum, which are signatures of the population of discrete states in the recoiling ^{233}U nuclei. These structures are absent in the C target data, as expected.

The corresponding excitation energy spectra are shown in Fig. 3.51. The left panel shows data taken with the CD_2 target, while the right plot shows data taken with the C target. For the CD_2 target data, excited states populated in the ^{232}U(d,p)^{233}U reaction are visible, corresponding to the bands observed in Fig. 3.50. In contrast, the spectrum obtained with the C target exhibits a smooth behaviour, with a significant and relatively flat background originating from reactions with carbon.

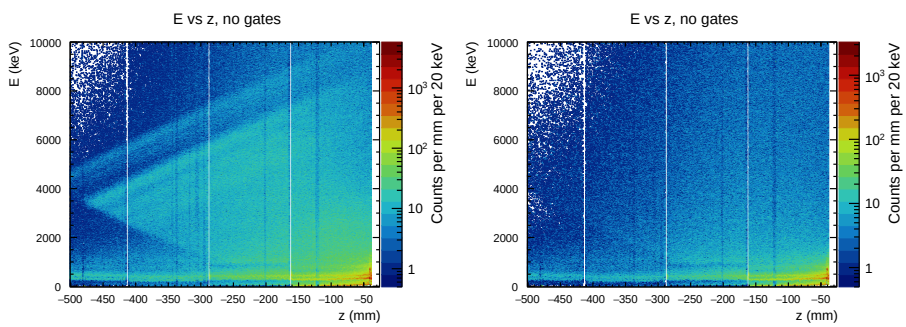

Figure 3.50: Energy of the particles detected in the ISS Si array as a function of their detection position relative to the target. The left panel shows data taken with the CD_2 target, while the right panel shows data taken with the C target. No software gates are applied. The horizontal band with increased counts at $E \approx 500$ keV, extending up to approximately 1000 keV is caused by noise in the array. The diagonal structures correspond to different excited states populated in ^{233}U.

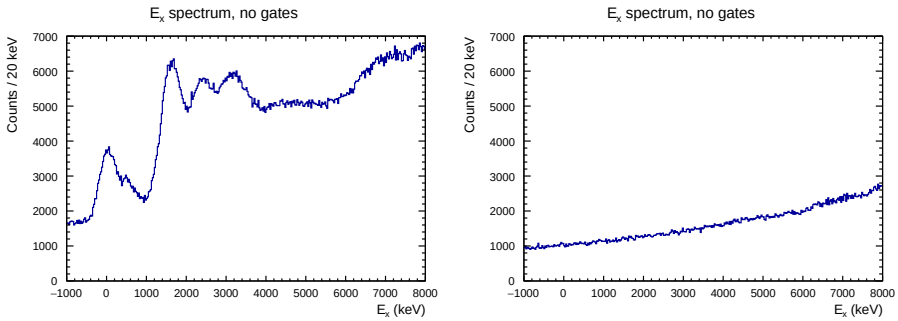

Figure 3.51: Excitation energy spectra reconstructed from particles detected in the ISS Si array. The left panel shows data taken with the CD_2 target, while the right panel shows data taken with the C target. No software gates are applied.

To extract the fission barrier of ^{233}U, it is necessary to examine the excitation energy spectra gated on the detection of one, or preferably two, fission fragments in coincidence. By comparing these spectra for the CD_2 and C targets, it is possible to subtract the carbon contribution from the CD_2 data by appropriately scaling and subtracting the C target spectrum. However, due to the challenges associated with the unambiguous identification of fission fragments from the reaction (described in the following subsection), the extraction of the fission barrier is still in progress.

3.9.4 Fission fragment detectors

Figure 3.52 shows the $\Delta E - E$ plot for particles detected in the fission fragment telescope using statistics collected in all runs in the experiment using the CD_2 and C targets, respectively. The fission fragment detector's gain-matching and calibration parameters were obtained from [117]. The spectra exhibit an almost identical shape, which suggests that there is a significant experimental background originating from reactions of the radioactive ^{232}U beam with carbon. However, a slight asymmetry can be observed: the data taken with the CD_2 target show more counts in the region corresponding to higher energies registered in the ΔE layer.

Moreover, the spectra exhibit distinguishable lines corresponding to different nuclear charges produced in the reactions. This is illustrated in Fig. 3.53, which shows the projection of the Fig. 3.52 plot onto the y-axis (energy deposited in the ΔE layer) after applying a linear correction along the x-axis (residual energy). Work on identifying these charges is ongoing at the time of writing this thesis.

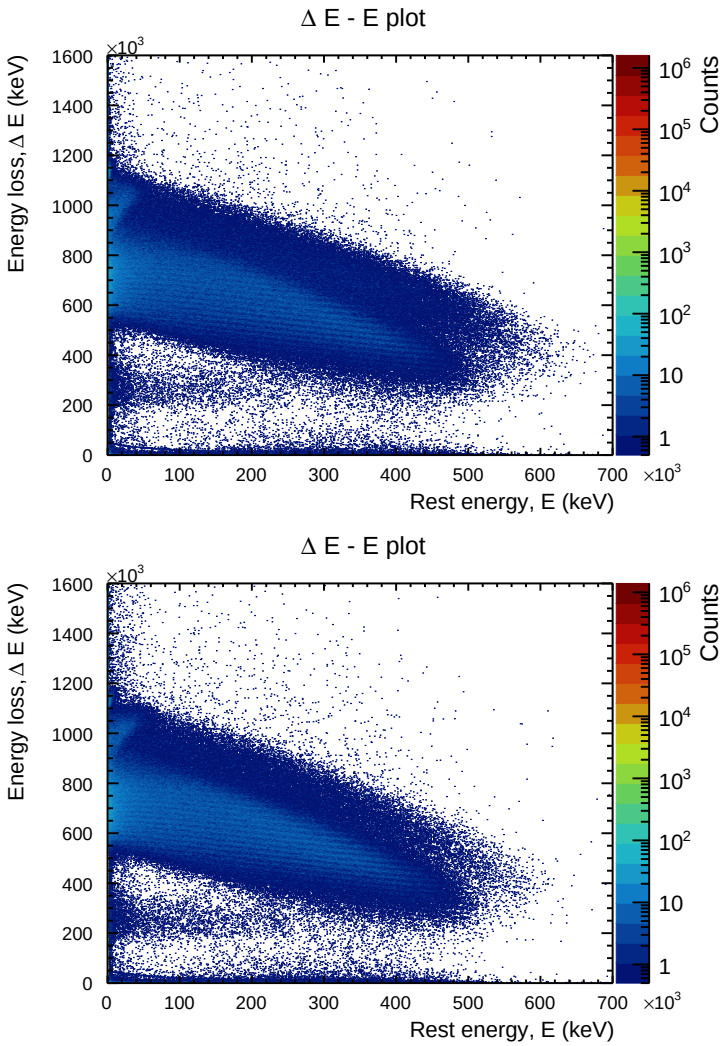

Figure 3.52: $\Delta E - E$ spectrum measured with the fission fragment telescope. The upper spectrum includes all runs with the CD_2 target, while the lower spectrum includes all runs using C target. The distinguishable lines are corresponding to different nuclear charges produced in the reactions.

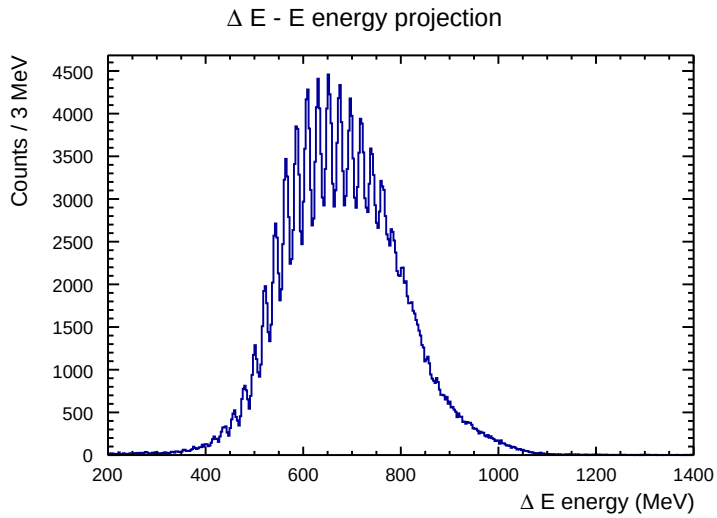

Figure 3.53: Projection of the $\Delta E - E$ spectrum onto the ΔE axis after applying a linear correction to the residual energy (E). Distinct lines corresponding to different nuclear charges produced in the reactions are visible. The plots shows the data obtained with the CD_2 target.

Figure 3.54 shows a $\Delta E - \Delta E$ plot for two particles detected in the fission fragment detector in coincidence in a single event. The upper panel presents data obtained with the CD_2 target, while the lower plot shows data obtained with the C target. A quasi-elliptical structure is visible in both plots, extending from approximately 200 MeV to 1000 MeV along both axes. This structure is believed to originate from fission, as the energy of one fission fragment is inversely correlated with the energy of the other. The structure does not exhibit a perfectly elliptical shape, which is believed to arise from the non-ideal detection efficiency of the detector system, particularly for the coincident detection of light and heavy fission fragments (the detection setup was optimised for the case of ^{230}Ac, and it was not possible to change the distance between the fission fragment detector and the target during the experiment). As a result, parts of the spectrum are effectively cut out. Work on simulating the efficiency and understanding the spectra is ongoing.

In addition, a shadow of the elliptical structure (referred to here as a "wing") is visible in the background, shifted towards higher energies relative to the main structure. The origin of that second structure is currently unknown. To investigate its origin, individual experimental runs were inspected. During the experiment, the ^{232}U beam could be extracted both with and without protons from the PS Booster hitting the primary ISOLDE target. Consequently, some runs

were taken without protons impinging on the ISOLDE target (during periods when ISOLDE did not receive protons from the PS Booster), while others were taken with protons.

We therefore investigated whether there were differences in the spectra under these two conditions. Figure 3.55 shows $\Delta E - \Delta E$ plots for two runs taken with the CD_2 target. The upper panel corresponds to a run with protons on the primary ISOLDE target, while the lower panel shows a run taken without protons.

This comparison indicates that the wing structure is correlated with the presence of protons on the primary ISOLDE target. The statistical significance of the wing structure was evaluated by comparing a ratio of the number of counts in the wing structure to the number of counts in the quasi-elliptical structure. It was found that, for runs with protons on the ISOLDE target, this ratio is approximately an order of magnitude larger than for runs without protons.

This observation may suggest that, with protons irradiation, an additional beam contaminant is produced with a charge-to-mass ratio sufficiently similar to that of ^{232}U in the 59^+ charge state to pass through HIE-ISOLDE. Work on identifying possible beam contaminants is ongoing, and we are in contact with ISOLDE beam experts regarding this issue. An analogue comparison for runs using the C target is shown in Fig. 3.56.

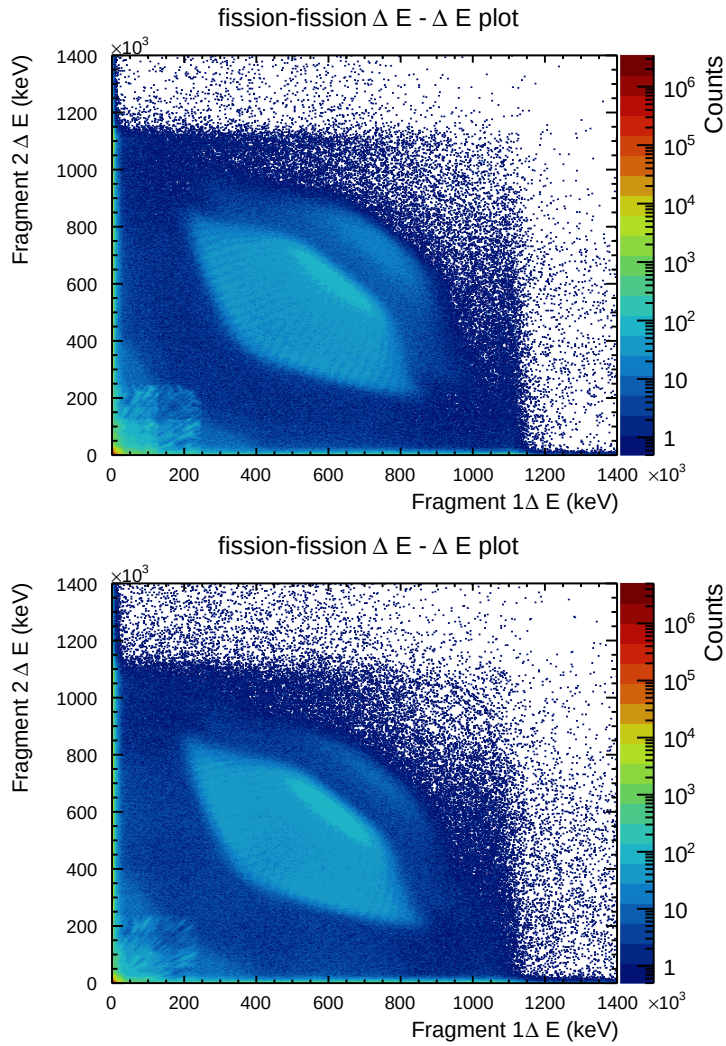

Figure 3.54: Energy of fission fragment 1 measured in the ΔE layer versus energy of fission fragment 2 measured in the ΔE layer. The upper panel shows all data obtained with the CD_2 target, while the lower panel shows data obtained with the C target.

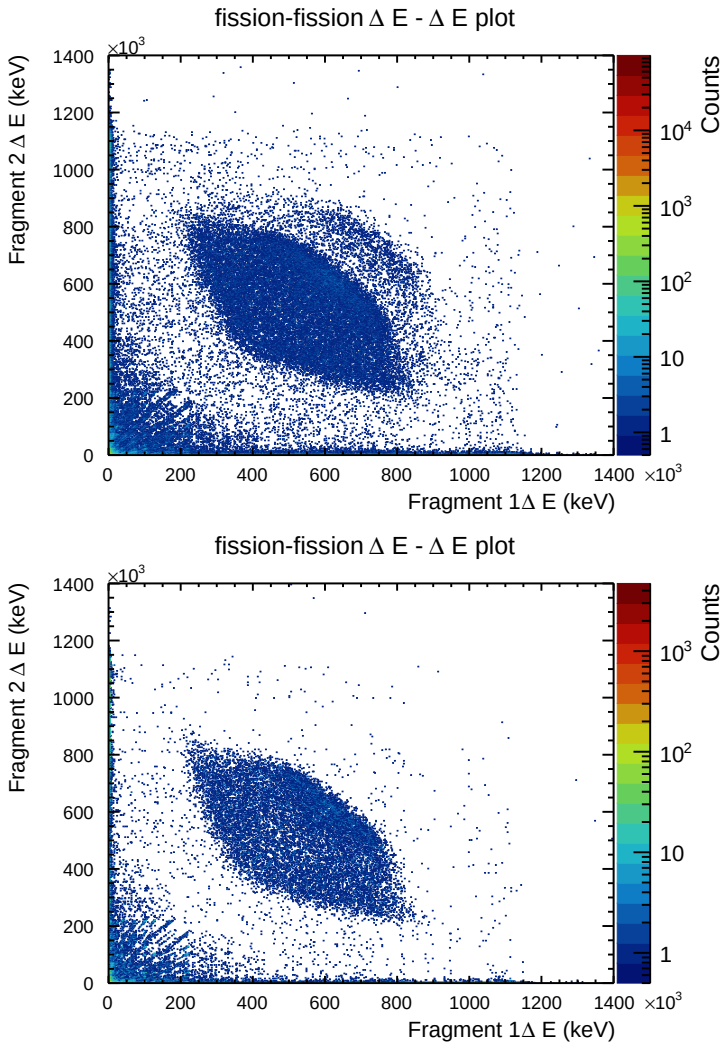

Figure 3.55: $\Delta E - \Delta E$ spectra for two runs using the CD_2 target. The upper panel is from a run taken with protons from the PS Booster on the primary ISOLDE target, while the lower panel shows a run taken without protons. The wing structure visible in the upper panel is correlated with the presence of protons on the primary ISOLDE target.

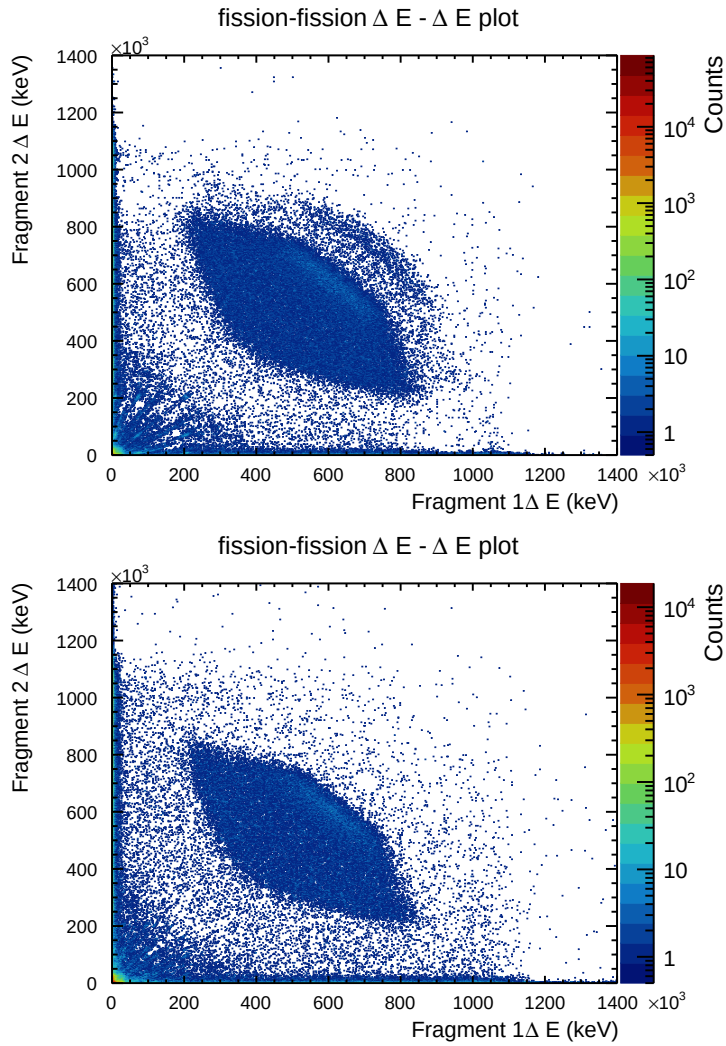

Figure 3.56: $\Delta E - \Delta E$ spectra for two runs using the C target. The upper panel corresponds to a run taken with protons from the PS Booster on the primary ISOLDE target, while the lower panel shows a run taken without protons.

3.9.5 LUME detectors

Figures 3.57 and 3.58 show the deposited energy as a function of hit position for particles detected in the LUME detectors 1 and 2, respectively. In both figures, the left panel shows all data taken with the CD_2 target, while the right panel

shows all data taken with the C target. Clear lines corresponding to different particle species are visible, as illustrated in Fig. 3.40.

A strong line at higher energies is visible in all spectra. This line corresponds to carbon elastically scattered from the target, as indicated by simulation results presented in Fig. 3.59. In the C target data, there is also a relatively strong line just above the carbon line with a steeper slope, which is believed to correspond to oxygen. A line corresponding to protons is also visible in the C target data. It is believed that the protons and oxygen originate from water contamination on the C target. In the CD_2 target data, a clear line corresponding to deuterons is visible. As expected, this line is absent in the data taken with the C target.

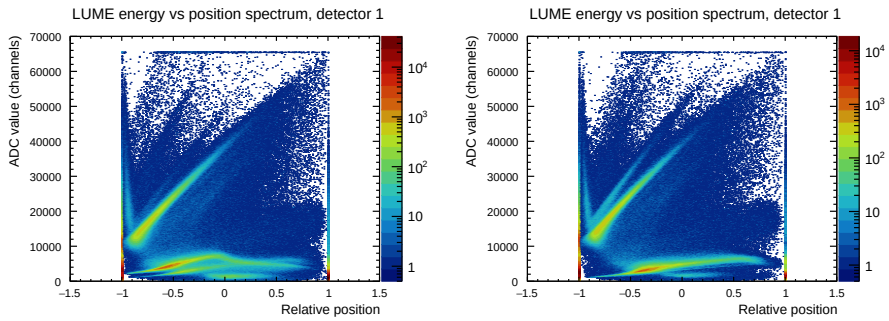

Figure 3.57: Energy as a function of hit position for particles detected in LUME detector 1. The left panel shows data taken with the CD_2 target, while the right panel shows data taken with the C target. The different branches correspond to particles identified with Fig. 3.59.

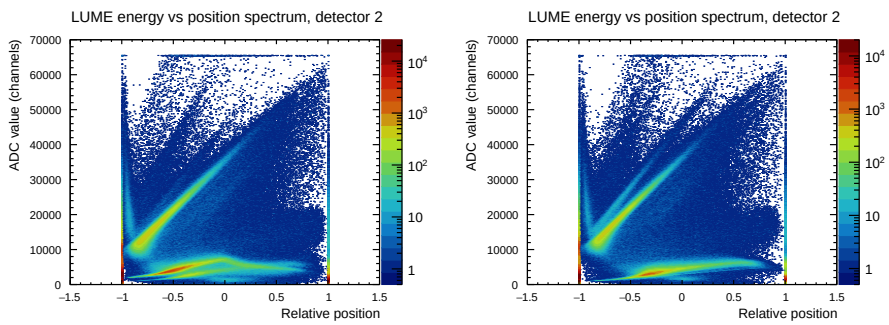

Figure 3.58: Energy as a function of hit position for particles detected in LUME detector 2. The left panel shows data taken with the CD_2 target, while the right panel shows data taken with the C target. The different branches correspond to particles identified with Fig. 3.59.

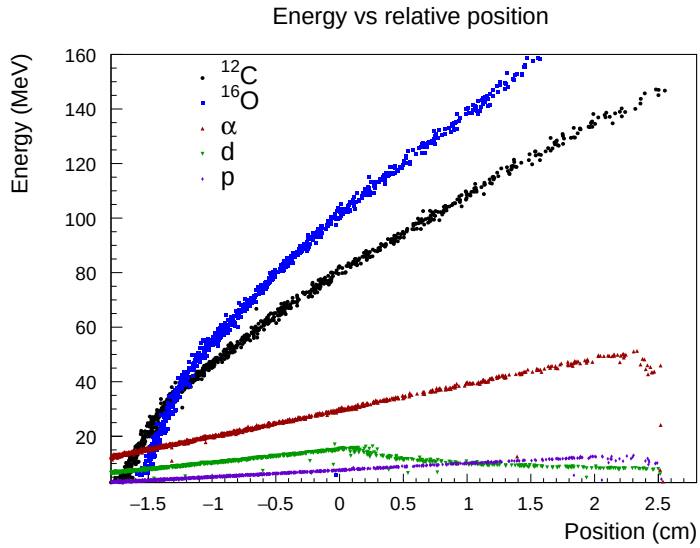

Figure 3.59: Simulated energy versus position along the detector spectra for the interaction of a ^{232}U beam with a CD_2 target at a beam energy of 7.34 MeV/u. The different structures correspond to ^{12}C, ^{16}O, α, elastically scattered deuterons (d), and protons (p). Simulations are taken from Ref.[117].

By counting the number of entries in the carbon line for both data taken with the CD_2 and the C targets for all accumulated runs, it is possible to determine the luminosities for each target. The ratio between the number of counts in the carbon line for the CD_2 target and the C target was determined to be approximately 1.4 for both LUME detectors.

3.9.6 Extraction of the fission barrier

As mentioned in Chapter 1, the solenoidal spectrometer technique has been successfully applied to transfer-induced fission measurements by studying the fission-barrier height of ^{239}U using the ^{238}U(d,pf) reaction in inverse kinematics [25]. The experiment was carried out at Argonne National Laboratory using a stable ^{238}U beam impinging on a CD_2 target, with the detection setup shown in Fig. 3.60.

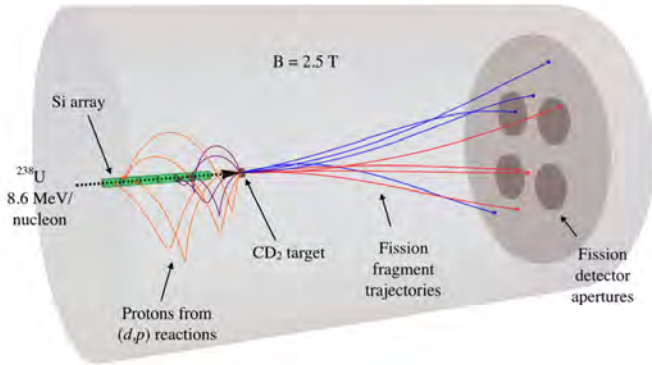

Figure 3.60: Detection setup employed in the ^{238}U(d,pf) experiment at Argonne National Laboratory. Example proton trajectories (orange and purple curves) and fission fragment trajectories (blue and red curves) are shown. Fission fragments were detected with four MWPC (multi-wire proportional counter) gas detectors, with approximately a 10 % detection efficiency compared to the CD Si telescope employed in IS739. For a detailed description, see Ref. [25].

In that experiment, the fission-barrier height was deduced by constructing the fission probability as a function of the excitation energy. The fission probability as a function of excitation energy E_x of the compound nucleus can be expressed as:

$$P_f\left(E_x\right) = \frac{N_{d,pf}\left(E_x\right)}{N_{d,p}\left(E_x\right) \cdot \epsilon_f}, \tag{3.1}$$

where $N_{d,p}(E_x)$ is the number of (d,p) events and $N_{d,pf}(E_x)$ is the number of (d,pf) events followed by fission (defined as events with at least one fission fragment detected in the fission fragment detectors). Here, ϵ_f denotes the total efficiency for detecting a fission event. The proton detection efficiency cancels out.

The carbon content of the CD_2 target led to a significant background in both the singles and fission-gated spectra. This is illustrated in Fig. 3.61, which shows the excitation-energy spectra obtained using CD_2 and C targets. The upper panel displays excitation-energy spectra for all events with a hit in the Si array (referred to as *singles*), where no coincidence with the detection of a fission fragment is required ($N_{d,p}(E_x)$). The lower panel presents the same data but gated on the detection of one or two fission fragments in the fission fragment detectors within the time-coincidence window (*coincidences*) ($N_{d,pf}(E_x)$).

Note that in both cases, the excitation energy is reconstructed as if the reaction takes place with a target deuteron. The carbon-induced background

exhibits a relatively smooth and featureless structure. It is believed that this background originates from multinucleon transfer-induced fission reactions in which light ejectiles are detected in the Si array. By scaling the spectra obtained with the pure C target to match the CD_2 target data in a region where both spectra have a similar shape, and subsequently subtracting the C contribution, it is possible to extract the excitation-energy spectra corresponding to the deuteron component. In particular, the scale can be adjusted at negative excitation energies, since they must be due to C nuclei; not to actual reactions with the assumed deuterons.

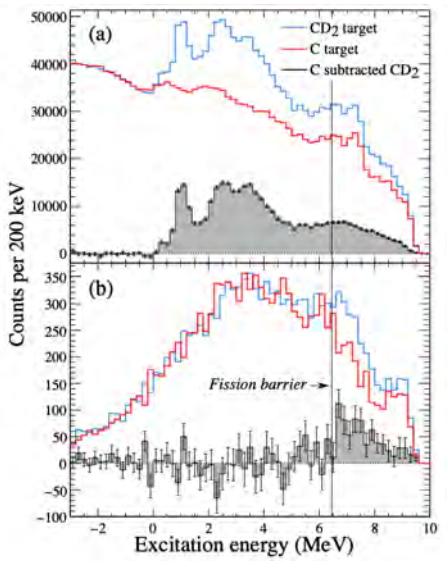

Figure 3.61: Excitation-energy spectra associated with all events for the Si array taken with both CD_2 and C targets where the C data have been scaled to match the CD_2 data, and the resulting carbon-subtracted CD_2 data. (b) Same as for (a), but for events in which ≥ 1 fission fragments are detected with the fission fragment detectors. For a detailed description, see Ref. [25].

The same approach for fission-barrier height extraction should, in principle, be applicable to the IS739 experiment. Figure 3.62 shows excitation-energy spectra associated with all events for Si array data taken with both CD_2 and C targets. The C spectra have been scaled to match the CD_2 data, and the resulting carbon-subtracted CD_2 data is also shown.

The scaling factor was determined by dividing the number of counts obtained with the CD_2 target in the range $E_x \in (-10000\ \text{keV}, -1000\ \text{keV})$ by the number of counts obtained with the C target in the same excitation-energy range. This

range was chosen such that both the CD_2 and C target spectra exhibit the same shape in that region.

The resulting scaling factor for singles data was 1.81. For coincidence events with the detection of one fission fragment, the scaling factor was 1.42, while for coincidences requiring the detection of two fission fragments, the scaling factor was 0.85.

In this analysis, a threshold of 1 MeV was applied to the energy of particles detected in the Si array in order to suppress noise.

The corresponding spectra, gated on the coincident detection of one and two fission fragments in coincidence with a proton detected in the Si array, are shown in the left and right panels of Fig. 3.63, respectively. For the fission fragment detection, a threshold of 200 MeV was applied. In the case where two fission fragments are required, an additional condition was imposed that the fission fragments must be detected in sectors separated by 16 ± 2 in the fission fragment detector (16 rings correspond to an azimuthal angle of about 180°).

The fission probability obtained using Eq. (3.1) (without applying the efficiency correction factor ϵ_f) is shown in Fig. 3.64. An excess of events is observed for excitation energies between 1 and 4 MeV, whereas significantly fewer events are present at excitation energies above 5 MeV. This behaviour is unexpected, given that the fission barrier predicted by GEF for ^{233}U is $B_\mathrm{f} = 4.34$ MeV [109]. Therefore, a higher fission probability would be expected above this energy, in contrast to what is observed.

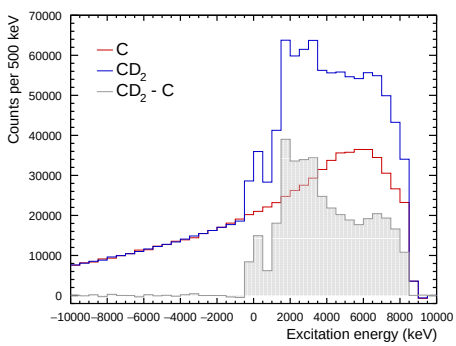

Figure 3.62: Excitation-energy spectra for all events detected in the Si array using CD_2 and C targets. The C data have been scaled to match the CD_2 data, and the carbon-subtracted CD_2 spectrum is also shown. A threshold of 1 MeV was applied to suppress low-energy noise.

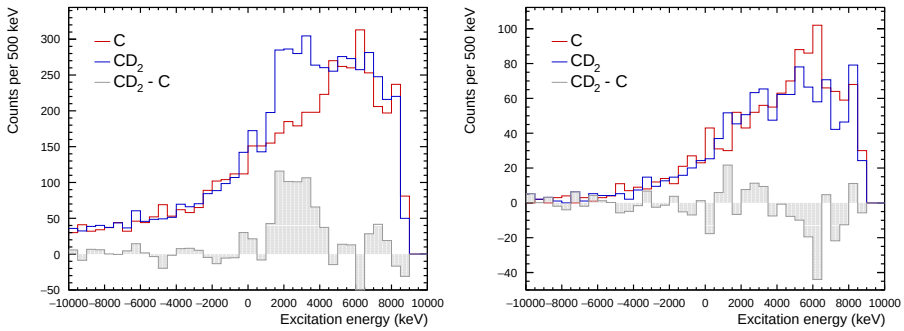

Figure 3.63: Excitation-energy spectra gated on coincident detection of fission fragments and a proton in the Si array. Left: events with at least one detected fission fragment. Right: events with two detected fission fragments satisfying the angular separation condition of 16 ± 2 detector sectors. In all cases, a threshold of 200 MeV was applied to the fission fragment energy.

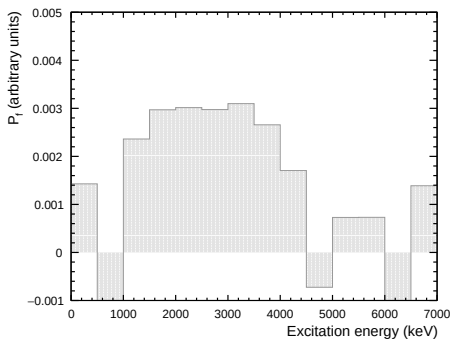

Figure 3.64: Fission probability as a function of excitation energy, obtained from the ratio of coincidence to singles spectra without applying the fission detection efficiency correction factor ϵ_f.

Currently, efforts are ongoing to investigate possible explanations for this unexpected trend, as well as to explore different threshold conditions for determining whether an event is classified as a fission event.

Several factors may contribute to the observed behaviour. One of them is an incomplete understanding of the fission fragment detection efficiency, ϵ_f, and its dependence on excitation energy. If ϵ_f decreases at higher excitation energies, this could artificially suppress the extracted fission probability in that region.

Another potential source of discrepancy is the presence of beam contaminants or competing reaction channels that result in a light ejectile emitted

upstream in the laboratory frame, accompanied by one or two heavier particles emitted downstream and subsequently detected in the fission fragment detector. These might contribute differently across the excitation-energy range and distort both the singles and coincidence spectra. Additionally, scaling and dividing the spectra introduces systematic uncertainties.

The choice of software thresholds may also play a significant role. The imposed energy cuts on the Si array and the fission fragment detectors could bias the selected event sample.

Uncertainties in the reconstruction of the excitation energy, as well as energy losses in the target and in the dead layers of detectors, although already taken into account to some degree, may lead to distortions of the observed distributions. Further systematic studies are required to quantify these effects.

3.10 Summary and outlook

This chapter has presented an experiment performed at ISOLDE, CERN aimed at developing a new method for studying the fission of neutron-rich nuclei, with the fission of ^{233}U investigated as a first case. The work presented in this thesis included the planning, proposal, design, and installation and commissioning of a new experimental setup for ISS.

The setup is capable of measuring several types of particles, including backscattered protons, fission fragments, deuterons, and γ rays in coincidence with comparably high detection efficiencies. This should enable the extraction of key observables such as the excitation energy of the formed nucleus, the fission probability as a function of excitation energy, the fission cross section, and total energy and multiplicity of the emitted γ rays. The setup operates within a 2 T magnetic field under a vacuum pressure below than 8×10^{-7} mbar. This work included extensive testing using radioactive sources, pulsers, and, finally, a stable beam. All detectors performed at least as expected, while the fission fragment detector exhibited better energy resolution than anticipated.

In preparation for the experiment, new analysis tools were developed, including the implementation of detector systems and additional spectra in the sorting code, as well as the calibration of the Si array. The author also contributed to testing the data acquisition system using newly acquired electronic modules and new software.

Efforts were made to extract physics observables from the data. This task proved more challenging than expected, for reasons that are not yet fully understood, although beam contaminants are considered as a likely cause. At the current stage of the data analysis, no final conclusions can be drawn from the IS739 experiment. However, several avenues remain to be explored in future work, which fall beyond the scope of the present thesis due to time constraints.

First, the charge resolution of the fission fragment detector could be further

exploited to better identify the reaction products observed in the experiment. This aspect is currently being investigated by another PhD student within the group.

In addition, information from γ rays emitted during the reaction may provide valuable insight into the underlying reaction mechanism. A dedicated analysis framework for extracting physics observables from the measured γ-ray data is currently being developed by a postdoctoral researcher in the group.

The identification of beam contaminants remains an ongoing effort carried out in collaboration with ISOLDE beam experts.

The ultimate goal of the IS739 experiment is to measure the fission-barrier height of a radioactive isotope using a radioactive ion beam in inverse kinematics within a solenoidal spectrometer. Once the limitations encountered in the present experiment are fully understood, a natural extension would be to perform similar measurements on other, more exotic isotopes. Such studies would improve our understanding of fission in neutron-rich nuclei and, in turn, provide a deeper insight into the role of fission in the r-process.

Chapter 4

Conclusions

This thesis has explored how nuclear structure and nuclear fission can be probed using neutron-transfer reactions in inverse kinematics. Two studies were performed, focusing on isospin symmetry breaking in light nuclei and fission of heavy systems.

In the first part, the investigation of isobaric analogue states in ^{18}O and ^{18}F is presented, using the HELIOS spectrometer at Argonne National Laboratory. By extracting and comparing relative spectroscopic factors, the degree to which isospin symmetry is conserved was examined. The results show that the analogue states exhibit very similar structures, with consistent mixtures of $\ell = 0$ and $\ell = 2$ transfer components. Within the experimental uncertainties, no statistically significant enhancement of isospin symmetry breaking is observed. At the same time, comparison with shell model calculations shows that, while the model reproduces general trends well, it fails to describe certain states, particularly those associated with cross-shell excitations.

The second part of the thesis focuses on the development of a new experimental setup at ISOLDE, CERN, aimed at studying fission in neutron-rich nuclei. A dedicated detection system was designed, installed, and commissioned within the ISS spectrometer to enable efficient, coincident measurements of reaction products, including fission fragments and γ rays. The setup performed as expected and enabled a proof-of-principle measurement of the fission of ^{233}U. Although the extraction of final physics observables is still in progress, the present work demonstrates the feasibility of the method and establishes a foundation for future studies of fission in exotic nuclei.

Taken together, these two parts of the thesis demonstrate the versatility and power of transfer reactions in inverse kinematics measured with solenoidal spectrometers as a method in nuclear physics. The same experimental approach is shown to be sensitive, both to detailed aspects of nuclear structure, such as single-particle configurations and isospin symmetry, and to more complex

reaction channels relevant for fission.

Overall, this work contributes both to our understanding of specific nuclear systems and to the advancement of experimental methods. It demonstrates that progress in nuclear physics relies on the interplay between precise measurements, theoretical interpretation, and continued advances in experimental techniques.

Appendix A

Input file for Front

```
=====================================================
 Front end for generating TWOFNR transfer data sets
 front version 20: J.A. Tostevin March 2017
=====================================================
 Data set identifier (xxx in tran.xxx: max 12 chars)
 >>>> 0d52E1982
 Output is to file:   tran.0d52E1982
 Input saved to file: in.0d52E1982
-----------------------------------------------------
 Enter title information (for info only, <= 46 chars)
 >>>> 0d52E1982
-----------------------------------------------------
 Reaction type: [ 1]  (p,d)
                [ 2]  (d,p)
                [ 3]  (n,d)
                [ 4]  (d,n)
                [ 5]  (d,t)
                [ 6]  (d,3He)
                [ 7]  (3He,d)
                [ 8]  (p,t)
                [ 9]  (t,p)
                [10]  (n,3He)
                [11]  (3He,n)
                [12]  (p,3He)
                [13]  (3He,p)
                [14]  (3He,a)
                [15]  (t,a)
-----------------------------------------------------

 Note: to store reaction transition amplitude, choose the
 negative of the above (e.g. -4 for (d,n)) and then input
 Euler angles 0,0,0 when asked. For the cross sections
 in a rotated coordinate system use the negative reaction
 type and input the appropriate three Euler angles
 ------
```

```
 Also, 5-->105 or -5-->-105 etc. for radial sensitivites
 >>>>            2

-----------------------------------------------------
 (d,p)   reaction has been selected
-----------------------------------------------------

 Entrance channel (deuteron) distorted wave:
 Options:
-----------------------------------------------------
    [0] Calculate - no print
    [1] Read      - no print
    [2] Read      -  print
    [3] Calculate -  print
    [4] Read (with tensor) - no print
    [5] Read (with tensor) - print
-----------------------------------------------------
 >>>>            0

 Exit channel (proton) distorted wave:
 Options:
-----------------------------------------------------
    [0] Calculate - no print
    [1] Read      - no print
    [2] Read      -  print
    [3] Calculate -  print
-----------------------------------------------------
 >>>>            0

 Laboratory incident energy per nucleon (MeV)
 >>>>    10.1199999
Total projectile energy =   20.2399998
 Target mass (a1) and charge (z1)
 >>>>    17.0000000       8.00000000
-----------------------------------------------------
 Integration ranges: [1] use defaults
 (defaults: 0-30 fm in 0.10 fm steps)
                     [2] specify values
-----------------------------------------------------
 Note: by default these rmax and step apply to the
 entrance channel values. To specify that the values
 apply to the exit channel, input instead -1 or -2
 >>>>            1
 integrations from 0 to   30.0000000      fm
 in  300 radial steps of 0.10000 fm
 step length in outgoing channel =   9.44444463E-02

 number of partial waves [1] default (=40)
                         [2] specify (<90)
 >>>>            1
 Input the required centre of mass angles info:
 number of angles: step (degrees): starting value
 (maximum number of angles is 181)
 (entering 0 0 0 will use 181  1.0  0.0 )
```

```
 >>>>    181.000000       1.00000000       0.00000000
-----------------------------------------------------
 sp quantum numbers L and J of transferred nucleon
 >>>>            2   2.50000000
 number of nodes in nucleon sp radial wave function
-----------------------------------------------------
 convention used here: the lowest state has nodes=0
 |+ 2|- 8|+  20|-  40|+     70|-    112|+       168|
 | 0s| 0p|1s,0d|1p,0f|2s,1d,0g|2p,1f,0h|3s,2d,1g,0i|
-----------------------------------------------------
 >>>>            0

 specify : [1] neutron separation energy (>0 MeV)
 or        [2] reaction Q-value (MeV)
 >>>>            2
 reaction Q-value (MeV)
 >>>>    4.34800005
  Separation energy is   6.57257318      MeV
=======================================================
 entrance channel cm energy    18.1094742
 exit     channel cm energy    22.4574738
 asymptotic wavenumbers and grazing angular momenta
 kin  =    1.24975383       L(in ) =    3.85616279
 kout =    1.01262534       L(out) =    3.12449408
 so L mismatch is of order     0.731668830      hbar
 from an estimated radius of    3.08553791      fm
 and a chosen L transfer of             2  hbar
=======================================================
 incident (deuteron) channel information
 nonlocality in incident channel [1] no
                                 [2] yes
 It is recommended you do NOT include a non-locality
 with an adiabatic description of the deuteron channel
 >>>>            1
 target spin in incident channel
 >>>>    2.50000000
 incident (deuteron) channel potential
            [1] from those built in
            [2] specify potential parameters
 >>>>            1
-------------------------------------------------------
 initial potential at Elab=   20.2399998      MeV
-------------------------------------------------------
 Optical potentials for DWBA

 [1] Lohr-Haeberli (A>40 8<E<13 MeV)
            see: ADNDT 17 (1976) p6
 [2] Perey-Perey (12<E<25 MeV) no spin-orbit
            see: ADNDT 17 (1976) p6
 [3] Daehnick Global (A>27 12<E<90 MeV)
     Phys. Rev. C 21, 2253 (1980)
 [4] Watanabe folding model potential from
     nucleon potentials
-------------------------------------------------------
```

```
 Adiabatic potentials for breakup

 [5] Zero range adiabatic potential
     Johnson-Soper PRC 1 (1970) 976
 [6] Finite range adiabatic potential
     Johnson-Tandy NPA 235 (1974) 56
-----------------------------------------------------
 >>>>            5
 ZR Adiabatic deuteron potential for a =  17.0
 z =  8.0 at  20.24 MeV deuteron energy
 from one of the nucleon potentials:
 Coulomb radius parameter =    1.29999995
=====================================================
 outgoing (proton) channel information
 nonlocality in outgoing channel [1] no
                                 [2] yes
 >>>>            1
 target spin in outgoing channel
 >>>>    2.00000000
 outgoing (proton) channel potential
            [1] from those built in
            [2] specify potential parameters
 >>>>            1
-----------------------------------------------------
 final potential at Elab=   23.7051105      MeV
 [1] Bechetti-Greenlees (A>40 20<E<50 MeV)
            Phys Rev 182 (1969) 1190
 [2] Chapel-Hill 89 Global set (A>40 E>10 MeV)
            Phys Rep 201 (1991) 57
 [3] Menet (30<E<60) see: ADNDT 17 (1976) p6
 [4] Perey (E<20MeV) see: ADNDT 17 (1976) p6
 [5] JLM microscopic optical potential
            Bauge implementation, PRC 58, 1120
 [6] Koning-Delaroche (KD02) global potential
            Nucl Phys A713 (2003) 231
-----------------------------------------------------
 >>>>            6
 KD02 potential for a =  18.0
 z =  8.0 at  23.71 MeV proton energy
 Coulomb radius parameter =    1.40458560
    v      rv     av     w      rw     aw
 49.736  1.149  0.675  2.270  1.149  0.675
    ws     rws    aws
  7.852  1.301  0.528
  vso    rso    aso    wso    rsoi   asoi
  5.261  0.939  0.590 -0.118  0.939  0.590
-----------------------------------------------------
 Now construct the Johnson-Tandy adiabatic potential:
 select the nucleon optical potentials for folding
 - usually these should be consistent with that used
 for the nucleon channel in (d,p), (n,d), ... etc.
 [1] Bechetti-Greenlees (A>40 20<E<50 MeV)
            Phys Rev 182 (1969) 1190
 [2] Chapel-Hill 89 Global set (A>40 E>10 MeV)
```

```
            Phys Rep 201 (1991) 57
 [3] JLM microscopic optical potential
            Bauge implementation PRC 58, 1120
 [4] Koning-Delaroche global potential
            Nucl Phys A713 (2003) 231
-----------------------------------------------------
 >>>>            4
 KD02 systematics for a =  17.0
 z =  8.0 at  10.12 MeV nucleon energy
   proton
     v      rv     av     w      rw     aw
 54.108  1.146  0.675  0.835  1.146  0.675
     ws     rws    aws
  8.149  1.302  0.528
  vso    rso    aso    wso    rsoi   asoi
  5.5515  0.9338  0.5900 -0.0400  0.9338  0.5900

   neutron
     v      rv     av     w      rw     aw
 49.448  1.146  0.675  0.906  1.146  0.675
     ws     rws    aws
  7.329  1.302  0.542
  vso    rso    aso    wso    rsoi   asoi
  5.4928  0.9338  0.5900 -0.0523  0.9338  0.5900
printout is in         303  steps of  0.100000001
potential is written to tran and folded
-----------------------------------------------------
 <p|d>  vertex constant D0
    [1] use default value -122.50 MeV fm^3/2
    [2] use Reid SC value -125.19 MeV fm^3/2
    [3] use AV18    value -126.11 MeV fm^3/2
 >>>>            1
 this gives D0^2 =    15006.2500      MeV^2 fm^3
 use this value [1] yes
                [2] no
 >>>>            1
-----------------------------------------------------
 Treatment of finite range (fnrng) of <d|p> vertex
          [1] zero-range (fnrng = 0)
          [2] local-energy (default values)
              default fnrng=0.745712 fm
          [3] local-energy (specify fnrng value)
 >>>>            2
-----------------------------------------------------
 Default finite range factor, fnrng=0.745712 fm
-----------------------------------------------------
 neutron binding potential
 radius and diffuseness (e.g. 1.25  0.65 fm)
 >>>>    1.10000002      0.649999976
 Spin-orbit: strength of l.sigma (~6.0 MeV)
 >>>>    6.00000000
 Bound state non-locality (0 usually)
 >>>>    0.00000000
 Bound state spin-orbit radius parameter
```

```
 (if 0 entered, use the same geometry as
  input for the real central interaction)
 >>>>    0.00000000

=====================================================
 tran.0d52E1982        dataset has been created:
 for the [ 17, 8] (d,p)  [ 18, 8] reaction
=====================================================
 when running twofnr the output files are as follows:

 Normal  kinematics observables
 ------------------------------
 20.0d52E1982    cm - with all spin observables
 21.0d52E1982    cm - sigma and Ay only
 22.0d52E1982    lab - light in - light out

 Inverse kinematics observables
 ------------------------------
 23.0d52E1982    lab - heavy in - heavy out
 24.0d52E1982    lab - heavy in - light out
=====================================================
```

Bibliography

[1] R. F. Casten, *Nuclear Structure from a Simple Perspective* (Oxford Univ. Press, New York, NY, 1999).

[2] P. Ring and P. Schuck, *The Nuclear Many-Body Problem* (Springer, Berlin, Heidelberg, 2004).

[3] "Nobel Symposium 152: Physics with Radioactive Beams", Physica Scripta **2013**, edited by C. Fahlander and B. Jonson, 10.1088/0031-8949/2013/T152/014023.

[4] H. Geiger and E. Marsden, "LXI. The laws of deflexion of a particles through large angles ", The London, Edinburgh, and Dublin Philosophical Magazine and Journal of Science **25**, 604–623 (1913), eprint: https://doi.org/10.1080/14786440408634197.

[5] P. G. Hansen, A. S. Jensen, and B. Jonson, "Nuclear halos", Annual Review of Nuclear and Particle Science **45**, 591–634 (1995).

[6] M. Lewitowicz, E. Widmann, and G.-E. Körner, eds., *NuPECC Long Range Plan 2024 for European Nuclear Physics* (2024).

[7] D. H. Wilkinson, ed., *Isospin in Nuclear Physics* (North-Holland Publishing Company - Amsterdam, 1969).

[8] T. Otsuka, A. Gade, O. Sorlin, T. Suzuki, and Y. Utsuno, "Evolution of shell structure in exotic nuclei", Reviews of Modern Physics **92**, 015002 (2020).

[9] D. J. Dean and M. Hjorth-Jensen, "Pairing in nuclear systems: from neutron stars to finite nuclei", Reviews of Modern Physics **75**, 607–656 (2003).

[10] A. Obertelli and H. Sagawa, *Modern nuclear physics: from fundamentals to frontiers*, UNITEXT for physics (Springer, Singapore, 2021).

[11] G. R. Satchler, *Direct nuclear reactions* (Oxford University Press, Oxford, 1983).

[12] N. K. Glendenning, *Direct nuclear reactions* (World Scientific, Singapore, 2004).

[13] H. Feshbach, A. Kerman, and R. Lemmer, "Intermediate structure and doorway states in nuclear reactions", Annals of Physics **41**, 230–286 (1967).

[14] Y. Blumenfeld, T. Nilsson, and P. V. Duppen, "Facilities and methods for radioactive ion beam production", Physica Scripta **2013**, 014023.

[15] M. Bentley and S. Lenzi, "Coulomb energy differences between high-spin states in isobaric multiplets", Progress in Particle and Nuclear Physics **59**, 497–561 (2007).

[16] M. Arnould, S. Goriely, and K. Takahashi, "The r-process of stellar nucleosynthesis: Astrophysics and nuclear physics achievements and mysteries", Physics Reports **450**, 97–213 (2007).

[17] F.-K. Thielemann, M. Eichler, I. Panov, and B. Wehmeyer, "Neutron star mergers and nucleosynthesis of heavy elements", Annual Review of Nuclear and Particle Science **67**, 253–274 (2017).

[18] J. J. Cowan, C. Sneden, J. E. Lawler, A. Aprahamian, M. Wiescher, K. Langanke, G. Martínez-Pinedo, and F.-K. Thielemann, "Origin of the heaviest elements: the rapid neutron-capture process", Rev. Mod. Phys. **93**, 015002 (2021).

[19] A. Wuosmaa, J. Schiffer, B. Back, C. Lister, and K. Rehm, "A solenoidal spectrometer for reactions in inverse kinematics", Nuclear Instruments and Methods in Physics Research Section A: Accelerators, Spectrometers, Detectors and Associated Equipment **580**, 1290–1300 (2007).

[20] J. Lighthall, B. Back, S. Baker, S. Freeman, H. Y. Lee, B. Kay, S. Marley, K. Rehm, J. Rohrer, J. Schiffer, D. Shetty, A. Vann, J. Winkelbauer, and A. Wuosmaa, "Commissioning of the HELIOS spectrometer", Nuclear Instruments and Methods in Physics Research Section A: Accelerators, Spectrometers, Detectors and Associated Equipment **622**, 97–106 (2010).

[21] A. Kawęcka, "To fission or not to fission: ^{230}Ac", Licentiate Thesis (Department of Physics, Chalmers University of Technology, 2024).

[22] W. Catford, "Nucleon transfer studies with radioactive beams", Nuclear Physics A **701**, 5th International Conference on Radioactive Nuclear Beams, 1–6 (2002).

[23] J. Chen, B. Kay, C. Hoffman, T. Tang, I. Tolstukhin, D. Bazin, R. Lubna, Y. Ayyad, S. Beceiro-Novo, B. Coombes, S. Freeman, L. Gaffney, R. Garg, H. Jayatissa, A. Kuchera, P. MacGregor, A. Mitchell, W. Mittig, B. Monteagudo, A. Munoz-Ramos, C. Müller-Gatermann, F. Recchia, N. Rijal, C. Santamaria, M. Serikow, D. Sharp, J. Smith, J. Stecenko, G. Wilson, A. Wuosmaa, C. Yuan, J. Zamora, and Y. Zhang, "Evolution of the nuclear spin-orbit splitting explored via the ^{32}Si(d,p)^{33}Si reaction using SOLARIS", Physics Letters B **853**, 138678 (2024).

[24] P. T. MacGregor, D. K. Sharp, S. J. Freeman, C. R. Hoffman, B. P. Kay, T. L. Tang, L. P. Gaffney, E. F. Baader, M. J. G. Borge, P. A. Butler, W. N. Catford, B. D. Cropper, G. de Angelis, J. Konki, T. Kröll, M. Labiche, I. H. Lazarus, R. S. Lubna, I. Martel, D. G. McNeel, R. D. Page, O. Poleshchuk, R. Raabe, F. Recchia, and J. Yang, "Evolution of single-particle structure near the $N = 20$ island of inversion", Phys. Rev. C **104**, L051301 (2021).

[25] S. A. Bennett, K. Garrett, D. K. Sharp, S. J. Freeman, A. G. Smith, T. J. Wright, B. P. Kay, T. L. Tang, I. A. Tolstukhin, Y. Ayyad, J. Chen, P. J. Davies, A. Dolan, L. P. Gaffney, A. Heinz, C. R. Hoffman, C. Müller-Gatermann, R. D. Page, and G. L. Wilson, "Direct Determination of Fission-Barrier Heights Using Light-Ion Transfer in Inverse Kinematics", Physical Review Letters **130**, 202501 (2023).

[26] J. A. Nolen and J. P. Schiffer, "Coulomb Energies", Annual Review of Nuclear and Particle Science **19**, 471–526 (1969).

[27] R. G. Thomas, "An Analysis of the Energy Levels of the Mirror Nuclei, C^{13} and N^{13}", Physical Review **88**, 1109–1125 (1952).

[28] J. B. Ehrman, "On the Displacement of Corresponding Energy Levels of C^{13} and N^{13}", Physical Review **81**, 412–416 (1951).

[29] V. Margerin, G. Lotay, P. J. Woods, M. Aliotta, G. Christian, B. Davids, T. Davinson, D. T. Doherty, J. Fallis, D. Howell, O. S. Kirsebom, D. J. Mountford, A. Rojas, C. Ruiz, and J. A. Tostevin, "Inverse Kinematic Study of the ^{26g}Al(d, p)^{27}Al Reaction and Implications for Destruction of ^{26}Al in Wolf-Rayet and Asymptotic Giant Branch Stars", Physical Review Letters **115**, 062701 (2015).

[30] G. Lotay, J. Henderson, W. Catford, F. Ali, J. Berean, N. Bernier, S. Bhattacharjee, M. Bowry, R. Caballero-Folch, B. Davids, T. Drake, A. Garnsworthy, F. Ghazi Moradi, S. Gillespie, B. Greaves, G. Hackman, S. Hallam, D. Hymers, E. Kasanda, D. Levy, B. Luna, A. Mathews, Z. Meisel, M. Moukaddam, D. Muecher, B. Olaizola, N. Orr, H. Patel, M. Rajabali, Y. Saito, J. Smallcombe, M. Spencer, C. Svensson, K. Whitmore, and M. Williams, "Single neutron transfer on ^{23}Ne and its relevance for the pathway of nucleosynthesis in astrophysical X-ray bursts", Physics Letters B **833**, 137361 (2022).

[31] M. H. Macfarlane and S. Pieper, Ptolemy. A Program for Heavy-Ion Direct-reaction Calculations.

[32] From ENSDF database as of December 10, 2025. Version available at http://www.nndc.bnl.gov/ensarchivals/.

[33] K. Yagi, Y. Nakajima, K. Katori, Y. Awaya, and M. Fujioka, "Energy-level structure of O^{19}, O^{18} and O^{17} investigated by (d,p) reactions with 15 MeV deuterons", Nuclear Physics **41**, 584–603 (1963).

[34] R. Moreh and T. Daniels, "The level structure of ^{18}O and ^{19}O by stripping reactions", Nuclear Physics **74**, 403–416 (1965).

[35] J. L. Wiza, R. Middleton, and P. V. Hewka, "$O^{17}(d, p)O^{18}$ Reaction and Nuclear Structure of O^{18}", Physical Review **141**, 975–979 (1966).

[36] T. K. Li, D. Dehnhard, R. E. Brown, and P. J. Ellis, "Investigation of the $(d_{\frac{5}{2}})^2$ and $(d_{\frac{5}{2}} s_{\frac{1}{2}})$ two-particle configurations in ^{18}O using the $^{17}O(d,p)^{18}O$ reaction at 18 MeV", Physical Review C **13**, 55–67 (1976).

[37] F. Ajzenberg-Selove, "Energy levels of light nuclei A = 18–20", Nuclear Physics A **190**, 1–18 (1972).

[38] F. Ajzenberg-Selove, "Energy levels of light nuclei A = 18–20", Nuclear Physics A **300**, 1–224 (1978).

[39] L. M. Polsky, C. H. Holbrow, and R. Middleton, "Nuclear Structure of F^{18}", Physical Review **186**, 966–977 (1969).

[40] V. Landre, P. Aguer, G. Bogaert, A. Lefebvre, J. P. Thibaud, S. Fortier, J. M. Maison, and J. Vernotte, "$^{17}O(^3He,d)^{18}F$ reaction and its implication in the ^{17}O destruction in the CNO cycle in stars", Physical Review C **40**, 1972–1984 (1989).

[41] J. Henderson, private communication.

[42] B. Brown and W. Rae, "The Shell-Model Code NuShellX@MSU", Nuclear Data Sheets **120**, 115–118 (2014).

[43] A. Magilligan and B. A. Brown, "New isospin-breaking "USD" Hamiltonians for the sd shell", Physical Review C **101**, 064312 (2020).

[44] R. S. Lubna, K. Kravvaris, S. L. Tabor, V. Tripathi, A. Volya, E. Rubino, J. M. Allmond, B. Abromeit, L. T. Baby, and T. C. Hensley, "Structure of ^{38}Cl and the quest for a comprehensive shell model interaction", Phys. Rev. C **100**, 034308 (2019).

[45] R. S. Lubna, K. Kravvaris, S. L. Tabor, V. Tripathi, E. Rubino, and A. Volya, "Evolution of the $N = 20$ and 28 shell gaps and two-particle-two-hole states in the FSU interaction", Physical Review Research **2**, 043342 (2020).

[46] J. Arianer and R. Geller, "The Advanced Positive Heavy Ion Sources", Annual Review of Nuclear and Particle Science **31**, 19–51 (1981).

[47] R. Scott, J. McLain, and R Vondrasek, "Status update of the ATLAS ECR ion sources at Argonne National Laboratory", Journal of Physics: Conference Series **2743**, 012093 (2024).

[48] R. Vondrasek, J. McLain, and R. Scott, "Design for an 18 GHz Open Hexapole Electron Cyclotron Resonance Ion Source", Journal of Physics: Conference Series **2743**, 012044 (2024).

[49] ATLAS Facility Layout with Beam Locations, https://www.anl.gov/atlas/reference/atlas-facility-layout-with-beam-locations, (accessed online 07.11.2025).

[50] L. Bollinger, R. Pardo, K. Shepard, J. Bogaty, B. Clifft, F. Munson, and G. Zinkann, "First operational experience with the positive-ion injector of ATLAS", Nuclear Instruments and Methods in Physics Research Section A: Accelerators, Spectrometers, Detectors and Associated Equipment **328**, 221–230 (1993).

[51] J. McLain, C. A. Dickerson, M. Gott, J. Greene, J. Nolen, G. Savard, J. Song, and R. C. Vondrasek, "nuCARIBU : An upgrade for the CARIBU facility at the Argonne Tandem Linac Accelerator System", Journal of Physics: Conference Series **2244**, 012062 (2022).

[52] R. C. Vondrasek, C. A. Dickerson, M. Hendricks, P. Ostroumov, R. Pardo, G. Savard, R. Scott, and G. Zinkann, "Charge breeding of radioactive isotopes at the CARIBU facility with an electron beam ion source", Review of Scientific Instruments **89**, 052402 (2018).

[53] C. Hoffman, T. Tang, M. Avila, Y. Ayyad, K. Brown, J. Chen, K. Chipps, H. Jayatissa, B. Kay, C. Müller-Gatermann, H. Ong, J. Song, and G. Wilson, "In-flight production of an isomeric beam of ^{16}N", Nuclear Instruments and Methods in Physics Research Section A: Accelerators, Spectrometers, Detectors and Associated Equipment **1032**, 166612 (2022).

[54] K. Rehm, J. Greene, B. Harss, D. Henderson, C. Jiang, R. Pardo, B. Zabransky, and M. Paul, "Gas cell targets for experiments with radioactive beams", Nuclear Instruments and Methods in Physics Research Section A: Accelerators, Spectrometers, Detectors and Associated Equipment **647**, 3–9 (2011).

[55] R. Pardo, J. Bogaty, S. Sharamentov, and K. Rehm, "An RF beam sweeper for purifying in-flight produced secondary ion beams at ATLAS", Nuclear Instruments and Methods in Physics Research Section A: Accelerators, Spectrometers, Detectors and Associated Equipment **790**, 1–5 (2015).

[56] J. C. Lighthall, "Commissioning of the Helical Orbit Spectrometer: A New Device for Measuring Nuclear Reactions in Inverse Kinematics", PhD thesis (Western Michigan University, 2011).

[57] Micron Semiconductor Ltd. QQQ1. 2025. http://www.micronsemiconductor.co.uk/product/qqq1/ (date accessed 11.12.2025).

[58] digios, https://github.com/calemhoffman/digios (accessed online 18.12.2025).

[59] R. Brun and F. Rademakers, "ROOT: An object oriented data analysis framework", Nuclear Instruments and Methods in Physics Research Section A: Accelerators, Spectrometers, Detectors and Associated Equipment **389**, edited by M. Werlen and D. Perret-Gallix, 81–86 (1997).

[60] H. An and C. Cai, "Global deuteron optical model potential for the energy range up to 183 MeV", Physical Review C **73**, 054605 (2006).

[61] Y. Han, Y. Shi, and Q. Shen, "Deuteron global optical model potential for energies up to 200 MeV", Physical Review C **74**, 044615 (2006).

[62] J. Bojowald, H. Machner, H. Nann, W. Oelert, M. Rogge, and P. Turek, "Elastic deuteron scattering and optical model parameters at energies up to 100 MeV", Physical Review C **38**, 1153–1163 (1988).

[63] W. W. Daehnick, J. D. Childs, and Z. Vrcelj, "Global optical model potential for elastic deuteron scattering from 12 to 90 MeV", Physical Review C **21**, 2253–2274 (1980).

[64] J. Lohr and W. Haeberli, "Elastic scattering of 9–13 MeV vector polarized deuterons", Nuclear Physics A **232**, 381–397 (1974).

[65] C. Perey and F. Perey, "Compilation of phenomenological optical-model parameters 1954–1975", Atomic Data and Nuclear Data Tables **17**, 1–101 (1976).

[66] Y. Zhang, D. Y. Pang, and J. L. Lou, "Optical model potential for deuteron elastic scattering with 1p-shell nuclei", Physical Review C **94**, 014619 (2016).

[67] A. Koning and J. Delaroche, "Local and global nucleon optical models from 1 keV to 200 MeV", Nuclear Physics A **713**, 231–310 (2003).

[68] R. Varner, W. Thompson, T. McAbee, E. Ludwig, and T. Clegg, "A global nucleon optical model potential", Physics Reports **201**, 57–119 (1991).

[69] J. J. H. Menet, E. E. Gross, J. J. Malanify, and A. Zucker, "Total-Reaction-Cross-Section Measurements for 30-60-MeV Protons and the Imaginary Optical Potential", Physical Review C **4**, 1114–1129 (1971).

[70] F. D. Becchetti and G. W. Greenlees, "Nucleon-Nucleus Optical-Model Parameters, $A > 40$, $E < 50$ MeV", Physical Review **182**, 1190–1209 (1969).

[71] F. G. Perey, "Optical-Model Analysis of Proton Elastic Scattering in the Range of 9 to 22 MeV", Physical Review **131**, 745–763 (1963).

[72] B. P. Kay, J. P. Schiffer, and S. J. Freeman, "Quenching of Cross Sections in Nucleon Transfer Reactions", Phys. Rev. Lett. **111**, 042502 (2013).

[73] B. P. Kay, private communication.

[74] J. A. Tostevin, M. Toyama, M. Igarashi, and N. Kishida, *TWOFNR and FRONT reaction codes*, University of Surrey version of the TWOFNR code and the FRONT code, Private communication, n.d.

[75] R. C. Johnson and P. J. R. Soper, "Contribution of Deuteron Breakup Channels to Deuteron Stripping and Elastic Scattering", Physical Review C **1**, 976–990 (1970).

[76] R. Johnson and P. Tandy, "An approximate three-body theory of deuteron stripping", Nuclear Physics A **235**, 56–74 (1974).

[77] C. Patrignani et al., "Review of particle physics", Chinese Physics C **40**, 100001 (2016).

[78] P. Federman and I. Talmi, "Shell model and deformed states in O^{18}", Physics Letters **15**, 165–167 (1965).

[79] J. B. McGrory and B. H. Wildenthal, "Shell-Model Calculations for $A = 18, 19,$ and20 Nuclei with Core Excitation Included Explicity", Physical Review C **7**, 974–993 (1973).

[80] O. Poleshchuk, R. Raabe, S. Ceruti, A. Ceulemans, H. De Witte, T. Marchi, A. Mentana, J. Refsgaard, and J. Yang, "The SpecMAT active target", Nuclear Instruments and Methods in Physics Research Section A: Accelerators, Spectrometers, Detectors and Associated Equipment **1015**, 165765 (2021).

[81] P. D. Parker, "$N^{14}(\alpha,\gamma)F^{18}$ Reaction", Physical Review **173**, 1021–1025 (1968).

[82] R. Bernas, E. Gradsztajn, H. Reeves, and E. Schatzman, "On the nucleosynthesis of lithium, beryllium, and boron", Annals of Physics **44**, 426–478 (1967).

[83] J. A. Johnson, "Populating the periodic table: Nucleosynthesis of the elements", Science **363**, 474–478 (2019), eprint: `https://www.science.org/doi/pdf/10.1126/science.aau9540`.

[84] E. M. Burbidge, G. R. Burbidge, W. A. Fowler, and F. Hoyle, "Synthesis of the Elements in Stars", Reviews of Modern Physics **29**, 547–650 (1957).

[85] A. G. Cameron, "Stellar evolution, nuclear astrophysics, and nucleogenesis. Second edition", (1957).

[86] S. Navas et al., "Review of particle physics", Phys. Rev. D **110**, 030001 (2024).

[87] M Lugaro, S. W. Campbell, V D'Orazi, A. I. Karakas, D. A. Garcia-Hernandez, R. J. Stancliffe, G Tagliente, C Iliadis, and T Rauscher, "Current hot questions on the s process in AGB stars", Journal of Physics: Conference Series **665**, 012021 (2016).

[88] Cseh, B., Lugaro, M., D´Orazi, V., de Castro, D. B., Pereira, C. B., Karakas, A. I., Molnár, L., Plachy, E., Szabó, R., Pignatari, M., and Cristallo, S., "The s process in AGB stars as constrained by a large sample of barium stars", Astronomy & Astrophysics **620**, A146 (2018).

[89] M. Lugaro, F. Herwig, J. C. Lattanzio, R. Gallino, and O. Straniero, "s-Process Nucleosynthesis in Asymptotic Giant Branch Stars: A Test for Stellar Evolution", The Astrophysical Journal **586**, 1305 (2003).

[90] F. Käppeler, R. Gallino, S. Bisterzo, and W. Aoki, "The *s* process: Nuclear physics, stellar models, and observations", Reviews of Modern Physics **83**, 157–193 (2011).

[91] D. Watson, C. Hansen, J. Selsing, A. Koch, D. Malesani, A. Andersen, J. Fynbo, A. Arcones, A. Bauswein, S. Covino, A. Grado, K. Heintz, L. Hunt, C. Kouveliotou, G. Leloudas, A. Levan, P. Mazzali, and E. Pian, "Identification of strontium in the merger of two neutron stars", Nature **574**, 497–500 (2019).

[92] B. P. Abbott et al., "GW170817: Observation of Gravitational Waves from a Binary Neutron Star Inspiral", Physical Review Letters **119**, 161101 (2017).

[93] C. Sneden and J. J. Cowan, "Genesis of the Heaviest Elements in the Milky Way Galaxy", Science **299**, 70–75 (2003), eprint: `https://www.science.org/doi/pdf/10.1126/science.1077506`.

[94] W. Weterings, C. Bracco, L. O. Jorat, M. Meddahi, R. Noulibos, and P. Van Trappen, "The new injection region of the CERN PS Booster", in 10th International Particle Accelerator Conference (2019), WEPMP039.

[95] F. Landua, "The CERN accelerator complex layout in 2022. Complexe des accélérateurs du CERN en janvier 2022", General Photo (2022).

[96] R. Catherall, W. Andreazza, M. Breitenfeldt, A. Dorsival, G. J. Focker, T. P. Gharsa, T. J. Giles, J.-L. Grenard, F. Locci, and P. Martins, "The ISOLDE facility", Journal of Physics G: Nuclear and Particle Physics **44**, 094002 (2017).

[97] F. Wenander, "Charge breeding of radioactive ions with EBIS and EBIT", Journal of Instrumentation **5**, C10004 (2010).

[98] F. Wenander et al., REXEBIS, the electron beam ion source for the REX-ISOLDE project: Design and simulations, CERN OPEN-2000-320 (2000).

[99] M. J. G. Borge and K. Riisager, "HIE-ISOLDE, the project and the physics opportunities", The European Physical Journal A **52**, 10.1140/epja/i2016-16334-4 (2016).

[100] Y. Kadi, M. A. Fraser and A.Papageorgiou-Koufidou, "HIE-ISOLDE: Technical Design Report for the Energy Upgrade", CERN Yellow Reports: Monographs, Vol. 1/2018, CERN-2018-002-M(CERN, Geneva, 2018).

[101] G. Battistoni, F. Cerutti, A. Fassò, A. Ferrari, S. Muraro, J. Ranft, S. Roesler, and P. R. Sala, "The FLUKA code: description and benchmarking", AIP Conference Proceedings **896**, 31–49 (2007), eprint: https://pubs.aip.org/aip/acp/article-pdf/896/1/31/11572161/31_1_online.pdf.

[102] R. Wolf, F. Wienholtz, D. Atanasov, D. Beck, K. Blaum, C. Borgmann, F. Herfurth, M. Kowalska, S. Kreim, Y. A. Litvinov, D. Lunney, V. Manea, D. Neidherr, M. Rosenbusch, L. Schweikhard, J. Stanja, and K. Zuber, "ISOLTRAP's multi-reflection time-of-flight mass separator/spectrometer", International Journal of Mass Spectrometry **349-350**, 100 years of Mass Spectrometry, 123–133 (2013).

[103] M. Au, private communication.

[104] S. Yuan, W. Yang, Y. Xu, Q. Pan, B. Xiong, J. He, D. Wang, Y. Li, T. Ma, and Z. Yang, "Search for β-delayed fission of the heavy neutron-rich isotope ^{230}Ac", The European Physical Journal A - Hadrons and Nuclei **10**, 1–3 (2001).

[105] M. Thoennessen and G. F. Bertsch, "Threshold for dissipative fission", Physical Review Letters **71**, 4303–4306 (1993).

[106] S. Bara, A. Algora, B. Andel, A. N. Andreyev, S. Antalic, R. A. Bark, M. J. G. Borge, A. Camaiani, T. E. Cocolios, J. G. Cubiss, H. De Witte, C. M. Fajardo-Zambrano, Z. Favier, L. M. Fraile, H. O. U. Fynbo, S. Goriely, R. Grzywacz, M. Heines, F. Ivandikov, J. D. Johnson, P. M. Jones, D. S. Judson, J. Klimo, A. Korgul, M. Labiche, R. Lica, M. Madurga, N. Marginean, C. Mihait, familyi=v., given=J., giveni=J., „ E. Nácher, C. Neacsu, J. N. Orce, C. A. A. Page, R. D. Page, J. Pakarinen, P. Papadakis, A. Perea, M. Piersa-Siłkowska, Z. Podolyák, R. Raabe, W. Ryssens, A. Sánchez-Fernándezík, familyi=v., given=A., giveni=A., „ O. Tengblad, J. M. Udías, V. Van Den Bergh, P. Van Duppen, N. Warr, A. Youssef, and Z. Yue, "New upper limits for β-delayed fission probabilities of ^{230,232}Fr and ^{230,232,234}Ac", Phys. Rev. C **111**, 065803 (2025).

[107] S. Wang, "Evaluation of nuclear fission barrier parameters for 17 nuclei", in *Communication of nuclear data progress no. 26*, edited by T. Li and Y. Zhang (China Nuclear Data Center, China Nuclear Information Centre, 2001).

[108] E.-M. Eckert, A. Kühmichel, J. Pochodzalla, K. D. Hildenbrand, U. Lynen, W. F. J. Müller, H. J. Rabe, H. Sann, H. Stelzer, W. Trautmann, R. Trockel, R. Wada, C. Cerruti, P. Lhénoret, R. Lucas, C. Mazur, C. Ng, M. Ribrag, E. Tomasi, A. Demeyer, and D. Guinet, "Transient times of fission in ^{40}Ar+^{232}Th peripheral collisions", Physical Review Letters **64**, 2483–2486 (1990).

[109] K.-H. Schmidt, B. Jurado, C. Amouroux, and C. Schmitt, "General Description of Fission Observables: GEF Model Code", Nuclear Data Sheets **131**, Special Issue on Nuclear Reaction Data, 107–221 (2016).

[110] L. Ghys, A. N. Andreyev, S. Antalic, M. Huyse, and P. Van Duppen, "Empirical description of β-delayed fission partial half-lives", Physical Review C **91**, 044314 (2015).

[111] H. T. Törnqvist, private communication.

[112] ISOLDE Solenoidal Spectrometer Collaboration, *Si-detector array*, `https://isolde-solenoidal-spectrometer.web.cern.ch/setup/si-detector-array`, Accessed online: 2026-01-27.

[113] E. A. M. Jensen, private communication.

[114] A. Dolan, "Probing the origins of deformation in the neutron-rich ^{93}Kr nucleus using transfer reactions with the ISOLDE Solenoidal Spectrometer", PhD thesis (University of Liverpool, 2024).

[115] A. Svärdström, private communication.

[116] Micron Semiconductor Ltd. S3. 2026. http://www.micronsemiconductor.co.uk/product/s3/ (date accessed 27.01.2026).

[117] M. V. Managlia, private communication.

[118] O. Tarasov and D. Bazin, "LISE++: Radioactive beam production with in-flight separators", Nuclear Instruments and Methods in Physics Research Section B: Beam Interactions with Materials and Atoms **266**, Proceedings of the XVth International Conference on Electromagnetic Isotope Separators and Techniques Related to their Applications, 4657–4664 (2008).

[119] J. N. Wilson et al., "Angular momentum generation in nuclear fission", Nature (London) **590**, 566 –570 (2021).

[120] S. Bennett, D. Sharp, and T. Wright, *Probing the fission and radiative decay of the ^{235}U+n system using (d,pf) and (d,pγ) reactions*, tech. rep. (CERN, Geneva, 2023).

[121] H. Johansson, R. Thies, S. Buller, A. Heinz, S. Lindberg, J. Magnusson, T. Nilsson, T. Rathsman, and the R3B collaboration, "GGLAND—command line simulations", in *GSI Scientific Report 2013*, edited by K. Große (GSI Helmholtzzentrum für Schwerionenforschung, Darmstadt, 2014), p. 154.

[122] J. Allison, K. Amako, J. Apostolakis, P. Arce, M. Asai, T. Aso, E. Bagli, A. Bagulya, S. Banerjee, G. Barrand, B. Beck, A. Bogdanov, D. Brandt, J. Brown, H. Burkhardt, P. Canal, D. Cano-Ott, S. Chauvie, K. Cho, G. Cirrone, G. Cooperman, M. Cortés-Giraldo, G. Cosmo, G. Cuttone, G. Depaola, L. Desorgher, X. Dong, A. Dotti, V. Elvira, G. Folger, Z. Francis, A. Galoyan, L. Garnier, M. Gayer, K. Genser, V. Grichine, S. Guatelli, P. Guèye, P. Gumplinger, A. Howard, I. Hřivnáčová, S. Hwang, S. Incerti, A. Ivanchenko, V. Ivanchenko, F. Jones, S. Jun, P. Kaitaniemi, N. Karakatsanis, M. Karamitros, M. Kelsey, A. Kimura, T. Koi, H. Kurashige, A. Lechner, S. Lee, F. Longo, M. Maire, D. Mancusi, A. Mantero, E. Mendoza, B. Morgan, K. Murakami, T. Nikitina, L. Pandola, P. Paprocki, J. Perl, I. Petrović, M. Pia, W. Pokorski, J. Quesada, M. Raine, M. Reis, A. Ribon, A. Ristić Fira, F. Romano, G. Russo, G. Santin, T. Sasaki, D. Sawkey, J. Shin, I. Strakovsky, A. Taborda, S. Tanaka, B. Tomé, T. Toshito, H. Tran, P. Truscott, L. Urban, V. Uzhinsky, J. Verbeke, M. Verderi, B. Wendt, H. Wenzel, D. Wright, D. Wright, T. Yamashita, J. Yarba, and H. Yoshida, "Recent developments in Geant4", Nuclear Instruments and Methods in Physics Research Section A: Accelerators, Spectrometers, Detectors and Associated Equipment **835**, 186–225 (2016).

[123] Liam P. Gaffney and Daniel J. Clarke and Håkan Johansson and ACeulemans and berjones and Patrick MacGregor and Hans Toshihide Törnqvist, *ISOLDESolenoidalSpectrometer/ISSSort: v3.0*, 2024.

[124] M. Shamsuzzoha Basunia and A. Chakraborty, "Nuclear Data Sheets for A=23", Nuclear Data Sheets **171**, 1–252 (2021).

[125] R. Stoller, M. Toloczko, G. Was, A. Certain, S. Dwaraknath, and F. Garner, "On the use of SRIM for computing radiation damage exposure", Nuclear Instruments and Methods in Physics Research Section B: Beam Interactions with Materials and Atoms **310**, 75–80 (2013).

[126] G. T. Seaborg, J. W. Gofman, and R. W. Stoughton, "Nuclear Properties of U^{233}: A New Fissionable Isotope of Uranium", Physical Review **71**, 378–378 (1947).

[127] R. Elson, W. Bentley, A. Ghiorso, and Q. Van Winkle, "The Thermal Neutron Fission and Capture Cross Section of U^{232}", Physical Review **89**, 320–320 (1953).

[128] G. Auchampaugh, C. Bowman, and J. Evans, "Neutron-induced fission cross section of ^{232}U", Nuclear Physics A **112**, 329–336 (1968).

[129] G. James, "The fission cross section of U^{232} from 4 eV to 400 eV", Nuclear Physics **55**, 517–522 (1964).

[130] B. I. Fursov, E. Y. Baranov, M. P. Klemyshev, B. F. Samylin, G. N. Smirenkin, and Y. M. Turchin, "Measurement of the fission cross section of ^{232}U for neutron energies in the range 0.06-7.40 MeV", Soviet Atomic Energy (Engl. Transl.); (United States) **61:5** (1987).